

https://dspace.org/

Insights into silver(I) phosphine complexes in targeting cell death and metastatic mechanisms in malignant cell lines

Roberts, Kim Elli

2023-09

University of the Witwatersrand, Johannesburg

https://hdl.handle.net/10539/42991

Roberts, Kim Elli. (2023). Insights into silver(I) phosphine complexes in targeting cell death and metastatic mechanisms in malignant cell lines. [PhD thesis, University of the Witwatersrand, Johannesburg]. https://hdl.handle.net/10539/42991

Downloaded from a DSpace repository. https://dspace.org/



UNIVERSITY OF THE
WITWATERSRAND,
JOHANNESBURG

Insights into silver(I) phosphine complexes in targeting cell death and metastatic mechanisms in malignant cell lines

by

Kim Elli Roberts

(959064)

Thesis

Submitted in fulfilment of the requirements for the degree

Philosophiae Doctor

in

Molecular and Cell Biology

in the Faculty of Science, University of the Witwatersrand, Johannesburg, South Africa

Supervisor: Professor Marianne Cronjé

Co-supervisor: Dr. Zelinda Engelbrecht

September 2023


It is in your hands to make of our world a better one for all.
- NELSON MANDELA

DECLARATION

I declare that this thesis is my own, unaided work. It is being submitted for the degree in Doctor of Philosophy, at The University of Witwatersrand, Johannesburg.

It has not been submitted before for any degree of examination at any other University.



_____

(Signature of candidate)

The **1st day** of **September 2023**, at **The University of Witwatersrand**, **Johannesburg**.

ACKNOWLEDGEMENTS

"If I have seen further, it is by standing on the shoulders of giants" – Sir Isaac Newton.

Throughout the experimental work and writing of this dissertation, I have received a significant amount of assistance.

I would like to extend my deepest gratitude and thanks to:

My supervisor, Prof. Marianne Cronjé, for her invaluable knowledge, assistance, and guidance throughout this study. Thank you for all your advice, motivation and for allowing me this opportunity. I am so grateful. I will always remember your "Himalayan Mountain" advice and use it throughout my life.

My co-supervisor and dearest friend, Dr. Zelinda Engelbrecht, thank you for your guidance, advice, continual expertise, and for always being by my side through it all. Thank you for the many conversations and laughs during our countless coffee (and carrot cake) breaks. You are truly appreciated.

Dr. Kariska Potgieter, for your help in the characterization of the silver (I) phosphine complexes and NMR spectra data analyzes.

Dr. Herna de Wit, for running the molecular docking simulations. Thank you for your time, kind assistance, and support.

To my loving parents, Michael and Conny Roberts, for always believing in me and encouraging me in all I have chosen to do. Thank you for your constant support and words of wisdom. Mom, you have been my rock throughout my studies. I cannot thank you enough for encouraging me throughout this challenging journey and for being a guiding light (I know I have given you countless grey hairs).

My twin brother, Justin Roberts, you always manage to put a smile on my face no matter the time of day. Thank you for being my source of resilience.

All my friends in and out of the lab, who have been supportive, especially Dr. Caitlynd Myburgh, Dr. Heather-Anne Byth-Illing, Dr. Mizan Ferreira, Alisha Badal, and Dr. Vanessa Meyer - thank you for all the encouragement.

My loving companions, who have sat by my side through early mornings and late nights with a wagging tail, a wet nose, and an extra cuddle when needed. ~ In memory of our beloved Treasure.

Lastly, I would like to thank God, the Almighty, who has guided me through difficulties and granted me countless blessings. I will keep trusting in you - **Psalm 61:2**.



DEDICATION

"May there be comfort in knowing that someone so special will never be forgotten"
– Julie Hébert

Elli Frieda Hassmann

(1928 - 1974)

Franz Hassmann

(1928 - 2012)

Leslie Lyall Roberts

(1934 - 2005)

Mark Richard Roberts

(1960 - 2006)

Danilo Mario Patini



(1989 - 2020)

PREFACE

Articles published, submitted and produced:

- Engelbrecht, Z., Roberts, K.E., Hussan, A., Amenuvor, G., Cronjé, M.J., Darkwa, J., Makhubela, B.C.E. and Sitole, L. 2020. Synthesis and anti-cancer activity of bis-amino-phosphine ligand and its ruthenium(II) complexes. *Bioorganic & Medicinal Chemistry Letter.* 30:(127492): 1 - 6.

- Roberts, K.E., Engelbrecht, Z., Potgieter, K., Meijboom, R. and Cronjé, M.J. 2023. Silver(I) bromide phosphines induce mitochondrial-mediated apoptosis in malignant human colorectal cells. *Submitted to Cytotechnology*.

Previous Patents

- Meijboom, R. and Cronjé, M.J. (2016). The use of silver(I) mono-dentate and bi-dentate phosphine complexes as active pharmaceutical ingredients (API's) including anticancer agents. South African Patent Application - 2015/08527.

- Meijboom, R. and Cronjé, M.J. (2013). Use of silver(I) complexes as anticancer agents. WO2013084185 A1, South Africa.

TABLE OF CONTENTS

List of Abbreviations and Symbols I
List of Figures VI
List of Tables XII
List of Molecular Docking Data XIII

Abstract 1
Narrative 2

Chapter One: Literature review 4
1.1. Introduction to Cancer 4
1.1.1. Cancer's toll 4
1.1.2. Defining cancer 4
1.2. Therapeutic Modalities for Cancer 8
1.2.1. Surgery 8
1.2.2. Radiotherapy 8
1.2.3. Photodynamic therapy 9
1.2.4. Immunotherapy 9
1.2.5. Hormone therapy 10
1.2.6. Metallo-chemotherapeutic drugs 10
(a) *Platinum complexes* 11
(b) *Gold complexes* 12
(c) *Ruthenium complexes* 13
(d) *Copper complexes* 13
(e) *Silver complexes* 14
1.3. Types of Cancer 15
1.3.1. Lung cancer 15
1.3.2. Colorectal cancer 16
1.3.3. Liver cancer 17
1.3.4. Breast cancer 17
1.3.5. Melanoma 20
1.3.6. Oesophageal cancer 20
1.4. Cell Death Pathways 22
1.4.1. Apoptosis 22
(a) *Proapoptotic function of GAPDH* 23
(b) *Intrinsic (mitochondrial-mediated) apoptotic pathway* 24
(c) *Extrinsic (receptor-mediated) apoptotic pathway* 25
1.4.2. Necrosis 27
1.4.3. Autophagy 28
1.5. Molecular Docking: a drug discovery tool 30
1.6. Hypotheses and Aims 32
1.7. Experimental Objectives 33
Part I 33
Part II 33
Part III 34
Part IV 35

Chapter Two:

In vitro cytotoxicity screening of silver(I) phosphine complexes in malignant and non-malignant cell lines 36

2.1. Prologue 36
2.2. Experimental methodology 37
2.2.1. 2.2.1. Silver(I) phosphine complexes: synthesis 37
2.2.1.1. Preparation and characterization 37
2.2.1.2. Synthesis of 1:2 [Silver(I)dicyclohexylphenylphosphine]SCN (Complex **1**) 37
2.2.1.3. Synthesis of 1:3 [Silver(I)dicyclohexylphenylphosphine]SCN (Complex **2**) 38
2.2.1.4. Synthesis of 1:2 [Silver(I) diphenyl-2-pyridylphoshine]Cl (Complex **3**) 39
2.2.1.5. Synthesis of 1:3 [Silver(I) diphenyl-2-pyridylphosphine]Br (Complex **4**) 39
2.2.1.6. Synthesis of 1:1 [Silver(I) benzylphenylphosphine]SCN (Complex **5**) 40
2.2.1.7. Synthesis of 1:2 [Silver(I) benzyldiphenylphosphine]SCN (Complex **6**) 40
2.2.1.8. Synthesis of 1:3 [Silver(I) benzyldiphenylphosphine]NO_3 (Complex **7**) 41
2.2.1.9. Synthesis of 1:1 [Silver(I) 4-(dimethylamino)phenyldiphenyl phosphine]NO_3 (Complex **8**) 41
2.2.1.10. Synthesis of 1:2 [Silver(I) 4-(dimethylamino)phenyldiphenyl phosphine]NO3 (Complex **9**) 42
2.2.1.11. Synthesis of 1:3 [Silver(I) 4-(dimethylamino)phenyldiphenyl phosphine]NO3 (Complex **10**) 42
2.2.1.12. Synthesis of 1:3 [Silver(I) 4-(dimethylamino)phenyldiphenyl phosphine]Cl (Complex **11**) 43
2.2.1.13. Synthesis of 1:2 [Silver(I) 4-(dimethylamino)phenyldiphenyl phosphine]Br (Complex **12**) 44
2.2.1.14. Synthesis of 1:3 [Silver(I) 4-(dimethylamino)phenyldiphenyl phosphine]Br (Complex **13**) 44
2.2.1.15. Complex and cisplatin preparation 45
2.2.2. Cell culture 45
2.2.2.1. Cell lines 45
2.2.2.2. Culturing cells from stock 46
2.2.2.3. Sub-culturing of cells 48
2.2.2.4. Cellular counting 48
2.2.3. Cytotoxicity screening studies 48
2.2.3.1. Plating of cells 48
2.2.3.2. Cell treatments 49
2.2.3.3. alamarBlue® proliferation assay 49
2.2.3.4. Cellular morphology of non-malignant cells 49
2.2.3.5. Dose responsive studies on malignant cells lines 49
2.2.4. Statistical analysis 50
2.3. Results 51
2.3.1. Silver(I) phosphine complexes' structural details 51
2.3.2. Silver(I) phosphine complexes were investigated for their cytotoxicity in non-malignant cells 54
2.3.3. Identifying successful silver(I) phosphine complexes in malignant cell lines 60
2.3.4. IC_{50} concentration studies on malignant cell lines 69
2.4. Discussion 81
2.4.1. Cytotoxic abilities of silver(I) phosphine complexes and ligands 81

(a) *Complex degree of cytotoxicity on non-malignant cells* 81
(b) *Toxicity investigations of the ligands on non-malignant and malignant cells* 82
(c) *Complex cytotoxicity against malignant cell lines* 83
2.4.2. The relationship between dosage and effect 84

Chapter Three:
Apoptogenic properties of selected complexes on malignant A375, Hep-G2 and HT-29 cell lines **86**
3.1. Prologue **86**
3.2. Experimental methodology **87**
3.2.1. Cell culture 87
3.2.1.1. Plating of cells 87
3.2.1.2. Cell treatments 87
3.2.2. Antiproliferative and apoptogenic analyses 87
3.2.2.1. Cellular morphology 87
3.2.2.2. Measuring GAPDH activity 88
3.2.2.3. CellTiter-Glo® luminescent cell viability assay 88
3.2.2.4. Quantification of cellular populations' reactive oxygen species 88
3.2.2.5. Measuring the change in mitochondrial membrane potential (ΔΨm) 89
3.2.2.6. Determining potential mode of cell death 89
3.2.2.7. Measuring cytochrome P450 (*CYP1B1*) activity 90
3.2.3. Investigation into possible antimetastatic activity of silver(I) phosphine complexes 90
3.2.3.1. Determining the inhibition of A549 lateral motility by selected silver(I) phosphine complexes 90
3.2.4. Statistical analysis 90
3.3. Results **91**
3.3.1. Morphological changes 91
3.3.2. Metabolic changes 91
3.3.3. Production of reactive oxygen species 99
3.3.4. Mechanism of action 103
3.3.5. CYP450: a possible drug target 111
3.3.6. Antimetastatic potential of silver(I) phosphine complexes on A549 cells 113
3.4. Discussion **120**
3.4.1. An investigation into the mitochondrial-mediated apoptotic pathway 120
3.4.1.1. Insights into energy metabolism, reactive oxygen species and apoptosis 121
(a) *Change in GAPDH activity, ATP levels and cellular viability* 121
(b) *Generation of reactive oxygen species* 123
(c) *Mitochondrial potential and cellular plasma permeabilization* 124
3.4.1.2. Identifying the mode of cell death in malignant cell lines 126
Ptd-L-Ser externalization 126
3.4.1.3. Targeting the drug metabolizing CYP450 enzyme 126
3.4.2. Silver(I) phosphine complexes inhibit A549 cell migration 128

Chapter Four:
A mini-comparative study investigating the key anticancer activities of three silver(I) phosphine complexes in MCF-7 and MDA-MB-231 breast cell lines **130**
4.1. Prologue **130**

4.2. Experimental methodology **131**
4.2.1. Cell culture 131
4.2.1.1. Plating of cells 131
4.2.1.2. Cell treatments 131
4.2.2. Antiproliferative and apoptogenic analyses 131
4.2.2.1. Cellular morphology 131
4.2.2.2. Quantification of cellular populations' reactive oxygen species 132
4.2.2.3. Measuring the change in mitochondrial membrane potential (ΔΨm) 132
4.2.2.4. Determining potential mode of cell death 132
4.2.2.5. Fluorescence microscopy analysis of mitochondrial integrity and the nuclear morphology 132
4.2.3. Statistical analysis 133
4.3. Results **134**
4.3.1. Morphological changes 134
4.3.2. Production of reactive oxygen species 134
4.3.3. Mechanism of action 139
4.4. Discussion **148**
4.4.1. Mechanistic insights into the anticancer effects of silver(I) phosphine complexes in MCF-7 and MDA-MB-231 cells 148
(a) *Generation of reactive oxygen species* 148
(b) *Mitochondrial potential and cellular plasma permeabilization* 149
3.4.1.2. Identifying the mode of cell death in malignant MCF-7 and MDA-MB-231 cell lines 150
(a) *Ptd-L-Ser externalization* 150
(b) *Cytochrome c release, mitochondrial integrity and DNA damage* 150

Chapter Five: *In silico* molecular modelling of complex 4 with estrogen receptors alpha and beta **152**
5.1. Prologue **152**
5.2. Methods **153**
5.2.1. Molecular Dockings 153
5.2.1.1. Protein preparation 153
5.2.1.2. Ligand (Complex **4**) preparation 154
5.2.1.3. Grid parameter file preparation and dockings 154
5.2.1.4. Visualization and analysis of docking results 155
5.3. Results **156**
5.4. Discussion **163**

Chapter Six: Conclusion **166**
6.1. Summary of final conclusions 166
6.2. Future studies 167

Reference List **169**

Appendix I 184
Appendix II 188
Appendix III 191

LIST OF ABBREVIATIONS AND SYMBOLS

Abbreviations

A375	malignant human melanoma cell line
A549	malignant human alveolar basal epithelial cell line
ADT4	AutoDockTools version 4.2.6
ADPP	[(2-aminophenyl)diphenylphosphine]
AgBr	silver bromide
AgCl	silver chloride
Ag-NHC	silver(I)N-heterocyclic carbene
$AgNO_3$	silver nitrate
AgNPs	silver nanoparticles
AgSCN	silver thiocyanate
AIF	apoptosis-inducing factor
ALA	aminolaevulinic acid
AMP, ADP, ATP	adenosine mono-, di-, or triphosphate
AMPK	AMP-activated protein kinase
AMPP	(2-aminophenyl)phosphines AMPP [(+)-(2-aminophenyl)methylphenyl-phosphine]
ANT	adenine nucleotide translocator
Apaf-1	apoptotic protease-activating factor 1
APC	adenomatous polyposis coli
APCs	antigen-presenting cells
ATG13	autophagy related gene 13
Bak	Bcl-2 homologous antagonist/killer
Bax	Bcl-2 associated X protein
Bcl-2	B-cell leukemia/lymphoma 2 protein
BHLH	basic helix–loop–helix
BPG	bisphosphoglycerate
BRAF	v-raf murine sarcoma viral oncogene homolog B1
BRCA1	breast cancer gene 1
BRCA2	breast cancer gene 2
BSA	bovine serum albumin
^{13}**C**	carbon 13 NMR
CAD	caspase-activated DNase
CARD	caspase activation and recruitment domain
Caspases	cysteine-aspartic proteases
$CDCl_3$	deuterated chloroform
CDDP	cis-diamminedichloroplatinum / cisplatin
CDKN2A	cyclin dependent kinase inhibitor 2A/multiple tumor suppressor 1
COVID-19	coronavirus disease 2019
CTLA-4	cytotoxic T-lymphocyte-associated protein 4

CTNNB1	catenin beta 1
CYP1B1	cytochrome P450 family 1B1 (isoform)
CYP450	cytochrome P450
CypA	cyclophilin A
CypD	cyclophilin D
dATP	deoxyadenosine triphosphate
DD	death domain
DED	death effector domain
Desolv	desolvation
DHE	dihydroethidium
DHE	dihydroergotamine mesylate
DISC	induced signalling cascade
DMEM	Dulbecco's minimal essential medium
DMSO	dimethyl sulfoxide
DPPE	bis(diphenylphosphino)ethane
DR	death receptor
DSV	discovery studio visualizer
EAC	adenocarcinoma
EDTA	disodium ethylenediaminetetraacetate dehydrate
EGFR	epithelial growth factor receptor
ELK1	ETS like-1 protein
EPG5	ectopic P-granules 5 autophagy tethering factor
ER	estrogen receptor
ER-α	estrogen receptor alpha (PBD ID: 6WOK nuclear protein)
ER-β	estrogen receptor beta (PDB ID: 2YLY receptor)
ESCC	squamous cell carcinoma
FADD	Fas-associated death domain protein
FDA	food and drug administration
FIP200	family interacting protein 200 kD kinase complex
FLC	fibrolamellar liver cancers
FMK	fluoromethyl ketone
FSC	forward scatter parameter
G-3-P	glyceraldehyde-3-phosphate
GA	genetic algorithm
GAPDH	glyceraldehyde 3-phosphate dehydrogenase
GERD	gastroesophageal reflux disorder
GPX7	glutathione peroxidase 7
GTP	guanosine triphosphate
^{1}**H**	proton NMR
H_2O_2	hydrogen peroxide
Hbond	hydrogen bonding
HBSS	hanks balanced salt solution
HCC	hepatocellular carcinoma
HDGF	hepatoma-derived growth factor

HEK-293	transformed embryonic human kidney cell line
HEP-G2	malignant human hepatoblastoma cell line
HER2	human epidermal growth factor receptor 2
HMGB1	high-mobility group box 1 protein
HNC	head and neck cancer
HOPS	homotypic fusion and protein sorting
HRAS	Harvey rat sarcoma viral oncogene homolog
HRP	horseradish peroxidase conjugate
HT-29	malignant human colorectal adenocarcinoma cell line
IAP	inhibitor of apoptosis protein
ICAD	inhibitor of caspase-activated DNase
IgG	immunoglobulin gamma
IL1β	interleukin 1 beta
IMM	inner mitochondrial membrane
IR	infra res spectrometry
ISC	intersystem crossing
K*RAS*	Kirsten rat sarcoma virus oncogene homolog (4A and 4B)
mAbs	monoclonal antibodies
MAL	methyl aminolevulinate
MAPK	mitogen-activated protein kinase
MCF-7	malignant hormone dependent epithelial human breast cancer cell line
MDA-MB-231	malignant triple negative epithelial human breast cancer cell line
MEK	mitogen-activated protein kinase kinase
MGL	molecular graphics laboratory
MHC	major histocompatibility complex
MIR-10b	microRNA 10b
MLKL	RIPK1-RIPK3-mixed lineage kinase domain-like protein
MOMP	mitochondrial outer membrane permeabilization
MPTP	mitochondrial permeability transition pore
MRHF	non-malignant human dermal fibroblast cell line
mTORC1	rapamycin complex 1
mTP	mitochondrial transmembrane potential
MYC	MYC proto-oncogene, BHLH transcription factor
NAC	N-acetyl-cysteine
NAD+ (H)	nicotinamide adenine dinucleotide (reduced form)
NADP (H)	nicotinamide adenine dinucleotide Phosphate (reduced form)
NCC	neural crest cells
NF-κB	nuclear factor kappa light chain enhancer of activated B cells
NMR	nuclear magnetic resonance spectrometry
NRAS	neuroblastoma RAS viral oncogene homolog
NSCLC	non-small cell lung cancer
OMM	outer mitochondrial membrane

^{31}**P**	phosphorus 31 NMR
p53	tumour suppressor protein p53 gene
PAGE	polyacrylamide gel electrophoresis
PARP	poly ADP-ribose polymerase
PBMC	peripheral blood mononuclear cells
PBS	phosphate buffered saline
PD-1	programmed cell death protein 1
PDB	protein data bank
PDT	photodynamic therapy
PDR-1	programmed cell death receptor 1
pH	percent hydrogen
PI	propidium iodide
PPh_3	triphenylphosphine
PR	progesterone receptor
Pro	proline
Ps	photosensitizer
Ptd-L-Ser	phosphatidylserine
PTEN	phosphatase and TENsin homolog deleted on chromosome 10
PTGER4	prostaglandin E2 receptor 4
PTP	permeability transition pores
RAS	receptor-linked tyrosine kinase
RAS/MAPK	RAS-mitogen-activated protein 3 kinase pathway
RIPK1	receptor-interacting protein kinase 1
RMSD	root-mean standard deviation
ROS	reactive oxygen species
SCLC	small cell lung cancer
SEM	standard error of the mean
sHCC	sarcomatoid hepatocellular cancers
SHOX2	human short stature homeobox 2
Smac/DIABLO	second mitochondria-derived activator of caspases/direct inhibitor of apoptosis-binding protein with low pI
SNO	malignant human esophageal cell line
SR	supplementary results
STAT3	signal transducer and activator of transcription 3
TBS	tris buffered saline
TCA	tricarboxylic acid
T cell	thymus lymphocyte
TERT	telomerase reverse transcriptase
TNBC	triple negative breast cancer
TNFR	tumour necrosis factor receptor
Topo II	DNA-topoisomerase
TP53	tumour suppressor protein *p53*
TPA	tissue plasminogen activator
TPP	triphenylphosphine
TR53	tumour protein 53
TRADD TNFR1	associated death domain protein

TRAF	TNFR associated factor
TRAIL	tumour necrosis factor-related apoptosis-inducing ligand
TRAIL-R1/R2	TNF-related apoptosis-inducing ligand receptor 1 / 2
Tregs	tumour-infiltrating lymphocytes
TrxR	thioredoxin reductase
ULK1	serine-threonine protein kinase
UV	ultraviolet light
VAD-peptide	valine-alanine-aspartic acid peptide
VDAC	voltage-dependent anion channel
vdW	van der Waals force
WHO	World Health Organization

Symbols

Å	ångström, unit of length equivalent to 0.1 nanometre
bp	base pair(s)
°C	temperature in degrees Celsius
Δ	delta
ΔΨm	(the change in) mitochondrial membrane potential
g	gram
Gy	gray (1 gray = 1 Joule/kilogram)
h	hour
kD	kilodalton
L	litre
MHz	one million hertz (megahertz)
min	minute
ml	millilitre
mM	millimolar
mmol	millimoles
mV	millivolts
MW	molecular weight
n	number of experimental repeats, technical and biological or the number of hours (*in vitro* scratch wound assay)
nm	nanometres (wavelength; 1 nm = 10^{-9} metre)
π	pi, the ratio of the circumference of a circle to its diameter, approximately 3.14159
ppm	parts per million
t	time
µl	microlitre
µm	micrometre
µM	micromolar
µm/h	micrometre per hour
v/cm^{-1}	volt per centimetre

LIST OF FIGURES

Chapter One

Figure 1.1. The Hallmarks of Cancer **7**

Figure 1.2. The chemical structures of the most used platinum-based complexes **11**

Figure 1.3. The five intrinsic subtypes constituting breast cancer **18**

Figure 1.4. An overview of (1) the intrinsic (mitochondrial-mediated) and (2) the extrinsic (ligand-mediated) apoptotic pathways **26**

Figure 1.5. Principle morphological changes in cancer cells undergoing apoptosis, necrosis and autophagy cell death **29**

Figure 1.6. *In silico* molecular docking approaches used to improve screening results. Ligand-based approaches combined with binding free energies scoring improve docking predictions and the selection of stable conformations **31**

Chapter Two

Figure 2.1. The schematic chemical structures of silver(I) phosphine complexes **1 – 13** **52 - 54**

Figure 2.2. The percentage of cellular viability of transformed **HEK-293** cells determined using the alamarBlue® proliferation assay. The following treatments were added to the cells: no treatment (untreated control) or treated with 1% DMSO (vehicle control), 100 µM CDDP (positive apoptotic control), 10 µM of silver(I) phosphine complexes (**1 - 13**) and 10 µM of respective ligands (**L1 - L4**) for 24 h and 48 h **56**

Figure 2.3. The percentage of cellular viability of non-malignant **MRHF** cells determined using the alamarBlue® proliferation assay. The following treatments were added to the cells: no treatment (untreated control) or treated with 1% DMSO (vehicle control), 100 µM CDDP (positive apoptotic control), 10 µM of silver(I) phosphine complexes (**1 - 13**) and 10 µM of respective ligands (**L1 - L4**) for 24 h and 48 h **57**

Figure 2.4. Morphological changes of transformed **HEK-293** cells induced by differential treatments after 24 h. The following treatments were added to the cells: no treatment or treated with 1% DMSO, 100 µM CDDP and 10 µM silver(I) phosphine complexes **1 – 4**, **6**, **7** and **11** **58**

Figure 2.5. Morphological changes of non-malignant **MRHF** cells induced by differential treatments after 24 h. The following treatments were added to the cells: no treatment or treated with 1% DMSO, 100 µM CDDP and 10 µM silver(I) phosphine complexes **1 - 4**, **6**, **7** and **11** **59**

Figure 2.6. The percentage cellular viability of malignant **A375** cells determined using the alamarBlue® proliferation assay. The following treatments were added to the cells: no treatment (untreated control) or treated with 1% DMSO (vehicle control), 100 µM CDDP (positive apoptotic control), 10 µM of silver(I) phosphine complexes (**1 - 13**) and 10 µM of respective ligands (**L1 - L4**) for 24 h and 48 h **61**

Figure 2.7. The percentage cellular viability of malignant **A549** cells determined using the alamarBlue® proliferation assay. The following treatments were added to the cells: no treatment (untreated control) or treated with 1% DMSO (vehicle control), 100 µM CDDP (positive apoptotic control), 10 µM of silver(I) phosphine complexes (**1 - 13**) and 10 µM of respective ligands (**L1 - L4**) for 24 h and 48 h **62**

Figure 2.8. The percentage cellular viability of malignant **HEP-G2** cells determined using the alamarBlue® proliferation assay. The following treatments were added to the cells: no treatment (untreated control) or treated with 1% DMSO (vehicle control), 100 µM CDDP (positive apoptotic control), 10 µM of silver(I) phosphine complexes (**1 - 13**) and 10 µM of respective ligands (**L1 - L4**) for 24 h and 48 h **63**

Figure 2.9. The percentage cellular viability of malignant **HT-29** cells determined using the alamarBlue® proliferation assay. The following treatments were added to the cells: no treatment (untreated control) or treated with 1% DMSO (vehicle control), 100 µM CDDP (positive apoptotic control), 10 µM of silver(I) phosphine complexes (**1 - 13**) and 10 µM of respective ligands (**L1 - L4**) for 24 h and 48 h **64**

Figure 2.10. The percentage cellular viability of malignant **SNO** cells determined using the alamarBlue® proliferation assay. The following treatments were added to the cells: no treatment (untreated control) or treated with 1% DMSO (vehicle control), 100 µM CDDP (positive apoptotic control), 10 µM of silver(I) phosphine complexes (**1 - 13**) and 10 µM of respective ligands (**L1 - L4**) for 24 h and 48 h **65**

Figure 2.11. The percentage cellular viability of malignant **MDA-MB-231** cells determined using the alamarBlue® proliferation assay. The following treatments were added to the cells: no treatment (untreated control) or treated with 1% DMSO (vehicle control), 100 µM CDDP (positive apoptotic control), 10 µM of silver(I) phosphine complexes (**1 - 13**) and 10 µM of respective ligands (**L1 - L4**) for 24 h and 48 h **66**

Figure 2.12. The percentage cellular viability of malignant **MCF-7** cells determined using the alamarBlue® proliferation assay. The following treatments were added to the cells: no treatment (untreated control) or treated with 1% DMSO (vehicle control), 100 µM CDDP (positive apoptotic control), 10 µM of silver(I) phosphine complexes (**1 - 13**) and 10 µM of respective ligands (**L1 - L4**) for 24 h and 48 h **67**

Figure 2.13. Dose-responsive studies of malignant **A375** cells determined using the alamarBlue® proliferation assay. The following treatments were an untreated control or treated with 1% DMSO (vehicle control), **(A - D)** a range of concentrations (1.25 µM to 20 µM) of complexes **1** - **4** respectively, **(E)** 6 and **(F)** 7 or **(G)** a range of concentrations (12.5 µM to 200 µM) of CDDP (positive apoptotic control) for 24 h **71 - 72**

Figure 2.14. Dose-responsive studies of malignant **A549** cells determined using the alamarBlue® proliferation assay. The following treatments were an untreated control or treated with 1% DMSO (vehicle control), **(A - D)** a range of concentrations (1.25 µM to 20 µM) of complexes **1 - 4** respectively**, (E) 6** and **(F) 7** or **(G)** a range of concentrations (12.5 µM to 200 µM) of CDDP (positive apoptotic control) for 24 h **73 - 74**

Figure 2.15. Dose-responsive studies of malignant **HEP-G2** cells determined using the alamarBlue® proliferation assay. The following treatments were an untreated control or treated with 1% DMSO (vehicle control), **(A - D)** a range of concentrations (1.25 µM to 20 µM) of complexes **1- 4** respectively and **(E)** a range of concentrations (12.5 µM to 200 µM) of CDDP (positive apoptotic control) for 24 h **75 - 76**

Figure 2.16. Dose-responsive studies of malignant **HT-29** cells determined using the alamarBlue® proliferation assay. The following treatments were an untreated control or treated with 1% DMSO (vehicle control), **(A)** a range of concentrations (1.25 µM to 20 µM) of complex **4** respectively and **(B)** a range of concentrations (12.5 µM to 200 µM) of CDDP (positive apoptotic control) for 24 h **77**

F**igure 2.17.** Dose-responsive studies of malignant **SNO** cells determined using the alamarBlue® proliferation assay. The following treatments were an untreated control or treated with 1% DMSO (vehicle control), **(A - E)** a range of concentrations (1.25 µM to 20 µM) of complexes **1 - 4**, **(E)** 7 and **(F) 11** respectively or **(G)** a range of concentrations (12.5 µM to 200 µM) of CDDP (positive apoptotic control) for 24 h **78 - 79**

Figure 2.18. Dose-responsive studies of malignant **MDA-MB-231** and **MCF-7** cells determined using the alamarBlue® proliferation assay. The following treatments were an untreated control or treated with 1% DMSO (vehicle control), **(A - C)** a range of concentrations (1.25 µM to 20 µM) of complexes **2**, **4** and **7** respectively or **(D)** a range of concentrations (12.5 µM to 200 µM) of CDDP (positive apoptotic control) for 24 **80**

Chapter Three

Figure 3.1. Morphological changes of malignant **A549** cells induced by differential treatments after 24 h. The following treatments were an untreated control or treated with 1% DMSO, 100 µM and 200 µM CDDP; and 10 µM and 20 µM silver(I) phosphine complexes **1** - **4**, **6** and **7** **93**

Figure 3.2. Morphological changes of malignant **HEP-G2** cells induced by differential treatments after 24 h. The following treatments were an untreated control or treated with 1% DMSO, 100 µM and 200 µM CDDP; and 10 µM and 20 µM silver(I) phosphine complexes **1** - **4** **94**

Figure 3.3. Morphological changes of malignant **HT-29** cells induced by differential treatments after 24 h. The following treatments were an untreated control or treated with 1% DMSO, 100 µM and 200 µM CDDP; and 10 µM and 20 µM of silver(I) phosphine complex **4** **95**

Figure 3.4. GAPDH activity in malignant **(A) A549**, **(B) HEP-G2** and **(C) HT-29** cells determined by a KDalert™ GAPDH assay. Cells were treated as follows: not treated (untreated control) or treated with 1% DMSO (vehicle control), 20 µM of complexes **1** - **4**, **6** and **7**, or 200 µM CDDP (positive apoptotic control) for 24 h **97**

Figure 3.5. The percentage cellular ATP (*coloured bar graph*) and viability (*grey bar graph*) in malignant **(A) A549 (B) HEP-G2** and **(C) HT-29** cells measured by the CellTiter-Glo® assay and alamarBlue® proliferation assay, respectively. Cells were treated as follows: not treated (untreated control) or treated with 1% DMSO (vehicle control), 20 µM (ATP) or 10 µM (viability) of complexes **1** - **4**, **6** and **7**, or 200 µM (ATP) or 100 µM (viability) CDDP (positive apoptotic control) for 24 h **98**

Figure 3.6. The detection of the total amount of ROS in malignant **(A)** **A549** **(B)** **HEP-G2** and **(C)** **HT-29** cells was quantified using a Muse® Oxidative Stress kit. The following treatments were an untreated control or treated with 1% DMSO (vehicle control), 200 µM CDDP (positive apoptotic control) or 20 µM of selected complexes **1** - **4**, **6** and **7** (respective to the specific cell line) for 24 **100 - 102**

Figure 3.7. Mitochondrial potential and cellular plasma permeabilization were quantified in malignant **(A)** **A549**, **(B)** **HEP-G2** and **(C)** **HT-29** cells using a Muse® MitoPotential kit. The following treatments were an untreated control or treated with 1% DMSO (vehicle control), 200 µM CDDP (positive apoptotic control) or 20 µM of selected complexes **1** - **4**, **6** and **7** (respective to the specific cell line) for 24 h **105 - 107**

Figure 3.8. The mode of cell death was quantified in malignant **(A)** **A549**, **(B)** **HEP-G2** and **(C)** **HT-29** cells using a Muse® Annexin V & Dead Cell kit. The following treatments were an untreated control or treated with 1% DMSO (vehicle control), 200 µM CDDP (positive apoptotic control), 50% H_2O_2 (positive necrotic control) or 20 µM of selected complexes **1** - **4**, **6** and **7** (respective to the specific cell line) for 24 h **108 - 110**

Figure 3.9. The CYP1B1 isoform activity in malignant **(A)** **A549**, **(B)** **HEP-G2** and **(C)** **HT-29** cells measured by a Cytochrome P450-Glo™ assay. The following treatments were an untreated control or treated with 1% DMSO, 20 µM of complexes **1** - **4**, **6** and **7** or 200 µM CDDP for 24 h **112**

Figure 3.10. Time-lapse micrographs of malignant **A549** cells taken at **0 h**, **24 h** and **48 h** after wound tracks were scored and cells were differentially treated at **0 h**. The following treatments were an untreated control or treated with 1% DMSO, 3.75 µM CDDP or 1.5 µM of silver(I) phosphine complexes (**1** - **4**, **6** and **7**) **114 - 115**

Figure 3.11. (A) Average wound area (µm^2) and **(B)** average wound width (µm) of malignant **A549** at **0 h**, **24 h** and **48 h** after wound tracks were scored. Respective cells were differentially treated at **0 h**. Cells were not treated, or they were treated with 1% DMSO, 3.75 µM CDDP or 1.5 µM of silver(I) phosphine complexes (**1** - **4**, **6** and **7**) **116**

Figure 3.12. The rate of cell migration (µm/h) of malignant **A549** at **0 h**, **24 h** and **48 h** after wound tracks were scored and cells were differentially treated at **0 h**. Cell migration rates were expressed in relation to 1% DMSO at the appropriate hour **117**

Figure 3.13. Percentage of wound closure of malignant **A549** at **24 h** and **48 h** after wound tracks were scored and cells were differentially treated at **0 h**. Percentages were expressed in relation to 1% DMSO at the appropriate hour **117**

Chapter Four

Figure 4.1. Morphological changes of malignant MCF-7 cells induced by differential treatments after 24 h. The following treatments were an untreated control or treated with 1% DMSO, 100 µM and 200 µM CDDP; and 10 µM and 20 µM silver(I) phosphine complexes **2**, **4** and **7** **135**

Figure 4.2. Morphological changes of malignant MDA-MB-231 cells induced by differential treatments after 24 h. The following treatments were an untreated control or treated with 1% DMSO, 100 µM and 200 µM CDDP; and 10 µM and 20 µM silver(I) phosphine complexes **2**, **4** and **7** **136**

Figure 4.3. The detection of the total amount of ROS in malignant **(A)** MCF-7 and **(B)** MDA-MB-231 breast cells was quantified using a Muse® Oxidative Stress kit. The following treatments were an untreated control or treated with 1% DMSO (vehicle control), 200 µM CDDP (positive apoptotic control) or 20 µM of selected complexes **2**, **4** and **7** for 24 h **137 - 138**

Figure 4.4. Mitochondrial potential and cellular plasma permeabilization were quantified in malignant **(A)** MCF-7 and **(B)** MDA-MB-231 breast cells using a Muse® MitoPotential kit. The following treatments were an untreated control or treated with 1% DMSO (vehicle control), 200 µM CDDP (positive apoptotic control), or 20 µM of selected complexes **2**, **4** and **7** for 24 h **141 - 142**

Figure 4.5. The mode of cell death was quantified in malignant **(A)** MCF-7 and **(B)** MDA-MB-231 breast cells using a Muse® Annexin V & Dead Cell kit. The following treatments were an untreated control or treated with 1% DMSO (vehicle control), 200 µM CDDP (positive apoptotic control), 50% H_2O_2 (positive necrotic control), or 20 µM of selected complexes **2**, **4** and **7** for 24 h **143 - 144**

Figure 4.6. Fluorescent images of malignant **(A)** MCF-7 and **(b)** MDA-MB-231 cells induced by control treatments after 24 h. Cells were treated with 1% DMSO, 100 µM and 200 µM CDDP respectively. The cells were examined using Hoechst-33258 (blue) which stains the nuclei, MitoTracker® Orange CMTMRos (red) and Alexa-Flour® 488 mouse anti-cytochrome *c* specific antibody (green) **145**

Figure 4.7. Fluorescent images of malignant MCF-7 cells induced by differential treatments after 24 h. Cells were treated with 10 µM and 20 µM silver(I) phosphine complexes **2**, **4** and **7** respectively. The cells were examined using Hoechst-33258 (blue), MitoTracker® Orange CMTMRos (red) and Alexa-Flour® 488 mouse anti-cytochrome *c* specific antibody (green) **146**

Figure 4.8. Fluorescent images of malignant MDA-MB-231 cells induced by differential treatments after 24 h. Cells were treated with 10 µM and 20 µM silver(I) phosphine complexes **2**, **4** and **7** respectively. The cells were examined using Hoechst-33258 (blue), MitoTracker® Orange CMTMRos (red) and Alexa-Flour® 488 mouse anti-cytochrome *c* specific antibody (green) **147**

Chapter Five

Figure 5.1. (A) 6WOK nuclear protein: crystal structure of **estrogen receptor alpha (ER-α)** in complex with receptor degrader 6 and **(B)** 2YLY receptor: sulfonamides as selective **estrogen receptor beta (ER-β)** agonists, obtained from the PDB and shown in ribbon style (https://www.rcsb.org/structure) **153**

Figure 5.2. Molecular model and schematic structure of complex **4**. The three-dimensional preparation of complex 4, [Silver(I) diphenyl-2-pyridylphosphine]Br in DSV **154**

Figure 5.3. RSMD Cluster Analysis. Clustering histograms of complex **4** docked with **(A)** estrogen receptor alpha (PBD ID: 6WOK nuclear protein) and **(B)** estrogen receptor beta (PDB ID: 2YLY receptor) **157**

Figure 5.4. Three-dimensional model of ER-α (PBD ID: 6WOK) shown as a ribbon style carrying docked complex **4**. **(A)** Overview of docked complex **4** to ER-α, **(B)** front view and **(C)** back view of complex **4** with the interacting amino acid residues and hydrogen bonding **159**

Figure 5.5. Three-dimensional model of ER-β (PBD ID: 2YLY) shown as a ribbon style carrying docked complex **4**. **(A)** Overview of docked complex **4** to ER-β, **(B)** front view, **(C)** side view and **(D)** back view of complex **4** with the interacting amino acid residues and hydrogen bonding **160**

Figure 5.6. The two-dimensional interactions of the best docked pose of complex **4** with **(A)** ER-α (PBD ID: 6WOK) and **(B)** ER-β (PDB ID: 2YLY), showing the protein-ligand interactions involved between the ligand and amino acid residues **161**

Figure 5.7. Physio-chemical scoring functions/energy values of bound conformational models (kcal/mol) between complex **4** and ER-α (PBD ID: 6WOK, red) and ER-β (PDB ID: 2YLY, orange) **162**

LIST OF TABLES

Chapter One

Table 1.1. Significant differences between the two primary types of cell death **28**

Chapter Two

Table 2.1. Detailed descriptions of the seven malignant and two non-malignant cell lines used during this study **47**

Table 2.2. The calculated IC_{50} concentrations (μM) for CDDP and complexes **1** - **4**, **6**, **7** and **11** (respective to the cell line). These values were calculated after 24 h of treatment in A375, A549, HEP-G2, HT-29 and SNO malignant cell lines, using the alamarBlue® proliferation assay **70**

Table 2.3. The calculated IC_{50} concentrations (μM) for CDDP and complexes 2, 4, 7 in MCF-7 and MDA-MB-231 malignant breast cell lines after 24 h of treatment, determined using the alamarBlue® proliferation assay **70**

Chapter Five

Table 5.1. The coordinates and number of points (npts) of the cubic box used for docking complex **4** to the 6WOK nuclear protein (ER-α) and 2YLY receptor (ER-β) **155**

Table 5.2. The GA parameters used for docking complex **4** to the 6WOK nuclear protein (ER-α) and 2YLY receptor (ER-β) **155**

Appendix II

Table A1. Single-dose screening (percentage cellular viability) of nine human cell lines were performed, using the alamarBlue® proliferation assay. Cells were treated with 100 μM CDDP (positive apoptotic control), 10 μM of silver(I) phosphine complexes (**1** - **13**) and 10 μM of respective ligands (**L1** - **L4**) for 24 h **188 - 190**

LIST OF MOLECULAR DOCKING DATA

Appendix III

Data A1. The ADT4 grid parameter file (`.gpf`) for 6WOK nuclear protein: crystal structure of estrogen receptor alpha in complex with receptor degrader 6, obtained from the PDB **191**

Data A2. The ADT4 grid parameter file (`.gpf`) for 2YLY receptor: sulfonamides as selective estrogen receptor beta agonists, obtained from the PDB **191**

Data A3. The ADT4 docking parameter file (`.dpf`) for 6WOK nuclear protein: crystal structure of estrogen receptor alpha in complex with receptor degrader 6 docked with complex **4** **192**

Data A4. The ADT4 docking parameter file (`.dpf`) for 2YLY receptor: sulfonamides as selective estrogen receptor beta agonists docked with complex **4** **193**

Data A5. The final GA docked state for complex **4** docked with the 6WOK nuclear protein: crystal structure of estrogen receptor alpha in complex with receptor degrader 6 **194**

Data A6. The final GA docked state for complex **4** docked with the 2YLY receptor: sulfonamides as selective estrogen receptor beta agonists **197**

ABSTRACT

Cancer is the leading cause of death worldwide, with 18.1 million new cases and 9.6 million deaths reported annually. Cisplatin, a popular chemotherapeutic drug, exhibits certain limitations in terms of selectivity and efficacy. This emphasizes the necessity for novel therapeutic approaches in addressing a variety of cancer types. Multiple studies have shown that silver-based compounds suppress cancer cell proliferation and induce apoptosis. Thirteen novel silver(I) mono-dentate phosphine complexes were investigated for their anticancer effects on seven different human malignant cell lines; A375 non-pigmented melanoma, A549 lung adenocarcinoma, HEP-G2 hepatocellular carcinoma, HT-29 colorectal adenocarcinoma, MCF-7 and MDA-MB-231 breast adenocarcinoma, and SNO oesophageal squamous cell carcinoma. Two non-malignant human cell lines, HEK-293 embryonic kidney cells and MRHF foreskin fibroblast cells, were used to assess the selectivity of the complexes. Cisplatin and the efficient silver(I) phosphine complexes were selected for dose-response experiments to determine IC_{50} concentrations for the respective cell lines. On the basis of these screening results (chapter two), five difficult-to-treat cancer cell lines, and their most efficient complexes were selected for further investigation. Various cellular characteristics were investigated in chapter three (A549, HEP-G2, HT-29); these included morphological changes, ATP levels, GAPDH levels, Ptd-L-Ser externalization, mitochondrial membrane potential, oxidative stress levels, and the activity of a metabolic enzyme, cytochrome P450 isoform CYP1B1. The antimetastatic activity of the selected complexes was assessed by evaluating their ability to impede the migration of A549 cells. The fourth chapter examines the anticancer effect of selected complexes on hormone-dependent (MCF-7) versus triple-negative (MDA-MB-231) breast cells. Changes in morphology, Ptd-L-Ser externalization, alterations in mitochondrial membrane potential, oxidative stress levels, cytochrome *c* release, and DNA damage were studied. Furthermore, in chapter five, molecular docking simulations were used to determine whether the most potent silver(I) phosphine complex across all cell lines bonds to estrogen receptor alpha (ER-α) and estrogen receptor beta (ER-β). Seven of the thirteen silver(I) phosphine complexes significantly reduced cell viability in malignant cell lines while being less toxic to non-malignant cells. Complex **4** best targeted all cancer types, with IC_{50} values ranging from 5.75 to 10.80 μM across malignant cell lines. In the malignant treated cells, morphological changes, reactive oxygen species production, mitochondrial membrane depolarization, and Ptd-L-Ser externalization were observed. Complexes **1** and **4** repressed cell migration in the A549 cells. The presence of damaged nuclei, metabolically inactive mitochondria and cytochrome *c* translocation from the mitochondria' intermembrane to the cytosol in MCF-7 cells were observed. These findings suggest that complexes **2**, **4** and **7** induced apoptotic cell death. Furthermore, *in silico* computational predictions suggested a promising interaction between complex **4**, and ER-α and ER-β. Overall, this study demonstrates the potential of silver(I) phosphine complexes as anticancer agents, with promising effects on various cancer cell lines.

NARRATIVE

Cancer is a primary cause of death worldwide, above cardiovascular disease (Sung *et al.*, 2021). The treatment approach for cancer is decided by the tumours' size and stage of development, with the option of using more than one type of procedure. There are several treatments available for cancer. Among them are surgery, chemotherapy, radiation, hormonal therapy, photodynamic therapy, immunotherapy, and gene therapy (Disis, 2014; Lee *et al.*, 2016). Chemotherapy uses a variety of drugs to target and destroy a tumour. The benefit is that drugs can be delivered to the majority of the body's tissues and target cells during the metastatic process. The most common type of metal-based chemotherapeutic drug used is cis-diamine-dichloro platinum (cisplatin). It is a platinum(II) based anticancer drug and the first ever to be used in clinical trials. Due to its limited selectivity and toxicity to healthy tissue, cisplatin has significant drawbacks, including unpleasant side effects (neurotoxicity and nephrotoxicity) and hospitalization for treatment (Bresciani *et al.*, 2022). It remains ineffective in treating certain forms of cancer, which eventually develop resistance to cisplatin, resulting in metastasis (Borst *et al.*, 2008; Cevik-Yildiz *et al.*, 2020). To prevent metastatic colonization in early- and late-stage cancer patients for whom standard treatment has failed, new strategies are required. Novel chemotherapeutic drugs based on metals are of considerable interest.

Silver-based complexes can inhibit cell proliferation. In a study by Ferreira *et al.* (2015), MCF-7 breast cancer cells were treated with various phosphine silver thiocyanate complexes. These complexes effectively induce apoptosis in a dose-dependent manner. Cevik-Yildiz *et al.* (2020) identified promising antiproliferative activities of silver (I)-N-heterocyclic carbene (Ag-NHC) complexes on malignant cells. Moreover, silver (I) complexes have shown anticancer potential in various malignant cell lines. The coordination and geometries of silver(I) phosphine complexes exhibit an extensive number of structural types that can be readily manipulated by varying the ligands, silver salts, and their ratios, thereby encouraging the study of silver(I) chemistry (Cevik-Yildiz *et al.*, 2020; Kyros *et al.*, 2009; Mann *et al.*, 1937; Meijboom *et al.*, 2009; Potgieter *et al.*, 2017). A novel family of silver(I) mono-dentate phosphine complexes was synthesized (Meijboom *et al.*, 2009). In the following years, a patent portfolio comprised of this specific family of silver(I) phosphine complexes gained international recognition.

The purpose of this research was to screen thirteen novel silver(I) mono-dentate phosphine complexes (and their ligands) to determine whether they were selective in effectively decreasing the cellular viability of seven human malignant cell lines (A375 melanoma, A549 lung, HEP-G2 liver, HT-29 colon, MCF-7 breast, MDA-MB-231 breast, and SNO oesophageal). Their cancer specificity

and cytotoxicity were tested on two non-malignant human cell lines (MRHF skin and HEK-293 kidney). The cytotoxicity screening analyzes the recovery rate of the malignant cells and their resistance to anticancer drugs. Therefore, time intervals of 24 h and 48 h were selected to investigate the cell survival rate following treatment. Thereafter, the selected silver(I) phosphine complexes and a positive apoptotic control, cisplatin, were used in multi-dose experiments to calculate their IC_{50} concentrations on the respective malignant cell lines.

Consequently, two studies were derived from the cytotoxicity screening data, and as a result, the work presented in this thesis is divided into chapters, each focusing on a different research question. Chapter two represents the screening cytotoxicity data and includes aspects of the selectivity shown by the silver(I) phosphine complexes, as mentioned above. In chapter three, the focus is on selected complexes and their potential to target the intrinsic, mitochondrial-mediated apoptotic pathway in three human malignant cell lines (A549 lung, HEP-G2 liver, and HT-29 colon), as well as any antimetastatic potential these complexes may have (A549 lung). In this study, the effects of thirteen complexes on cellular respiration (viability and ATP levels), a possible mode of cell death, variations in mitochondrial membrane potential, oxidative stress levels, and the activity of a metabolic enzyme, cytochrome P450 isoform CYP1B1, were evaluated. The ability of these complexes to inhibit the lateral migration of A549 lung adenocarcinoma cells was used to determine their antimetastatic activity.

Targeting hormone-dependent breast cancer cells (MCF-7) versus triple-negative breast cancer cells (MDA-MB-231) with selected complexes is briefly compared in chapter 4. To determine whether these complexes effectively induce apoptosis, morphological changes, a potential mode of cell death, alterations in mitochondrial membrane potential, oxidative stress levels, cytochrome *c* release, and DNA damage were observed. This indicates which complexes (if any) were effective in treating these two invasive breast cancer subtypes. Chapter five presents the first *in silico* molecular docking evidence to determine if a selected hit-to-lead silver(I) phosphine complex binds to estrogen alpha and beta receptors. This provides insight into the type of treatment that these complexes may provide and whether a combination of hormonal and chemotherapeutic benefits exists.

CHAPTER ONE:
LITERATURE REVIEW

1.1. Introduction to Cancer

1.1.1. Cancer's toll

Cancer is a primary cause of worldwide morbidity and mortality, accounting for an estimated 18.1 million new cases and over 9.6 million global deaths reported annually. This statistical data gathered is closely related to the standard of living and socioeconomic development (Cai and Lui, 2021). It is estimated that by 2025 and 2035, the number of global cancer cases will increase to 9.7 million and 24 million, respectively (Gao *et al.*, 2021). Previous data reported by Bray *et al.* (2018) found that the following cancer types had greater incidence rates in both males and females; lung cancer (11.6%), breast cancer (11.6%), colorectal cancer (10.2%), prostate cancer (7.1%) and stomach cancer (5.7%). The cancer types that had the highest mortality rates were lung cancer (18.4%), colorectal cancer (9.2%), liver cancer (8.3%), stomach cancer (8.2%) and breast cancer (6.6%) (Cai and Lui, 2021; Sung *et al.*, 2021). Data collected for the year 2020 states that breast cancer had the highest incidence rate, with 2.26 million new cases and estimated 685000 women had passed from this disease (Arnold *et al.*, 2022). Lung cancer had the highest mortality rate with 1.80 million deaths worldwide, followed by colorectal cancer with 935000 deaths worldwide (Sung *et al.*, 2021; WHO, 2021). It should be mentioned that the coronavirus disease 2019 (COVID-19) pandemic impeded cancer diagnosis and treatment thereof. Due to limited access to healthcare facilities, there were diagnostic delays, which accelerated the disease's progression. This resulted in a temporary decline in incidence rates and an increase in mortality rates in various world regions. However, methods used for estimates were gathered at a national level (Arnold *et al.*, 2022; Kaur *et al.*, 2020; Siegel *et al.*, 2021; Siegel *et al.*, 2022; Sung *et al.*, 2021).

1.1.2. Defining cancer

Cancer is a collection of multifactorial diseases that affect different parts of the body and are caused by the unregulated growth of abnormal cells. Proliferation is increased, which results in the development of malignant tumours. Cancer cells resist cell death and have developed mechanisms that allow them to evade apoptosis (programmed cell death). Internal risk factors include genetic and metabolic variants, hereditary susceptibility, as well as immunological or hormone disorders (Siegel *et al.*, 2021). As genetic instability modifies the genotype of cells, proto-oncogenes and tumour suppressor genes mutate. Proto-oncogenes are the original genes that usually encode for proteins involved in cell division. Oncogenes are mutated proto-oncogenes that are unable to carry out their normal function, consequently causing the cells they regulate to become cancerous (Nyga *et al.*, 2022). Oncogenes act as growth factors, signal transducers and transcription factors which drive cell

proliferation. They are no longer effectively regulated inside the cell. The most common dysfunctional proto-oncogenes belong to the Ras family and include neuroblastoma RAS viral oncogene homolog (*NRAS*), Harvey rat sarcoma viral oncogene homolog (*HRAS*), Kirsten rat sarcoma virus oncogene homolog (*KRAS4A* and *KRAS4B*) as well as MYC proto-oncogene, basic helix–loop–helix (BHLH) transcription factor (*MYC*), the tumour suppressor protein p53 gene (*p53*), and the proto-oncogene, non-receptor tyrosine kinase (*SRC*). Tumour suppressor genes inhibit cell proliferation by arresting the cell cycle or inducing apoptosis when a cell is damaged. In cancer cells, these genes become dysfunctional and no longer inhibit processes related to proliferation. The genes include *p53*, breast cancer gene 1 (*BRCA1*), breast cancer gene 2 (BRCA2) and B-cell leukemia/lymphoma 2 protein (*Bcl2*) among others (Hart, 2004; Ralph *et al.*, 2010; Nyga *et al.*, 2022). In addition to internal factors, cells may become cancerous when DNA is damaged, lost or added during replication and repair. This results in the production of dysfunctional proteins. Epigenetic modifications cause DNA methylation, changes in histones, inactivation of microRNAs and chromosomes, and the loss of genome imprint (Babar *et al.*, 2022). Epigenetic changes control gene expression without altering the DNA sequence and offer details on how and when genetic information is used. Epigenetic modifications were among the initial alterations identified during the process of carcinogenesis (reviewed by Feinberg *et al.*, 2006). Huang and Yu (2018) further explain that hypermethylation in promoter regions of DNA sequences has been detected in different cancer types. Hypermethylation supports genomic instability and initiates the inhibition of tumour suppressor genes. Oesophageal cancer has hypermethylated adenomatous polyposis coli (*APC*) and cyclin dependent kinase inhibitor 2A/multiple tumor suppressor 1 (*CDKN2A*) genes, which disrupt the cell-regulatory pathway, while in lung cancer the human short stature homeobox 2 (*SHOX2*) and prostaglandin E2 receptor 4 (*PTGER4*) are affected (Locke *et al.*, 2019).

External factors may also cause cancer. These include the excessive use of alcohol, following an unhealthy diet, a lack of physical activity/exercise, exposure to excessive ultraviolet (UV) or ionizing radiation, exposure to harmful chemicals, as well as parasites, bacteria (*Helicobacter pylori*), and viruses (human papillomavirus, hepatitis virus and the Epstein-Barr virus) (Cai and Lui, 2021; WHO, 2021). The most common external risk factor for cancer is smoking. It should be emphasized that the tobacco epidemic significantly elevated the mortality rate for lung cancer over the twentieth century (Siegel *et al.*, 2021).

Cells are labelled cancerous when there are fourteen physiological alterations that allow for a healthy cell to express a malignant phenotype, these are represented in **Figure 1.1**. They are characterized as the hallmarks of cancer, of which eight are hallmark capabilities and four are emerging characteristics (reviewed in detail by Hanahan 2022). The eight hallmark capabilities are the following: (1) cells can replicate indefinitely by resisting inhibitory growth signals; and (2) cells

have independent growth signals and growth factor ligands. These stimulate the formation of new blood vessels (angiogenesis) and can alter healthy cells positioned near a tumour for the supply of various growth factors. (3) In order to avoid cell death mechanisms such as apoptosis, necrosis, and autophagy, cells undergo reversible dormancy. This state of dormancy permits the cells to temporarily cease their activities and conserve energy. (4) Cells are able to migrate and invade healthy tissue and (5) metastasize to distant organs within the body, while (6) inducing angiogenesis. (7) These cells can regulate their energy metabolism by limiting it to glycolysis (even when oxygen is accessible), which enables the biosynthesis of macromolecules required for the assembly of abnormal cells. (8) Cancerous cells are able to evade the immune system by remaining undetected within the body. The four emerging characteristics are the following: (9) cells are able to unlock phenotypic plasticity. During organogenesis, terminal differentiation allows progenitor cells to exit the cell cycle and acquire a mature phenotype. Cancer cells are able to evade terminal differentiation. (10) Nonmutational epigenetic reprogramming contributes to tumour development and oncogenic mutations, and (11) polymorphic variability in the microbiome of individuals impact cancer phenotypes, progression and the response to treatment. Several bacterial species have the ability to directly facilitate the characteristic of proliferative signals. Additionally, these species can modify the activity of tumour suppressors in various sections of the intestine, influencing growth suppression. Their influence on other hallmarks such as angiogenesis and colonization of cancer cells, remains unclear. Lastly (14) senescent cells have the ability to stimulate an inflammatory environment that aids in the growth and survival of tumours in the early stages of carcinogenesis. Senescent cells secrete a number of substances that can encourage angiogenesis, invasion, and metastasis. Furthermore, the progression of diseases associated with age, such as cancer, may be facilitated by the development of senescent cells within bodily tissues (Cooper, 2000; Hanahan and Weinberg, 2000; Hanahan and Weinberg, 2011, Hanahan, 2022). Ultimately, cancer arises from a dysregulation in the equilibrium between the proliferation of normal cells and the eventual apoptotic demise of these cells (Hart, 2004).

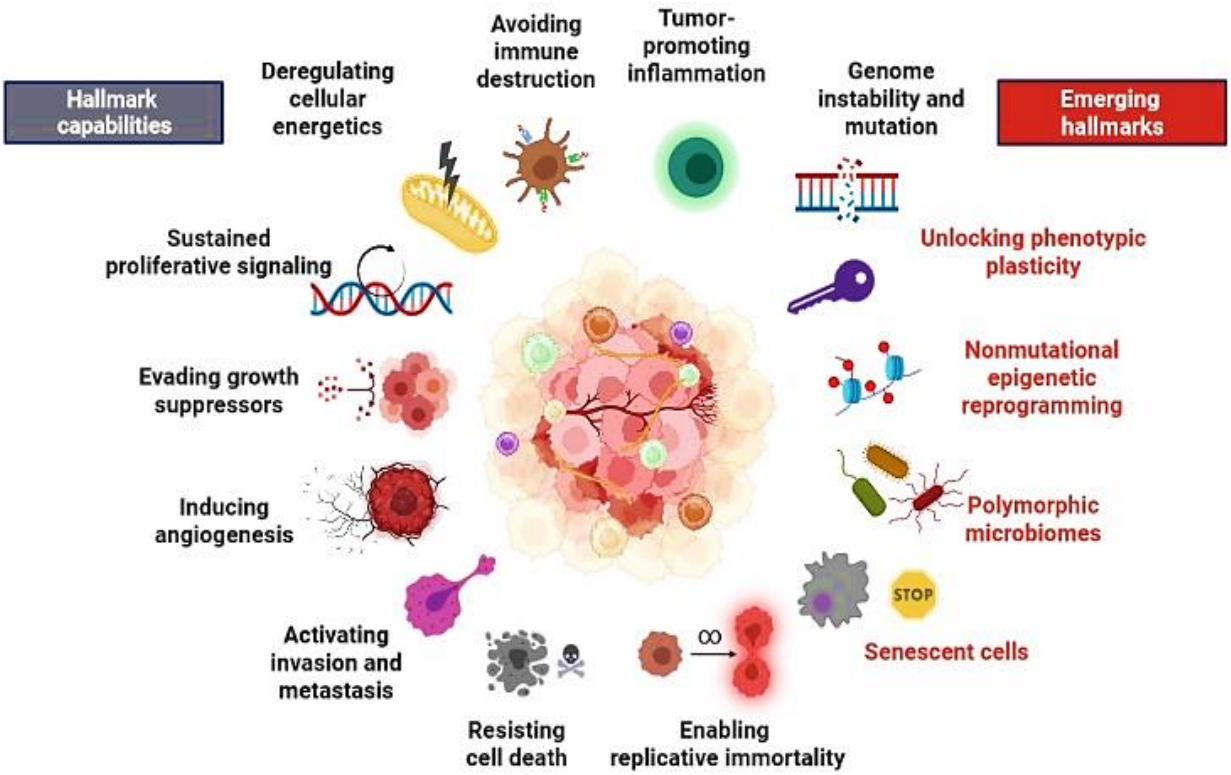


Figure 1.1. The Hallmarks of Cancer (Adapted from "*The Hallmarks of Cancer: Circle*", created with BioRender.com, 2023; Hanahan and Weinberg, 2011; Hanahan, 2022).

1.2. Therapeutic Modalities for Cancer

The progression and type of cancer are important in determining the best approach for treatment. This progression is evaluated and labelled as a particular stage of advancement. The conventional types of treatment for cancer are surgery, radiotherapy, and chemotherapy (Čanivic *et al.*, 2017). Less well-known cancer therapies include photodynamic therapy (PDT) and techniques involving antibodies, stem cell transplantation, targeted therapy and hormone therapy. Cancer survival depends on early detection, and screening should be a routine activity for all individuals. Mammograms, pap smears, colonoscopies, prostate-specific antigen testing, and mole analysis are common screening tests (Moses *et al.*, 2016; Roy and Sakia, 2016).

1.2.1. Surgery

Surgery was the very first form of treatment for cancer and is the most effective treatment method available. However, this success lies closely with the stage, form, and localization of the tumour. A primary, localized, solid mass detected at an early stage is inclined to be successfully removed. However, completing resection procedures requires access to well-equipped hospitals, which can be a challenge for less developed countries in terms of their healthcare system. There are several reasons for this, including the variability in skill sets and equipment availability between rural and urban areas, the system's limited ability to adapt to changing patient needs, and issues with staff shortage and mismanagement. Countries are known to have different approaches to cancer treatment, due to their resources available (Dare *et al.*, 2015). In 2015 the American College of Surgeons published technical guidelines for cancer surgery to address this shortcoming by developing an operational standard, and in 2020 they issued the most recent edition of the manual, "Optimal Resources for Cancer Care". These manuals address disease staging, medical management and guidelines for resection. Records are collected annually, and a 70% compliance rate is anticipated in 2023. These were designed to improve the outcome of patients who undergo oncologic surgery (Katz *et al.*, 2022). Following the removal of many tumours, further therapies including chemotherapy, radiotherapy, or immunotherapy may be utilized to treat any cancer cells that are still present within the body.

1.2.2. Radiotherapy

Radiotherapy is a significant treatment technique utilized mostly as an adjuvant treatment (following primary therapy such as surgery). By causing DNA damage, ionizing radiation can eliminate cancerous cells. Radiation results in oxidative stress, which damages the four chemical bases that make up DNA: adenine, guanine, cytosine, and thymine. It includes DNA base modifications, single-stranded breaks, double-stranded breaks and DNA-protein cross-links (Vedoya *et al.*, 2021). Most radiation is delivered via an external beam of high-energy photons (6 – 25 mV) that penetrate deeply into cancerous tissue. As an adjuvant treatment, radiation is given throughout for 6 – 8 weeks in daily fractions of 1.8 – 2 Gy (absorbed ionizing energy per unit of mass) (Allen *et al.*, 2017).

However, radiation may result in side effects that worsen the malignancy, such as an increase in new primary tumours and the recurrence of proliferating cells that survive the initial treatment of radiation. The risk of a systemic reaction is also possible (Vedoya *et al.*, 2021). Recent improvements (imaging tools and molecularly targeted therapies) have made it possible to personalize radiotherapy to each patient, thereby increasing the likelihood of a more promising outcome (Allen *et al.*, 2017).

1.2.3. Photodynamic therapy

PDT is a two-phase process that is minimally invasive. PDT relies on three elements with low to no toxicity when used independently on non-malignant and malignant cell lines. These elements include the following: (1) visible light irradiation, generally triggered by a laser at a particular wavelength (nm). The quantity of cellular damage caused by the laser on the target tissue is referred to as 'light' toxicity. This, together with the administration and preferential absorption of (2), a light-sensitive agent known as a photosensitizer (Ps), and (3) the generation of singlet reactive oxygen species ($^1O_2$, ROS), initiates a cell death response within a biological system. For PDT to be effective, ROS must be produced when a Ps is irradiated within the cancerous tissue (Mroz *et al.*, 2011; Theodosius *et al.*, 2019).

PDT is a modality focused on treating superficial cancer types, usually where laser irradiation can easily infiltrate the tumour. This is usually seen as a limitation for this type of therapy nonetheless PDT can target melanoma, breast and lesions within hollow organs such as the oesophagus, colon and lung (Theodosius *et al.*, 2019). PDT has the following advantages over other treatment options: (1) a Ps has low toxicity, and repetitive doses are well tolerated within the body; (2) it is a selective form of treatment as the laser reaches a targeted tumour and, (3) PDT can be combined with chemotherapy, surgery or radiotherapy (Davids and Kleemann, 2013).

1.2.4. Immunotherapy

Cancer's resistance to the immune system elimination is one of its defining hallmarks (**Figure 1.1**) (Hanahan and Weinberg *et al.*, 2011). The immune system is responsible for detecting pathogens and malignant cells and protecting the body from disease. Immunotherapy utilizes the host's immune system to attack tumours and eliminate cancerous cells (Abbott and Ustoyev, 2019; Kennedy and Salama, 2020). The immune system consists of both (1) innate immunity and (2) acquired immunity. Innate immunity utilizing cytokines is generally a nonspecific response to an antigen. It is present from birth and is the body's initial defense mechanism, using physical and chemical barriers namely the skin, mucus membranes, temperature, and pH. Whereas, acquired immunity encompasses the generation of antibodies by B cells and the activation of effector cytotoxic T cells, which are responsible for eliminating antigens. Memory B cells facilitate a stronger immune response when the body is re-exposed to the same antigens (Abbott and Ustoyev, 2019).

When the disease progresses, many natural immune defenses against malignant cells are evaded. Immunotherapy employs agents to activate the acquired immune system to specifically attack malignant cells (Riley *et al.,* 2019). Cancer immunotherapy can either be active or passive. An active approach employs cancer vaccinations to directly stimulate an acquired immune response and memory. A passive approach employs monoclonal antibodies, which are disadvantageous due to their low efficacy and the frequent administration often required. Cancer immunotherapy is a promising therapeutic, but further development is needed because not all malignancies react to this type of treatment. In addition, it results in high toxicity such as capillary leakage or multiorgan failure (Abbott and Ustoyev, 2019; Kennedy and Salama, 2020).

1.2.5. Hormone therapy

Estrogen receptors, alpha and beta (ER-α and ER-β, respectively), are nuclear transcription receptors that bind and dimerize to the promotor and regulatory domains of target genes, they are also located within the cytoplasm. Estrogen receptor (ER) overexpression is associated with cancers that are dependent on estrogen as 'fuel', such as breast and gynaecological malignancies (Maruthanila *et al.,* 2019). Although altered ER and progesterone receptor (PR) expression have been identified in Hodgkin's lymphoma, melanoma, prostate, lung, colorectal and liver cancer. Hormone therapy inhibits ER and PR, which are known to promote the proliferation of cancer cells, through two main mechanisms: (1) reducing the body's hormone production capability, or (2) inhibiting or limiting the functional mechanism of these hormones. In severe situations, ovaries and testicles are surgically removed. Hormone therapy, although less effective than chemotherapy, is useful in treating certain types of cancer and postmenopausal symptoms; however, it remains systemic and is not a targeted form of therapy (Barzaman *et al.,* 2020; Mitra *et al.,* 2022).

Hormone replacement therapy is when estrogen or progesterone is replaced with a drug that works in the same way that these hormones do. It is often used in treating cancer survivors who reach the age of physiological menopause. Hormone replacement therapy is often used on individuals who have survived breast cancer. However, this treatment has a few problems. Tibolene, a complex metabolized by estrogen isomers, has been shown to increase the recurrence of breast cancer a few years after treatment; consequently, the safety of this drug has been questioned (reviewed by Deli *et al.,* 2020).

1.2.6. Metallo-chemotherapeutic drugs

Due to the increase in drug resistance observed in multiple types of cancer, there are fewer available anticancer drugs. Therefore, the development of safe and effective chemotherapeutic agents is urgent and constantly under investigation. Metals other than platinum, such as gold, ruthenium, copper and silver have been studied for this purpose (Mashat *et al.,* 2019). Metals bound to ligands exhibit

significant structural diversity, as different ratios of ligands can bind to the transition metal or replace existing ligands. This structural versatility contributes to their effective redox and catalytic properties. They are beneficial in medical applications, and therefore the development of these complexes continues (Banti *et al.,* 2021; Gao *et al.,* 2021; Gasser and Metzler-Nolte, 2012; Kalinowska-Lis *et al.,* 2016; Lee *et al.,* 2020).

(a) *Platinum complexes*

Platinum anticancer agents have been the most promising metal-based drugs developed thus far and have been used for multiple cancers for many decades. Cisplatin (*cis-diamminedichloroplatinum*; CDDP), and its derivatives, carboplatin, oxaliplatin, lobaplatin, nedaplatin and heptaplatin are the most commonly used platinum-based chemotherapeutic drugs. The Food and Drug Administration (FDA) has authorized their administration to cancer patients worldwide. Carboplatin and oxaliplatin have both been shown to be less toxic at higher dosages. **Figure 1.2** presents the structures of these most used platinum-based complexes (Raju *et al.,* 2022). CDDP was synthesized by chemist Dr. Michele Peyrone and clinically approved in 1978 (Zaki *et al.,* 2016). It remains one of the most widely used platinum anticancer agents. CDDP interferes with the synthesis of DNA and RNA transcription, whereby DNA adducts arrest the cell cycle and induce apoptosis. When the chloride ligands of CDDP are removed, the subsequent electrophilic platinum(II) complex binds to biological ligands by exchange of water molecules. This disfigures the DNA strand and inhibits transcription (Ranasinghe *et al.,* 2022). CDDP is highly effective against cervical, ovarian, testicular, bladder and small-cell lung cancers (Lupidi *et al.,* 2013).

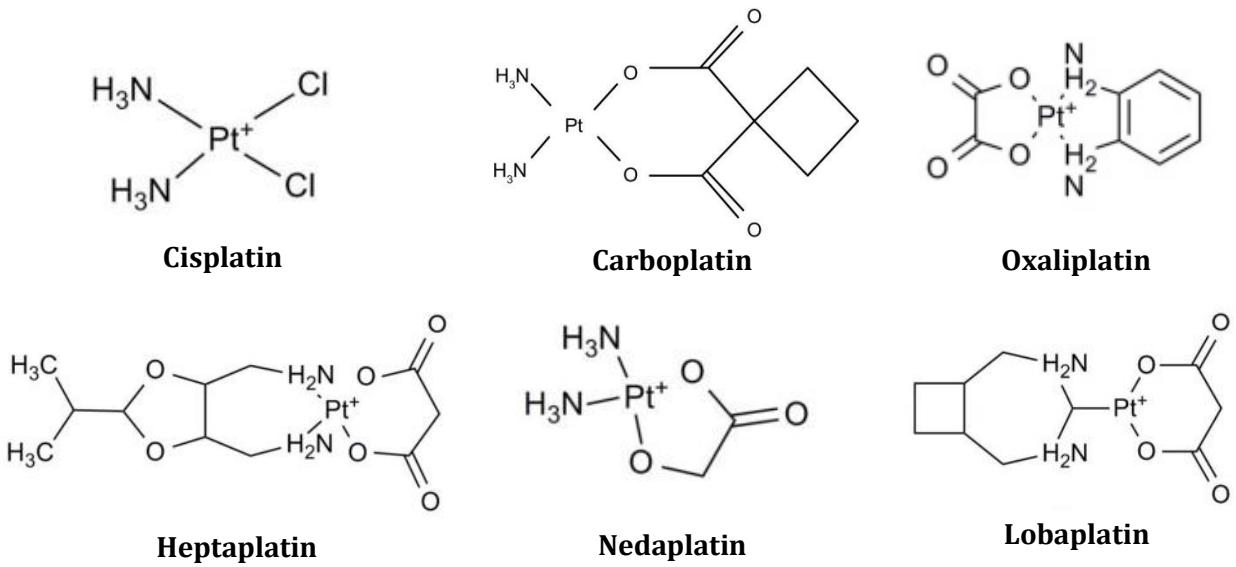


Figure 1.2. The chemical structures of the most used platinum-based complexes (Adapted from Raju *et al.,* 2022).

Although these complexes have been FDA-approved, unfortunately, they cause severe adverse effects in patients, such as nephrotoxicity (which develops as early as ten days after treatment), neurotoxicity, ototoxicity (hearing and balance difficulties), hypertension, vascular damage, and myocardial damage due to mitochondrial dysfunction in cardiomyocytes. Sadly, it has been reported that the accumulation of platinum in children led to their deaths by gastro-intestinal toxicity, cardiovascular disease, or respiratory disease (Chrysouli *et al.,* 2018; Ota *et al.,* 2021: Raji *et al.*, 2022; Ranasinghe *et al.*, 2022; Zaki *et al.,* 2016). In addition, cancer cells have developed a resistance to CDDP therapy by repressing apoptosis and regulating redox homeostasis; however, studies investigating the reasons for this are still under investigation (Ranasinghe *et al.,* 2022).

(b) *Gold complexes*

Gold (Au) complexes have gained attention over the years in their use as cytotoxic and anticancer agents. Epidemiological and experimental studies show that gold metallo-drugs possess anticancer properties (Chrysouli *et al.,* 2018). Past research by Berners-Price *et al.* (1986), showed that $[Au(DPPE)_2]Cl$ (DPPE: bis(diphenylphosphino)ethane) was effective against *in vivo* B16 melanoma and P388 leukemia and exhibited cytotoxic activity against *in vitro* B16 and P388 cells. Due to their lipophilic nature, they are able to specifically target cellular and mitochondrial membranes to enable $[Au(DPPE)_2]Cl$ access to essential cellular targets. The development of complexes with lipophilic counterparts was driven by the significant toxicity and mitochondrial uptake observed in many cancer cell lines (Kriel and Coates, 2012).

Auranofin was first used to treat rheumatoid arthritis. It was the first Au(I) monophosphine derivative shown to have antiproliferative properties in both *in vivo* (P388 murine leukemia) and *in vitro* (B16 melanoma and P388 leukemia) cells (Lupidi *et al.,* 2013), along with treating microbial infections (Kim *et al.,* 2019). In the proceeding years, gold(I) complexes with diphosphine donor ligands were shown to possess anticancer activity and recently inhibit DNA-topoisomerase II (Topo II) (Caruso *et al.,* 2007). Topo I and II are involved in DNA replication: they mediate the stability of the genome and chromosome separation during mitosis (reviewed in detail by Lee and Berger, 2019). Martin-Encinas *et al.* (2020) synthesized Au(I) with phosphine sulphide ligands and studied the effects these complexes incurred in A549 and SKOV3 (ovarian cancer) cells. IC_{50} values revealed cytotoxic activity below 50 µM in A549 and below 5 µM in SKOV3 cells. Studies showed that these complexes inhibited the enzymatic activity of Topo I, by hindering DNA relaxation and increasing the supercoiling of DNA.

In addition, Dandash *et al.* (2017) studied the effect of Au(III) tetraphenyl-porphyrin chloride [Au(TPP)]Cl on colorectal HT-29 and HCT-116 malignant cells. Their data revealed that apoptosis was induced by the intrinsic pathway and caspases -3, -9 and PARP were cleaved via upregulation

of the Bcl-2 associated X protein (Bax). Below is a detailed explanation of the apoptotic pathway (*1.4.1. Apoptosis*). Kim *et al.* (2019) synthesized gold(I) complexes bearing phosphine ligands. These complexes produced high levels of ROS within OVCAR8 (ovarian cancer) cells and increased levels of caspase activity. Nevertheless, gold complexes have limitations, as Au may accumulate within the cell. This presents various skin conditions such as dermatitis, nephropathy, and platelet deficiency (thrombocytopenia). Ongoing studies are being performed to gain a better understanding of using Au phosphine complexes as effective anticancer agents (Ott, 2009).

(c) *Ruthenium complexes*

Among the transition metals used in various medical applications, ruthenium (Ru) complexes have been established for their bioactivity and anticancer properties in chemo-resistant tumours. Ru is stable in two oxidation states, specifically Ru(II) and Ru(III). Ru complexes typically assume octahedral molecular geometry, are soluble in water, and ligands are able to bind at a slow exchange rate (Čanivic *et al.*, 2017; Engelbrecht *et al.*, 2020).

Dwyer *et al.* (1952) revealed the earliest biological activity of Ru ions by developing a novel series of Ru polypyridyl complexes **1 - 3**. This sparked interest in the cancer research field, and since then, various Ru complexes have been developed (Lee *et al.*, 2020). Čanivic *et al.* (2017) synthesized two Ru(II) polypyridyl complexes that induced an apoptotic response in treated A549, MCF-7, HeLa (cervical carcinoma), and Hs294T (melanoma) cells through cytochrome *c* release and the subsequent autocatalytic cleavage of caspase-3. A study by Liang *et al.* (2022) synthesized three Ru(II) complexes with a ligand containing an imidazole ring. Moderate cytotoxicity against four treated cancerous cell lines was observed. In the B16 (melanoma) cell line, these complexes increased ROS levels, this caused mitochondrial dysfunction and induced apoptosis. In addition, Engelbrecht *et al.* (2020) synthesized two arene Ru(II) complexes (referred to as **GA105** and **GA113**) with bis-amino-phosphine ligands. Treated malignant A375 cells presented a dose-dependent decrease in viability and IC_{50} concentrations of 6.72 µM (**GA105**) and 8.76 µM (**GA113**) respectively, while remaining nontoxic to non-malignant HEK-293 (embryonic kidney) cells. Complex **GA113** induced morphological changes diagnostic to apoptosis and cells were shifted into the late apoptotic flow cytometric quadrant (28.83% at 10 µM; 73.97% at 20 µM) (Engelbrecht *et al.*, 2020). Overall, Ru(II) complexes target the DNA and proteins within a cancer cell and are promising anticancer agents (Čanivic *et al.*, 2017).

(d) *Copper complexes*

Copper (Cu) is essential to numerous biological processes. It functions as a structural and catalytic cofactor in most pathways; however, intracellular concentrations of Cu are toxic to malignant cells (Pathaw *et al.*, 2020). Several copper coordination complexes with stable Cu(I), Cu(II) and Cu(III)

oxidation states have been reported. Thus far, copper(I) phosphine complexes with tetrahedral ligands have presented anticancer properties. Cu complexes are an alternative to CDDP because (1) both exert their anticancer effects targeting the mitochondria and bind to components of the tricarboxylic acid (TCA) cycle and DNA, (2) they are able to target tumour vasculature by inhibiting the formation of new blood vessels that supply nutrients to the tumour, (3) Cu complexes have demonstrated greater selectivity towards malignant cells than CDDP, and (4) have a lower toxicity profile, making them a promising alternative to CDDP (reviewed by Tsvetkov *et al.,* 2022).

Pathaw *et al.* (2020) synthesized five copper(I) phosphine complexes with various 3-substituted 1-pyridin-2-ylimidazo[1,5-a]pyridine ligands. They treated A549 cells with these complexes, and after 24 h, IC_{50} values obtained were below 74 µM. This was comparable to CDDP's IC_{50} of 69 µM. After 48 h of treatment, the IC_{50} values obtained were below 70 µM, with the exception of one complex having a lower IC_{50} of 34 µM, while CDDP's IC_{50} was 40 µM. Overall, these complexes increased ROS production, inhibited the cell cycle, and possibly induced apoptosis in A549 cells. In addition, Cu(I) bis-phosphine polypyridyl complexes have potential anticancer properties, and studies reveal these complexes are more cytotoxic than CDDP. A study by Mashat *et al.* (2019) treated MCF-7, HEP-G2, PC-3 (prostate) and MOLT-4 (leukemia) cells with $CuBr(PPh_3)_3$ and $CuBr(PPh_3)$(phen) complexes. These complexes had comparable antiproliferative effects when compared to CDDP. Cu complexes have been considered as an alternative option for CDDP in treating a variety of cancer types (Tsvetkov *et al.,* 2022).

(e) *Silver complexes*

Silver has been used for its antibacterial and antifungal effects for many decades. Silver nanoparticles (AgNPs) are recognized antibacterial agents that release silver ions that damage the bacterial cell membrane. This causes the generation of ROS and hinders ATP synthesis. Mohammed *et al.* (2023) investigated the incorporation of AgNPs and chitosan in hydrogels. Chitosan is a polysaccharide that is applied to numerous biomedical products due to its antibacterial and biodegradable qualities. Chitosan-AgNPs were discovered to be efficient against both Gram-positive and Gram-negative bacteria. This discovery has potential medical applications (Mohammed *et al.,* 2023). Recent research has refocused on the use of silver in medical applications, increasing its application beyond antibacterial advantages.

Several studies have investigated the anticancer effects of silver complexes. Silver(I) metallo-drugs decrease proliferation, and cause mitochondrial dysfunction by inducing ROS, as silver ions interact with thiol groups involved in redox reactions (Banti *et al.,* 2021). This disrupts electron transfer and cellular respiration and inhibits enzymes that bind to DNA. When silver ions are coordinated to a ligand, this improves anticancer activity. The structural diversity of silver complexes with phosphine

ligands allows the synthesis of numerous complexes that exhibit anticancer activity. Under physiological conditions, silver complexes have ligand exchange rates similar to those of platinum complexes. Ag shows minimal to no toxicity in healthy, non-malignant cells and has been reintroduced as an anticancer agent (Human *et al.*, 2015; Potgieter *et al.*, 2016; Ranasinghe *et al.*, 2022).

Previous research has demonstrated that silver(I) phosphine complexes are more cytotoxic than CDDP, with higher anticancer activities reported. They have a propensity to interact with various cellular components (mitochondria, DNA and enzymes). This interaction is accompanied by enhanced internalization into malignant cells (Engelbrecht *et al.*, 2018; Human *et al.*, 2015; Human-Engelbrecht *et al.*, 2017; Ferreira *et al.*, 2015; Kalinowska-Lis *et al.*, 2016; Santini *et al.*, 2011). These studies warrant the need to further investigate silver(I) phosphines within the same family, as potential anticancer chemotherapeutic agents.

1.3. Types of Cancer

Cancer is characterized by physiological alterations (i.e., hallmarks) (**Figure 1.1**), which allow cells to randomly mutate to evade the tight regulations imposed on them. These mutations allow for the development of over one hundred different molecular types of cancer, with some being more prevalent than others. The types of cancers discussed below were used in this study.

1.3.1. Lung cancer

Lung cancer is the deadliest form of cancer in both men and women. It had the greatest incidence rate with 2.26 million new cases in 2020 and was the leading cause of cancer-related deaths worldwide. Following breast cancer, lung cancer is the most commonly diagnosed cancer worldwide (Cai and Lui, 2021, Ranasinghe *et al.*, 2022; Sung *et al.*, 2021, WHO, 2021). With a survival rate of approximately 40% after one year of diagnosis, its prognosis is poor (Aceituno *et al.*, 2016). The main reason for the emergence of lung cancer is the advancement of the tobacco industry over the last 30 years. An increase in the incidence rate of this disease is closely related to the increase in tobacco consumption (Diaz *et al.*, 2021).

Lung cancer falls into two categories: (1) Small Cell Lung Cancer (SCLC); although clinically aggressive, it is responsible for only 20% of all diagnosed cases. (2) Non-Small Cell Lung Cancer (NSCLC). Eighty-five percent of all lung cancer patients develop NSCLC, with less than 18% of patients surviving five years from diagnosis (Cheng *et al.*, 2015; Eunji *et al.*, 2015). NSCLC can be defined as either one of three subtypes: adenocarcinoma, squamous cell carcinoma, or large cell undifferentiated carcinoma. The most common subtype of lung cancer, accounting for 40% of cases in both smokers and non-smokers, is adenocarcinoma. Squamous cell carcinoma usually presents

itself in individuals who have a history of smoking and is known to metastasize at a later stage. Large cell carcinoma remains the most difficult type to treat, as it may appear anywhere within the lung. It also proliferates quickly and is known to metastasize at an early onset stage of the disease (Collins *et al.,* 2007; Dela Cruz *et al.,* 2011). Approximately 30 - 40% of NSCLC patients have acquired metastatic disease by the time they are diagnosed. Screening and early identification are critical for a successful prognosis and for the prevention of metastases (Raviadaran *et al.,* 2021). The progression of the disease dictates the treatment option chosen. PDT is a therapeutic option for NSCLC patients who have small, unresectable, early stage tumours within the airway (less than 1 cm in diameter). Persistent tumours and lesions require surgery, chemotherapy, radiotherapy or a combination thereof (Wang and Chen, 2021).

1.3.2. Colorectal cancer

Among men and women, colorectal cancer death rates are 9% and 8%, respectively, making it the third deadliest cancer in the world (Siegel *et al.,* 2021). Only 5% of cases reported to date have been inherited. Unhealthy dietary factors, for example, the consumption of processed meats, red meat, and the excessive consumption of alcohol contribute to the development of colorectal cancer. Non-dietary factors also play a role, these include smoking and the frequent use of non-steroidal anti-inflammatory drugs, or genome instability. Crohn's disease and/or ulcerative colitis patients are more likely to develop colon cancer (Labianca *et al.,* 2010).

The progression of colorectal cancer may appear as colorectal polyps, adenomas, carcinomas or adenocarcinomas. Late-stage colorectal cancer is challenging to treat as colonoscopy and colectomy are no longer options in treating such a developed stage (IV or V) of cancer. Surgery remains the best treatment option; however, once it progresses to metastatic disease, chemotherapy is required (Romeo *et al.,* 2021; Yang *et al.,* 2009). CDDP and 5-Fluorouracil are the most common chemotherapeutic drugs used in treating colorectal cancer (Jiang *et al.,* 2020). Wang (2020) states that 5-Fluorouracil initiates apoptosis by activating caspase-6. However, this type of cancer presents certain abnormalities within the apoptotic pathway that result in chemoresistance (Anaya-Eugenio *et al.,* 2020). The primary abnormalities include, (1) a mutation in the *p53* gene, which deactivates apoptosis, and (2) changes to the B-cell lymphoma (Bcl) protein which decreases the sensitivity of these cells to chemotherapeutic drugs (Yang *et al.,* 2009). P53, is an important tumour suppressor regulatory protein that initiates apoptosis, DNA repair and cell cycle arrest. Patients who present with any mutation of *p53* were found to have a poor response to treatment when compared to those who do not have a *p53* mutation (Wang 2020; Yang *et al.,* 2009).

Surgery and radiotherapy, or a combination of two or more of these are available as alternatives to chemotherapy for colorectal cancer. The resection of primary tumours in late-stage metastatic cancer

with adjuvant chemotherapy is often done in patients who may present complications at the primary site of the disease, such as intestinal obstruction or haemorrhage (Labianca *et al.*, 2010; Yang *et al.*, 2009).

1.3.3. Liver cancer

Hepatocellular carcinoma (HCC) is well recognized as the most commonly observed type of liver cancer, making up about 90% of cases. Other types of HCC, such as fibrolamellar liver cancer (FLC) and sarcomatoid hepatocellular cancer (sHCC), are rare (Wege *et al.*, 2021). Liver cancer has the fourth highest mortality rate of 8.3% (approximately 830 000 deaths in 2020) and the sixth highest incidence rate of 4.7% worldwide, for men and women combined. According to estimates, by 2025, there will be more than one million cases of liver cancer worldwide, and by 2030, it will be the third deadliest cancer worldwide (Llovet *et al.*, 2021: Sung *et al.*, 2021). Chronic liver cirrhosis as well as infection with the hepatitis viruses (hepatitis B and C) contribute to 90% of liver cancer cases, followed closely by alcohol abuse, drug-induced liver damage, obesity, and diabetes mellitus (Cai and Lui, 2021; Sung *et al.*, 2021). Genome instability occurs in approximately 25% of HCC tumours. Genetic mutations occur in telomerase reverse transcriptase (*TERT*), tumour protein 53 (*TR53*), and catenin beta 1 (*CTNNB1*), although the prevalence of these mutations is less than 10% (Llovet *et al.*, 2021).

If diagnosed at an early stage, treatment involves hepatic resection and liver transplantation. Non-surgical treatment options for advanced stages of HCC include (1) trans-arterial chemoembolization with radiotherapy and (2) the use of the chemotherapeutic drug, sorafenib. This was the first drug approved by the FDA for advanced liver cancer. This drug is a multikinase inhibitor and works by inhibiting the MAP kinase cascade, hindering cell proliferation and angiogenesis. He *et al.* (2023) recently identified that dihydroergotamine mesylate (DHE) suppresses cell proliferation in liver cancer cells. Their findings showed that DHE inhibited and downregulated the signal transducer and activator of transcription 3 (STAT3) pathway at low concentrations. DHE did not induce apoptosis; however, when combined with sorafenib, apoptosis was induced by enhanced STAT3 suppression. However, HCC is known to present chemoresistance within six months of treatment with sorafenib; therefore, the need for new chemotherapeutic drugs is imperative (Anwanwan *et al.*, 2020).

1.3.4. Breast cancer

Invasive breast cancer is the most common type of cancer in women worldwide. The incidence rate is 30%, and the mortality rate is 15%. Breast cancer is the second prominent cause of mortality worldwide, following lung cancer. It is anticipated that by 2040, 3 million cases will be diagnosed annually, and the mortality rate will increase by more than 50% to 1 million deaths per year. Early diagnosis is necessary to prevent further progression. The World Health Organization (WHO)

advises mammography screening or self-screening for the presence of symptomatic lesions every two years for women aged between 50 and 69 years (Amaral *et al.*, 2018; Arnold *et al.*, 2022; Cheng *et al.*, 2015; Moses *et al.*, 2016). For cancer cells to evade cell death mechanisms, heterogeneous mutations occur at multiple levels within one type of cancer (Allison and Sledge, 2014). MCF-7 and MDA-MB-231 are both invasive ductal breast cancer cells, yet they are phenotypically and genotypically distinct from one another while originating from the same primary site inside the body (Theodosius *et al.*, 2019).

Significant proteins (hormone receptors) are used to diagnose and classify breast cancer. These proteins are ER, PR, and the human epidermal growth factor receptor 2 (HER2). Breast cancer can manifest in three different ways: (1) expressing ER and/or PR; (2) expressing HER2 or (3) no expression of ER, PR, or HER2. These types are further devised into five intrinsic subtypes (**Figure 1.3**). The most prevalent subtype is luminal A, followed by normal breast-like, then luminal B, HER2-enriched, and triple-negative. The hormone receptors each intrinsic subtype express as well as treatment options are detailed in **Figure 1.3**. (AAAS, 2020; Barzaman *et al.*, 2020; Orrantia-Borunda *et al.*, 2022).

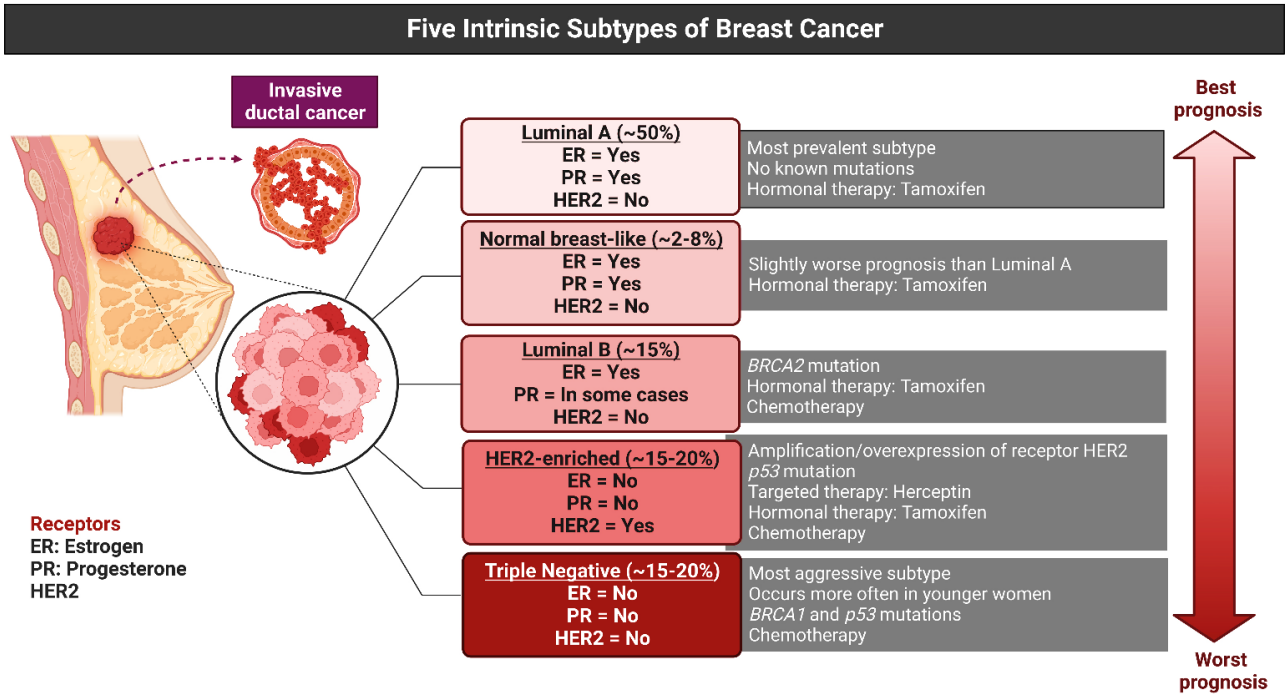


Figure 1.3. The five intrinsic subtypes constituting breast cancer (Adapted from "*Intrinsic and Molecular Subtypes of Breast Cancer*", created with BioRender.com, 2023; Barzaman *et al.*, 2020; Orrantia-Borunda *et al.*, 2022).

Hormone receptor-positive malignancies multiply quicker because ER and PR maintain proliferation. These hormone receptors influence how the cancer is treated. This type of breast cancer constitutes 14% of all cancers (Maruthanila *et al.,* 2019). Breast cancer is termed hormone-receptor negative if these proteins are absent, and the subtype is termed triple-negative breast cancer (TNBC) (Barzaman *et al.,* 2020). ERs fall into the family of intracellular nuclear transcription factors that bind to DNA and regulate the activity of various genes (Maruthanila *et al.,* 2019). The estrogen receptor consists of two subtypes, which are estrogen receptor alpha (ER-α) and estrogen receptor beta (ER-β). These subtypes are encoded by distinct genes and exhibit substantial homology in their DNA and ligand binding domains (Eid *et al.,* 2018). ER-α positive breast cancers (luminal A, B and normal-breast like), are the most common types, as ER-α mediates the development of the mammary gland and estrogen-induced cell proliferation, an inducer for the development of cancer. ERs are known to co-operate with cyclin D and the proto-oncogene *MYC*, which further proliferates cancer cells. Patients diagnosed with breast cancer are always screened for the ER as this can be used to predict the type of treatment needed. This receptor responds well to hormone therapy and is a popular target for breast cancer therapies (Arnold *et al*., 2022; Barzaman *et al.,* 2020; Tan *et al.,* 2009).

An antiestrogen is a complex that inhibits or blocks estrogen. Consequently, this prevents the growth of cancer cells; among these are tamoxifen, cyclofenil and raloxifene. Bioactive antiestrogens (thymoquinone, tehranolide and deoxybouvardin) are naturally derived from plants and limit cell proliferation. Tamoxifen is the most popular estrogen antagonist used to treat pre- and postmenopausal women. It binds to ERs and inhibits the transactivation site and, subsequently, estrogen-induced cell proliferation. Over the years, tamoxifen has significantly reduced the risk of recurrences. Although this drug has shown promise over the years, gastrointestinal disturbances, bleeding, menstrual dysregulation, and vaginal discharge are the typical adverse effects. Patients with elevated ER levels have been shown to acquire intrinsic resistance to tamoxifen, prompting the use of alternative therapies (Eid *et al.,* 2018; Muchtaridi *et al.,* 2017). Therefore, there is an emerging need for novel ER-targeting estrogen (Maruthanila *et al.,* 2019).

HER2-positive or HER2-negative breast cancer can be identified based on the presence or lack of HER2 (AAAS, 2020). HER2-positive breast cells proliferate at a quicker rate than the luminal subtypes (Orrantia-Borunda *et al.,* 2022). The use of monoclonal antibodies as a treatment for HER2-enriched cells has shown great promise (reviewed by von Arx *et al.,* 2023). TNBC lacks the significant hormone receptors ER, PR, and HER2, and is extremely challenging to treat due to its aggressive behaviour. Women of African descent and those younger than 40 years old have a higher risk of developing TNBC. Unfortunately, TNBC has a prevalence rate of 80% and is characterized by its high proliferation rate and its ability to weaken DNA repair genes. Subsequently, women with this subtype tend to relapse after treatment, returning to a far more advanced stage (Arnold *et al.,*

2022; Orrantia-Borunda *et al.,* 2022). Chemotherapy as well as combination therapy with monoclonal antibodies are used to treat TNBC. After surgery or a mastectomy, radiotherapy is utilized as an adjuvant therapy to ensure no cells remain in the primary site of resection (Barzaman *et al.,* 2020; Vedoya *et al.,* 2021; Welsh, 2013). The MDA-MB-231 cell line is frequently applied as a model to represent invasive late-stage triple-negative breast cancer (Welsh, 2013). It is one of the cell lines used in the experiments for this study.

1.3.5. Melanoma

It is estimated that in 2023, there will be 89000 cases of melanoma diagnosed in the United States alone (Siegel *et al.,* 2022). Melanocytes are specialized types of pigmentary skin cells derived from embryonic neural crest cells (NCC) and unregulated proliferation of these cells result in the development of melanoma. Melanocytes are present in the epidermis, the uveal tract of the eye, and within hair follicles. They produce the pigment melanin, which absorbs UVA and UVB radiation and provides protection from their damaging effects (Anestopoulos *et al.,* 2022; Rippey and Rippey, 1984).

Previous research indicates that exposure to UV radiation from the sun and/or tanning beds is the predominant cause of melanoma. This repetitive exposure damages DNA. At a genetic level, melanoma is characterized by numerous mutation patterns in genes. These genes are the following: v-raf murine sarcoma viral oncogene homolog B1 (*BRAF*), *NRAS, KRAS,* phosphatase and TENsin homolog deleted on chromosome 10 (*PTEN*) and *p53* (Anestopoulos *et al.,* 2022; Davids and Kleemann, 2013; Davies *et al.,* 2008). The most prominent mutation is the substitution of glutamic acid for valine, at codon 600 ($BRAF^{V600E}$) in the *BRAF* gene. This mutation hyperactivates the RAS-mitogen-activated protein 3 kinase pathway (RAS/MAPK), which controls cell progression and migration. In addition, mutations at codon 61 in $NRAS^{Q61}$ negatively affect guanosine triphosphate (GTP) hydrolysis. This consequently causes the continual activation of the NRAS protein. This protein plays an essential role in the RAS signalling cascade and is responsible for heightened cell proliferation. Mediators of signal transduction such as mitogen-activated protein kinase kinase (MEK) have been used to prevent the activation of downstream mechanisms in the MAPK pathway (Alessi *et al.,* 1995; Anestopoulos *et al.,* 2022; Bertolotto 2013, Costa *et al.,* 2006, Davies *et al.,* 2008; Miraflor *et al.,* 2017).

Among the numerous treatment options (surgery, chemotherapy, radiation, immunotherapy), targeted therapy has demonstrated the most promise as a potential treatment for metastatic melanoma. Pembrolizumab, vemurafenib and dabrafenib are the most effective FDA-approved prescription drugs, while combination therapy with ipilimumab and nivolumab have shown to be more effective than using either drug alone (Fujisawa *et al.,* 2018). Ipilimumab, nivolumab and

pembrolizumab are immune checkpoint inhibitor monoclonal antibodies. Ipilimumab inhibits the cytotoxic T-lymphocyte-associated protein 4 (CTLA-4) receptor-ligand interactions and, along with nivolumab, is classified as an anti-PD-1 inhibitor. These inhibitory elements are present on T cells and impede the immune cells in a tumour from functioning. Vemurafenib and dabrafenib inhibit the *BRAF* gene's production of BRAF protein. They are employed to treat patients with the $BRAF^{V600E}$ mutation. In addition, targeted drugs that inhibit MEK were developed to delay the onset of treatment resistance towards mediations that target the *BRAF* gene. Trametinib, cobimetinib and binimetinib are approved MEK inhibitor mediations (Halpern *et al.,* 2022; Luo and Shen, 2017).

Screening of moles is essential for early prognosis. Melanoma usually presents itself as a black or brown spot that over time develops into a mole. These moles can appear on the skin's surface, in the eye, or in the intestine, and are typically larger than healthy moles. They are asymmetric and/or have an irregular border. Advanced melanoma is resistant to many therapeutic modalities, despite the new developments in treatment strategies (Anestopoulos *et al.,* 2022; Davids and Kleemann, 2013).

1.3.6. Oesophageal cancer

The estimated incidence and mortality rates for oesophageal cancer in 2020 were 3.1% and 5.5%, respectively, with 540000 deaths reported. This ranks it the eighth most common and fifth deadliest cancer worldwide. In South Africa, however, it is the second most deadly cancer in men (Sung *et al.,* 2021; Gao *et al.,* 2023). It is believed that mycotoxin-contaminated corn is fermented to produce alcohol. Men who consume an excessive amount of alcohol or who eat corn as a staple food are at risk, as mycotoxins damage the cell membrane of the oesophagus and are carcinogenic (Devnarain *et al.,* 2017). There are various other risk factors such as smoking and gastroesophageal reflux disorder (GERD), reoccurring heartburn, and regurgitation of gastric acid that damage the oesophageal tract (Huang and Yu, 2018; Jajosky and Elliot, 2022).

Most of the time, oesophageal cancer appears at an advanced stage or has metastasized to additional parts of the body. In these cases, the survival rates were less than a year. Two histological subtypes of oesophageal cancer are adenocarcinoma (EAC) and squamous cell carcinoma (ESCC). ESCC tends to be more aggressive and has a higher mortality rate than EAC. EAC originates from the gastroesophageal junction as it is exposed to gastric acid, while ESCC originates from either the upper or middle region of the oesophagus which results in chronic mucosal injury (Jajosky and Elliot, 2022).

With regards to chemotherapy, 5-flououracil is the most effective drug used in treating advanced oesophageal cancer. Usually, a combination of surgery (oesophagostomy) and chemoradiation therapy is used to treat oesophageal cancer that has not yet advanced. If surgery is not possible,

immunotherapy with chemotherapy is an option. Immunotherapy for oesophageal cancer involves the use of monoclonal antibodies (mAbs) that target the programmed cell death receptor 1 (PDR-1) and the CTLA-4. The T-cell costimulatory receptor, CD28, is closely associated with CTLA-4, as both interact with the same ligands, B7-1 (CD80) and B7-2 (CD86). These ligands are located on the surfaces of antigen-presenting cells (APCs). CTLA-4 plays a crucial role in the regulation of the immune response through its ability to decrease T cell activation. When CTLA-4 engages with its ligands, it transmits inhibitory signals to the T lymphocytes. This restricts their activation, proliferation, and cytokine production (Barron *et al.,* 2023; reviewed in detail by Gao *et al.,* 2023).

1.4. Cell Death Pathways

Multicellular organisms must maintain homeostasis in order to survive. It is important to maintain an equilibrium between the generation and removal of damaged and/or unnecessary cells. This constant turnover is essential for the formation of structures and the prevention of diseases, such as cancer. Cell death pathways allow for this turnover to be successful through the removal of abnormal or mature cells that have the potential to become malignant (Stoian *et al.,* 2014; Tower, 2015; Yu *et al.,* 2021). Apoptosis and necrosis are the two primary forms of cell death; however, in recent years, several other pathways of cell death have been publicized, these are onychosis, pyroptosis, and autophagy (reviewed in detail by D'Arcy, 2019). Understanding these cell death pathways is crucial for the development of anticancer therapeutics. Below is a summary of the principal forms of cell death.

1.4.1. Apoptosis

In a study published by Kerr *et al.* (1972), the term apoptosis was first used to describe programmed cell death. Apoptosis originates from the Greek word "απόπτωσις". This means "falling off" and is an analogy to leaves falling off a tree when they die (Kerr *et al.,* 1972; D'Arcy, 2019). Apoptosis is a tightly controlled process involving a number of significant cascades. Apoptosis is necessary for maintaining cellular homeostasis and in the elimination process of abnormal cells. This genetically regulated cell death mechanism is characterized by two pathways: (1) an intrinsic pathway regulated by mitochondria and (2) an extrinsic pathway involving death receptors (Aslam *et al.,* 2023).

Numerous anticancer drugs aim to induce apoptosis, as it is characterized by physical and physiological alterations (Johnstone *et al.,* 2002). In the initial stages of apoptosis, primary changes are observed on the cell's surface, where phosphatidylserine (Ptd-L-Ser), a negatively charged phospholipid, is translocated from the inner leaflet facing the cytosol to the plasma membrane's outer layer. Ptd-L-Ser is exposed to the external cell surface however, this is not distinctive to apoptosis but also necrosis. The exposed Ptd-L-Ser signals macrophages to engulf the cell. Even though Ptd-

L-Ser externalization is a ubiquitous occurrence in apoptosis, it is cell type-specific and may not be required in several apoptotic cell lines (Elmore, 2007; Tower, 2015; Vermes *et al*., 1995).

Apoptosis can be observed via light microscopy due to the morphological changes that occur; an apoptotic cell proceeds to round up, followed by blebbing of the cell membrane, which is easily recognizable in adherent cells (Kerr *et al.,* 1972). The cell's nucleus begins to condense and segregate (pyknosis), undergoes destructive fragmentation (karyorrhexis) and/or marginalizes against the nuclear membrane. Cytoplasmic condensation occurs and intracellular substrates undergo proteolytic cleavage. The compacted cell is then reorganized and disintegrates into "apoptotic bodies". These double membrane-bound vesicles contain a variety of cellular components, including organelles, condensed nuclei, and cytosolic material. Eventually, these apoptotic bodies are taken up and degraded by lysosomal enzymes and macrophages(Häcker, 2000).

(a) *Proapoptotic function of GAPDH*

Recent research suggests that glyceraldehyde-3-phosphate dehydrogenase (GAPDH) is more than just an enzyme in the sixth step of glycolysis. It may also have other roles in the body. Under normal conditions, This enzyme catalyzes the phosphorylation and oxidation of glyceraldehyde-3-phosphate (G-3-P) to 1,3-bisphosphoglycerate (BPG). Nicotinamide adenine dinucleotide (NAD^+) acts as the electron acceptor for this reaction, which allows for the glycolytic breakdown of glucose when converted to nicotinamide adenine dinucleotide (NAD) + hydrogen (H), (NADH) (Berry and Boulton, 2000; Chuang *et al.,* 2005). Other functions separate from its participation in glycolysis include endocytosis, cytoskeletal dynamics, DNA repair and nuclear RNA export (Tatton *et al.,* 2000).

GAPDH responds to intracellular and extracellular stress by activating pathways that either recover stressed cells or initiate a cell death signalling pathway. GAPDH is reversibly inactivated by S-thiolation when a cell is exposed to oxidative stress, allowing it to maintain a balanced oxidation/reduction state. However, when there is an increase in GAPDH levels in the mitochondria, GAPDH activates apoptotic mechanisms and induces proapoptotic mitochondrial membrane permeabilization, which is believed to be the initial event in the intrinsic pathway. This enables proapoptotic (soluble) proteins such as cytochrome *c* and the apoptosis-inducing factor (AIF) to be released (Aslam *et al.,* 2023; Colell *et al.,* 2009; Schuppe-Koistinen *et al.,* 1994; Tarze *et al.,* 2007; Tristan *et al.,* 2011). The role that GAPDH plays in apoptosis was first seen in overexpressed GAPDH in cultured apoptotic cerebellar cells (Ishitani *et al.,* 1996). Overexpression of GAPDH has been previously noted in apoptotic thymocytes, PC12 (embryonic rat adrenal medulla) cells, and HEK-293 cells (Tatton *et al.,* 2000). Additional earlier studies had indicated that GAPDH expression

in the nucleus increased in cells undergoing apoptosis, indicating that GAPDH may initiate apoptosis from this organelle (Tarze *et al.,* 2007).

(b) *Intrinsic (mitochondrial-mediated) apoptotic pathway*

It is well known that mitochondria are the powerhouse organelles of the cell. They produce ATP and serve as a key regulatory component in the intrinsic apoptotic pathway (Synytsya *et al.,* 2003; McBride *et al.,* 2006). This cell death pathway is brought on by internal stressors such as the accumulation of ROS, cytoskeleton disruption, DNA damage (condensation or fragmentation), the loss of osmotic regulation, or the activation of oncogenes. Due to its function as a sensor for cellular stress, the tumour suppressor gene *p53* serves as an initiator for this pathway as well as maintaining cellular homeostasis and genome stability (Cai *et al.,* 1998; Johnstone *et al.,* 2002; Wang, 2020).

In biological systems, ROS are continuously produced and removed, which is crucial for several normal biochemical activities as well as dysfunctional and pathological ones (Lupidi *et al.,* 2013). ROS are involved in processes such as cellular respiration and include singlet oxygen ($^1O_2$), superoxide anion (O_2^-), hydrogen peroxide (H_2O_2) and hydroxyl radicals (•OH). Excessive levels of ROS however result in damage to mitochondrial functioning and initiate apoptosis within cancer cells (Hu *et al.,* 2022).

Apoptosis is induced in mitochondria (**Figure 1.4**) through the recruitment of Bcl-2 proteins. Bax and the Bcl-2 homologous antagonist/killer (Bak) translocate to the outer mitochondrial membrane (OMM), and subsequently oligomerize to form the mitochondrial permeability transition pore (MPTP) protein. This process is referred to as the mitochondrial outer membrane permeability (MOMP). The MPTP complex is composed of the voltage-dependent anion channel (VDAC), the adenine nucleotide translocator (ANT), cyclophilin D (CypD), and the c-subunit ring of the F1F0 ATP synthase (Aslam *et al.,* 2023; Kim *et al.,* 2017). Mitochondrial separation and transmembrane potential depolarization (mTP) are regulated by the formation of permeability transition pores (PTP) in the inner mitochondrial membrane (IMM). This causes the mitochondria to rupture, releasing proapoptotic factors from the intermembrane into the cytosol. This is thought to be an irreversible event in the apoptotic cascade (Peña-Blanco and Garcia-Sàez, 2018). Proapoptotic factors include secondary mitochondria-derived activators of caspases or inhibitors of apoptosis proteins (Smac/DIABLO), HtrA2/OMI, heat shock protein 10, endonucleases G and AIF and cytochrome *c* (Saelens *et al.,* 2004).

Cytochrome *c* is located in the IMM respiratory chain and is a well conserved nuclear DNA-encoded protein. In healthy mitochondria, cytochrome *c* functions as an electron transport shuttle between complex III (ubiquinol) and complex IV (cytochrome oxidase), while in damaged mitochondria it

promotes apoptosis (Cai *et al.,* 1998; Pessoa, 2022). This pathway is controlled by the Bcl family of proteins (Yang *et al.,* 2009). Released cytochrome *c* binds to the adaptor molecule Apaf-1, which facilitates the combination of dATP with Apaf-1. Caspases (cysteine-aspartic proteases) are proteolytic enzymes that regulate cell death and inflammation. They are zymogens defined by three domains: an N-terminal peptide (the pro-domain), the large catalytic (~ p20) subunit and the small catalytic (~ p10) subunit (Boice and Bouchier-Hayes, 2020). Inactivated caspases (procaspases) are present in the cytoplasm and are activated through autocatalytic cleavage. The recruitment and activation of initiator procaspase-9 is mediated by the interaction of caspase recruitment domains, CARD-CARD with Apaf-1 (Saelens *et al.,* 2004). Upon activation, caspase-9 signals the transfer of procaspases-3, -6, and/or -7 to the apoptosome, where they are subsequently activated. These effector caspases then digest intracellular substrates implicated in the apoptosis execution phase (Kumar *et al.,* 2005; Tower, 2015; Ricci and Zong, 2006).

(c) *Extrinsic (receptor-mediated) apoptotic pathway*

Extracellular binding of signalling ligands to transmembrane death receptors activates the extrinsic pathway (**Figure 1.4**). Death receptors consist of an external domain and a cytosolic domain (Ricci and Zong, 2006). This apoptotic cascade is associated with death receptors that form part of the subfamily of tumour necrosis factor receptors (TNFR). Fas, TNF receptor-1 (TNFR1), TNF-related apoptosis-inducing ligand (TRAIL) receptors-1 and -2 (TRAIL-R1 / DR4 and TRAIL-R2 / DR5), and death receptors 3 and 6 (DR3 and DR6). These receptors are composed of cysteine-rich external death effector domains (DED) that are specific to a collection of protein motifs, whereas only specific ligands have an intracellular death domain (DD) (Cullen and Martin, 2015; Ricci and Zong, 2006). Upon ligand binding, the DD undergoes a conformational change, which engages numerous adaptor protein factors to stimulate the death-induced signalling cascade (DISC). Procaspases-8 and -10 bind to the DISC and upon activation facilitate the autocatalytic cleavage of the caspase-3 cascade (Cullen and Martin, 2015; Walczak *et al.,* 2013).

The Fas receptor/ligand (FasR/FasL) and TNFR/TRAIL mechanisms orchestrate the extrinsic apoptotic pathway (Cullen and Martin, 2015; Ricci and Zong, 2006). The interaction of FasL/TRAIL with signaling adaptors, such as the Fas-associated death domain (FADD), is triggered by the engagement of FasL/TRAIL. This activates downstream signalling of caspase-8 and/or -10, which mediates the cleavage of Bid to form tBid. Thereafter, tBid is translocated to the mitochondria, which activates the Bcl-2 protein family (Bax and Bak, mentioned above). This promotes the expulsion of proapoptotic factors, specifically cytochrome *c* and Smac/DIABLO which participate in the intrinsic pathway and mediate the autocatalytic cleavage of effector caspases-3, -6, and -9 (Cullen and Martin, 2015; Tower, 2015; Moffitt *et al.,* 2010; Mroz *et al.,* 2011).

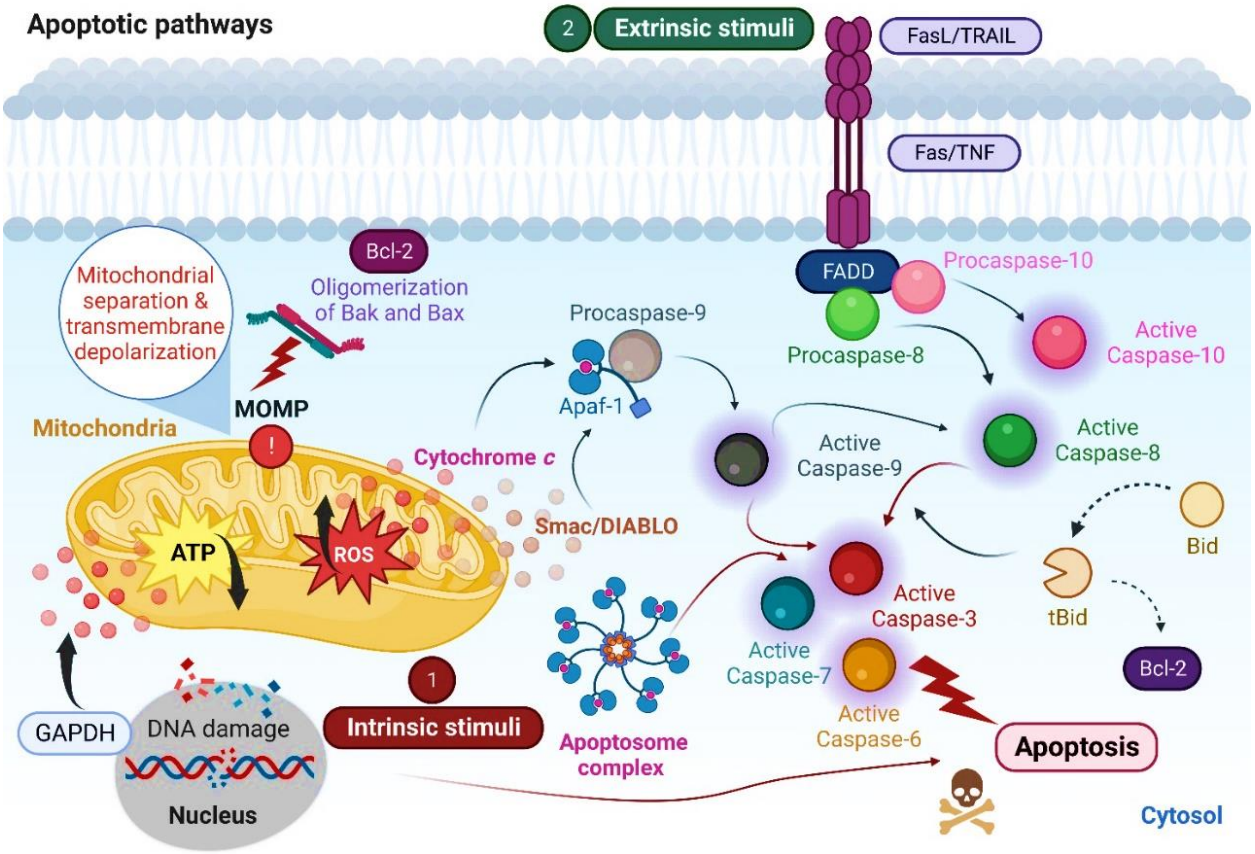


Figure 1.4. An overview of (1) the intrinsic (mitochondrial-mediated) and (2) the extrinsic (ligand-mediated) apoptotic pathways (created with BioRender.com, 2022). (1) Intrinsic stimuli (i.e., oxidative stress and DNA damage) activate Bcl-2 proteins, Bak and Bax to oligomerize. This causes the mitochondrial outer membrane to become permeable (MOMP). The soluble proteins cytochrome *c* and Smac/DIABLO are released into the cytosol. Together with procaspase-9, they bind to the Apaf-1 molecule and create the apoptosome complex. Initiator caspase-9 cleaves downstream effector caspases caspases-3, -6 and/or -7 which results in apoptosis. (2) Extrinsic stimuli (i.e., severe injury to epithelial tissue and radiation) initiate the activation of tumour necrosis receptors (FasL/TRAIL), upon ligation of death receptors, numerous adaptor molecules are recruited (FADD). Caspase-8 is activated, which cleaves Bid to form tBid. This activates the Bcl-2 proteins and consequently downstream caspase-3, -6 and -7 activity. Recruiting initiator caspases-8 or -10 as procaspases induces the formation of DISC and conformational changes in the DD. The DISC activates and releases procaspases-8 and/or -10 into the cytosol which trigger effector caspases-3, -6, and -7 (Aslam *et al.*, 2023; Cullen and Martin, 2015; Kim *et al.*, 2017; Saelens *et al.*, 2004; Tower, 2015; Moffitt *et al.*, 2010; Mroz *et al.*, 2011).

1.4.2. Necrosis

Necrosis, a pathological progression of cell death, is typically triggered by external factors (i.e., an infection or an injury). In contrast to apoptosis, its activation is not dependent on the Bcl-2 or caspase protein families, but on the inhibition of cellular energy production (ATP), the production of ROS, and/or a dysfunction in homeostatic ion channels and/or pumps. **Table 1.1** shows the main differences between apoptosis and necrosis (D'Arcy, 2019; Nikoletopoulou *et al.,* 2013; Stoian *et al.,* 2014; Tower, 2015; Yu *et al.,* 2021; Zong and Thompson, 2006). Necrosis is distinguished by the disruption of cell membrane integrity, the enlargement of organelles, and the expulsion of intracellular contents into the extracellular space. In addition, necrosis leads to the loss of functional homeostatic ion channels such as the intracellular calcium (Ca^{2+}) flux. It results in damage to membrane lipids and the depletion of ATP (Bold *et al.,* 1997; Ricci and Zong, 2006; Zong and Thompson, 2006). Leakage of intracellular factors, including proteins and nucleic acids, during necrosis is known to initiate an inflammatory response. High-mobility group box 1 (HMGB1) and the hepatoma-derived growth factor (HDGF) are among these factors. They are identified by a variety of proteins, including the activated core protein of the inflammasome, nucleotide-binding and leucine-rich repeat 3 protein (NLRP3). These proteins initiate the release of the pro-inflammatory cytokine interleukin-1 beta (IL1) (Festjens *et al.,* 2006; Nikoletopoulou *et al.,* 2013; Yuan *et al.,* 2016).

Necrosis has repeatedly been termed an uncontrolled cell death process; however late 1980s research suggested that necrosis may be a form of programmed cell death. Two regulated types of necrosis are necroptosis and pyroptosis (Yuan *et al.,* 2016; Zong and Thompson, 2006). When apoptosis is repressed, either by inhibition of caspases or the depletion of ATP, FasL and TRAIL ligands are activated to initiate necroptosis. This process is facilitated by receptor-interacting protein kinase 1 (RIPK1), particularly when caspase-8 is compromised. DRs mediate the formation of a RIPK1-RIPK3-mixed lineage kinase domain-like protein (MLKL)/complex II. The MLKL is then phosphorylated by RIPK3. This causes dysfunction in ionic pumps, depolarization of the mitochondrial membrane and subsequent cell lysis (Nikoletopoulou *et al.,* 2013; Yu *et al.,* 2021). Morphological characteristics of necroptosis are (1) cellular and organelle swelling, (2) chromatin condensation, and (3) the loss of plasma membrane integrity (Yu *et al.,* 2021).

Table 1.1. Significant differences between the two primary types of cell death, apoptosis and necrosis.

Apoptosis	Necrosis
Programmed and controlled	Pathological and uncontrolled
Does not trigger an inflammatory response	Triggers an inflammatory response
Cellular contents are enveloped into small vesicles (apoptotic bodies) and removed by phagocytosis	Spillage of cellular contents into extracellular space and subsequent damage to surrounding tissue
Cellular shrinkage and chromatin condensation	Cellular and organelle swelling
Intact plasma membrane	Loss of plasma membrane integrity

1.4.3. Autophagy

Unlike necrosis, autophagy is a conserved form of cell death. It is distinguished by the absence of chromatin condensation and the confinement of cellular components for degradation within lysosomes (Kim and Lee, 2014). Autophagy is initiated by oxidative stress, toxic stimuli or gamma-radiation, which damage organelles. Cellular elements are then arranged to isolate a part of the cytoplasm into a structure known as the autophagosome. The autophagosome is then translocated to the lysosyme and fused for proteolysis. Lysosomes can break down these components into essential elements that are either (1) collected and 'recycled' to create new cellular structures or (2) processed further and used as an energy source (D'Arcy, 2019; Kim and Lee, 2014; Tower, 2015). **Figure 1.5** shows the principal morphological changes in cancer cells undergoing apoptosis, necrosis and autophagic cell death.

Autophagy can essentially be explained in four processes: (1) The initiation process whereby serine-threonine protein kinase (ULK1) leads autophagy. ULK1 interacts with the autophagy-related gene 13 (ATG13)-family interacting protein 200 kD (FIP200) kinase complex. This interaction allows for the initiation of rapamycin complex 1 (mTORC1) and AMP-activated protein kinase (AMPK). (2) The nucleation process begins when ULK1 activates the Beclin-1-VPS34 complex. It is believed that these activation stages contribute to the formation of the membrane of autophagic vesicles (3) In the maturation process, elongation by ATG protein conjugation systems contributes to the establishment of the autophagosome once the isolation membrane has been enclosed. The multiprotein homotypic fusion and protein sorting (HOPS) complex and adaptor proteins such as syntaxin 17 and the ectopic P-granules 5 autophagy tethering factor (EPG5) facilitate autophagosome-lysosyme fusion. Lastly, (4) in the degradation process, the cellular components within the autophagosome are degraded through lysosomal hydrolases (reviewed in detail by Kim and Lee, 2014 and Onorati *et al.,* 2018).

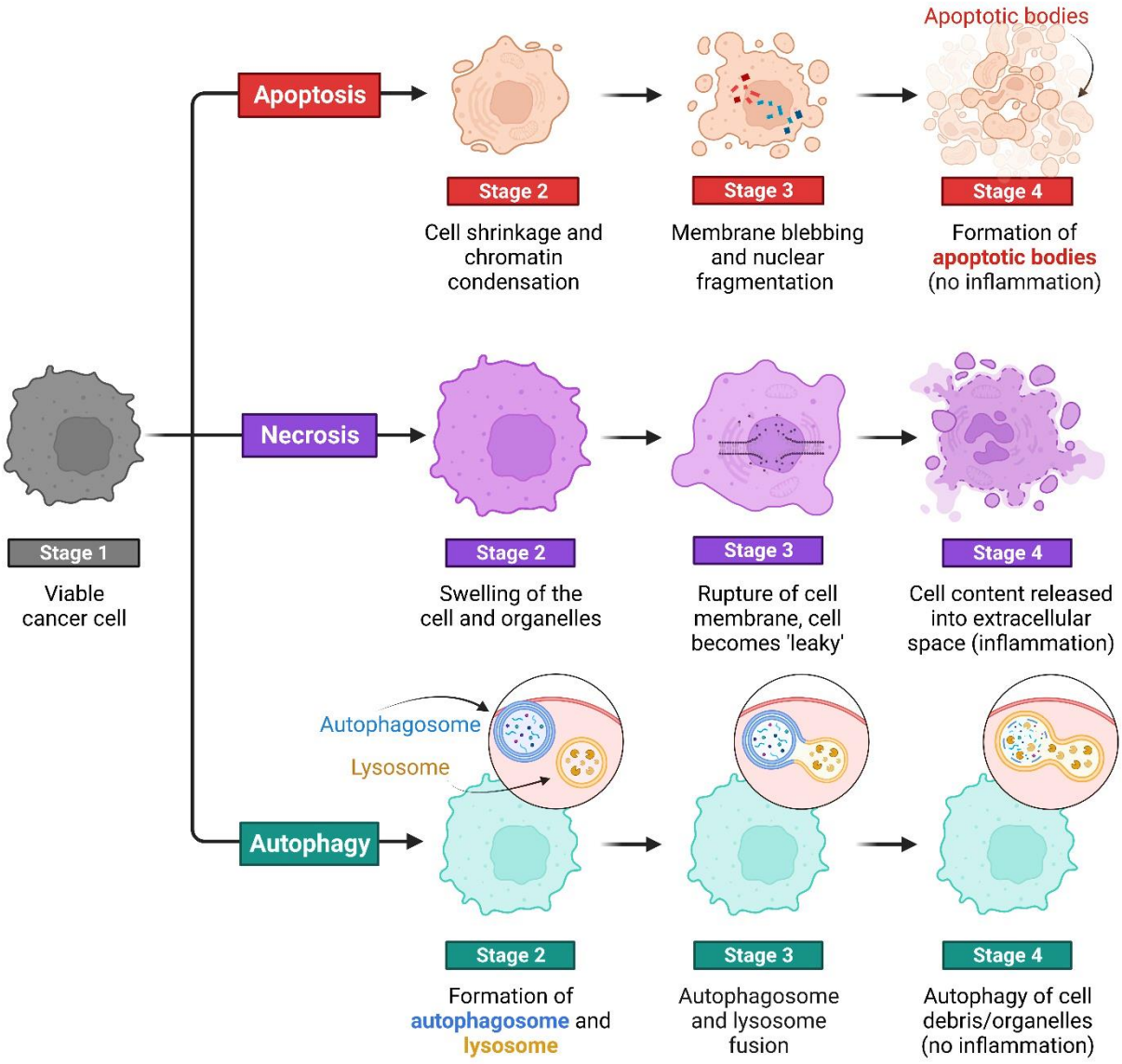


Figure 1.5. Principle morphological changes in cancer cells undergoing apoptosis, necrosis and autophagy cell death (Adapted from "*Types of Cell Death in Cancer Cells*", created with BioRender.com, 2023).

1.5. Molecular Docking: A drug discovery tool

Molecular or computational (*in silico*) docking first appeared in the mid-1970s. It is now a well-developed and accurate method of understanding how compounds or lead drugs of interest interact with molecular targets within the body. Docking predicts the optimal orientation of a ligand within the active site of a target receptor to produce a stable complex. Numerous studies have reported its use in ligand (potential drug)-receptor binding by identifying structural determinants (Eid *et al.*, 2018; Khazanov and Carlson, 2013; Muchtaridi *et al.*, 2017). The objective of molecular docking is to achieve a binding conformation between the ligand and the receptor that minimizes the system's total free energy. Molecular docking can analyze relationships between molecular targets in diseases such as cancer. It sheds light on several biological processes and the discovery of drug lead complexes (Ruvinsky, 2007; Pinzi and Rastelli, 2019).

Identifying the target protein of interest is the first step in docking and identifying the ligand or the receptor. The target protein must have a predictable three-dimensional crystallographic structure. It is usually accessible from the Protein Data Bank (PDB). The lowest energy indicates a stable and effective affinity between the ligand and active site of the protein. The bound conformation and binding free energies were predicted using docking software (**Figure 1.6**). MGLTools with AutoDockTools is the most frequently used docking software. These tools are visual interfaces applied to prepare coordinates and interpret the data (Forli *et al.*, 2016). According to Muchtaridi *et al*. (2017), molecular docking scoring functions calculate binding affinities that rank ligands (drugs or complexes) according to their potential use in the development of drugs. The interaction between a ligand and the selected target protein occurs at the atomic level, and scoring functions predict multiple conformations. However, the conformation with the lowest binding energy is selected, as the relative orientation between the ligand and the receptor is considered highly stable. In this study (findings presented in chapter five), a single docking of a ligand-protein with binding free energy estimates was investigated for stable conformations (Pinzi and Rastelli, 2019).

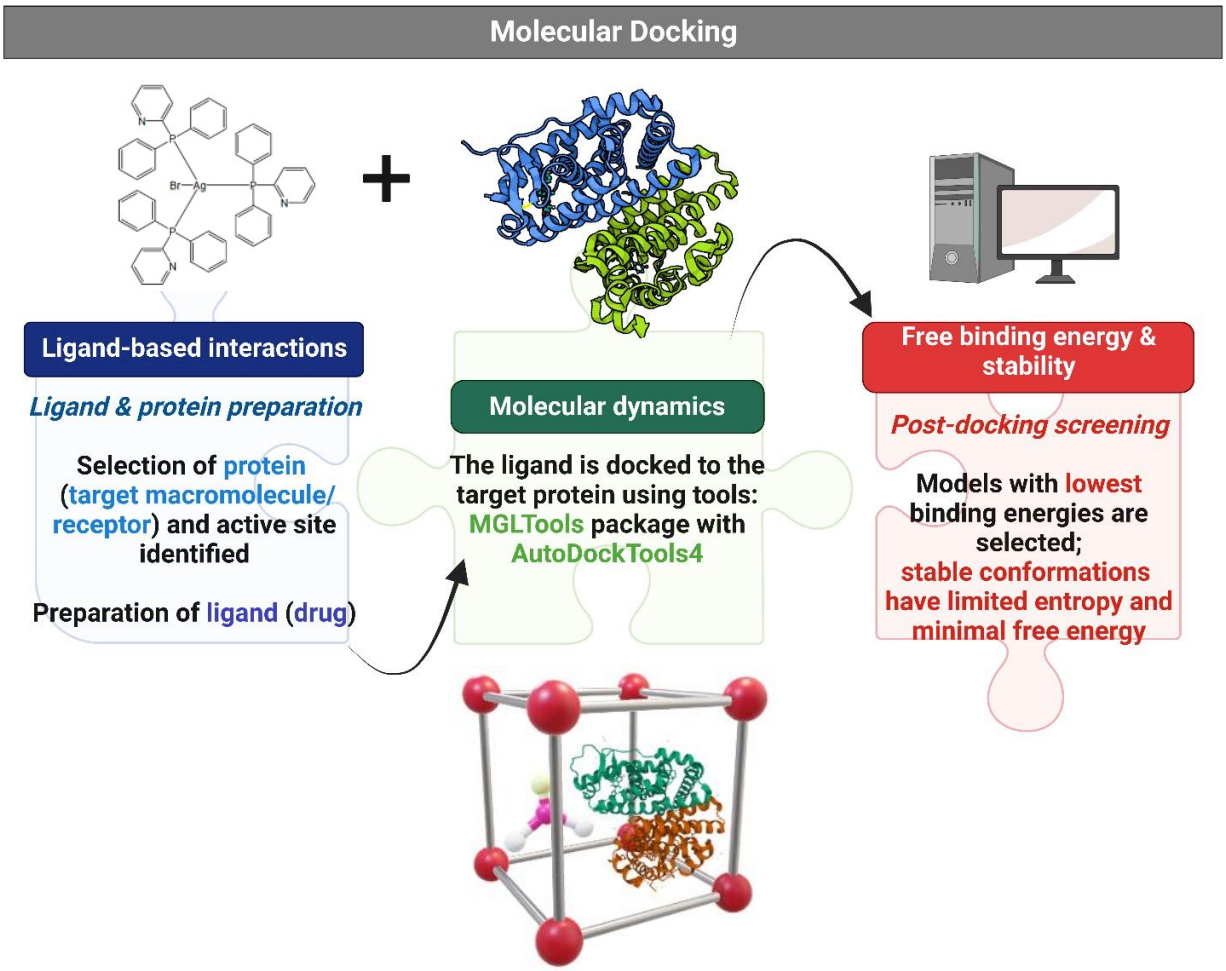


Figure 1.6. *In silico* molecular docking approaches used to improve screening results. Ligand-based approaches combined with free binding energies scoring improve docking predictions and the selection of stable conformations (Adapted from Pinzi and Rastelli, 2019; created with BioRender.com, 2023).

Cancer poses significant challenges in terms of treatment, owing to the ability of malignant cells to overcome normal biological systems and processes. Hence, there is growing interest in promoting the advancement of novel anticancer therapeutics that induce programmed cell death, with a specific focus on intrinsic apoptosis. In this study, a series of thirteen novel lipophilic silver mono-dentate phosphine complexes were assessed for their anticancer properties against various malignancies. Investigations were conducted into targeting essential points in the apoptotic pathway, antimetastatic activity, and whether silver (I) phosphine complexes could be utilized as antiestrogens in hormonal therapy.

1.6. Hypotheses and Aims

Hypotheses

- Silver(I) phosphine complexes are selective for malignant cell lines with minimal toxicity to transformed HEK-293 (kidney) and non-malignant MRHF (skin) cells.
- Silver(I) phosphine complexes are effective anticancer agents that target an apoptotic cell death mechanism in A549 (lung), HEP-G2 (liver), HT-29 (colon), MCF-7 and MDA-MB-231 (breast) malignancies.
- Silver(I) phosphine complexes could potentially prevent metastasis (cell migration) in A549 malignant cells.
- A potential hit-to-lead silver(I) phosphine complex targets and binds to estrogen receptor alpha and estrogen receptor beta in MCF-7 (breast) cells.

Aims

- To identify complexes that overcome sustained proliferative signalling in various malignant cell lines and determine their IC_{50} concentrations.
- To determine if phosphine silver mono-dentate complexes with different ligands, silver salts and their ratio will induce the intrinsic mitochondrial-mediated apoptotic pathway in malignant cell lines.
- To identify if selected complexes exhibit any antimetastatic activity in A549 cells.
- Determining the specificity of silver(I) phosphine complexes towards a distinct malignant cell line will allow for targeted anticancer therapy. This includes identification of a possible hit-to-lead complex that initiates cell death in all malignancies.
- To achieve an optimal binding conformation between a potential hit-to-lead silver(I) phosphine complex and the estrogen alpha, and estrogen beta receptors in MCF-7 cells.

1.7. Experimental Objectives

This study consists of four parts, and the main objectives of each part are summarized below:

Part I

In vitro cytotoxicity screening of silver(I) phosphine complexes in malignant and non-malignant cell lines

- Culture seven human-derived malignant cell cultures: A375 non-pigmented melanoma, A549 lung adenocarcinoma, HEP-G2 hepatocellular carcinoma, HT-29 colorectal adenocarcinoma, MCF-7 and MDA-MB-231 breast adenocarcinomas, SNO oesophageal squamous cell carcinoma; and two non-malignant cell cultures: MRHF foreskin fibroblast cells and HEK-293 embryonic kidney cells.
- Determine the cytotoxicity of thirteen novel silver(I) phosphine complexes attached to different ligands (benzyl-diphenyl-phosphane, (4-diphenylphosphanyl-phenyl)-dimethylamine, dicyclohexyl-phenyl-phosphane and 2-diphenylphosphanyl-pyridine) and silver salts with different ratios, in non-malignant and malignant cell lines after 24 h and 48 h of treatment.
- Determine the cytotoxicity of the specific un-complexed phosphine ligands on non-malignant and malignant cell lines after 24 h and 48 h of treatment.
- Select effective silver(I) phosphine complexes for each malignant cell line. These complexes decrease cell viability in the respective malignant cells after 24 h and 48 h, while remaining non-toxic to the non-malignant cells.
- Analyze the cellular morphology of the non-malignant cells: MRHF and transformed HEK-293 cells, treated with the selected silver(I) phosphine complexes, using a light microscope.
- Establish IC_{50} (maximal inhibitory) concentrations of the selected silver(I) phosphine complexes only in the above malignant cells by means of dose-responsive studies.

Part II

Apoptogenic properties of selected complexes on malignant A549, HEP-G2 and HT-29 cell lines

- Culture three human-derived malignant cell cultures: A549 lung adenocarcinoma, HEP-G2 hepatocellular carcinoma, and HT-29 colorectal adenocarcinoma.
- Select the respective silver(I) phosphine complexes for each malignant cell line from the cytotoxicity *in vitro* screening data presented in **Part I**.
- Examine the cellular morphology of malignant cells treated with their selected silver(I) phosphine complexes under a light microscope.

- Study the changes in cellular energy metabolism by measuring GAPDH activity within cells treated with selected silver(I) phosphine complexes.
- Study the cytotoxic effect of these complexes by using a CellTiter-Glo® luminescence assay which quantifies ATP.
- Confirm if selected silver(I) phosphine complexes induce intracellular ROS in malignant cells using the flow cytometric Muse® Oxidative Stress kit.
- Determine the potential mode of cell death by monitoring if these complexes cause phosphatidylserine externalization in malignant cells by using the flow cytometric Muse® Annexin V and Dead Cell Assay kit.
- Measure the change in mitochondrial potential and cellular plasma permeabilization by using the flow cytometric Muse® MitoPotential kit.
- Identify a possible drug target by measuring cytochrome P450 isoform CYP1B1 activity within cells treated with selected silver(I) phosphine complexes.
- Determination of the migratory behaviour of treated A549 malignant cells. An *in vitro* wound healing scratch assay was used to determine the metastatic/migratory potential of the cells. This assay indicates whether any of the selected silver(I) complexes inhibit or impede metastasis in A549 cells.

Part III

A mini-comparative study investigating key anticancer activities of three silver(I) phosphine complexes in MCF-7 and MDA-MB-231 breast cell lines

- Culture two human-derived malignant cell cultures: MCF-7 and MDA-MB-231 breast adenocarcinomas.
- Select effective silver(I) phosphine complexes for the MDA-MB-231 malignant cell line from the cytotoxicity *in vitro* screening data identified in **Part I**. These complexes will be investigated on the MCF-7 to allow for a comparison study.
- Analyze the cellular morphology of MCF-7 and MDA-MB-231 cells treated with selected silver(I) phosphine complexes using a light microscope.
- Confirm if selected silver(I) phosphine complexes induce intracellular ROS in malignant breast cells using the flow cytometric Muse® Oxidative Stress kit.
- Determine the potential mode of cell death by monitoring if these complexes cause phosphatidylserine externalization in malignant breast cells by using a flow cytometric Muse® Annexin V and Dead Cell Assay kit.
- Measure the change in mitochondrial potential and cellular plasma permeabilization by using the flow cytometric Muse® MitoPotential kit.

- Establish if selected complexes target the intrinsic mitochondrial-mediated pathway of apoptosis by labelling metabolically active mitochondria, the translocation of cytochrome *c* and the chromatin/DNA integrity of malignant cells. Malignant breast cells will be stained with fluorescent probes: Alexi-Fluor® 488 mouse anti-cytochrome *c* specific antibody and MitoTracker® Orange CMTMRos. As confirmation of DNA damage by apoptosis, cells will be stained with Hoechst-33258.

Part IV

In silico molecular modelling of complex 4 with estrogen receptors alpha and beta

- Determine whether a selected hit-to-lead complex (from studies conducted in **Part I**) targets the estrogen receptor alpha and estrogen receptor beta by molecular docking studies, using MGL Tools with AutoDockTools4 and Discovery Studio Visualizer.

CHAPTER TWO:
IN VITRO CYTOTOXICTY SCREENING OF SILVER(I) PHOSPHINE COMPLEXES IN MALIGNANT AND NON-MALIGNANT CELLS

2.1. Prologue

AgXL*n* is the formula for tertiary silver(I) phosphine complexes, where X is the covalent or non-covalent anion, L is the tertiary phosphine of which there are 4; and *n* is the ratio for the ligand, which may range from 1 to 4. These complexes were synthesized by combining a silver(I) salt with the correct amount of silver phosphine ligand. Silver(I) halides (Cl or Br), pseudo-halides (SCN), or nitrate derivatives were present in these salts (NO_3). The product crystallized after being heated in an acetonitrile solution under a reflux reaction. This method was used to obtain dry powder forms of respective silver(I) phosphine complexes (Meijboom *et al.,* 2009). In previous studies, numerous silver(I) phosphine complexes, including the complex designated **UJ3**, induced apoptosis in melanoma, malignant breast, and oesophageal cells. A prior study conducted by Engelbrecht *et al.* (2018) revealed that **UJ3** induced apoptosis effectively in oesophageal cancer. This article received media attention and resulted in the production of an electronic file made available on Eurekalert (AAAS, 2020). This file includes interviews with Professor Cronjé, Professor Meijboom and Dr. Engelbrecht as well as a narrative slide show. As an improved anticancer agent, preliminary studies on rats and extensive "batch" testing on several types of cancer cells have shown great promise (Engelbrecht and Cronjé, 2018; Engelbrecht *et al.,* 2018; Human-Engelbrecht *et al.,* 2017; Human *et al.,* 2015). This success motivates the investigation of additional phosphine-silver mono-dentate complexes containing various phenyl derivative ligands. It is of interest to ascertain whether these complexes induce apoptotic cell death and possibly prevent metastasis in additional cancer types.

Cytotoxicity *in vitro* screening prioritizes complexes predominantly by their selectivity towards malignant and non-malignant cell lines. In this chapter, a series of silver(I) phosphine complexes **1** - **13** and their related ligands (**L1** - **L4**) were screened on two non-malignant and seven malignant cell lines at a concentration of 10 µM after 24 h and 48 h of treatment. Complexes were regarded successful if **a)** the ligands (**L1** - **L4**) of the respective complexes induced minimal toxicity to non-malignant and malignant cell lines; **b)** 24 h and 48 h of treatment decreased cellular viability of malignant cell lines selectively, with minimal levels or no toxicity to non-malignant cells; **c)** silver(I) phosphine complexes significantly decreased the cellular viability of malignant cells; and **d)** the cells did not recover as indicated by an increase in viability. Successful complexes only were then evaluated against the respective malignant cell lines at six consecutive concentrations, and an IC_{50} value after 24 h of treatment was determined. This is an essential quantitative measure of the potency of a substance. It is the highest concentration of a substance that inhibits biological processes by ±50% (Englebrecht *et al.,* 2017; Larsson *et al.,* 2020). The purpose of cytotoxicity screening was to detect which silver(I)

phosphine complexes were most successful at inducing a cell death response and whether certain complexes were selective for a particular cell line. The selected silver(I) phosphine complexes were compared to cisplatin (CDDP), one of the most prescribed anticancer (metal-containing) drugs on the market. These findings will shed light on the specificity of a drug candidate towards a particular cell line, allowing for a targeted and more successful type of chemotherapy.

2.2. Experimental methodology

All reagents and equipment were used according to the manufacturer's guidelines. **Appendix I** contains a comprehensive inventory of the manufacturer information for all materials and tools used in chapter two's experimental analyzes.

2.2.1. Silver(I) phosphine complexes: synthesis

2.2.1.1. Preparation and characterization

Dr. Gouda Naganagowda from the University of Johannesburg's Department of Chemical Sciences, in Johannesburg (South Africa) synthesized a series of the silver(I) phosphine complexes. The silver salts used for these complexes were characterized prior to being used in biological studies. The Stuart Scientific SMP10 Melting Point instrument and a microscope-equipped with melting point apparatus were used to measure the melting points of the complexes. FT-IR spectra were captured with a PIKE Miracle Gate ATR attachment on a Bruker Tensor 27 FT-IR spectrometer. Nuclear magnetic resonance (NMR) spectra were measured and recorded using an Ultrashield Avance III Bruker analyzer operating at 400 MHz for ^{1}H nuclei;75 MHz for $^{13}C\{H\}$ nuclei; and 161 MHz for $^{31}P\{H\}$ nuclei, respectively. Parts per million (ppm) measurements for all chemical changes were made, with H or C serving as internal standards. The chemical shifts of all ^{31}P-H NMR data were compared to H_3PO_4, an external reference. Dr. Edith Antunes performed elemental analysis at Rhodes University's Department of Chemistry in the Eastern Cape (South Africa) utilizing a Thermo Flash 2000 series CHNS/O, Organic Elemental Analyzer.

2.2.1.2. Synthesis of 1:2 [Silver(I)dicyclohexylphenylphosphine]SCN (**Complex 1**)

AgSCN salt (0.1014 g; 0.611 mmol) was added to dicyclohexylphenylphosphine (0.335 g and 1.222 mmol) (**L1**) in acetonitrile (50 ml). The solution underwent a reflux process for a period of 6 h, followed by filtration. The solvent was then subjected to a reduction process, resulting in a volume of approximately 10 ml, and allowed to crystallize at room temperature for 24 h. This led to the formation of small, white crystal needles, which were isolated from the solution.

Melting point: 191 - 200˚C.

Elemental Analysis: Calculated for $C_{37}H_{54}AgNP_2S$: C, 62.18%; H, 7.62%; Ag, 15.09%; N, 1.96%; P, 8.67%; S, 4.49%. Found: C 62.99%; H, 8.39%; N, 1.99%; S, 3.46%.

IR (v/cm^{-1}): 2923.12, 2845.96 (ν (=C-H), w), 2063.86 (ν (SCN), s), 1482.37, 1445.42, 1432.75

(ν (aromatic, C-H bend, meta), s), 999.89, 918.04, 884.80, 848.46 (ν (aromatic, C-H bend, meta), s), 747.30, 728.36, 696.86 (ν (aromatic, C-H bend, ortho), m).

^{1}H-NMR (400 MHz, $CDCl_3$) δ ppm: 1.076 – 1.442 (m, cyclohexyl H), 1.687 (m, cyclohexyl H), 1.829 (d, cyclohexyl H), 2.05 (d, cyclohexyl H), 2.310 (t, cyclohexyl H), 7.369 – 7.476 (m, aromatic H), 7.580 (d, aromatic H).

^{13}C{H}-NMR (100 MHz, $CDCl_3$) δ ppm: 25. 91 (s, cyclohexyl C), 26.74 (d, cyclohexyl C), 28.52 (s, cyclohexyl carbon), 29.57 (s, cyclohexyl C), 32.31 (s, cyclohexyl C), 128.46 (s, aromatic C), 130.58(s, aromatic C), 134.79 (s, cyclohexyl C).

^{31}P{H} NMR (161 MHz, $CDCl_3$) δ ppm: 33.23 (s).

2.2.1.3. Synthesis of 1:3 [Silver(I)dicyclohexylphenylphosphine]SCN (**Complex 2**)

AgSCN salt (0.1014 g; 0.611 mmol) was added to dicyclohexylphenylphosphine (0.503 g and 1.833 mmol) (**L1**) in acetonitrile (50 ml). The solution underwent a heat reflux process for 6 h, followed by filtration. The solvent was then subjected to a reduction process, resulting in a volume of approximately 10 ml, and allowed to crystallize at room temperature for 24 h. This led to the formation of small, white crystal needles, which were isolated from the solution.

Melting point: 188 - 191˚C.

Elemental Analysis: Calculated for $C_{55}H_{81}AgNP_3S$: C, 66.79%; H, 8.25%; Ag, 10.91%; N, 1.42%; P, 9.39%; S, 3.24%. Found: C, 62.50%; H, 7.87%; N, 1.93%; S, 4.63%.

IR (v/cm^{-1}): 2923.11, 2845.75 (ν (=C-H), w), 2063.40 (ν(SCN), s), 1481.50, 1445.47, 1432.88 (ν (aromatic, C-H bend, meta), s), 1000.16, 916.63, 886.47, 848.80, 817.80 (ν (aromatic, C-H bend, meta), s), 746.09, 728.52, 696.77 (ν (aromatic, C-H bend, ortho), m).

^{1}H-NMR (400 MHz, $CDCl_3$) δ ppm: 1.079 – 1.451 (m, cyclohexyl H), 1.615 (s, cyclohexyl H), 1.705(d, cyclohexyl H), 1.836 (d, cyclohexyl H), 2.053 (d, cyclohexyl H), 2.317 (t, cyclohexyl H), 7.369 (t,aromatic H), 7.388 (d, aromatic H), 7.405 (s, aromatic H), 7.439 (t, aromatic H), 7.457 (t, aromaticH), 7.569 (d, aromatic H).

^{13}C{H}-NMR (100 MHz, $CDCl_3$) δ ppm: 25.88 – 32.50 (s, cyclohexyl C), 128.5 – 135 (3 singlets, aromatic C).

^{31}P{H} NMR (161 MHz, $CDCl_3$) δ ppm: 24.58 (s).

2.2.1.4. Synthesis of 1:2 [Silver(I) diphenyl-2-pyridylphoshine]Cl (**Complex 3**)

AgCl salt (0.0444 g; 0.31 mmol) was added to diphenyl-2-pyridylphosphine (0.1632 g and 0.62 mmol) (**L2**) in acetonitrile (50 ml). The solution underwent a heat reflux process for 6 h, followed by filtration. The solvent was then subjected to a reduction process, resulting in a volume of approximately 10 ml, and allowed to crystallize at room temperature for 24 h. This led to the formation of small, white crystal needles, which were isolated from the solution.

Melting point: 181 - 186˚C.

Elemental Analysis: Calculated for $C_{34}H_{28}AgClN_2P_2$: C, 60.96%; H, 4.21%; Ag, 16.10%; Cl, 5.29%; N, 4.18%; P, 9.25%. Found: C, 60.92%; H, 4.46%; N, 4.16%.

IR (v/cm^{-1}): 1569.94, 1541.34, 1479.01, 1449.28, 1433.82, 1419.38 (ν (aromatic, C-H bend, meta), s), 1219.66, 1184.57, 1151.19 (ν, C-N), 1094.53, 1046.15, 1027.22, 986.38 (ν (aromatic, C-H bend, meta), s), 772.50, 741.50, 721.22, 691.70, 617.06 (ν (aromatic, C-H bend, ortho), m).

^{1}H-NMR (400 MHz, $CDCl_3$) δ ppm: 7.179 – 7.218 (m, aromatic H), 7.261 – 7.306 (m, aromatic H), 7.345 – 7.388 (m, aromatic H), 7.516 – 7.598 (m, aromatic H), 7.667 – 7.704 (m, aromatic H), 8.624 (dt, pyridyl H).

^{13}C{H}-NMR (100 MHz, $CDCl_3$) δ ppm: 123.558 (s, aromatic C), 128.686 (d, aromatic C), 130.054 (s, aromatic C), 130.318 (s, aromatic C), 132.013 (s, aromatic C), 132.245 (s, aromatic C), 134.324 (d, aromatic C), 136.109 (d, aromatic C), 150.610 (d, aromatic C), 158.297 (s, pyridyl C), 158.699 (s, pyridyl C).

^{31}P{H} NMR (161 MHz, $CDCl_3$) δ ppm: 7.48 (s).

2.2.1.5. Synthesis of 1:3 [Silver(I) diphenyl-2-pyridylphosphine]Br (**Complex 4**)

AgBr salt (0.1333 g; 0.71 mmol) was added to diphenyl-2-pyridyl phosphine (0.561 g and 2.13 mmol) (**L2**) in acetonitrile (50 ml). The solution underwent a heat reflux process for 6 h, followed by filtration. The solvent was then subjected to a reduction process, resulting in a volume of approximately 10 ml, and allowed to crystallize at room temperature for 24 h. This led to the formation of small, white crystal needles, which were isolated from the solution.

Melting point: 183 - 186˚C.

Elemental Analysis: Calculated for $C_{51}H_{42}AgBrN_3P_3$: C, 62.66%; H, 4.33%; Ag, 11.03%; Br, 8.17%. N, 4.30%; P, 9.51%. Found: C, 62.84%; H, 4.37%; N, 4.42%.

IR (v/cm^{-1}): 1569.99, 1479.34, 1448.83, 1433.24, 1417.92 (ν (aromatic, C-H bend, meta), s), 1277.34, 1151.29, (ν, C-N), 1092.28, 1046.53, 1028.20, 997.43, 987.26 (ν (aromatic, C-H bend, meta), s), 742.47, 720.25, 691.33, 617.77, 521.03 (ν (aromatic, C-H bend, ortho), m).

^{1}H-NMR (400 MHz, $CDCl_3$) δ ppm*:* 7.140 – 7.183 (m, aromatic H), 7.251 – 7.295 (m, aromatic H),7.337 – 7.377 (m, aromatic H), 7.476 – 7.548 (m, aromatic H).

^{13}C{H}-NMR (100 MHz, $CDCl_3$) δ ppm: 123.100 (s, aromatic C), 128.589 (d, aromatic C), 129.507 (s, aromatic C), 129.731 (d, aromatic C), 133.245 (d, aromatic C), 134.331 (d, aromatic C), 135.872

(d, aromatic C), 150.377 (d, pyridyl C), 159.800 (s, pyridyl C), 160.106 (pyridyl C).

^{31}P{H} NMR (161 MHz, $CDCl_3$) δ ppm: 3.63 (s).

2.2.1.6.Synthesis of 1:1 [Silver(I) benzylphenylphosphine]SCN (**Complex 5**)

Solid AgSCN (0.1179 g; 0.71 mmol) was added to a solution of benzyldiphenylphosphine (0.1961 g and 0.71 mmol) (**L3**) in acetonitrile (50 ml). The solution underwent a heat reflux process for 6 h, followed by filtration. The solvent was then subjected to a reduction process, resulting in a volume of approximately 10 ml, and allowed to crystallize at room temperature for 24 h. This led to the formation of small, white crystal needles, which were isolated from the solution.

Melting point: 170 - 172°C.

Elemental Analysis: Calculated for $C_{20}H_{17}AgNPS$: C, 54.31%; H, 3.87%; Ag, 24.39%; N, 3.17%; P, 7.00%; S, 7.25%. Found: C, 54.16%; H, 3.86%; N, 3.02%; S, 7.01%.

IR (v/cm^{-1}): 3028.69 (ν (=C-H),w), 2094.32 (ν (SCN), s); 1600.33 (ν (C=C aromatic), m), 1495.39, 1480.86, 1454.63, 1433.83, 1307.61 (ν (aromatic, C-H bend, meta), s), 771.99, 750.56, 739.02, 689.55 (ν (aromatic, C-H bend, ortho), m).

^{1}H-NMR (400 MHz, $CDCl_3$) δ ppm: 3.67 (s, 2H, CH_2), 7.009 - 7.410 (m, 18H, Ar-H).

^{13}C{H}-NMR (100 MHz, $CDCl_3$) δ ppm: 134.36, 133.32, 133.17, 131.77, 131.52, 131.13, 130.47, 129.70, 129.64, 128.87, 128.79, 128.66, 128.64, 128.56, 128.44, 127.56, 126.81, 126.78 (s, Aromatic Carbon), 35.35, 35.25 (s, 4-CH_2).

^{31}P{H} NMR (161 MHz, $CDCl_3$) δ ppm: 11.88 (Single Peak).

2.2.1.7.Synthesis of 1:2 [Silver(I) benzyldiphenylphosphine]SCN (**Complex 6**)

Solid AgSCN (0.1179 g; 0.71 mmol) was added to a solution of benzyldiphenylphosphine (0.3812 g and1.43 mmol) (**L3**) in acetonitrile (50 ml). The solution underwent a heat reflux process for 6 h, followed by filtration. The solvent was then subjected to a reduction process, resulting in a volume of approximately 10 ml, and allowed to crystallize at room temperature for 24 h. This led to the formation of small, white crystal needles, which were isolated from the solution.

Melting point: 270 - 272°C.

Elemental Analysis: Calculated for $C_{39}H_{34}AgNP_2S$: C, 65.19%; H, 4.77%; Ag, 15.01%; N, 1.95%; P, 8.62%; S, 4.46%. Found: C, 64.66%; H, 4.75%; N, 1.78%; S, 4.24%.

IR (v/cm^{-1}): 3054.41 (ν (=C-H), w), 2078.47 (ν(SCN), s); 1598.50 (ν (C=C aromatic), m), 1494.50, 1480.35, 1451.84, 1433.66, 1308.23 (ν (aromatic, C=C aromatic, m), 1219.00 (s), 1182.23 - 998.31, 907.59, 833.41 (ν (aromatic, C-H bend, meta), s), 773.31, 742.45, 717.84, 691.73 (ν (aromatic, C-H bend, ortho), m).

^{1}H-NMR (400 MHz, $CDCl_3$) δ ppm: 3.65 (s, 4H, CH_2), 7.710 - 7.737 (m, 36H, Ar-H).

^{13}C{H}-NMR (100 MHz, $CDCl_3$) δ ppm: 134.73, 133.27, 133.11, 131.95, 131.72, 131.22, 131.13, 130.40, 130.18, 130.13, 129.63, 129.57, 128.84, 128.75, 128.67, 128.65, 128.54, 128.42, 128.35,

126.77, 126.73, 126.67 (s, Aromatic Carbon), 35.36, 35.27 (s, 4-CH_2).

^{31}P{H} NMR (161 MHz, $CDCl_3$) δ ppm: 11.38 (Single Peak).

2.2.1.8. Synthesis of 1:3 [Silver(I) benzyldiphenylphosphine]NO_3 (**Complex 7**)

Solid $AgNO_3$ (0.1207 g; 0.71 mmol) was added to a solution of benzyldiphenylphosphine (0.5885 g and 2.13 mmol) (**L3**) in acetonitrile (50 ml). The solution underwent a heat reflux process for 6 h, followed by filtration. The solvent was then subjected to a reduction process, resulting in a volume of approximately 10 ml, and allowed to crystallize at room temperature for 24 h. This led to the formation of small, white crystal needles, which were isolated from the solution.

Melting point: 232 - 234°C.

Elemental Analysis: Calculated for $C_{57}H_{51}AgNO_3P_3$: C, 68.54%; H, 5.15%; Ag, 10.80%; N, 1.40%; O, 4.81%; P, 9.30%. Found: C, 68.34%; H, 4.88%; N, 1.71%. *IR (v/cm^{-1})*: 3049.09 (ν (=C-H), w), 2360.48, 2342.81 (ν (alkane, C-H, stretch), asymm, w), 1734.12, 1700.27, 1684.27, 1653.02, 1635.50 (w), 1558.54, 1539.52, 1506.83, (ν (aromatic, C=C aromatic, m), 1495.87, 1453.32, 1436.07, 1387.21, 1304.37 (ν (C=C aromatic), m), 1219.11 (s), 1182.54 - 833.31 (ν (aromatic, C-H bend, meta), s), 771.37, 752.84, 743.27, 692.76 (ν (aromatic, C-H bend, ortho), m).

^{1}H-NMR (400 MHz, $CDCl_3$) δ ppm: 3.57 (s, 6H, CH_2), 6.953 - 7.423 (m, 54H, Ar-H).

^{13}C{H}-NMR (100 MHz, $CDCl_3$) δ ppm: 135.09, 133.25, 133.09, 132.48, 132.29, 131.83, 131.23, 131.14, 130.29, 129.60, 129.54, 128.83, 128.74, 128.56, 128.54, 128.43, 126.66, 126.63 (s, aromatic carbon), 35.31, 35.24 (s, 6-CH_2).

^{31}P{H} NMR (161 MHz, $CDCl_3$) δ ppm: 9.24 (Single Peak).

2.2.1.9. Synthesis of 1:1 [Silver(I) 4-(dimethylamino)phenyldiphenyl phosphine]NO_3 (**Complex 8**)

Solid $AgNO_3$ (0.1207 g; 0.71 mmol) was added to a solution of 4-(dimethylamino)phenyl diphenyl phosphine (0.2168 g and 0.71 mmol) (**L4**) in acetonitrile (50 ml). The solution underwent a heat reflux process for 6 h, followed by filtration. The solvent was then subjected to a reduction process, resulting in a volume of approximately 10 ml, and allowed to crystallize at room temperature for 24 h. This led to the formation of small, white crystal needles, which were isolated from the solution.

Melting point: 200 - 203˚C.

Elemental Analysis: Calculated for $C_{20}H_{20}AgN_2O_3P$: C, 50.55%; H, 4.24%; Ag, 22.70%; N, 5.89%; O, 10.10%; P, 6.52%. Found: C, 50.60%; H, 4.61%; N, 5.97%.

IR (v/cm^{-1}): 1592.22, 1544.62, 1512.90, (ν (aromatic, C=C aromatic, m), 1464.67, 1433.15, (ν (C=C aromatic), m), 1363.14, 1268.06, 1228.85, 1204.90 (ν, C-N, s), 1098.19, 1011.15, 999.13, 944.71 (ν (aromatic, C-H bend, meta), s), 812.08, 801.74, 746.23, 694.78 (ν (aromatic, C-H bend, ortho), m)

^{1}H-NMR (400 MHz, $CDCl_3$) δ ppm: 3.036 (s, CH3), 6.737 (dd, dimethylaminophenyl), 7.312 – 7.365(m, aromatic H), 7.422 – 7.476 (m, aromatic H).

^{13}C{H}-NMR (100 MHz, $CDCl_3$) δ ppm: 39.94 (s, methyl C), 111.60 (s, 4-(dimethylamino)phenyl

C), 112.22 (t, 4-(dimethylamino)phenyl C), 129.175 (d, aromatic C), 130.82 (s, aromatic C),130.95 (d, aromatic C), 131.24 (s, aromatic C), 133.41 (d, aromatic C), 135.67 (d, aromatic C), 152.365 (d,4-(dimethylamino)phenyl C). **^{31}P{H} NMR (161 MHz, $CDCl_3$) δ ppm**: 16.96 (s).

2.2.1.10. Synthesis of 1:2 [Silver(I) 4-(dimethylamino)phenyldiphenyl phosphine]NO_3

(**Complex 9**)

Solid $AgNO_3$ (0.1207 g; 0.71 mmol) was added to a solution of 4-(dimethylamino)phenyl diphenyl phosphine (0.4335 g and 1.42 mmol) (**L4**) in acetonitrile (50 ml). The solution underwent a heat reflux process for 6 h, followed by filtration. The solvent was then subjected to a reduction process, resulting in a volume of approximately 10 ml, and allowed to crystallize at room temperature for 24 h. This led to the formation of small, white crystal needles, which were isolated from the solution.

Melting point: 237 - 240˚C.

Elemental Analysis: Calculated for $C_{40}H_{40}AgN_3O_3P_2$: C, 61.55%; H, 5.17%; Ag, 13.82%; N, 5.38%; O, 6.15%; P, 7.94%. Found: C, 60.98%; H, 5.12%; N, 5.38%.

IR (ν/cm^{-1}): *1594.93, 1544.00, 1512.79* (ν (aromatic, C=C aromatic, m), 1479.50, 1437.01 (ν (C=C aromatic), m), 1384.46, 1361.30, 1308.84, 1221.47, 1202.23 (ν, C-N, s), 1096.81, 1039.13, 997.39, 942.70 (ν (aromatic, C-H bend, meta), s), 813.30, 801.36, 749.25, 695.52, 609.42 (ν (aromatic, C-H bend, ortho), m).

^{1}H-NMR (400 MHz, $CDCl_3$) δ ppm: 2.988 (s, methyl H), 6.653 (dt, 4-(dimethylamino) H), 7.301 – 7.409 (m, aromatic H).

^{13}C{H}-NMR (100 MHz, $CDCl_3$) δ ppm: 39.98 (s, methyl C), 112.25 (s, (dimethylamino)phenyl C), 129.175 (d, aromatic C), 128.78 (s, aromatic C),129.91 (s, aromatic C), 133.46 (s, aromatic C), 135.67 (s, aromatic C), 151.80 (s, 4-(dimethylamino)phenyl C).

^{31}P{H} NMR (161 MHz, $CDCl_3$) δ ppm: 10.68 (s).

2.2.1.11. Synthesis of 1:3 [Silver(I) 4-(dimethylamino)phenyldiphenyl phosphine]NO_3

(**Complex 10**)

Solid $AgNO_3$ (0.1207 g; 0.71 mmol) was added to a solution of 4-(dimethylamino)phenyl diphenyl phosphine (0.650 g and 2.13 mmol) (**L4**) in acetonitrile (50 ml). The solution underwent a heat reflux process for 6 h, followed by filtration. The solvent was then subjected to a reduction process, resulting in a volume of approximately 10 ml, and allowed to crystallize at room temperature for 24 h. This led to the formation of small, white crystal needles, which were isolated from the solution.

Melting point: 212 - 215˚C.

Elemental Analysis: Calculated for $C_{60}H_{60}AgN_4O_3P_3$: C, 66.36%; H, 5.57%; Ag, 9.93%; N, 5.16%; O, 4.42%; P, 8.56%. Found: C, 66.04%; H, 5.31%; N, 5.10%.

IR (ν/cm^{-1}): 1596.20, 1543.21, 1513.33 (ν (aromatic, C=C aromatic, m), 1478.69, 1445.70, 1431.82 (ν (C=C aromatic), m), 1358.92, 1305.43, 1226.49, 1201.55 (ν, C-N, s), 1039.02, 1026.19, 999.72,

944.54 (ν (aromatic, C-H bend, meta), s), 825.02, 816.01, 809.58, 743.10, 696.39, 634.36, 620.08 (ν (aromatic, C-H bend, ortho), m).

^{1}H-NMR (400 MHz, $CDCl_3$) δ ppm: 2.969 (s, methyl H), 6.500 (d, 4-(dimethylamino) H), 7.093 – 7.215 (m, aromatic H), 7.327 – 7.367 (m, aromatic H)

^{13}C{H}-NMR (100 MHz, $CDCl_3$) δ ppm: 39.98 (s, methyl C), 112.19 (d, 4-(dimethylamino)phenyl C), 128.72 (d, aromatic C), 129.65 (s, aromatic C), 132.143 (s, aromatic C), 133.37 (d, aromatic C), 133.83 (d, aromatic C), 135.59 (d, aromatic C), 151.61 (s, 4-(dimethylamino)phenyl C).

^{31}P{H} NMR (161 MHz, $CDCl_3$) δ ppm: 6.18 (s).

2.2.1.12. Synthesis of 1:3 [Silver(I) 4-(dimethylamino)phenyldiphenyl phosphine]Cl

(**Complex 11**)

AgCl salt (0.1018 g; 0.71 mmol) was added to a solution of 4-(dimethylamino)phenyl diphenyl phosphine (0.650 g and 2.13 mmol) (**L4**) in acetonitrile (50 ml). The solution underwent a heat reflux process for 6 h, followed by filtration. The solvent was then subjected to a reduction process, resulting in a volume of approximately 10 ml, and allowed to crystallize at room temperature for 24 h. This led to the formation of small, white crystal needles, which were isolated from the solution.

Melting point: 213- 217˚C.

Elemental Analysis: Calculated for $C_{60}H_{60}AgClN_3P_3$: C, 68.02%; H, 5.71%; Ag, 10.18%; Cl, 3.35%; N, 3.97%; P, 8.77%. Found: C, 67.99%; H, 5.65%; N, 3.63%.

IR (ν/cm^{-1}): 1596.76, 1544.22, 1511.71 (ν (aromatic, C=C aromatic, m), 1477.11, 1447.32, 1432.98 (ν (C=C aromatic), m), 1360.98, 1230.66, 1200.67 (ν, C-N, s), 1092.32, 1025.10, 999.24, 943.54 (ν (aromatic, C-H bend, meta), s), 804.55, 755.83, 749.22, 741.70, 694.62, 620.16, 608.59 (ν (aromatic, C-H bend, ortho), m).

^{1}H-NMR (400 MHz, $CDCl_3$) δ ppm: 2.967 (s, methyl H), 6.616 (d, 4-(dimethylamino) H), 7.223 – 7.365 (m, aromatic H).

^{13}C{H}-NMR (100 MHz, $CDCl_3$) δ ppm: 40.32 (s, methyl C), 112.50 (s, 4-(dimethylamino)phenyl C), 128.48 (d, aromatic C), 129.15 (s, aromatic C), 133.55 (d, aromatic C), 135.47 (d, aromatic C), 135.80 (d, 4-(dimethylamino)phenyl C).

^{31}P{H} NMR (161 MHz, $CDCl_3$) δ ppm: 2.01 (s).

2.2.1.13. Synthesis of 1:2 [Silver(I) 4-(dimethylamino)phenyldiphenyl phosphine]Br

(**Complex 12**)

AgBr salt (0.1333 g; 0.71 mmol) was added to a solution of 4-(dimethylamino)phenyl diphenyl phosphine (0.4335 g and 1.42 mmol) (**L4**) in acetonitrile (50 ml). The solution underwent a heat reflux process for 6 h, followed by filtration. The solvent was then subjected to a reduction process, resulting in a volume of approximately 10 ml, and allowed to crystallize at room temperature for 24 h. This led to the formation of small, white crystal needles, which were isolated from the solution.

Melting point: 185 - 190˚C.

Elemental Analysis: Calculated for $C_{40}H_{40}AgBrN_2P_2$: C, 60.17%; H, 5.05%; Ag, 13.51%; Br, 10.01%; N, 3.51%; P, 7.76%. Found: C, 60.43%; H, 5.15%; N, 3.14%.

IR (v/cm^{-1}):1596.03, 1545.34, 1512.18 (ν (aromatic, C=C aromatic, m), 1478.86, 1434.41 (ν (C=C aromatic), m), 1361.35, 1292.37, 1202.41 (ν, C-N, s), 1106.25, 1096.01, 1024.58, 996.87, 943.59 (ν (aromatic, C-H bend, meta), s), 812.73, 798.58, 749.15, 695.09, 618.88, 609.14 (ν (aromatic, C-H bend, ortho), m).

^{1}H-NMR (400 MHz, $CDCl_3$) δ ppm: 2.962 (s, methyl H), 6.616 (d, 4-(dimethylamino) H), 7.229 – 7.384 (m, aromatic H).

^{13}C{H}-NMR (100 MHz, $CDCl_3$) δ ppm: 40.12 (s, methyl C), 112.28 (d, 4 (dimethylamino)phenyl C), 128.55 (d, aromatic C), 129.46 (s, aromatic C), 133.60 (d, aromatic C), 133.56 (s, aromatic C), 134.11 (s, aromatic C), 135.87 (d, 4-(dimethylamino)phenyl C).

^{31}P{H} NMR (161 MHz, $CDCl_3$) δ ppm: 5.13 (s).

2.2.1.14. Synthesis of 1:3 [Silver(I) 4-(dimethylamino)phenyldiphenyl phosphine]Br

(**Complex 13**)

AgBr salt (0.1333 g; 0.71 mmol) was added to a solution of 4-(dimethylamino)phenyl diphenyl phosphine (0.650 g and 2.13 mmol) (**L4**) in acetonitrile (50 ml). The solution underwent a heat reflux process for 6 h, followed by filtration. The solvent was then subjected to a reduction process, resulting in a volume of approximately 10 ml, and allowed to crystallize at room temperature for 24 h. This led to the formation of small, white crystal needles, which were isolated from the solution.

Melting point: 209 - 211˚C.

Elemental Analysis: Calculated for $C_{60}H_{60}AgBrN_3P_3$: C, 65.29%; H, 5.48%; Ag, 9.77%; Br, 7.24%; N, 3.81%; P, 8.42%. Found: C, 65.94%; H, 5.63%; N, 3.35%.

IR (v/cm^{-1}):1596.59, 1543.18, 1511.06 (ν (aromatic, C=C aromatic, m), 1477.84, 1445.91, 1432.75 (ν (C=C aromatic), m), 1360.98, 1291.93, 1229.74, 1200.46 (ν, C-N, s), 1093.15, 1026.00, 998.57, 943.35 (ν (aromatic, C-H bend, meta), s), 804.66, 773.41, 742.27, 694.50, 619.56, 607.95 (ν (aromatic, C-H bend, ortho), m).

^{1}H-NMR (400 MHz, $CDCl_3$) δ ppm: 2.971 (s, methyl H), 6.625 (d, 4-(dimethylamino) H), 7.231 – 7.369 (m, aromatic H).

^{13}C{H}-NMR (100 MHz, $CDCl_3$) δ ppm: 40.14 (s, methyl C), 112.21 (s, 4-(dimethylamino)phenyl C), 128.46 (d, aromatic C), 129.08 (s, aromatic C), 133.52 (d, aromatic C), 135.23 (d, aromatic C), 135.79 (d, 4-(dimethylamino)phenyl C).
^{31}P{H} NMR (161 MHz, $CDCl_3$) δ ppm: 1.53 (s).

2.2.1.15. Complex and cisplatin preparation

One millimolar stock solutions of silver(I) phosphine complexes (**1 - 13**) and ligands (**L1 - L4)** were prepared by solubilizing the differential silver(I) phosphine complexes and uncoordinated ligand powders in cell culture graded dimethyl sulfoxide (DMSO). Complex solutions were heated for 1 h and 30 min in a dry bath pre-set to 70°C. In 0.9% (w/v) filtered saline (NaCl) solution, a stock solution of 3.33 mM CDDP was made up. This solution was subsequently heated for 24 h in a dry bath pre-set to 20°C. Every two weeks, new CDDP stock solutions were prepared. Prior to treatment, complex and ligand stocks were reheated for a period of 45 min in a dry bath pre-set at 70°C. Stock solutions were maintained at 4°C in the dark.

2.2.2. Cell culture

Prior to use, all reagents for culture, subculture, and plating were heated in a pre-set water bath of 37°C.

2.2.2.1. Cell lines

This study made use of the following malignant cell lines: adherent human A375 non-pigmented melanoma *(gifted by the University of Cape Town, RSA),* A549 lung adenocarcinoma *(Cellonex™, RSA),* HEP-G2 hepatocellular carcinoma *(Cellonex™, RSA),* HT-29 colorectal adenocarcinoma *(Cellonex™, RSA),* MCF-7 breast adenocarcinoma *(Cellonex™, RSA),* MDA-MB-231 breast adenocarcinoma *(gifted by the University of KwaZulu-Natal, RSA)* and SNO oesophageal squamous cell carcinoma *(gifted by the University of Witwatersrand, RSA).* The non-malignant cell lines used were adherent human MRHF foreskin fibroblast cells *(Cellonex™, RSA)* and transformed HEK-293 embryonic kidney cells *(gifted by the University of KwaZulu-Natal, RSA).* The cell lines acquired were accompanied by a certificate verifying their absence of mycoplasma contamination. **Table 2.1** contains detailed characteristics of each cell line.

2.2.2.2. Culturing cells from stock

Respective supplemented Dulbecco's modified Eagles media (13.53 g/L DMEM) with additionally sodium bicarbonate (3.7 g/L $NaHCO_3$), McCoy's 5A media, or Roswell Park Memorial Institute media (10. 65 g/L RPMI 1640) with additional $NaHCO_3$ (2 g/L) and HEPES buffer solution (25 ml/L) were prepared (**Table 2.1** lists the culture media used for the respective cell lines). Fetal calf serum (FCS) was added as a supplement to all culture media, at a concentration of 5% (v/v). A 75 cm^2 tissue culture treated flask was filled with 20 ml of the respective supplemented media. Cell stocks were kept in cryogenic 2 ml vials and frozen at -80°C for preservation. As soon as the cells had thawed in the water bath, they were aspirated and added to the media in the flask. At 37°C, cells were incubated in a sterile, humidified, 5% CO_2 atmosphere. A Nüve EC 160 incubator was utilized. The media was removed the next day and replaced with fresh supplemented media. Cells were cultured until they attained confluency, extending up to a passage of 3 before seeded for experimentation.

Table 2.1. Detailed descriptions of the seven malignant and two non-malignant cell lines used during this study.

Description	Malignant cell lines							Non-malignant cell lines	
	A375	A549	HEP-G2	HT-29	MCF-7	MDA-MB-231	SNO	HEK-293	MRHF
Species	Human *(Homo sapiens)*								
Example of a genotype alternation and consequence thereof	Loss of *Apaf*-1 expression: impairment in p53-dependent apoptosis & unfailingly chemo resistant (Soengas *et al.,* 2001)	Overexpression of *EZH2*: oncogene, enhanced metastasis, tumour growth & poor clinical outcome (Xu *et al.,* 2013)	Inactivation or mutations of p53 gene: increase in cellular proliferation & dysfunctional DNA checkpoints (Farazi & DePinho, 2006)	Inactivation or deletion of p53 gene: dysfunction in cell arrest and apoptotic pathway (Arizti *et al.,* 2020) Resistant to CDDP (Zaki *et al.,* 2016)	Overexpression of Bcl-2 proto-oncogene: chemo resistant (Akar *et al.,* 2008) Metastatic hormone dependent cells have estrogen & progesterone receptors, & are HER2 positive	Upregulation of miR-10b: enhanced invasion and proliferation (Shi *et al.,* 2017) Metastatic and triple negative: no estrogen or progesterone receptors & is HER2 negative	Loss of *GPX7* expression: enhanced drug resistance, promotes tumour growth by activation of oncogenic NF-kB-dependent signalling pathway (Peng *et al.,* 2014)	High mRNA levels of E1A and E1B: an impediment to cell cycle and transcriptional control pathways for continuous growth. Immortalization by transfection of sheared viral DNA of adenovirus 5 (Malm *et al.,* 2020)	None relating to malignancy
Gender	Female	Male	Male	Female	Female	Female	Male	Unknown	Male
Morphology	Epithelial spindle shaped	Squamous-epithelial	Epithelial	Epithelial-like cuboidal shaped	Epithelial-like	Epithelial-like spindle shaped	Squamous epithelial	Epithelial	Fibroblast
Tissue type	Skin	Lung	Liver	Colon	Breast mammary gland	Breast mammary gland	Oesophagus	Embryonic kidney	Skin (dermis layer)
Disease	Malignant melanoma	Lung carcinoma	Hepatocellular carcinoma	Colorectal adeno-carcinoma	Breast adeno-carcinoma	Breast adeno-carcinoma	Oesophageal carcinoma	None (Transformed)	None
Company and/or reference code	ATCC® CRL-1619™ (thawed)	Cellonex™ CA54-FL (flask)	Cellonex™ HEP-G2_FL (flask)	Cellonex™ CHT-FL (flask)	Cellonex™ CMC-FL (flask)	ATCC® HTB-26™ (thawed)	Highveld Biological Ltd. (Pty), (thawed)	ATCC® CRL-1573™ (thawed)	Cellonex™ CFIB-FL (flask)
Culture media	DMEM	DMEM	RPMI 1640	McCoy's 5A	DMEM	DMEM	DMEM	DMEM	DMEM

2.2.2.3. Sub-culturing of cells

Seven adherent malignant human cell lines and two adherent non-malignant human cell lines were selected to investigate the *in vitro* cytotoxic effectiveness of complexes **1 - 13**. Utilizing supplemented DMEM / McCoy's 5A / RPMI media, cells were cultured from stock. An additional 0.6% (v/v) Penicillin/Streptomycin/Amphotericin B was added to DMEM / McCoy's 5A / RPMI media. A 75 cm^2 tissue culture treated flask was used to grow cells for ±48 h (all malignant cell lines, and the non-malignant HEK-293 cell line) and ±72 h (non-malignant MRHF cell line). At 37°C, cells were incubated in a sterile, humidified, 5% CO_2 atmosphere. Ten millilitres of Hanks Balanced Salt Solution (HBSS 10X: 100 ml/L) with supplementary sodium bicarbonate (0.35g/L $NaHCO_3$) was used to wash confluent cultures. Malignant cell lines were detached with the enzymatic lifting of 6 ml 1% trypsin/ versene solution for ±5 - 10 min (time dependent on the cell line), while the non-malignant MRHF cell line was lifted by gentle agitation. To deactivate the trypsin, 10 ml of the respective supplemented media (**Table 2.1**) was added. Cells were accumulated by centrifugation with a Nüve NF 400R benchtop centrifuge at 797 x*g* for 4 min (non-malignant HEK-293 and malignant cell lines) and 165 x*g* for 5 min (non-malignant MRHF cell line). To resuspend the different cell lines, 1 ml of the respective supplemented media was added to the corresponding pellet (**Table 2.1**). This was expanded into two or three 75 cm^2 culture flasks with ±25 ml supplemented DMEM/McCoy's 5A/RPMI media. Cells were either seeded for experimentation between culture passages 2 and 5 or stored as cell stocks. When preparing cell stocks, the pellet was resuspended in 90% (v/v) FCS with 10% (v/v) DMSO. The suspension was transferred into cryogenic 2 ml vials and maintained at -80˚C.

2.2.2.4. Cellular counting

The removal and collection of the respective cells from culture flasks were performed as described in point *2.2.2.3*. The cells were resuspended by adding 3 ml of respective supplemented media. A 10 µl aliquot of this cell suspension was combined with 10 µl of Trypan blue dye (1:1) and gently aspirated. This suspension was pipetted onto a cell counting slide in a volume of 10 µl. The slide was placed into the Countess™ automated cell counter, where the cellular viability percentage and total number of live and dead cells/ml were measured.

2.2.3. Cytotoxicity screening studies

2.2.3.1. Plating of cells

The cells from each cell line were removed from the culture flasks separately, pooled into their respective groups, and counted as detailed in points *2.2.2.3* and *2.2.2.4.* For all nine cell lines, an optimal concentration of 2 x 10^5 cells/ml was calculated using the Countess™ automated cell counter. In each well of a tissue culture-treated 96-well plate, 100 µl (2 x 10^4 cells) were added. Before treatment, malignant and non-malignant cells were seeded in triplicate and left to proliferate for either 24 h or 48 h.

2.2.3.2. Cell treatments

The various cell lines were differentially treated as follows: either not treated and left as an untreated negative control (UC) or treated with 1% (v/v) DMSO (VC, vehicle control), 100 µM of CDDP (positive apoptotic control), or treated with 10 µM of silver(I) phosphine complexes **1 - 13** and 10 µM of their respective ligands, **L1 - L4**. Previous studies have shown that a greater CDDP concentration is needed to initiate the same apoptotic cell death response in malignant cells (10 µM versus 100 µM)(Engelbrecht and Cronjé, 2018; Engelbrecht *et al.*, 2018; Human-Engelbrecht *et al.*, 2017; Human *et al.*, 2015; Potgieter *et al.*, 2016). The cells were left to incubate for an additional 24 h and 48 h.

2.2.3.3. alamarBlue® proliferation assay

To identify which silver(I) phosphine complexes were selected for further investigation, their ability to initiate a cell death response was studied. An alamarBlue® proliferation assay was used. This assay measures changes in mitochondrial activity. To the 100 µl of the differentially treated cells (point *2.2.3.2*), 10 µl of alamarBlue® dye was added. Prior to fluorescence analyses, cells were left to incubate for 2 h in the dark, at 37°C. Each treatment was replicated three times per plate, and each experiment was performed at least three times. The cellular viabilities for each treatment were expressed in relation to the DMSO-treated cells. The cells were analyzed using a VICTOR® Nivo™ multimode plate reader. The wavelengths 530/30 nm for excitation and 580/20 nm for emission were selected. To standardize background fluorescence, 100 µl of cell-free culture medium was included as a negative control.

2.2.3.4. Cellular morphology of non-malignant cell lines

Changes to cellular morphology following differential treatments (point *2.2.3.2*) on transformed HEK-293 cells and non-malignant MRHF cells were observed with a Zeiss Axiovert 25 inverted light microscope. The Zeiss AxioCam MRC camera and Axiovision 3.1 imaging software were used to capture micrographs at a 200 x magnification.

2.2.3.5. Dose responsive studies on malignant cell lines

Only complexes that decreased cellular viability in malignant cell lines after 48 h while remaining non-toxic towards the HEK-293 and MRHF cell lines were selected for further investigation. The following treatments were applied to the malignant cell lines: control-treated cells where cells were not treated (UC) or they were treated with 1% DMSO (VC) or treated with the selected complexes. These complexes were administered at a starting concentration of 20 µM per well with subsequent serial dilutions of 10 µM, 5 µM, 2.5 µM and 1.25 µM. In addition, a starting concentration of 200 µM per well of CDDP was used to treat the cells, following subsequent serial dilutions of 100 µM, 50 µM, 25 µM and 12.5 µM. Cells were then left for 24 h before fluorescence analysis using the alamarBlue® proliferation assay, detailed in point *2.2.3.3*. Sigmoidal curves were constructed, and an IC_{50} value was calculated using a polynomial order of three equations. Data was represented as bar graphs for the respective malignant

cell lines, indicating each selected complex and CDDP, respectively.

2.2.4. Statistical analysis

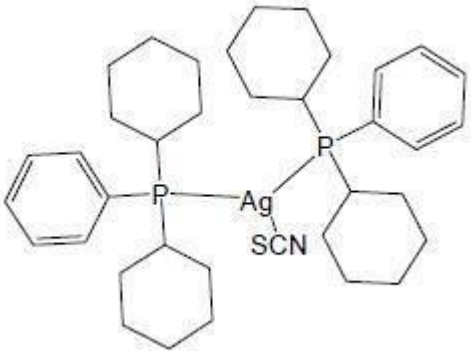
A representation of $n = 6$ was achieved using data consisting of three separate biological repeats and two independent technical repeats. To determine statistically significant variations, the Standard Error of the Mean (SEM) and a two-tailed heteroscedastic Student's t-test were used. Screening data and dose-response data were represented as bar graphs, while the error bars represented the SEM for each differential treatment. The probability values (P value) of * $P < 0.05$, ** $P < 0.01$ and *** $P < 0.001$ were statistically significant in relation with DMSO-treated cells. Statistical analyzes were performed in Microsoft Office Excel 2013.

Results

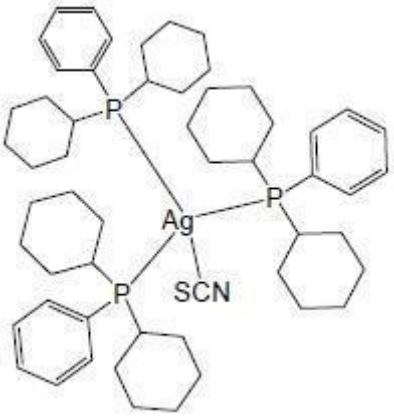
2.3.1. Silver(I) phosphine complexes' structural details

Thirteen novel silver(I) phosphine complexes were synthesized and characterized by the Department of Chemical Sciences at the University of Johannesburg (South Africa) (point *2.2.1*). Different silver salts and different phosphine ligands were used to synthesize complexes **1 - 13**. The silver salts used were silver bromide (AgBr), silver chloride (AgCl), silver thiocyanate (AgSCN) and silver nitrate ($AgNO_3$). The phosphine ligands used were dicyclohexyl-phenylphosphine (**L1**), diphenyl-2-pyridylphosphine (**L2**), benzyl-diphenyl phosphine (**L3**) and 4-(dimethylamino)-phenyldiphenyl-phosphine (**L4**) (**Figure 2.1**).

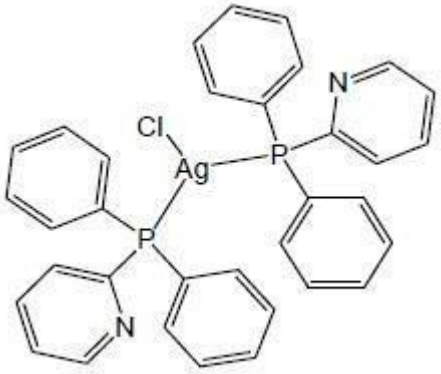
Complexes **1 - 13** consist of one silver salt core surrounded by either one, two, or three phosphine ligands. Both complexes **1** and **2** were synthesized using the same AgSCN salt and dicyclohexyl-phenylphosphine ligand, but their ligand ratios were 1:2 and 1:3, respectively. Complexes **3** and **4** were synthesized from the same diphenyl-2-pyridylphosphine ligand. Complex **3** presented a AgCl salt core and complex **4** presented a AgBr salt core. Complexes **3** and **4** orientate as a tetrahedral geometry with three phosphine ligands surrounding the silver salt core (1:3 ratio). Complexes **5** and **6** were synthesized with AgSCN salt and complex **7** with $AgNO_3$ salt and the benzyldiphenylphosphine ligand. Complex **5** orientates as a 1:1 silver(I) halide to ligand stoichiometry, while complex **6** orientates as a 1:2 stoichiometry and complex **7** orientates as tetrahedral geometry. The last set of complexes, **8 - 13** were all synthesized with the 4-(dimethylamino)-phenyldiphenyl- phosphine ligand with varying silver salts. Complexes **8 - 10** presented a $AgNO_3$ salt core orientating as a 1:1, 1:2 and 1:3; silver (I) nitrate : ligand ratio, respectively. Complex **12** was synthesized with AgBr salt and orientated as a 1:2 stoichiometry. Complex **13** presented tetrahedral geometry with the salt core, AgBr. Due to their limited solubility in hydrophobic solutions, all complexes studied were lipophilic in nature (Meijboom *et al.,* 2009). Analogues of lipophilic cationic complexes have been discussed in literature: for example, 1:2 adducts of Au(I) with 1,2-bis(din-pyridylphosphino)ethane (McKeage *et al.,* 2000) and silver(I) complexes with tris(*p*-tolyl) phosphine (Kyros *et al.,* 2010) were successful in inducing an anticancer effect on *in vitro* sarcoma malignant cells.



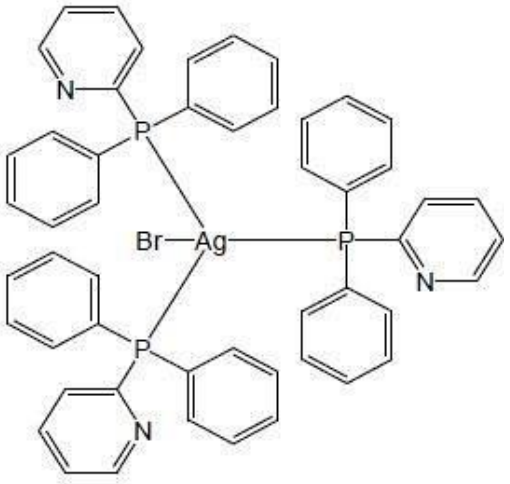
Complex 1
[Silver(I)dicyclohexylphenylphosphine]SCN



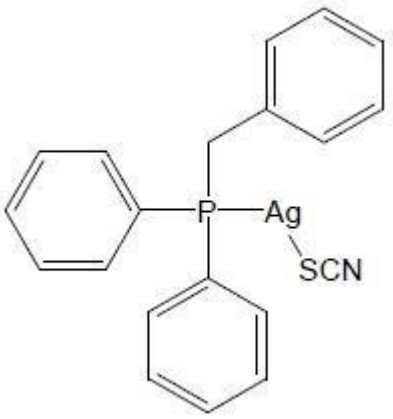
Complex 2
[Silver(I)dicyclohexylphenylphosphine]SCN



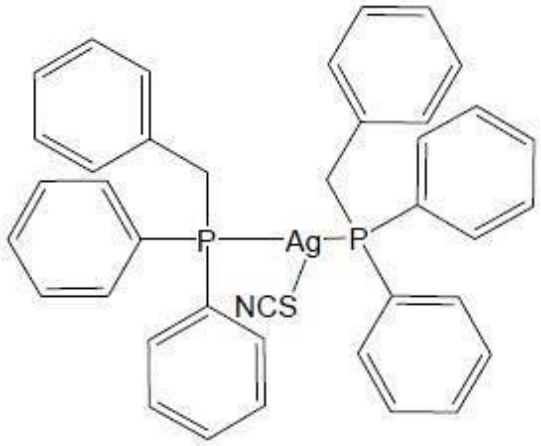
Complex 3
[Silver(I) diphenyl-2-pyridylphoshine]Cl



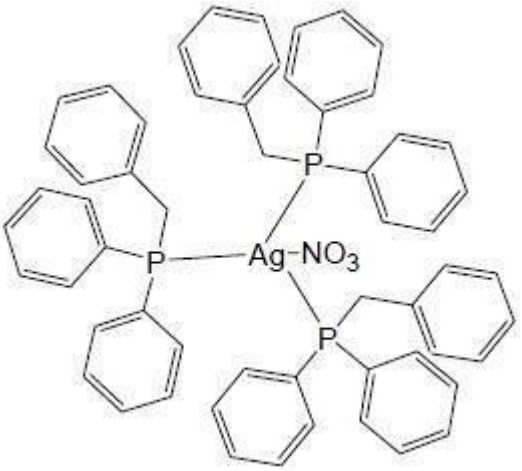
Complex 4
[Silver(I) diphenyl-2-pyridylphosphine]Br



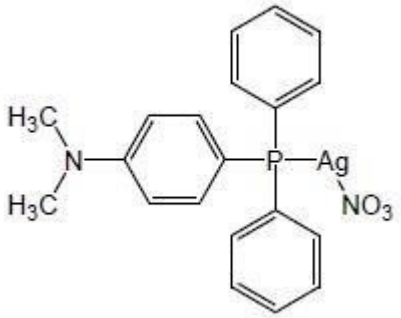
Complex 5
[Silver(I) benzylphenylphosphine]SCN



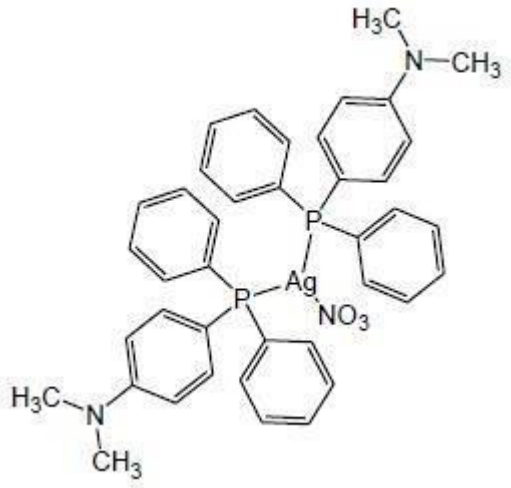
Complex 6
[Silver(I) benzyldiphenylphosphine]SCN



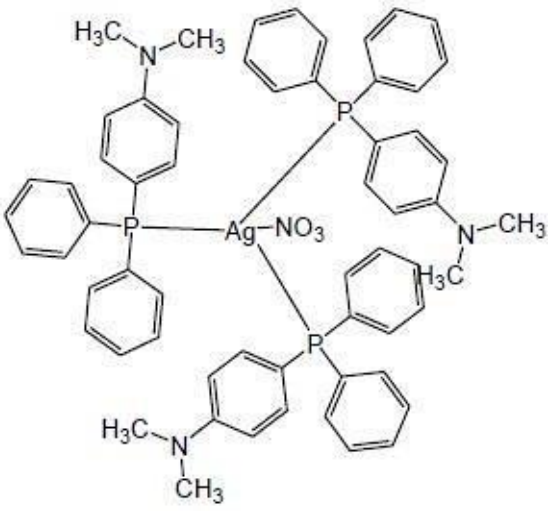
Complex 7
[Silver(I) benzyldiphenylphosphine]NO_3



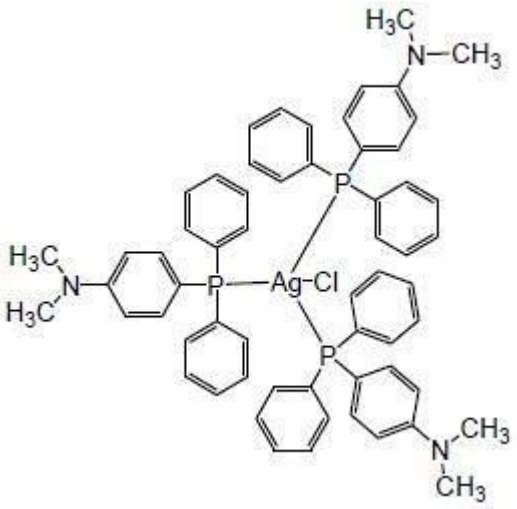
Complex 8
[Silver(I) 4-(dimethylamino)phenyldiphenyl phosphine]NO_3



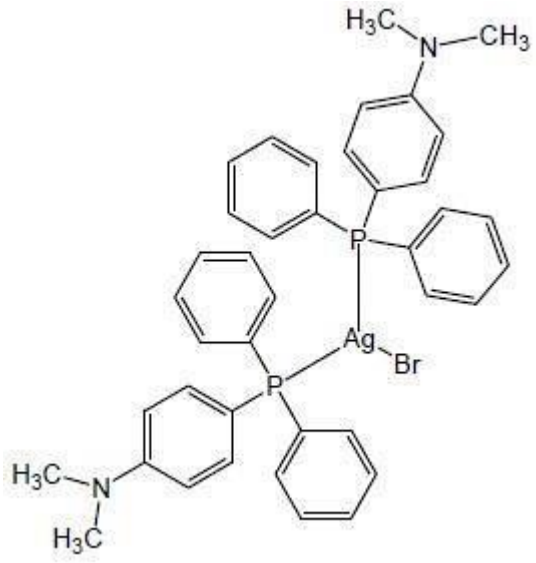
Complex 9
[Silver(I) 4-(dimethylamino)phenyldiphenyl phosphine]NO_3



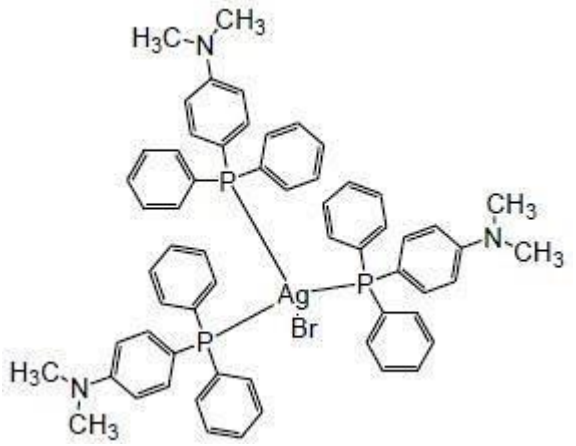
Complex 10
[Silver(I) 4-(dimethylamino)phenyldiphenyl phosphine]NO_3



Complex 11
[Silver(I) 4-(dimethylamino)phenyldiphenyl phosphine]Cl



Complex 12
[Silver(I) 4-(dimethylamino)phenyldiphenyl phosphine]Br



Complex 13
[Silver(I) 4-(dimethylamino)phenyldiphenyl phosphine]Br

Figure 2.1. The schematic chemical structures of silver(I) phosphine complexes **1 - 13**.

2.3.2. Silver(I) phosphine complexes were investigated for their cytotoxicity in non-malignant cells

All screening data is represented as bar graphs. The cytotoxicity of the ligands with their respective complexes is grouped accordingly on the *x-axis* (**L1** = complexes **1** and **2**; **L2** = complexes **3** and **4**; **L3** = complexes **5 - 7**, and **L4** = complexes **8 - 13**). The percentage of cellular viability is represented on the *y-axis*. All screening data represented in this chapter as well as the dose-response studies were expressed in relation to the vehicle control, DMSO (**Figures 2.2** to **2.17**).

To correctly identify a drug with anticancer activity, it is important that the complex under investigation shows minimal to no toxicity towards non-malignant healthy cells. This ensures that the drug remains selective and will target only cancerous cells. Cellular screening of silver(I) phosphine complexes **1** - **13** on transformed HEK-293 embryonic kidney cells and non-malignant MRHF foreskin fibroblast cells were determined using the alamarBlue® proliferation assay and light microscopy. The cellular membrane is permeable to the non-toxic dye alamarBlue®. Resazurin is converted into resorufin through an oxidation-reduction process that occurs in a metabolically active cell. Resorufin production is directly correlated with cell viability and metabolic activity. AlamarBlue® is used to quantify the continuous proliferation of cells over time (Sakaguchi and Powers, 2012). Light microscopy shows if selected complexes cause typical apoptotic morphological changes in the cells.

Overall, DMSO was not cytotoxic towards the HEK-293 and MRHF cells, with cellular viabilities similar to those obtained 24 h and 48 h after treatment for the untreated control cells. **Figure 2.2** represents the screening data on the HEK-293 cells, cellular viability after 24 h and 48 h of ligands (**L1** - **L4**) and complexes (**1** - **13**) remained above 80% and 85% respectively. Complex **13** was the least toxic, with a viability of over 100% after 48 h (113.49%). Followed by complexes **12** (109.95%), **7** (107.14%), **10** (106.59%) and **2** (106.39%). Cytotoxicity on the MRHF cells (**Figure 2.3**) showed that the ligands (**L1** - **L4**) and complexes **1** - **9** and **13** viability remained above 80% after 24 h and 48 h. Complexes **10**- **12** significantly decreased ($P < 0.001$) the viability of the MRHF cells after 24 h when compared to the DMSO vehicle control (72.73%, 60.86%, and 74.25%, respectively). However, these cells recovered after an additional 24 h of treatment, with viabilities of 107.35%, 113.78%, and 87.56%, respectively; indicating a high sustained proliferative signal in these cells. Even though these complexes decreased cellular viability of the MRHF cells; in comparison to the malignant cell lines, their cytotoxic ability was limited. Complex **11** was only selective against the SNO cells (**Figure 2.9**), while complex **12** was only selective against the MCF-7 cells (**Figure 2.11**), where their cytotoxic effect on these malignancies was substantially larger than in the MRHF cells. After 48 h, complex **5** was the least cytotoxic on the MRHF cells, and again viability was above 100% (115.18%). Followed by complexes **7** (114.68%), **11** (113.78%) and **3** (108.42%). CDDP caused a significant decrease ($P < 0.05$) in the HEK-293 cells after 24 h and 48 h, resulting in viability below 80%. In the MRHF cells, cellular viability significantly decreased ($P < 0.001$) after 48 h (73.05%), with CDDP appearing slightly more cytotoxic towards the MRHF cells when compared to the HEK-293 cells.

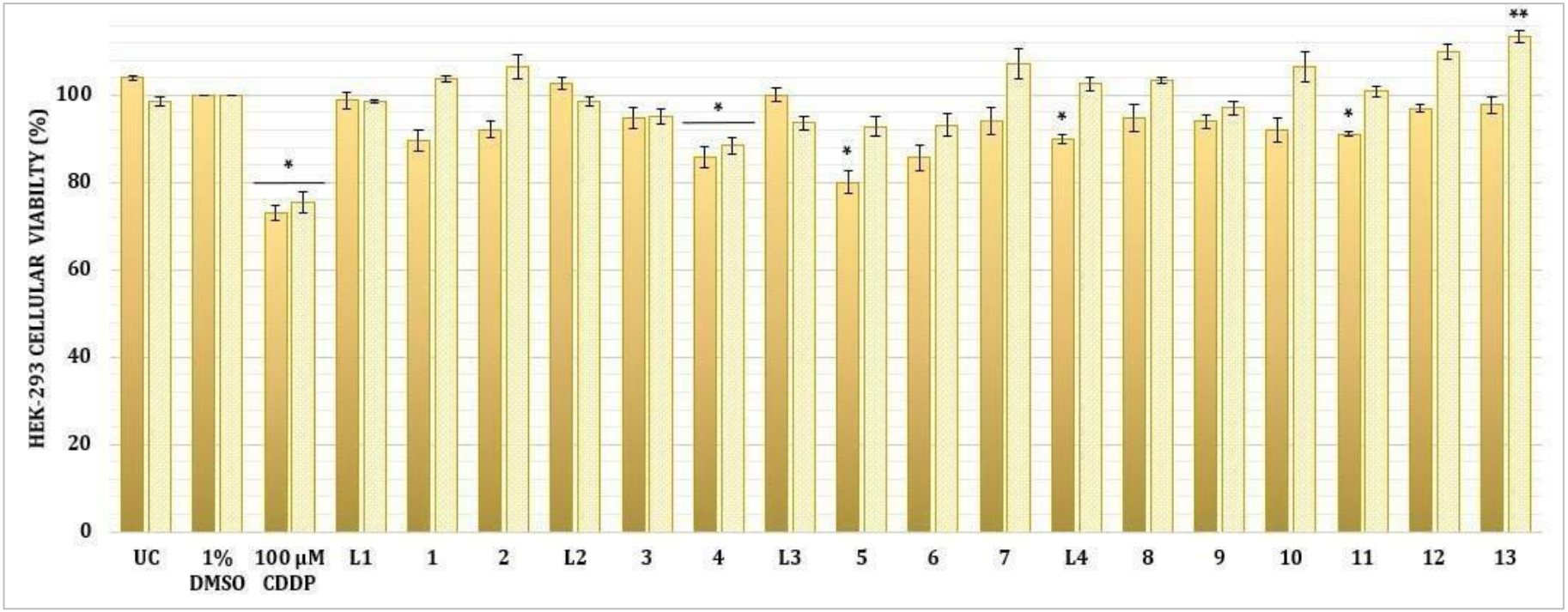


Figure 2.2. The percentage of cellular viability of transformed **HEK-293** cells determined using the alamarBlue® proliferation assay. The following treatments were added to the cells: no treatment (untreated control) or treated with 1% DMSO (vehicle control), 100 µM CDDP (positive apoptotic control), 10 µM of silver(I) phosphine complexes (**1** - **13**) and 10 µM of respective ligands (**L1** - **L4**) for 24 h and 48 h (gradient filled bars represent 24 h and patterned filled bars represent 48 h). Percentages were expressed in relation to 1% DMSO (100 %). The ± SEM (n = 6) were represented as error bars and P values were calculated using a two-tailed Student's t-test. Significant differences are denoted by asterisks (* $P < 0.05$; ** $P < 0.01$ and *** $P < 0.001$).

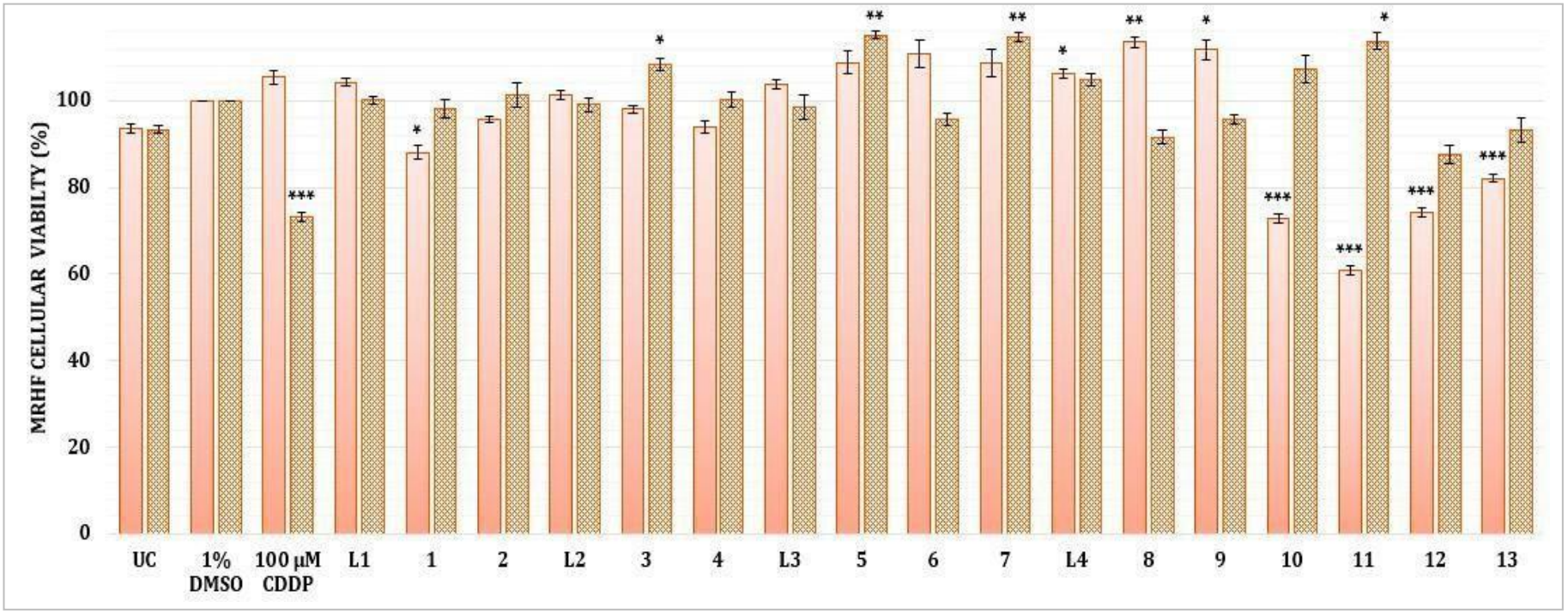


Figure 2.3. The percentage of cellular viability of non-malignant **MRHF** cells determined using the alamarBlue® proliferation assay. The following treatments were added to the cells: no treatment (untreated control) or treated with 1% DMSO (vehicle control), 100 µM CDDP (positive apoptotic control), 10 µM of silver(I) phosphine complexes (**1** - **13**) and 10 µM of respective ligands (**L1** - **L4**) for 24 h and 48 h (gradient filled bars represent 24 h after treatment and patterned filled bars represent 48 h after treatment). Percentages were expressed in relation to 1% DMSO (100 %). The ± SEM (n = 6) were represented as error bars and P values were calculated using a two-tailed Student's t-test. Significant differences are denoted by asterisks (* $P < 0.05$; ** $P < 0.01$ and *** $P < 0.001$).

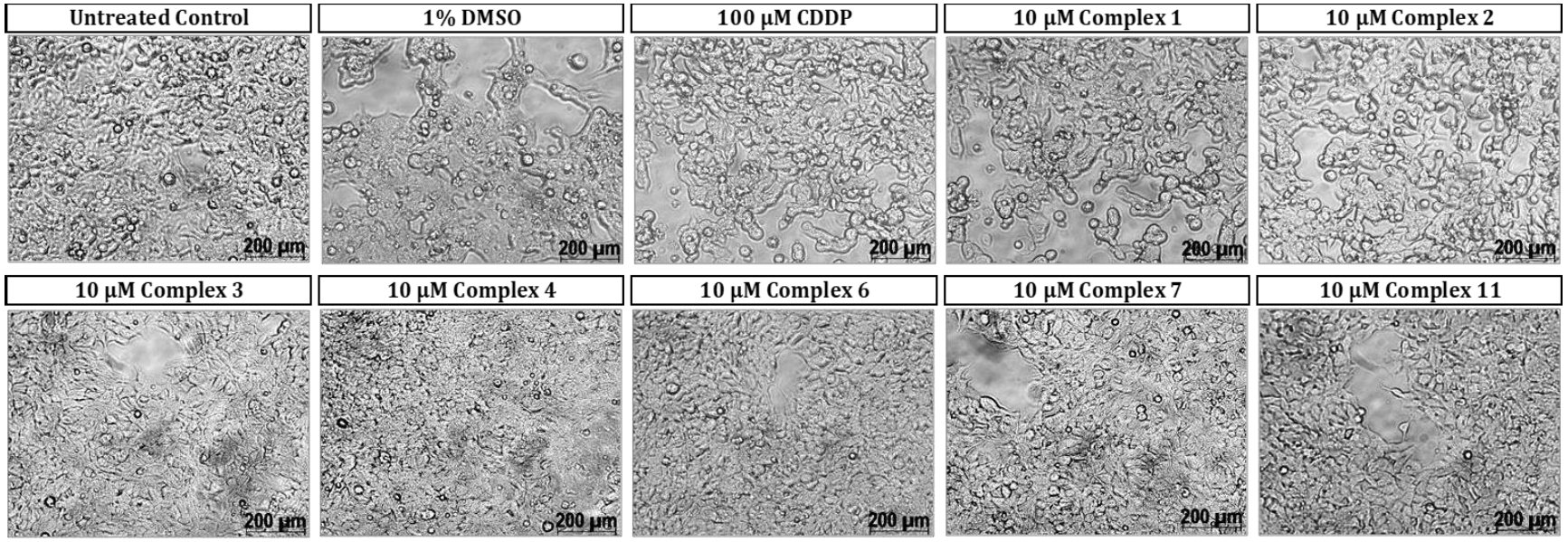


Figure 2.4. Morphological changes of transformed **HEK-293** cells induced by differential treatments after 24 h. The following treatments were added to the cells: no treatment or treated with 1% DMSO, 100 µM CDDP and 10 µM silver(I) phosphine complexes **1** - **4**, **6**, **7** and **11**. Untreated control cells show typical, healthy HEK-293 cells, respectively. After 24 h, cells treated with CDDP, and the respective silver(I) phosphine complexes did not induce any typical apoptotic or necrotic features. The cells remained heathy. Light micrographs were captured with a Zeiss Axiovert 25 inverted light microscope and Axio Vision 3.1 software at 200 x magnification.

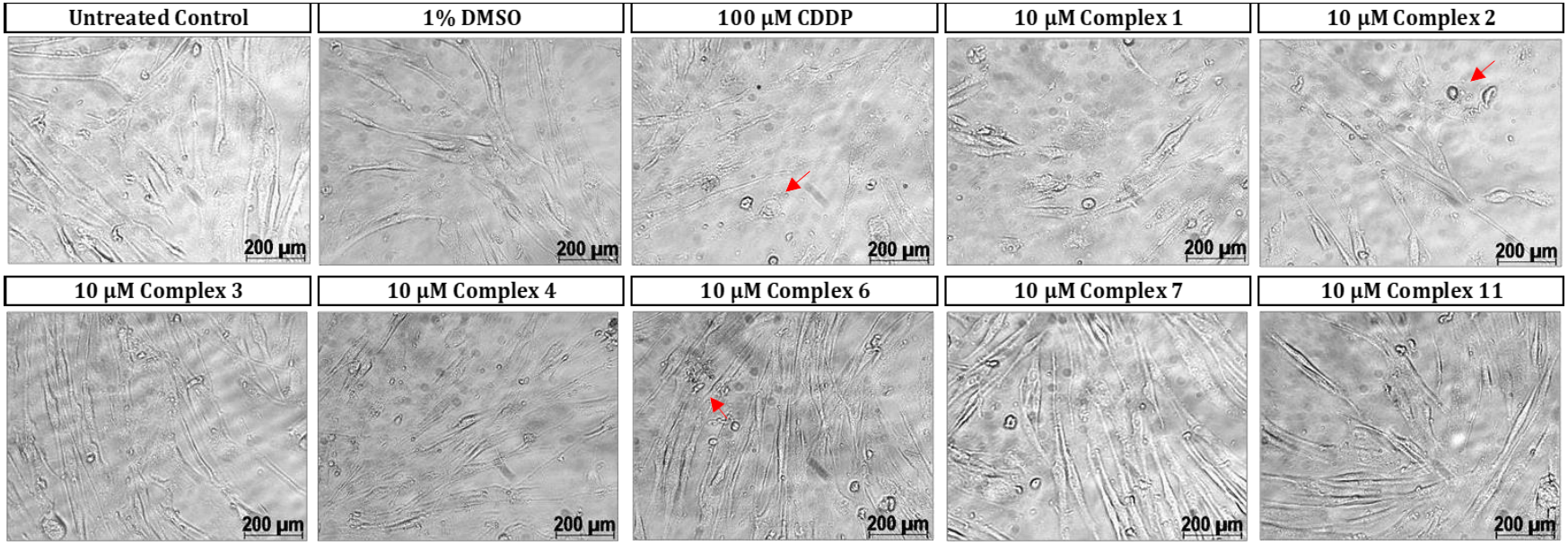


Figure 2.5. Morphological changes of non-malignant **MRHF** cells induced by differential treatments after 24 h. The following treatments were added to the cells: no treatment or treated with 1% DMSO, 100 µM CDDP and 10 µM silver(I) phosphine complexes **1** - **4**, **6**, **7** and **11**. Untreated control cells show typical, healthy elongated MRHF cells, respectively. After 24 h, cells treated with respective silver(I) phosphine complexes **1**, **3**, **4**, **7** and **11** did not induce any typical apoptotic or necrotic features. The cells remained heathy. Only CDDP, complexes **2** and **6** showed minimal indications of cellular stress, indicated by the red arrows. Light micrographs were captured with a Zeiss Axiovert 25 inverted light microscope and Axio Vision 3.1 software at 200 x magnification.

Morphological changes were analyzed in the HEK-293 and MRHF cells. Non-malignant cells were treated as follows: with the vehicle control (1% DMSO), 100 µM CDDP or 10 µM of complexes **1**, **2**, **3**, **4**, **6**, **7** and **11**. These complexes were selected as their cytotoxic effect was significantly greater for certain malignant cell lines after 48 h and not only after 24 h (described further in section *2.3.3*).

The morphology of the HEK-293 cells (**Figure 2.4**) and the MRHF cells (**Figure 2.5**) treated with the DMSO resembled their respective untreated control cells. In comparison to the elongated MRHF cells, the HEK-293 cells are more spherical. For all treatments, no significant morphological changes were observed. The HEK-293 cells remained confluent and appeared viable; there was no sign of cell death. When compared to untreated control cells, the MRHF cells treated with complexes **2**, **6** and CDDP showed minimal signs of cellular stress such as rounding (indicated by red arrows), although the entire population still was healthy.

2.3.3. Identifying successful silver(I) phosphine complexes in malignant cell lines

The seven malignant cell lines screened were A375 non-pigmented melanoma, A549 lung adenocarcinoma, HEP-G2 hepatocellular carcinoma, HT-29 colorectal adenocarcinoma, MCF-7 breast adenocarcinoma, MDA-MB-231 breast adenocarcinoma, and SNO oesophageal squamous cell carcinoma. Malignant cells were treated as follows: 10 µM of silver(I) phosphine complexes (**1 - 13**), 10 µM of the respective ligands (**L1 - L4**), 100 µM CDDP and 1% DMSO. Cellular viability was analyzed after 24 h and 48 h of treatment. It should be highlighted that complexes were chosen based on how effectively they corresponded with CDDP for each malignant cell line that was investigated.

In the A375 cells (**Figure 2.6**), complexes **5** and **8 - 13** resulted in no significant decline in cellular viability after 48 h as the viability had increased above 100%, apart from complex **13** (82.19%). Complexes **1 - 4**, **6** and **7** caused a significant decrease in cellular viability at 24 h and further at 48h ($P < 0.001$) after treatment. These complexes were successful in initiating cell death in malignant A375 cells. Cellular viabilities similar or lower in percentage were of interest only, keeping in mind that the CDDP treatment concentration of 100 µM is ten times that of the silver(I) phosphine complexes. With a cellular viability as low as 2.93% after 48 h, complex **2** appeared to be the most cytotoxic in the A375 cells. This was followed by complexes **1** (5.26%), **3** (8.26%), and **4** (24.53%). The least cytotoxic complexes were **8**, **12**, **11**, **10**, **9** and **5** with viability well above 100%. From the A549 data represented in **Figure 2.7** complexes **5** and **8 - 13** caused no significant decrease in cellular viability after 48h as the viability had increased as the treatment time had progressed. Complexes **1**, **2**, **3**, **4**, **6** and **7** resulted in a significant decrease ($P < 0.001$) in cellular viability after 24 h and 48 h. The most cytotoxic complex was **2**, with a low viability in the A549 cells of only 1.96%. This was followed by complex **1** (6.54%), **7** (9.11%), **6** (21.40%), **4** (23.26%) and **3** (47.73%). These complexes were deemed successful in initiating a cell death response in malignant A549 cells.

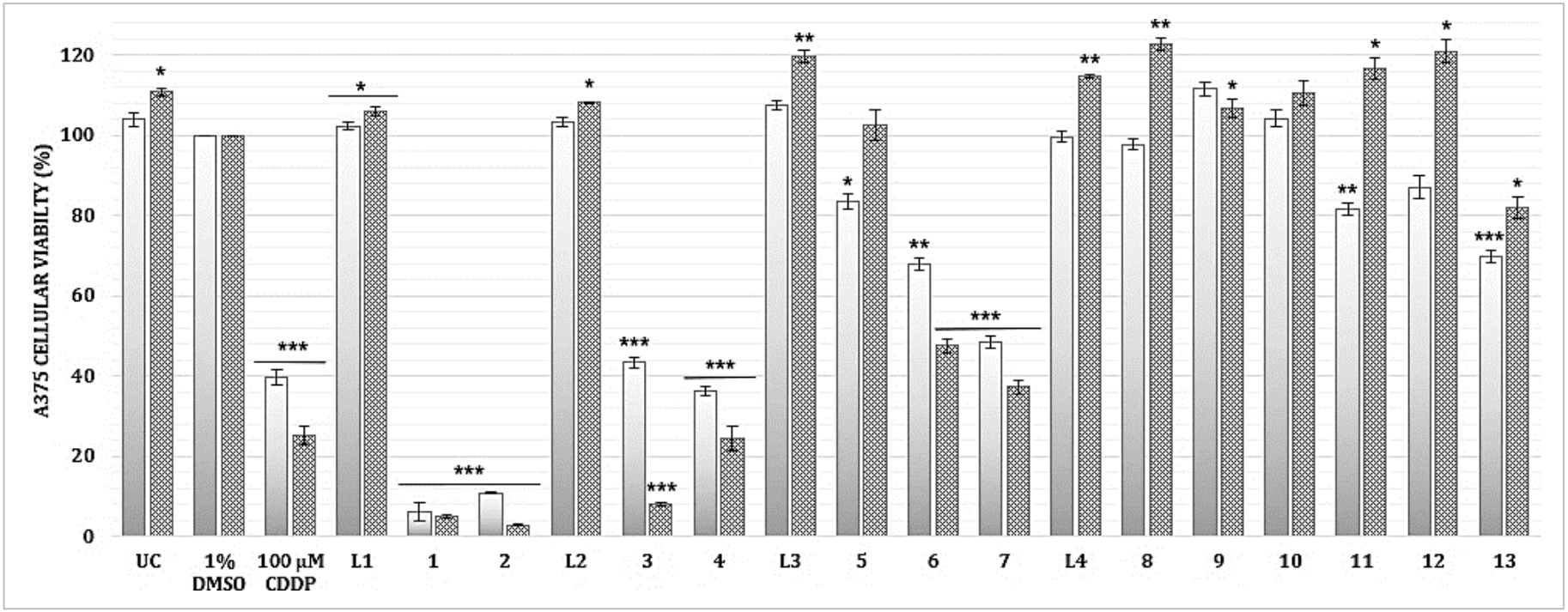


Figure 2.6. The percentage cellular viability of malignant **A375** cells determined using the alamarBlue® proliferation assay. The following treatments were added to the cells: no treatment (untreated control) or treated with 1% DMSO (vehicle control), 100 µM CDDP (positive apoptotic control), 10 µM of silver(I) phosphine complexes (**1** - **13**) and 10 µM of respective ligands (**L1** - **L4**) for 24 h and 48 h (gradient filled bars represent 24 h after treatment and patterned filled bars represent 48 h after treatment). Percentages were expressed in relation to 1% DMSO (100 %). The ± SEM (n = 6) were represented as error bars and P values were calculated using a two-tailed Student's t-test. Significant differences are denoted by asterisks (* $P < 0.05$; ** $P < 0.01$ and *** $P < 0.001$).

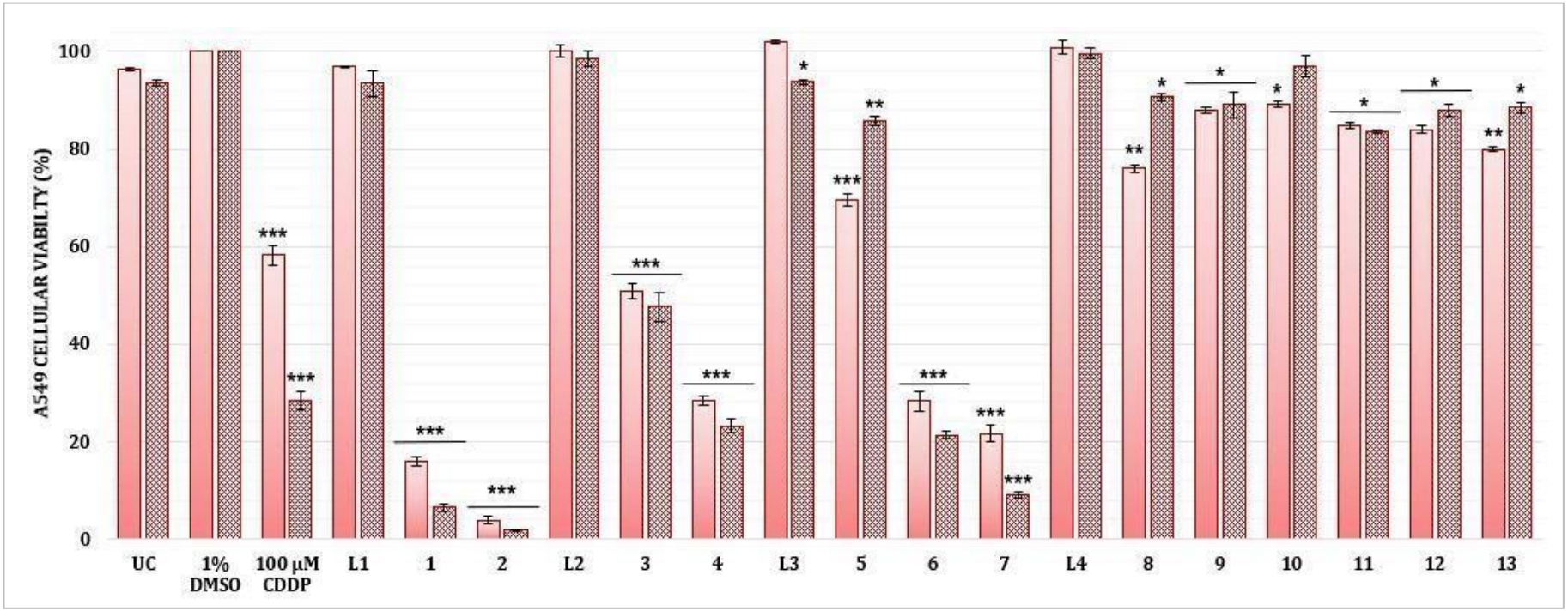


Figure 2.7. The percentage cellular viability of malignant **A549** cells determined using the alamarBlue® proliferation assay. The following treatments were added to the cells: no treatment (untreated control) or treated with 1% DMSO (vehicle control), 100 µM CDDP (positive apoptotic control), 10 µM of silver(I) phosphine complexes (**1** - **13**) and 10 µM of respective ligands (**L1** - **L4**) for 24 h and 48 h (gradient filled bars represent 24 h after treatment and patterned filled bars represent 48 h after treatment). Percentages were expressed in relation to 1% DMSO (100 %). The ± SEM (n = 6) were represented as error bars and P values were calculated using a two-tailed Student's t-test. Significant differences are denoted by asterisks (* $P < 0.05$; ** $P < 0.01$ and *** $P < 0.001$).

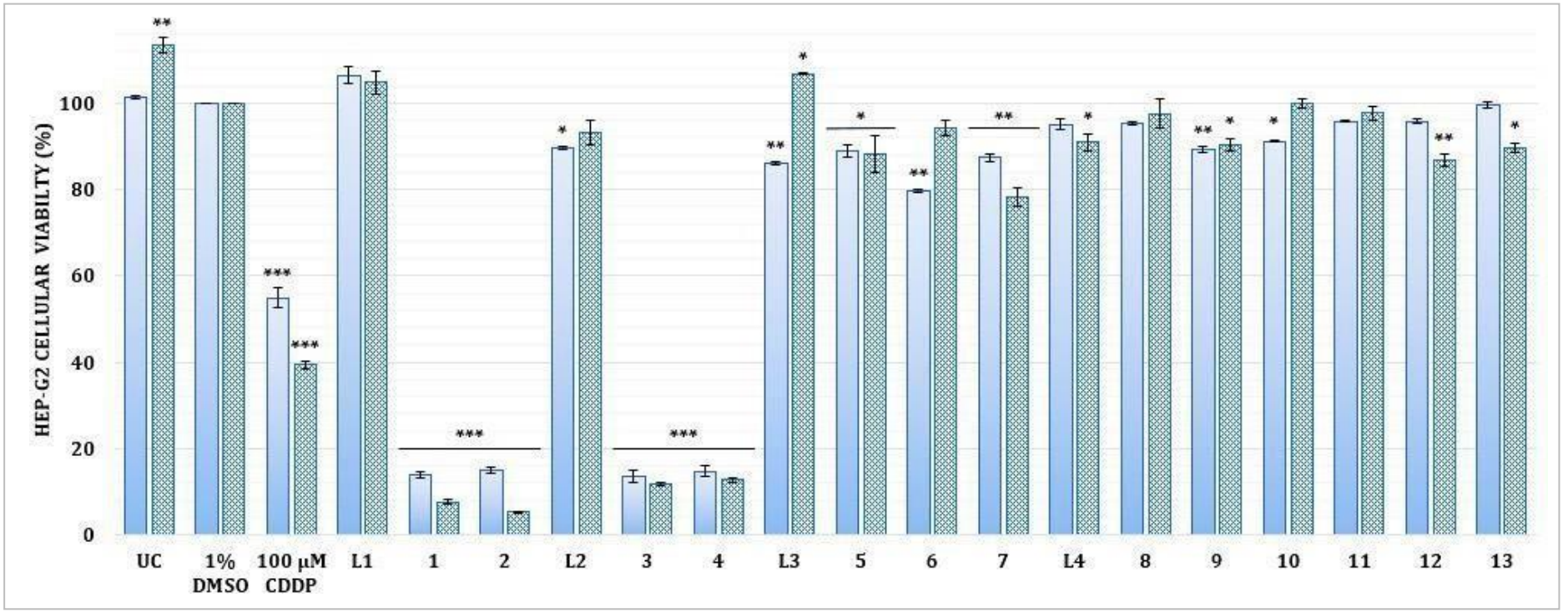


Figure 2.8. The percentage cellular viability of malignant **HEP-G2** cells determined using the alamarBlue® proliferation assay. The following treatments were added to the cells: no treatment (untreated control) or treated with 1% DMSO (vehicle control), 100 µM CDDP (positive apoptotic control), 10 µM of silver(I) phosphine complexes (**1** - **13**) and 10 µM of respective ligands (**L1** - **L4**) for 24 h and 48 h (gradient filled bars represent 24 h after treatment and patterned filled bars represent 48 h after treatment). Percentages were expressed in relation to 1% DMSO (100 %). The ± SEM (n = 6) were represented as error bars and P values were calculated using a two-tailed Student's t-test. Significant differences are denoted by asterisks (* $P < 0.05$; ** $P < 0.01$ and *** $P < 0.001$).

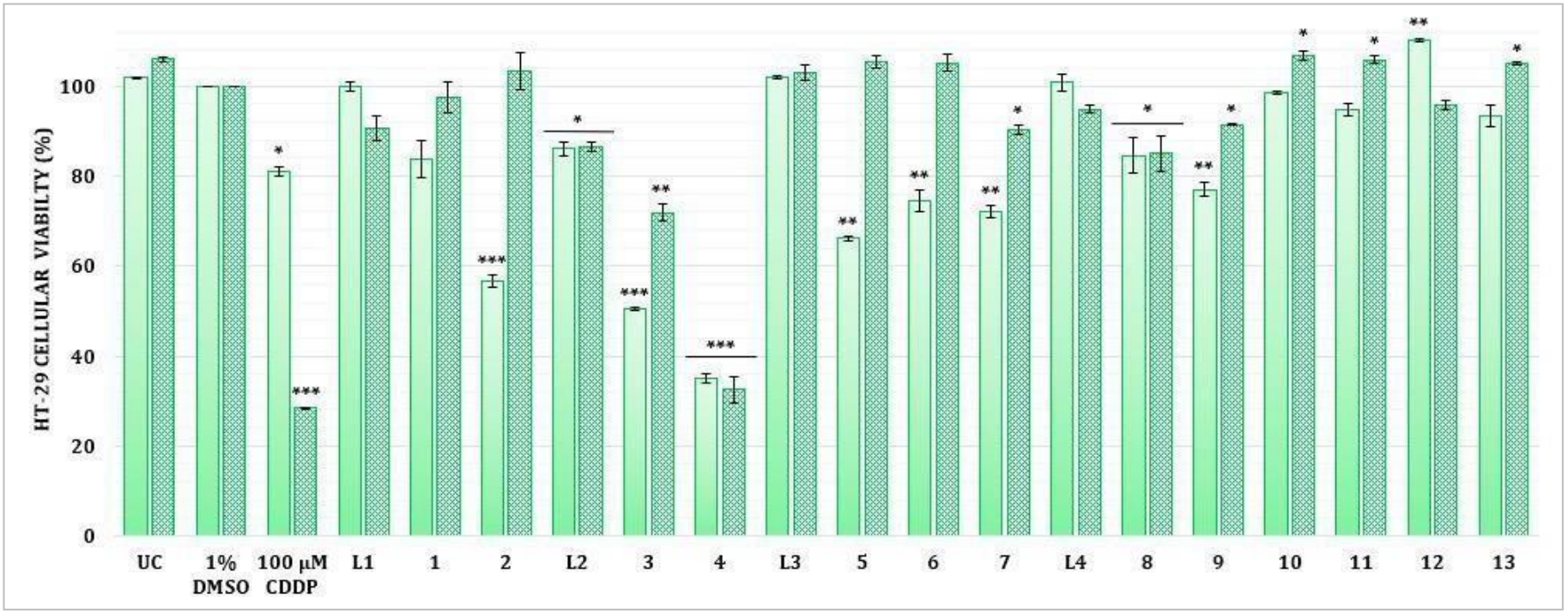


Figure 2.9. The percentage cellular viability of malignant **HT-29** cells determined using the alamarBlue® proliferation assay The following treatments were added to the cells: no treatment (untreated control) or treated with 1% DMSO (vehicle control), 100 µM CDDP (positive apoptotic control), 10 µM of silver(I) phosphine complexes (**1** - **13**) and 10 µM of respective ligands (**L1** - **L4**) for 24 h and 48 h (gradient filled bars represent 24 h after treatment and patterned filled bars represent 48 h after treatment). Percentages were expressed in relation to 1% DMSO (100 %). The ± SEM (n = 6) were represented as error bars and P values were calculated using a two-tailed Student's t-test. Significant differences are denoted by asterisks (* $P < 0.05$; ** $P < 0.01$ and *** $P < 0.001$).

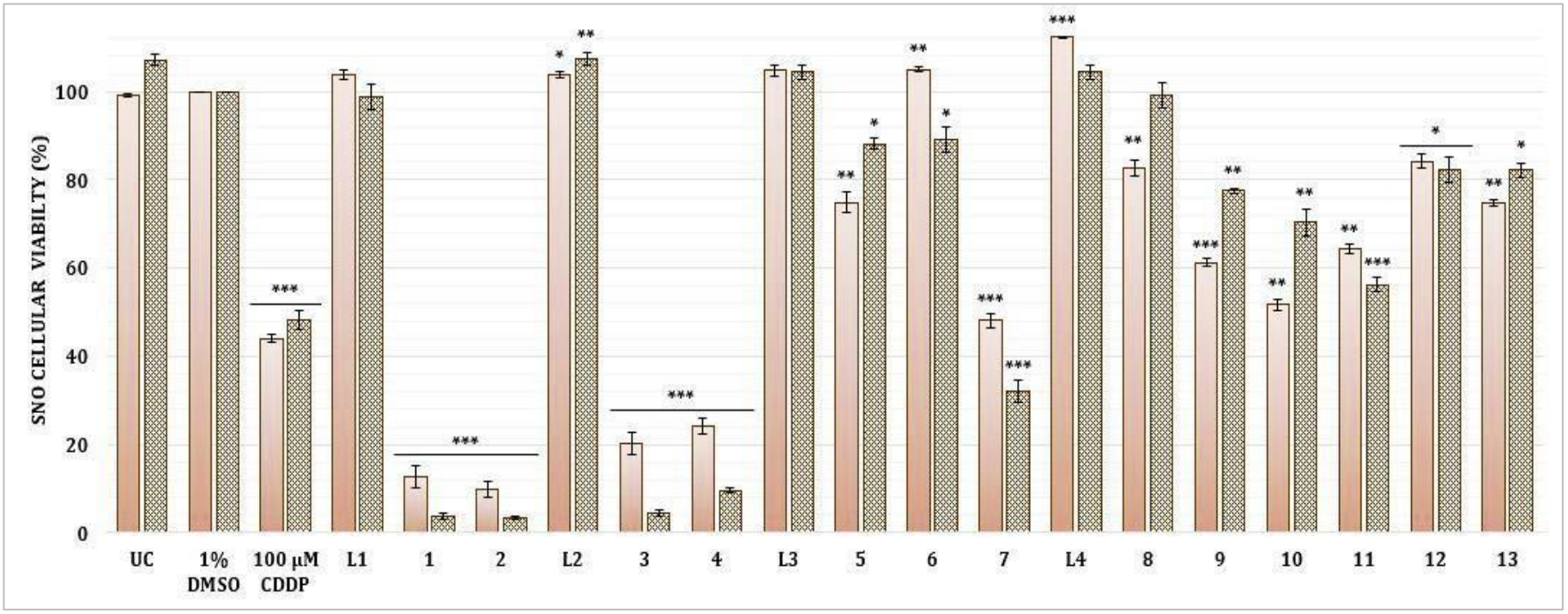


Figure 2.10. The percentage cellular viability of malignant **SNO** cells determined using the alamarBlue® proliferation assay. The following treatments were added to the cells: no treatment (untreated control) or treated with 1% DMSO (vehicle control), 100 µM CDDP (positive apoptotic control), 10 µM of silver(I) phosphine complexes (**1** - **13**) and 10 µM of respective ligands (**L1 - L4**) for 24 h and 48 h (gradient filled bars represent 24 h after treatment and patterned filled bars represent 48 h after treatment). Percentages were expressed in relation to 1% DMSO (100 %). The ± SEM (n = 6) were represented as error bars and P values were calculated using a two-tailed Student's t-test. Significant differences are denoted by asterisks (* $P < 0.05$; ** $P < 0.01$ and *** $P < 0.001$).

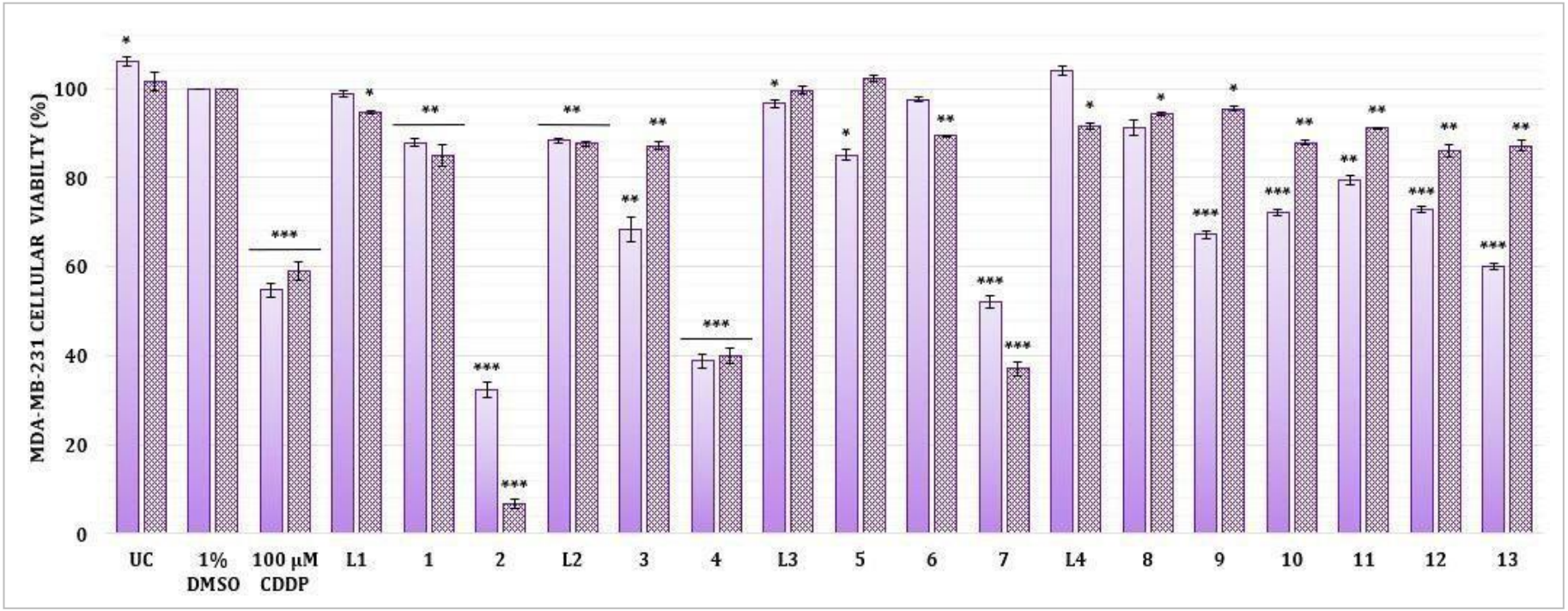


Figure 2.11. The percentage cellular viability of malignant **MDA-MB-231** cells determined using the alamarBlue® proliferation assay. The following treatments were added to the cells: no treatment (untreated control) or treated with 1% DMSO (vehicle control), 100 µM CDDP (positive apoptotic control), 10 µM of silver(I) phosphine complexes (**1** - **13**) and 10 µM of respective ligands (**L1** - **L4**) for 24 h and 48 h (gradient filled bars represent 24 h after treatment and patterned filled bars represent 48 h after treatment). Percentages were expressed in relation to 1% DMSO (100 %). The ± SEM (n = 6) were represented as error bars and P values were calculated using a two-tailed Student's t-test. Significant differences are denoted by asterisks (* $P < 0.05$; ** $P < 0.01$ and *** $P < 0.001$).

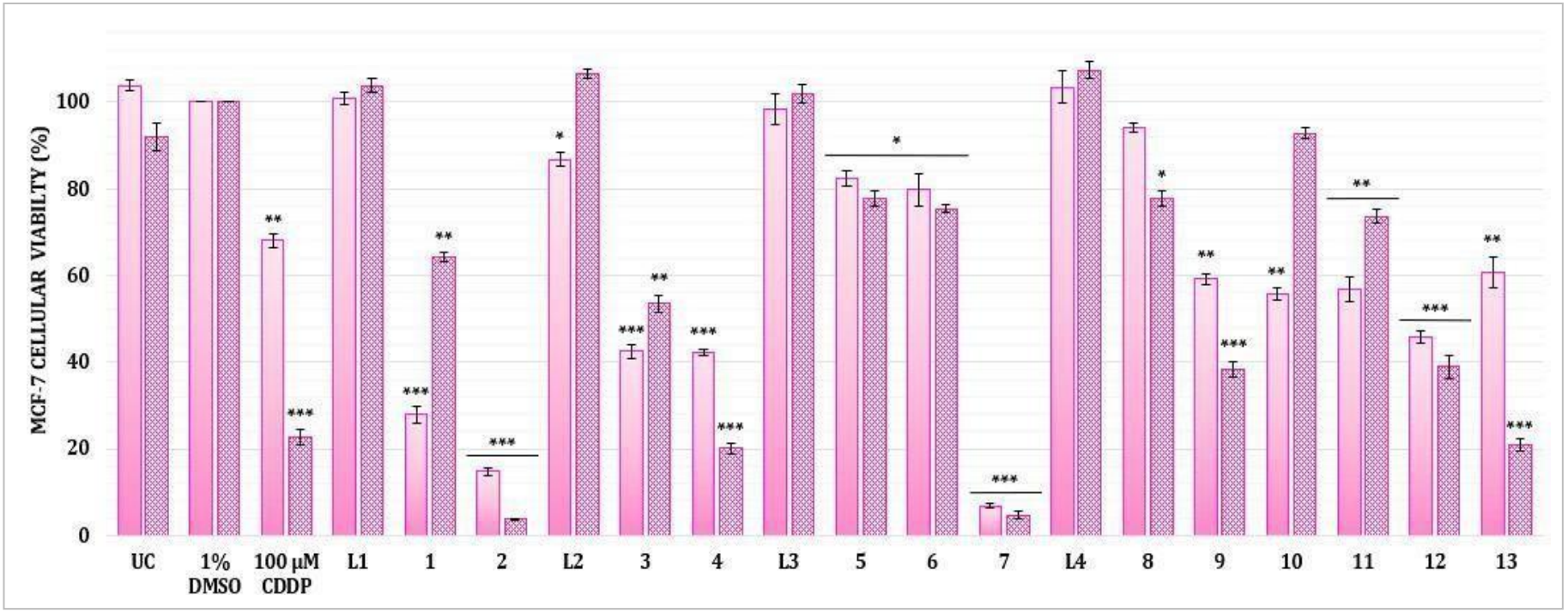


Figure 2.12. The percentage cellular viability of malignant MCF-7 cells determined using the alamarBlue® proliferation assay. The following treatments were added to the cells: no treatment (untreated control) or treated with 1% DMSO (vehicle control), 100 µM CDDP (positive apoptotic control), 10 µM of silver(I) phosphine complexes (**1** - **13**) and 10 µM of respective ligands (**L1** - **L4**) for 24 h and 48 h (gradient filled bars represent 24 h after treatment and patterned filled bars represent 48 h after treatment). Percentages were expressed in relation to 1% DMSO (100 %). The ± SEM (n = 6) were represented as error bars and P values were calculated using a two-tailed Student's t-test. Significant differences are denoted by asterisks (* $P < 0.05$; ** $P < 0.01$ and *** $P < 0.001$).

After 48 hours of treatment, complexes **5**, **6**, **8**, **9**, **10** and **11** had little to no impact on the viability of HEP-G2 cells (**Figure 2.8**). Despite causing a notable decrease in cellular viability at 24 h and 48 h, complexes **7**, **12**, and **13** still maintained a cellular viability of over 78% (78.35%, 86.81%, and 89.62%, respectively). Only complexes **1** - **4** showed a significant decrease ($P < 0.01$) in viability after 24 h and 48 h after treatment and were therefore considered successful. Complex **2** was the most cytotoxic, with 5.45% viability, followed by complexes **1** (7.63%), **3** (11.86%) and **4** (12.72%). Complexes **1** - **13**, excluding complex **4**, resulted in no significant decrease in viability in HT-29 cells after 48 h of treatment (**Figure 2.9**). Although complexes **2** and **3** resulted in a statistically significant decline ($P < 0.001$) in viability after 24 h (below 60%), the cells recovered after a further 24 h incubation, with an increase in cellular viability of 103.41% and 71.82%, respectively. It was observed that complex **4** resulted in a significant decrease ($P < 0.001$) in viability at 24 h (35.11%) and 48 h (32.58%). This was the only complex that was successful as an antiproliferative agent in malignant HT-29 cells. The viability of malignant SNO cells continued to decline after 48 h, suggesting that complexes **1** - **4**, **7** and **11** were effective in triggering a cell death response (**Figure 2.10**). Although complexes **6** and **12** resulted in a slight decrease in cellular viability after 48 h, viabilities were above 80% (89.09% and 82.22%, respectively). The most cytotoxic complex was **2**, with a viability of only 3.37%, closely followed by complex **1** (3.63%), **3** (4.46%), **4** (9.55%) and **7** (31.99%).

In **Figure 2.12**, complexes **2**, **4**, **7**, **9**, **12** and **13** were effective in decreasing cellular viability in MCF-7 cells after 48 h of treatment. These complexes negatively affect the recovery rate of MCF-7 cells. Interestingly, complexes **9**, **12** and **13** were selective only for MCF-7 cells. Though complexes **12** and **13** significantly ($P < 0.001$) decreased cellular viability in the MRHF cells after 24 h treatment, the cells had recovered after 48 h. When reviewing the structure of these complexes, they were all synthesized with the 4-(dimethylamino)-phenyldiphenyl-phosphine ligand. Complex **9** had a $AgNO_3$ salt core and 1:2 ratio stoichiometry, while complexes **12** and **13** share a AgBr salt core but differ in a 1:2 and 1:3 ratio, respectively. Future studies exploring the cell death mechanisms of complexes **9**, **12** and **13** in MCF-7 cells are of interest here. However, after 48 h, only three silver(I) phosphine complexes **2**, **4**, and **7** were effective in MDA-MB-231 cells (**Figure 2.11**). They were selected for further research and cell death mechanisms were compared between the two breast cell lines. Complex **2** resulted in the lowest viability in both MCF-7 (3.67%) and MDA-MB-231 (6.68%) cells after 48 h. Followed by complex **7** (4.71% MCF-7 and 37.03% MDA-MB-231) and **4** (20.01% MCF-7 and 39.96% MDA-MB-231), respectively.

With regard to CDDP, this platinum-based complex was most cytotoxic towards the MCF-7 cells after 48 h (25.43%), closely followed by the A375 cells (25.43%), HT-29 cells (28.50%), and HEP-G2 cells

(39.37%). The SNO (48.23%) and MDA-MB-231 (58.88%) cells recovered marginally after 48 h while the decrease in cellular viability remained significant ($P < 0.001$).

Overall, silver(I) phosphine complexes **1** - **4**, **6**, **7** and **11** were deemed successful in reducing cell viability of malignant cell lines. After 48 h, the most cytotoxic complex was **2** for the A375, A549, HEP-G2, SNO, MDA-MB-231, and MCF-7 cell lines, although it had no cytotoxic effect on the HT-29 cells. The only complex that had a cytotoxic effect on all seven malignant cell lines was complex **4**. In **Appendix II** a summarized table (**Table A1**) of the cellular viabilities obtained after 24 h of treatment from the cytotoxic *in vitro* screening data is reported. Data from 24 h studies were only provided in **Table A1** because the IC_{50} concentrations were calculated at that hour, and all subsequent experiments were conducted at 24 h after treatment with the selected silver(I) phosphine complexes.

2.3.4. IC_{50} concentration studies on malignant cell lines

The successful complexes for each respective malignant cell line were further analyzed by dose-response studies. The seven malignant cell lines were either not treated or treated with 1% DMSO or given consecutive concentrations of selected silver(I) phosphine complexes (1.25 µM, 2.5 µM, 5 µM, 10 µM and 20 µM) or CDDP (12.5 µM, 25 µM, 50 µM, 100 µM and 200 µM). The selected complexes for each cell line were the following: A375 = complexes **1** - **4**, **6** and **7**; A549 = complexes **1** - **4**, **6** and **7**; HEP-G2 = complexes **1** - **4**; HT-29 = complex **4**; SNO = complexes **1** - **4**, **7** and **11**; MCF-7 and MDA-MB-231 = complexes **2**, **4** and **7**. Dose-response studies analyze the relationship between the anticancer complex and mitochondrial activity of the cells by sigmoidal-fitting (Larsson *et al.*, 2020). This was achieved using the alamarBlue® proliferation assay. After 24 hours of treatment, IC_{50} values were calculated applying the polynomial function equation with nine independent repeats. Data was represented as bar graphs for each malignant cell line (**Figure 2.13** to **2.17**). **Tables 2.2** and **2.3** provide a summary of the calculated IC_{50} concentrations.

CDDP resulted in IC_{50} concentrations exceeding 20 µM while selected silver(I) phosphine complexes resulted in IC_{50} concentrations below 20 µM. For A375, MDA-MB-231 and MCF-7 cells, complex **7** had the lowest IC_{50} value of 5.82 µM, 4.81 µM and 2.95 µM, respectively. In the A549 and SNO cells, complex **1** had the lowest IC_{50} value of 6.35 µM and 6.63 µM, respectively, followed closely by complex **2** for the A549 cells and complex **7** for the SNO cells. The most successful complex in targeting all cancer types was complex **4**, which was also the only complex to significantly ($P < 0.001$) decrease cellular viability in the HT-29 cells after 24 h and 48 h of treatment (**Figure 2.8**). Complex **4** (active across all malignancies) resulted in IC_{50} values that did not drastically vary between the different malignant cells lines (±7 µM, highlighted by a red border), the two outliers being the A375 cells (10.80 µM) and the HEP-G2 cells (5.75 µM). Complex **11** was the only complex selective for SNO cells, while

complex **6** was only complex selective for the A375 and A549 cell lines.

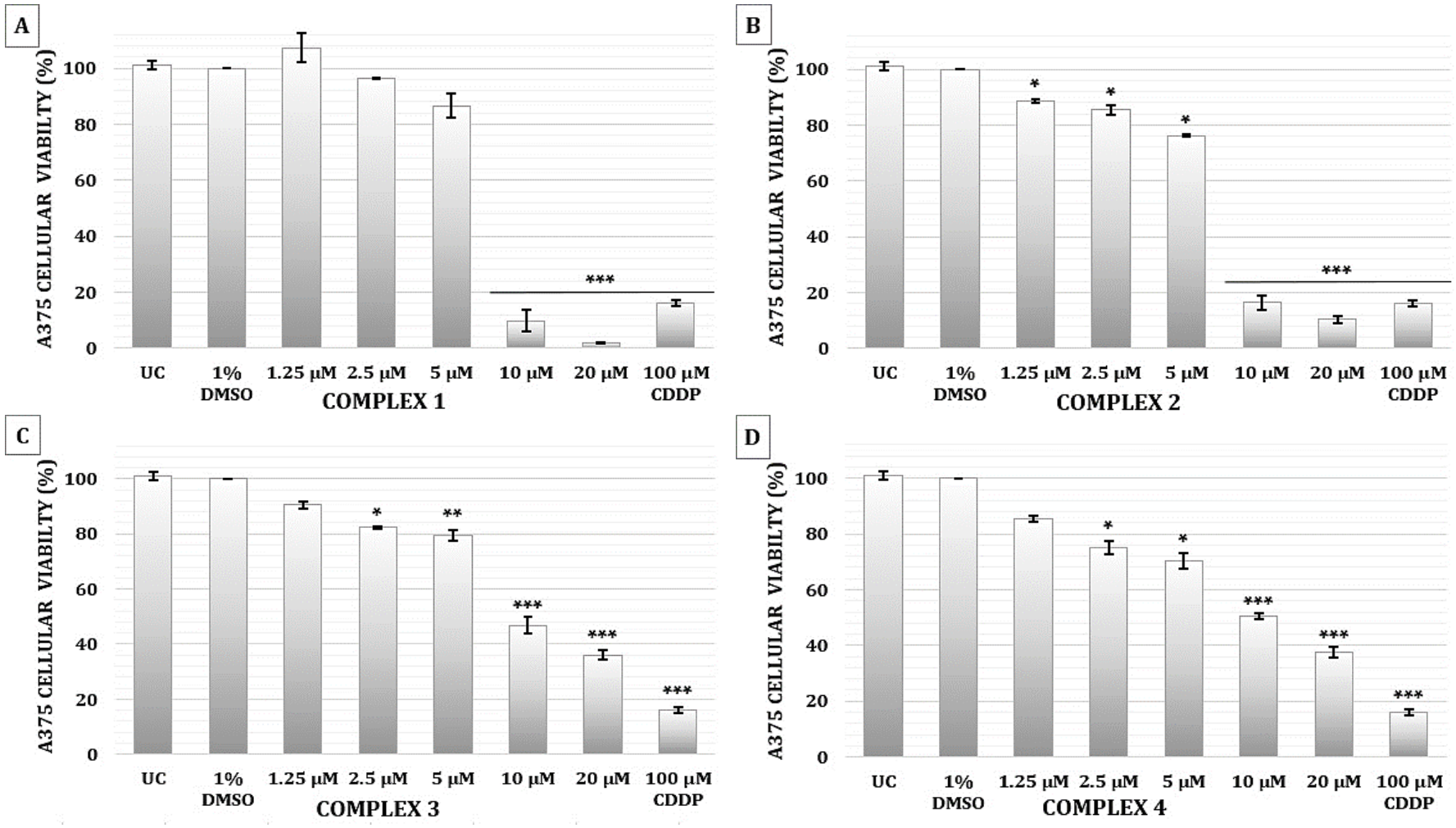
Table 2.2. The calculated IC_{50} concentrations (µM) for CDDP and complexes **1** - **4**, **6**, **7** and **11** (respective to the cell line). These values were calculated after 24 h of treatment in A375, A549, HEP-G2, HT-29 and SNO malignant cell lines, determined using the alamarBlue® proliferation assay. The standard mean of error (±SEM) is indicated in brackets and a polynomial function with nine independent repeats was used.

Various malignant cell lines					
Complex	**A375**	**A549**	**HEP-G2**	**HT-29**	**SNO**
CDDP	49.91 (± 3.69)	59.35 (± 8.29)	109.36 (± 5.30)	200.96 (± 10.35)	88.81 (± 5.46)
1	8.02 (± 4.00)	6.35 (± 1.99)	7.08 (± 0.82)	-	6.63 (± 1.11)
2	8.63 (± 2.38)	7.19 (± 1.11)	6.50 (± 1.10)	-	8.09 (± 0.56)
3	12.47 (±1.56)	11.89 (± 2.15)	3.02 (± 0.57)	-	9.63 (± 2.65)
4	10.80 (± 1.71)	7.38 (± 1.40)	5.75 (± 0.51)	7.49 (± 0.20)	7.48 (± 1.67)
6	10.81 (± 3.48)	7.56 (± 0.72)	-	-	-
7	5.08 (± 0.75)	8.82 (± 1.56)	-	-	6.93 (± 4.90)
11	-	-	-	-	16.99 (± 1.74)

Table 2.3. The calculated IC_{50} concentrations (µM) for CDDP and complexes **2**, **4**, **7** in MCF-7 and MDA-MB-231 malignant breast cell lines after 24 h of treatment, determined using the alamarBlue® proliferation assay. The ±SEM is indicated in brackets and a polynomial function with nine independent repeats was used.

Malignant breast cell lines		
Complex	**MDA-MB-231**	**MCF-7**
CDDP	80.59 (± 9.45)	153.79 (± 8.30)
2	6.21 (± 0.46)	4.58 (± 0.53)
4	7.61 (± 0.82)	7.18 (± 1.60)
7	4.81 (± 0.41)	2.95 (± 0.38)

An important aspect illustrated by the screening data is how small alterations in the structure of these silver(I) phosphine complexes can result in substantial differences in cytotoxicity. For example, complex **3** and complex **11** differ in their ligands, but they have the same AgCl salt core and tetrahedral geometry. Complex **11** was active only on the SNO cells, with a slightly higher IC_{50} concentration of 16.99 µM. Similar results were seen when comparing complexes **3** and **4**, the only difference being their silver salt cores (AgCl and AgBr, respectively). While complex **4** significantly decreased cellular viability in all malignancies, complex **3** did not affect the HT-29 or the breast cell lines. This structural difference resulted in different preferences in malignant cell lines. The following dose-response curves with the equation of the line were used to calculate the respective IC_{50} concentrations (µM) for the malignant cell lines.


A
A375 CELLULAR VIABILTY (%)
100
80
60
40
20
0
***
UC
1% DMSO
1.25 µM
2.5 µM
5 µM
10 µM
20 µM
100 µM CDDP
COMPLEX 1
B
A375 CELLULAR VIABILTY (%)
*
*
*
***
UC
1% DMSO
1.25 µM
2.5 µM
5 µM
10 µM
20 µM
100 µM CDDP
COMPLEX 2
C
A375 CELLULAR VIABILTY (%)
*
**
***
***
***
UC
1% DMSO
1.25 µM
2.5 µM
5 µM
10 µM
20 µM
100 µM CDDP
COMPLEX 3
D
A375 CELLULAR VIABILTY (%)
*
*
***
***
***
UC
1% DMSO
1.25 µM
2.5 µM
5 µM
10 µM
20 µM
100 µM CDDP
COMPLEX 4

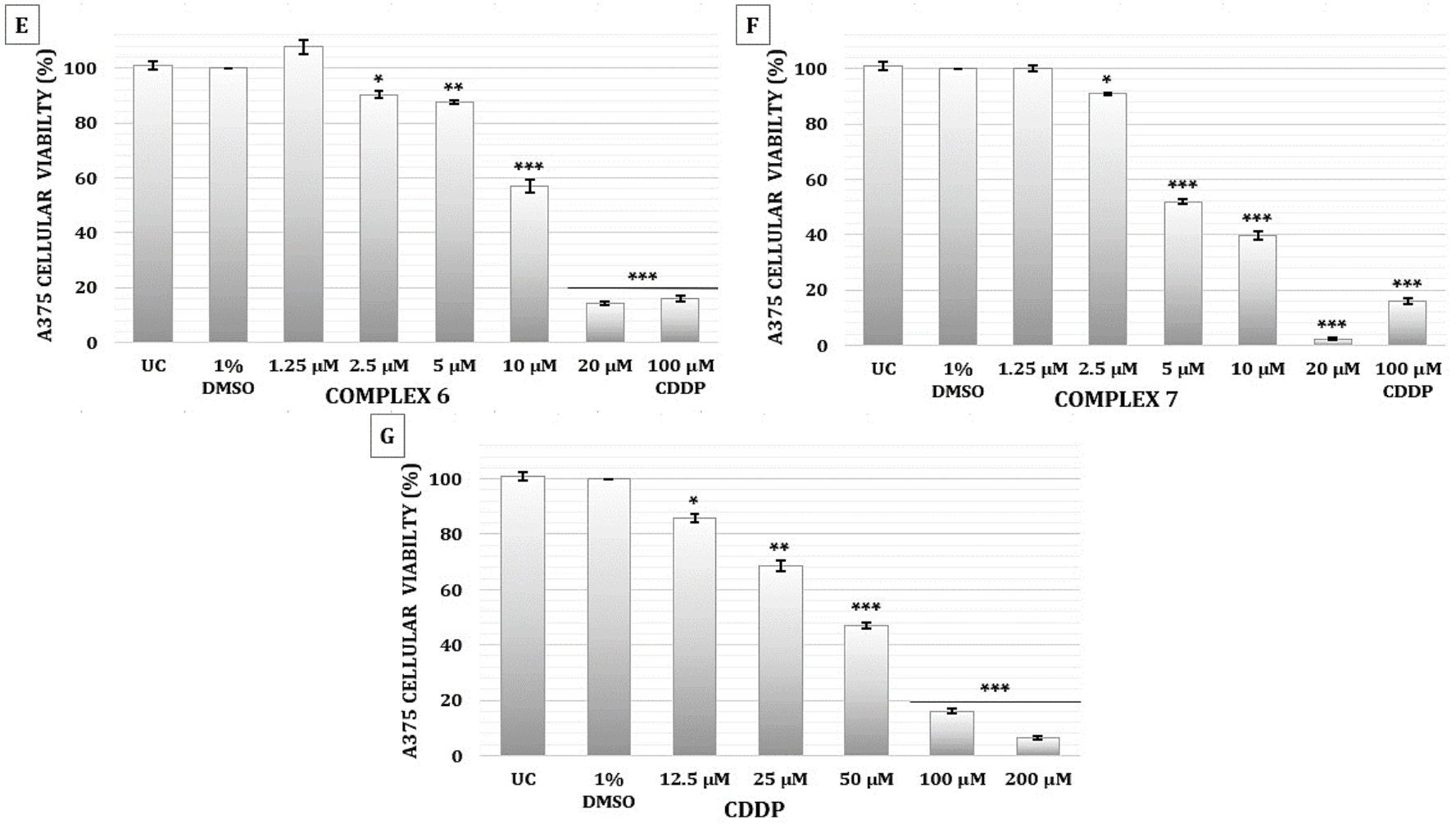
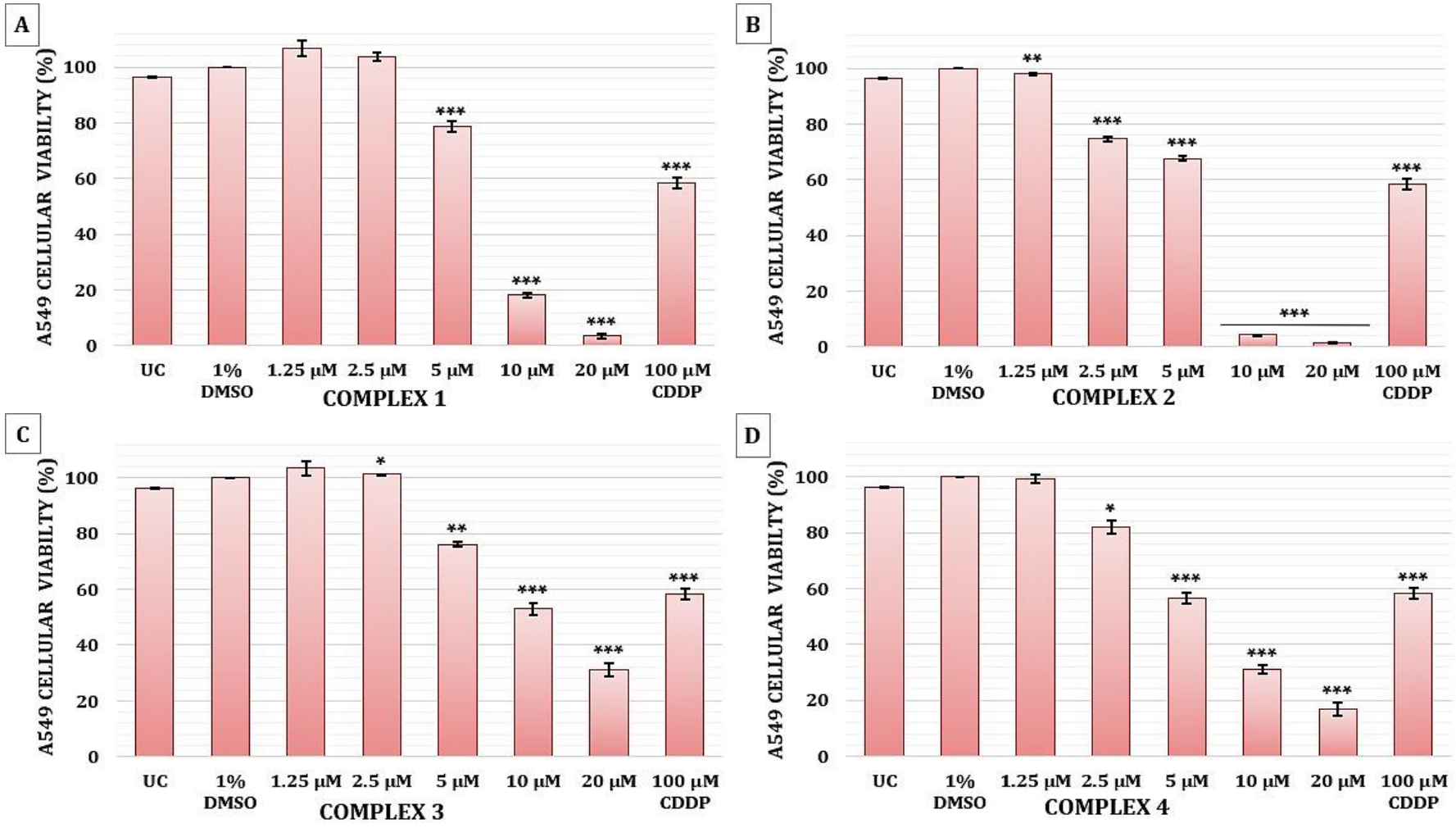


Figure 2.13. Dose-responsive studies of malignant A375 cells determined using the alamarBlue® proliferation assay. The following treatments were an untreated control or treated with 1% DMSO (vehicle control), **(A - D)** a range of concentrations (1.25 µM to 20 µM) of complexes **1** - **4** respectively, **(E) 6** and **(F) 7** or **(G)** a range of concentrations (12.5 µM to 200 µM) of CDDP (positive apoptotic control) for 24 h. Percentages were expressed in relation to 1% DMSO (100 %). The ± SEM (n = 9) were represented as error bars and P values were calculated using a two-tailed Student's t-test. Significant differences are denoted by asterisks (* $P < 0.05$; ** $P < 0.01$ and *** $P < 0.001$).


A
A549 CELLULAR VIABILTY (%)
0
20
40
60
80
100
***
***
***
UC
1% DMSO
1.25 µM
2.5 µM
5 µM
10 µM
20 µM
100 µM CDDP
COMPLEX 1
B
A549 CELLULAR VIABILTY (%)
**
***
***
***
***
UC
1% DMSO
1.25 µM
2.5 µM
5 µM
10 µM
20 µM
100 µM CDDP
COMPLEX 2
C
A549 CELLULAR VIABILTY (%)
*
**
***
***
***
UC
1% DMSO
1.25 µM
2.5 µM
5 µM
10 µM
20 µM
100 µM CDDP
COMPLEX 3
D
A549 CELLULAR VIABILTY (%)
*
***
***
***
***
UC
1% DMSO
1.25 µM
2.5 µM
5 µM
10 µM
20 µM
100 µM CDDP
COMPLEX 4

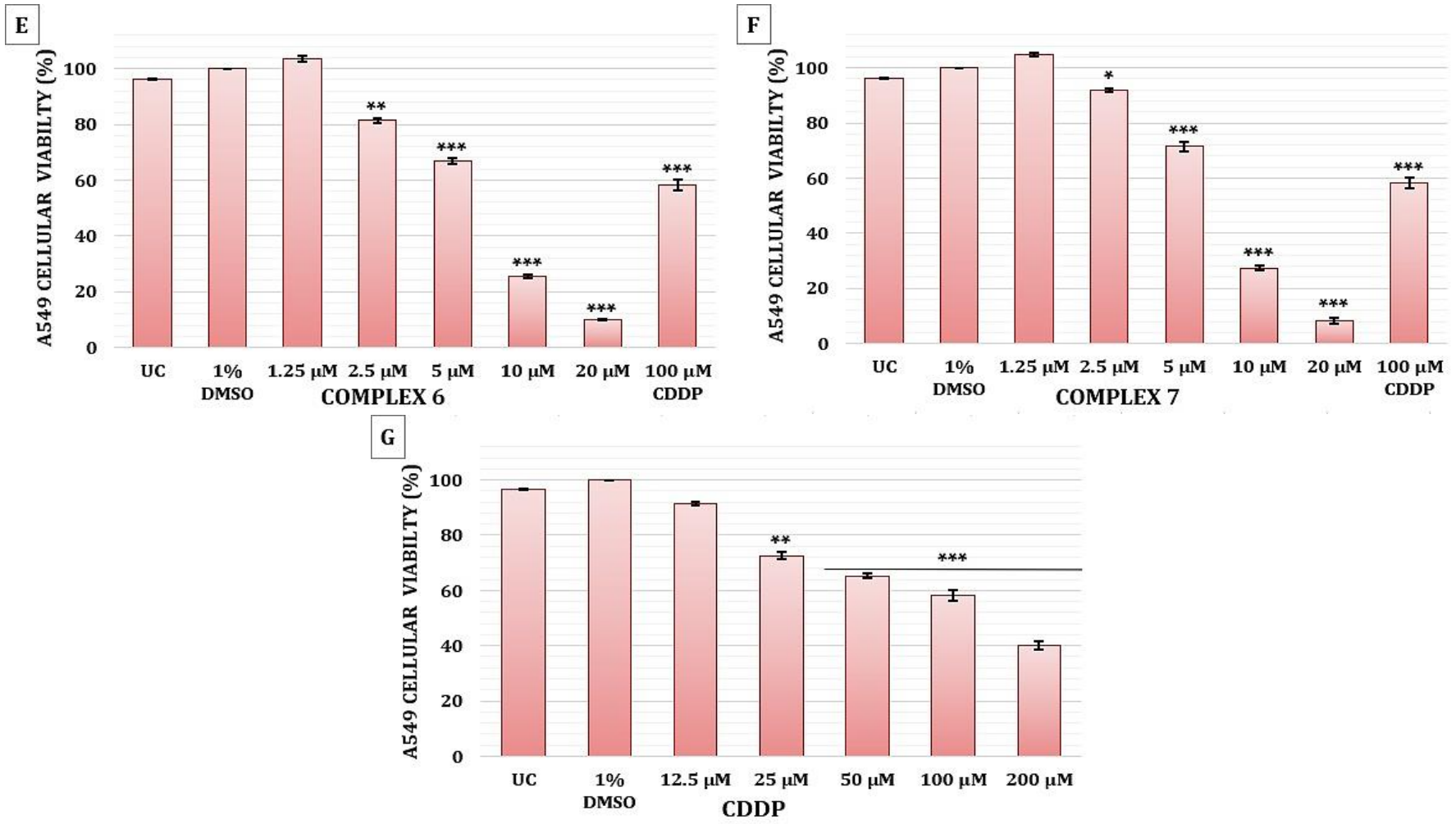
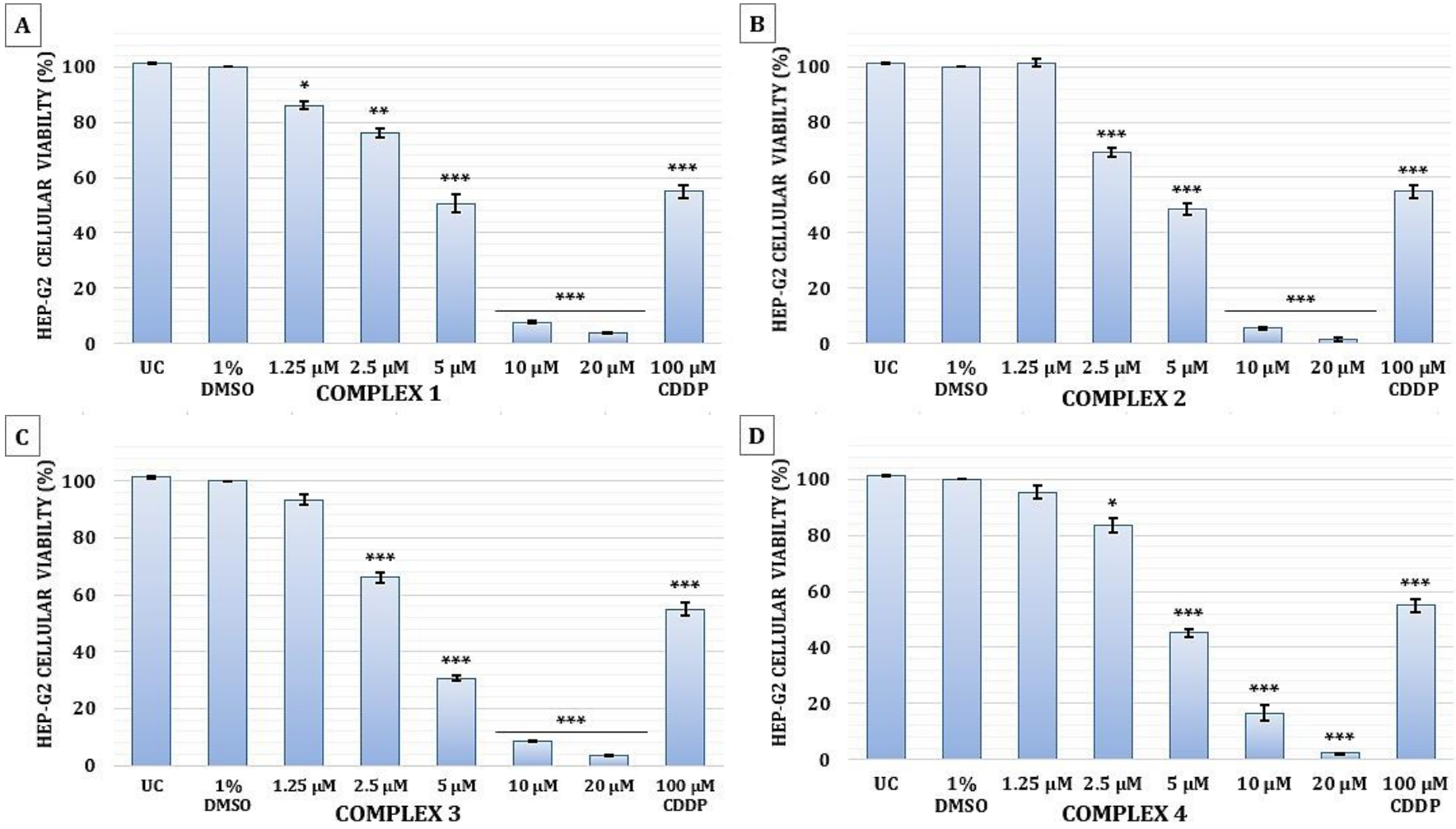


Figure 2.14. Dose-responsive studies of malignant **A549** cells determined using the alamarBlue® proliferation assay. The following treatments were an untreated control or treated with 1% DMSO (vehicle control), **(A - D)** a range of concentrations (1.25 µM to 20 µM) of complexes **1 - 4** respectively**, (E) 6** and **(F) 7** or **(G)** a range of concentrations (12.5µM to 200 µM) of CDDP (positive apoptotic control) for 24 h. Percentages were expressed in relation to 1% DMSO (100 %). The ± SEM (n = 9) were represented as error bars and P values were calculated using a two-tailed Student's t-test. Significant differences are denoted by asterisks (* $P < 0.05$; ** $P < 0.01$ and *** $P < 0.001$).


A
HEP-G2 CELLULAR VIABILTY (%)
100
80
60
40
20
0
*
**
***
***
***
UC
1% DMSO
1.25 µM
2.5 µM
5 µM
10 µM
20 µM
100 µM CDDP
COMPLEX 1
B
HEP-G2 CELLULAR VIABILTY (%)
***
***
***
***
UC
1% DMSO
1.25 µM
2.5 µM
5 µM
10 µM
20 µM
100 µM CDDP
COMPLEX 2
C
HEP-G2 CELLULAR VIABILTY (%)
***
***
***
***
UC
1% DMSO
1.25 µM
2.5 µM
5 µM
10 µM
20 µM
100 µM CDDP
COMPLEX 3
D
HEP-G2 CELLULAR VIABILTY (%)
*
***
***
***
***
UC
1% DMSO
1.25 µM
2.5 µM
5 µM
10 µM
20 µM
100 µM CDDP
COMPLEX 4

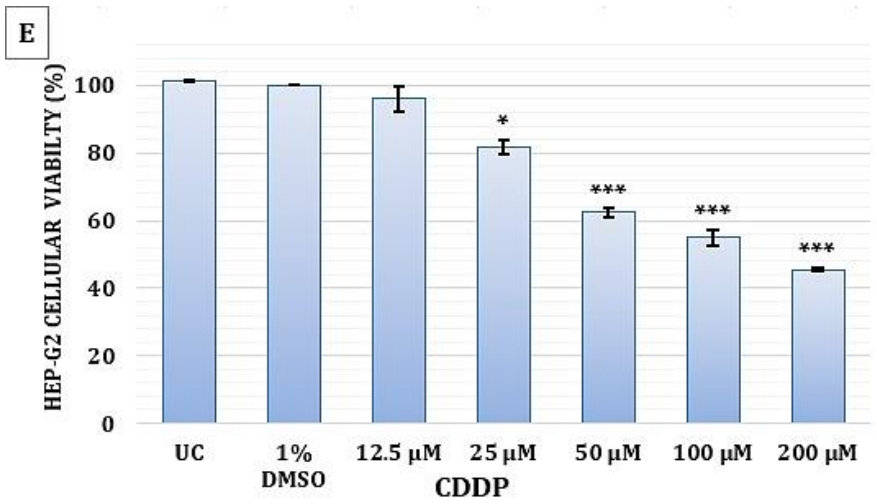


Figure 2.15. Dose-responsive studies of malignant **HEP-G2** cells determined using the alamarBlue® proliferation assay. The following treatments were an untreated control or treated with 1% DMSO (vehicle control), **(A - D)** a range of concentrations (1.25 µM to 20 µM) of complexes **1** - **4** respectively and **(E)** a range of concentrations (12.5 µM to 200 µM) of CDDP (positive apoptotic control) for 24 h. Percentages were expressed in relation to 1% DMSO (100 %). The ± SEM (n = 9) were represented as error bars and P values were calculated using a two-tailed Student's t-test. Significant differences are denoted by asterisks (* $P < 0.05$; ** $P < 0.01$ and *** $P < 0.001$).

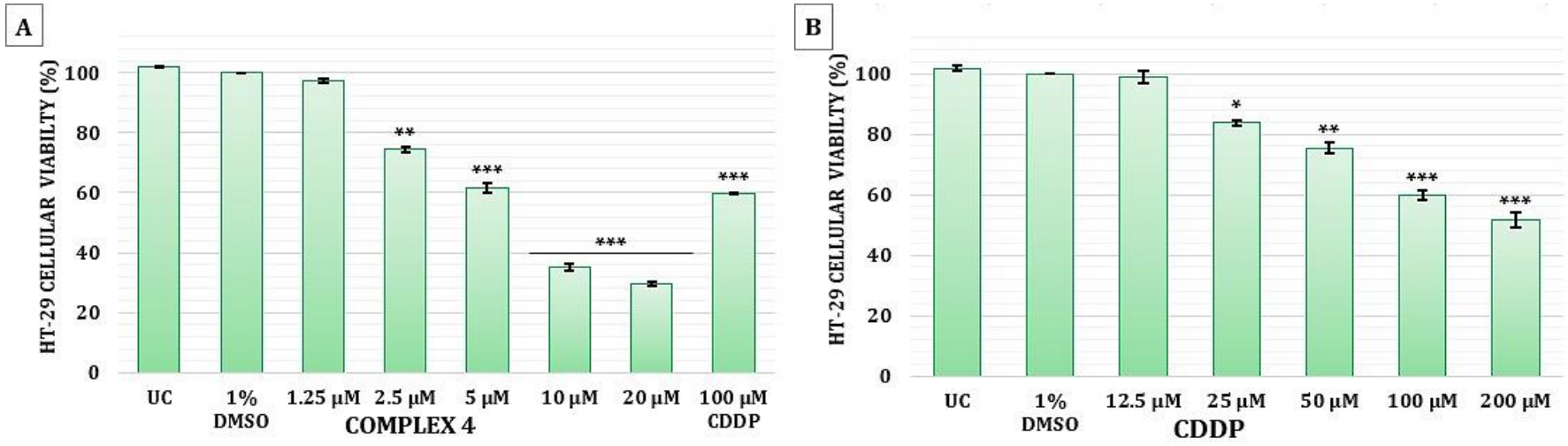
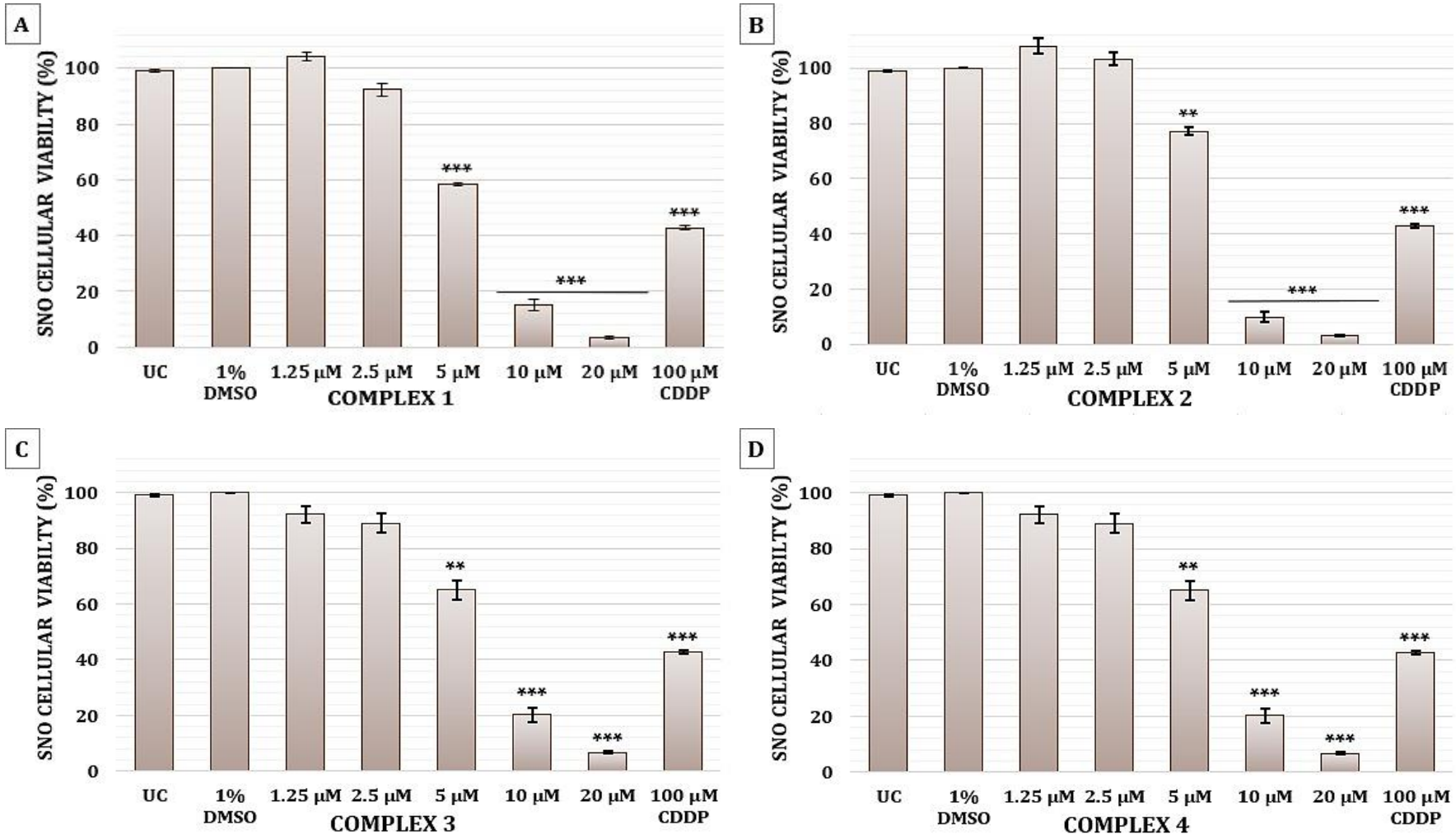


Figure 2.16. Dose-responsive studies of malignant **HT-29** cells determined using the alamarBlue® proliferation assay. The following treatments were an untreated control or treated with 1% DMSO (vehicle control), **(A)** a range of concentrations (1.25 µM to 20 µM) of complex **4** respectively and **(B)** a range of concentrations (12.5 µM to 200 µM) of CDDP (positive apoptotic control) for 24 h. Percentages were expressed in relation to 1% DMSO (100 %). The ± SEM (n = 9) were represented as error bars and P values were calculated using a two-tailed Student's t-test. Significant differences are denoted by asterisks (* $P < 0.05$; ** $P < 0.01$ and *** $P < 0.001$).


A
SNO CELLULAR VIABILITY (%)
0
20
40
60
80
100
***
***
***
UC
1% DMSO
1.25 µM
2.5 µM
5 µM
10 µM
20 µM
100 µM CDDP
COMPLEX 1
B
SNO CELLULAR VIABILITY (%)
0
20
40
60
80
100
**
***
***
UC
1% DMSO
1.25 µM
2.5 µM
5 µM
10 µM
20 µM
100 µM CDDP
COMPLEX 2
C
SNO CELLULAR VIABILITY (%)
0
20
40
60
80
100
**
***
***
***
UC
1% DMSO
1.25 µM
2.5 µM
5 µM
10 µM
20 µM
100 µM CDDP
COMPLEX 3
D
SNO CELLULAR VIABILITY (%)
0
20
40
60
80
100
**
***
***
***
UC
1% DMSO
1.25 µM
2.5 µM
5 µM
10 µM
20 µM
100 µM CDDP
COMPLEX 4

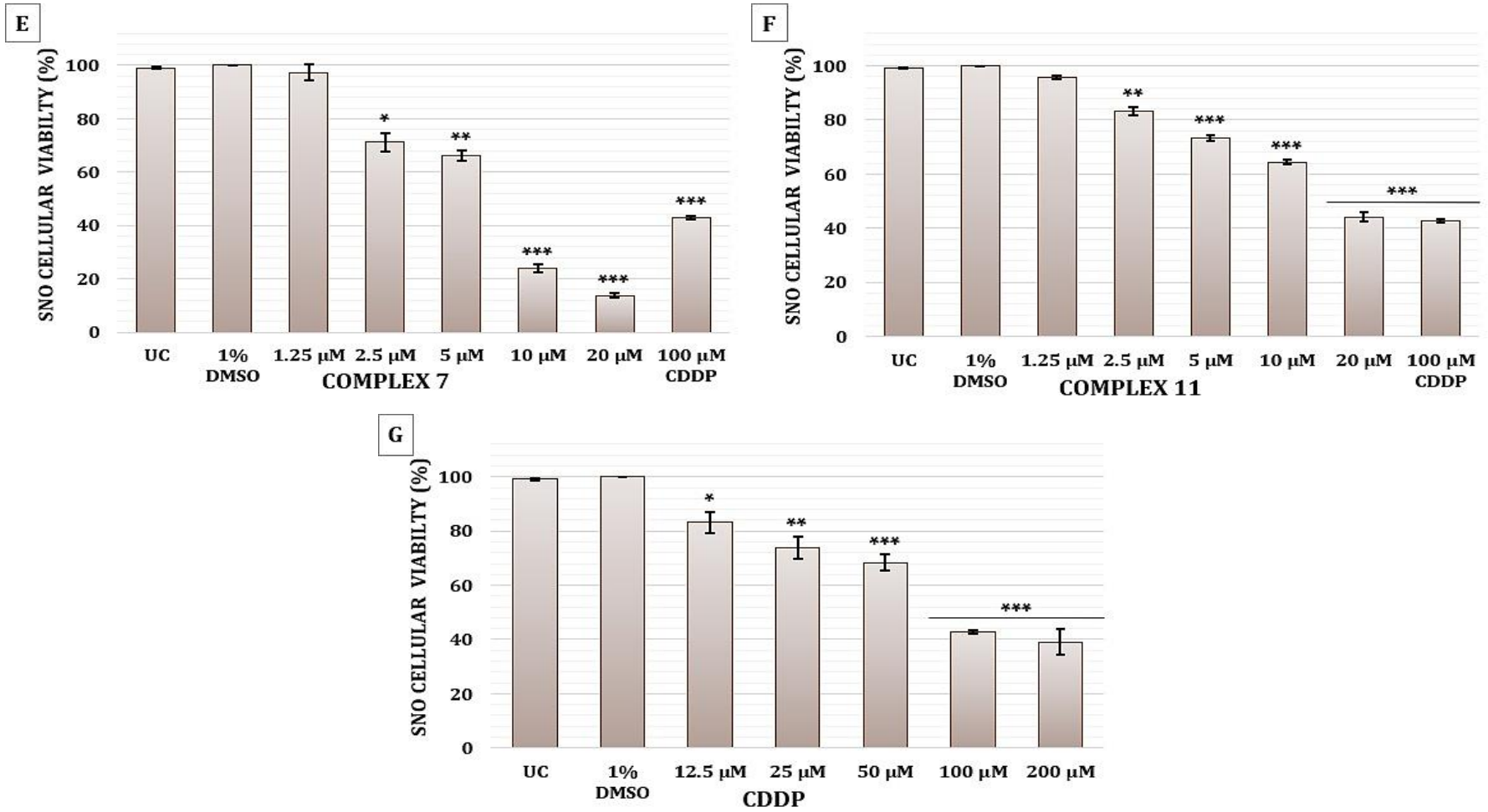


Figure 2.17. Dose-responsive studies of malignant **SNO** cells determined using the alamarBlue® proliferation assay. The following treatments were an untreated control or treated with 1% DMSO (vehicle control), **(A - E)** a range of concentrations (1.25 µM to 20 µM) of complexes **1** - **4** respectively, **(E) 7** and **(F) 11** respectively or **(G)** a range of concentrations (12.5 µM to 200 µM) of CDDP (positive apoptotic control) for 24 h. Percentages were expressed in relation to 1% DMSO (100 %). The ± SEM (n = 9) were represented as error bars and P values were calculated using a two-tailed Student's t-test. Significant differences are denoted by asterisks (* $P < 0.05$; ** $P < 0.01$ and *** $P < 0.001$).

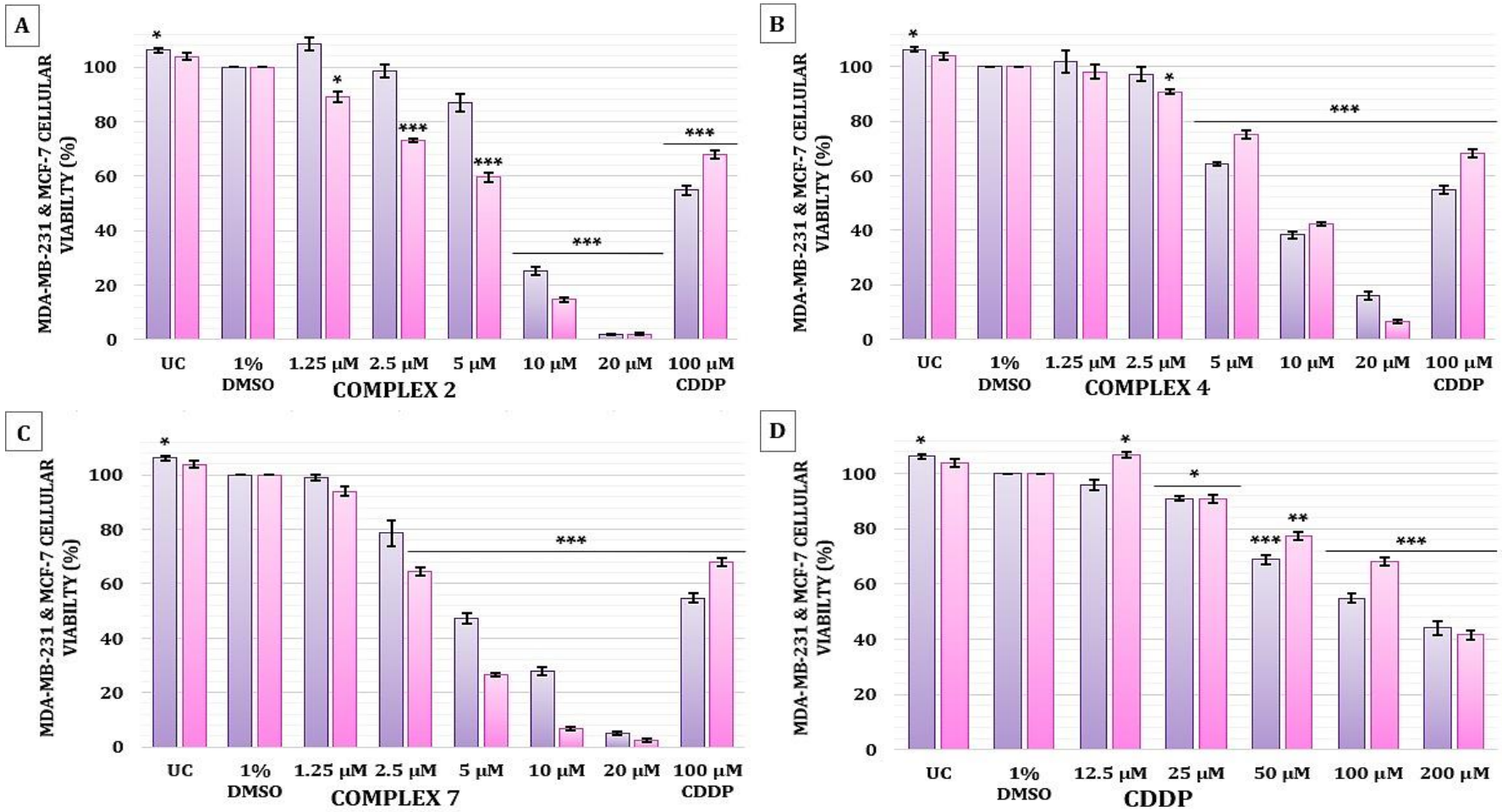


Figure 2.17. Dose-responsive studies of malignant **MDA-MB-231** and **MCF-7** cells determined using the alamarBlue® proliferation assay. The following treatments were an untreated control or treated with 1% DMSO (vehicle control), **(A - C)** a range of concentrations (1.25 µM to 20 µM) of complexes **2, 4** and **7** respectively or **(D)** a range of concentrations (12.5 µM to 200 µM) of CDDP (positive apoptotic control) for 24 h. Percentages were expressed in relation to 1% DMSO (100 %). The ± SEM (n = 9) were represented as error bars and P values were calculated using a two-tailed Student's t-test. Significant differences are denoted by asterisks (* $P < 0.05$; ** $P < 0.005$ and *** $P < 0.001$).

2.4. Discussion

The ability to recognize whether a complex induces toxicity is fundamental for new and developing anticancer drug candidates that seem promising. Studies have revealed that a diversity of transition-based metals and ligands could be used as antineoplastic agents, as there are many possibilities in their geometry and their nature of coordination (Bresciani *et al.*, 2022; Meijboom *et al.*, 2009).

2.4.1. Cytotoxic abilities of silver(I) phosphine complexes and ligands

Previous research has shown a connection between the biological activity of silver(I) phosphine complexes and their structure. McKeage *et al.* (1998) synthesized various Au(I), Ag(I) and Cu(I) complexes containing (2-aminophenyl)phosphines AMPP [(+)-(2-aminophenyl)methylphenyl-phosphine] and ADPP [(2-aminophenyl)diphenylphosphine] ligands. The structures of these complexes were of tetrahedral stereochemistry. It was found that the cytotoxicity of the complexes were not greatly influenced by the nature of the metal ion or the counterion, but rather by the number of phosphines, whereby complexes with tertiary phosphines exhibited greater cytotoxicity. In addition, Santini *et al.* (2011) explains that the structure-activity relationship is based on the hydrophilic/lipophilic balance of diphosphine and phosphinopyridyl metal complexes, as this effects cellular uptake and cytotoxicity. They observed that decreasing the overall lipophilicity of the molecule is an effective method for increasing the cytotoxic activity of tertiary phosphine complexes.

Thirteen novel silver(I) phosphine complexes were synthesized. To determine their ability in targeting seven various malignancies as well as two non-malignant cell lines, cytotoxicity experiments were conducted. These thirteen complexes and their related uncoordinated ligands were tested at a single-dose screening concentration of 10 µM after 24 h and 48 h of treatment. As formerly mentioned in the prologue (section *2.1.*), complexes **1** - **13** were regarded as successful if **a)** the ligands (**L1** - **L4**) induced low levels of toxicity to non-malignant and malignant cell lines; **b)** complexes were selective for malignant cell lines with minimal or no toxicity to non-malignant cells following 24 h and 48 h incubation periods; **c)** complexes significantly decreased the cellular viability of malignant cells; and **d)** the cells did not recover (the cellular viability decreased after 48 h). All complexes selected were successful in conforming to points **a** - **d**.

(a) *Complex degree of cytotoxicity on non-malignant cells*

Treatment comparisons on transformed HEK-293 and non-malignant MRHF cells validated the promising qualities of selected silver(I) phosphine complexes. The specificity these complexes possess towards malignant cells is critical to their development as improved anticancer agents. In **Figures 2.2** to **2.5**, HEK-293 and MRHF cells treated with DMSO exhibited similar morphology and percentage viability to the untreated control cells. The vehicle (mock) control must continue to be non-toxic to both non-malignant and malignant cell lines in order to confirm that the drug is the element that causes

cytotoxicity. Complexes of silver(I) phosphine were dissolved in DMSO. This solvent has several appealing properties, including the ability to solubilize both polar and non-polar components and pass through hydrophobic barriers. According to de Abreu Costa *et al*. (2017) this is important for intracellular complexes; hence, DMSO is a commonly utilized solvent and carrier for pharmacological agents. However, a low concentration of this solvent needs to be used, as higher concentrations could possibly alter cell activation in *in vitro* culture. The studies herein used a final DMSO concentration that never exceeded 1%.

The positive control for apoptosis, CDDP, was slightly cytotoxic after 48 h of treatment on the HEK-293 and MRHF cells. Singh *et al.* (2018) observed a dose-dependent relationship after treating HEK-293 cells with increasing concentrations of CDDP. As concentrations of CDDP increased, cellular viability of HEK-293 cells decreased. Nevertheless, after 48 h, (**Figures 2.2** and **2.3**), cellular viability remained above 70%. When evaluating the cellular viability of the HEK-293 and MRHF cells treated with complexes **1 - 13** after 24 h and 48 h, minimal to no toxicity was observed through mitochondrial and morphological studies. Previous studies confirm the low degree of toxicity activated in normal, healthy cells by silver(I) phosphine complexes (Engelbrecht and Cronjé, 2018; Engelbrecht *et al.*, 2018). Poyraz *et al.* (2011) suggest silver(I) complexes with phosphine ligands exhibit lower proliferation activity in MRC-5 (human fetal lung fibroblast) cells. Cellular viability as well as morphology imaging of SNO, HDF-α (human dermal fibroblast), and HEK-293 cells were investigated after treatment with a silver(I) thiocyanate complex. Engelbrecht *et al.* (2018) observed a statistically significant decline in cellular viability in treated SNO cells after 24 h, while HDF-α and HEK-293 cells treated with silver(I) phosphine complexes remained less cytotoxic with 88.22% and 74.11% viability, respectively. Minimal morphological alterations were observed in HEK-293 cells, while slight changes were seen in HDF-α cells treated with silver(I) thiocyanate. These observations support the results obtained herein. In **Figures 2.2** and **2.3**, the viability of cells treated with complexes **1 - 13** remained above 60.86% (MRHF) and 80.00% (HEK-293) after 24 h. These cells had recovered and sustained proliferative signalling with a viability of 87.56% (MRHF) and 88.40% (HEK-293) after 48 h. No morphologicalchanges were observed in HEK-293 cells (**Figure 2.4**), while minimal alterations were seen in the MRHF cells in the presence of complexes **2** and **6** (**Figure 2.5**).

(b) *Toxicity investigations of the ligands on non-malignant and malignant cells*

When compared to their cohesive complexes, all four uncoordinated ligands (**L1 - L4**) did not substantially reduce viability after treatment periods of 24 h and 48 h and remained non-toxic towards non-malignant and malignant cell lines (**Figures 2.2** to **2.12**). Limited toxicity was present in all nine cell lines, with viabilities greater than 85% after 48 h of treatment. Similar results were observed in findings from Human-Engelbrecht *et al.,* (2017). A silver(I) phosphine complex, $[Ag(PPh_3)_2]NO_3$, derived from the same family of complexes used in the above cytotoxicity screening studies, was found

to be cytotoxic towards SNO cells and not the HDF-α cells. The ligand, triphenylphosphine at a concentration of 10 µM, was evaluated against the cells and minimal toxicity was observed, with viabilities higher than 88%. In another study by Kumar *et al.* (2011) diphenyl-(2-pyridyl)-phosphine (PPh_2Py) and polypyridyl ligands were complexed with cationic ruthenium(II). These complexes were evaluated for their effect on TopoII activity in *Setaria cervi* (parasitic roundworms) and was found to have an inhibitory effect when complexed with PPh_2Py ligands. Functional silver(I) phosphine complexes increased cytotoxicity in MCF-7 and LMS (leiomyosarcoma) cells than their respective ligand, triphenylphosphine and o-hydroxybenzoic acid (Poyraz *et al.*, 2011). Pathaw *et al.* (2020) screened uncoordinated ligands used to synthesize copper(I) phosphine complexes on A549 and L132 (human lung epithelial) cell lines. These ligands were not toxic on these cell lines, even at concentrations as high as 250 µM after treatment for 24 h and 48 h.

It has been noted that transition metals carrying various ligands result in structures with catalytic abilities. In general, the interaction of the ligands with the functional silver(I) complex appears to be the reason for their anticancer properties. Ligands derived from mono- and bidentate phosphine ligands have attracted much attention when coordinated with silver due to these properties. Sofyan *et al.* (2018) suggest that toxicity towards malignant cell lines is reliant on the type of ligand, due to the possibility that this will increase the complex's stability and hydrophilicity-lipophilicity (Kalinowska-Lis *et al.*, 2016). The silver salts used to synthesize complexes **1 - 13**, are not dissolvable in DMSO and therefore cytotoxicity studies were not achievable.

(c) *Complex cytotoxicity against malignant cell lines*

Silver(I) complexes with tris(*p*-tolyl) phosphine (Kyros *et al.*, 2010); triphenylphosphines with salicylic acid (Poyraz, *et al.*, 2011); 3-benzyl-1,3-thiazolidine-2-thione ligands with triphenylphosphine and tri(o-tolyl)phosphine (Sofyan *et al.*, 2018); and thiocyanate (Ferreira *et al.*, 2015; Human *et al.*, 2015; Human-Engelbrecht *et al.*, 2017; Engelbrecht and Cronjé, 2018; Engelbrecht *et al.*, 2018) decreased cellular viability in various malignant cell lines at a greater level than CDDP. Single-dose screening of complexes **1 - 13** against seven malignant cell lines allowed for the identification of specificity of a complex towards a particular cell line. Overall, it can be seen from **Figures 2.2** to **2.12**, certain complexes induced antiproliferative effects on one or more malignant cell lines after 24 h and significantly affected the recovery rate of these cells after a further 24 h of treatment. In a previous study, Potgieter *et al.* (2016) compared the cellular viability of SNO cells treated for 24 h with 10 µM of four silver(I) *p*-substituted phenyl diphenyl phosphine complexes. These complexes resulted in viabilities ranging from 17 - 21%. Similar viabilities after 24 h were observed in the cytotoxicity screening data presented herein (**Appendix II**, **Table A1**).

2.4.2. The relationship between dosage and effect

Dose-response experiments (**Figures 2.13** to **2.17**) were conducted to evaluate the degree of toxicity of complexes **1 - 4**, **6**, **7** and **11**. The IC_{50} concentrations represented in **Tables 2.2** and **2.3** correspond with previous literature focused on the same phosphine silver mono-dentate family with various phenyl derivative ligands. Engelbrecht *et al*. (2017) demonstrated that a silver(I) cyanide phosphine complex can induce apoptosis in malignant SNO cells. Using the alamarBlue® proliferation assay, dose-response studies were performed, and a 4.02 µM IC_{50} concentration was calculated. Complexes **1**, **2** and **6** were synthesized with silver thiocyanate, and the IC_{50} concentrations calculated were below 10 µM in the A375, A549, HEP-G2 and SNO cells for complexes **1** and **2**. Complex **6** was selective towards the A375 and A549 cells, IC_{50} values of 10.81 µM and 7.56 µM were calculated, respectively. These values were lower than those obtained for CDDP, and this corresponds with the findings seen in Engelbrecht *et al.* (2017), who calculated an IC_{50} value of 47.39 µM for CDDP. Ferreira *et al.* (2015) previously described the extent of the toxicity of CDDP and silver(I) phosphine complexes, they explored the potential anti-cancer properties of these complexes in MCF-7 cells. Four silver(I) thiocyanate phosphine complexes resulted in IC_{50} values ranging from 3 to 3.59 µM, this is comparable to complex **2**, which was also synthesized with AgSCN and resulted in an IC_{50} value of 4.58 µM in the MCF-7 cells. In addition, Engelbrecht *et al.* (2018) obtained a low IC_{50} value of 3.50 µM when treating SNO cells with a silver(I) thiocyanate 4-methoxyphenyl phosphine, which was considerably lower than CDDP (42.89 µM). Interestingly, recent research by Bresciani *et al.* (2022), determined IC_{50} values for A549 and A2780 (human ovarian carcinoma) cells treated with a gold(I) phosphine complex, [AuCl(PPh_3)], an analogue to silver(I) phosphine complexes (Chrysouli *et al.*, 2018). IC_{50} values of 18.6 µM (A549 cells) and 12.6 µM (A2780 cells) were obtained. However, the IC_{50} values obtained for CDDP were greater for both cell lines, 40 µM and 15.1 µM, respectively. According to the literature mentioned above, some transition metal complexes have a higher antiproliferative effect on malignant cells than CDDP. Furthermore, copper(I) complexes carrying nitrate salts, pyridin-2-ylimidazo[1,5-a]pyridine ligands or triphenylphosphine ligands were screened by Pathaw *et al.* (2020) for their activity in malignant A549 cells and non-malignant L134 cells. These copper(I) complexes exhibited dose- and time-dependent cytotoxic effects against A549 cells, while activity against L134 cells was insignificant. Calculated IC_{50} values were from 42 µM to 72 µM on the A549 cells, while IC_{50} values were above 250 µM on the L134 cells. In addition, Sofyan *et al.* (2018) measured the cytotoxicity of complexes synthesized using silver nitrate with 3-benzyl-1,3-thiazolidine-2-thione ligands. These complexes inhibited MDA-MB-231, MCF-7, and HT-29 cells with calculated IC_{50} concentrations of 1.9 µM, 2.9 µM and 15.1 µM, respectively. Similar results were noted herein as the uncoordinated ligands had no cytotoxic effect on non-malignant or malignant cell lines. Overall, complexes were selective for malignant cell lines, and the calculated IC_{50} concentrations for silver(I) phosphine complexes were more potent than those calculated for CDDP.

The order of inhibitory activity for the respective selected silver(I) phosphine complexes against proliferation in the following malignancies were: A375 = **7** > **1** > **2** > **4** > **6** > **3**; A549 = **1** > **2** > **4** > **6** > **7** > **3**; HEP-G2 = **3** > **4** > **2** > **1**; HT- 29 = **4**; SNO = **1** > **7** > **4** > **2** > **3** > **11**; MCF-7 and MDA-MB-231 **=** **7** > **2** > **4**. Complex **7** showed the strongest activity against malignant melanoma and breast cell lines, while **1** was the strongest for lung and oesophageal carcinoma, **3** against hepatocellular carcinoma, and **4** only against colorectal adenocarcinoma. In addition, complex **4** was the only one that presented an antiproliferative effect in all seven malignancies tested. From the *in vitro* screening data obtained, there are several complexes that have potential as chemotherapeutic agents; however, the determination of their mode of action is important towards their development. Therefore, further investigations into the mechanisms of cell death were conducted in chapters three and four on selected malignant cell lines.

CHAPTER THREE:
APOPTOGENIC PROPERTIES OF SELECTED COMPLEXES ON MALIGNANT A375, HEP-G2 AND HT-29 CELL LINES

3.1. Prologue

Building upon the findings of the previous chapter, a deliberate selection was made to investigate three specific malignant cell lines in greater detail. These cell lines were the A549 lung adenocarcinoma, HEP-G2 hepatocellular carcinoma, and HT-29 colorectal adenocarcinoma. In recent years, these cancer types had the greatest mortality rates; lung cancer had the highest mortality rate of 18.4%, followed by colorectal cancer (9.2%), and liver cancer (8.3%) (Cai and Lui, 2021; Sung *et al.,* 2021). Moreover, studies have not yet explored the cell death mechanism that selected silver(I) phosphine complexes target in the cell lines mentioned above. Previous findings have revealed that other complexes within the same phosphine silver mono-dentate family induce the apoptotic pathway. Engelbrecht and Cronjé (2018) explain that a silver(I) methoxyphenyl phosphine complex initiated the intrinsic apoptotic pathway in malignant oesophageal cells. This was determined by the presence of apoptotic bodies, decreased ATP levels, PS externalization, depolarized $\Delta\Psi m$ and increased levels of ROS. In addition, Colell *et al.* (2009) observed the increase of GAPDH levels in the mitochondria prior to cell death and its subsequent proapoptotic functioning. In colon cancer cells, silver nanoparticles have been found to dose-dependently dysregulate GAPDH expression (Gioria *et al.,* 2018). The features mentioned above are diagnostic of apoptosis were the focus points studied in this chapter. Moreover, the CYP1B1 isoform of cytochrome P450 was measured. This enzyme is involved in metabolizing xenobiotics and when cells are exhausted of CYP1B1, apoptosis is induced (Bruno and Njar, 2007; Presa *et al.,* 2021). Investigating whether silver(I) phosphine complexes target this enzyme could be beneficial in developing these complexes as a targeted type of treatment.

As previously mentioned in chapter one, lung cancer is the deadliest cancer worldwide, with approximately 85% cases developing into NSCLC. When lung cancer cells disperse through the blood or lymphatic system to additional areas within the body, this is known as metastasis. Most lung cancer patients will have already developed metastatic disease before diagnosis (Raviadaran *et al.,* 2021). According to research, delaying or even regulating metastatic-associated pathways may significantly slow the progression of NSCLC (Cheng *et al.,* 2015; Eunji *et al.,* 2015). Therefore, the antimetastatic activity of selected silver(I) phosphine complexes on A549 cells only was assessed using an *in vitro* wound healing scratch assay. The discovery of anticancer and antimetastatic therapies is essential for lung cancer treatment (Xu *et al.,* 2013).

3.2. Experimental methodology

All reagents and equipment were used according to the manufacturer's guidelines. **Appendix I** contains a comprehensive inventory of the manufacturer information for all materials and tools used in chapter three's experimental analyzes.

3.2.1. Cell culture

Prior to use, all reagents for culture, subculture, and plating were heated in a pre-set water bath of 37°C.

3.2.1.1. Plating of cells

A549 lung adenocarcinoma, HT-29 colorectal adenocarcinoma and HEP-G2 liver carcinoma cells were cultured and removed from culture flasks, and counted as described in chapter two, points *2.2.2.2*, *2.2.2.3* and *2.2.2.4* respectively. An optimal concentration of 2 x 10^5 cells/ml in 3 ml of the respective media for each cell line: DMEM / McCoy's 5A / RPMI (6 x 10^5 cells) was calculated using a Countess™ automated cell counter and seeded in 35 mm tissue culture-treated dishes. Before treatment, cells were further incubated for 24 h.

3.2.1.2. Cell treatments

Cells were plated as detailed above in point *3.2.1.1.* After 24 h of incubation, the used media was discarded and 1 ml of fresh supplemented DMEM / McCoy's 5A / RPMI media was added to the 35 mm culture dishes. For all experimental assays (unless stated otherwise), cells were differentially treated as follows: either left as an untreated negative control (UC) or treated with 1% (v/v) DMSO (VC), 200 µM of CDDP (positive apoptotic control), or treated with 20 µM of selected silver(I) phosphine complexes. For A549, complexes **1**, **2**, **3**, **4**, **6** and **7** were selected. For HEP-G2 cells, complexes **1 - 4** were selected and for HT-29 cells, only complex **4** was selected. These complexes with CDDP were prepared as specified in point *2.2.1.15* of chapter two. A necrotic positive control was included when applicable, in which cells were treated with 1 ml of 50% (v/v) hydrogen peroxide (H_2O_2). Prior to antiproliferative and apoptogenic analyzes, cells were incubated for an additional 24 h.

3.2.2. Antiproliferative and apoptogenic analyses

3.2.2.1. Cellular morphology

Changes to cellular morphology and features following differential treatments on A549, HEP-G2 and HT-29 cells were observed using the Zeiss Axiovert 25 inverted light microscope. Cells were differentially treated as follows: either not treated (UC) or treated with 1% (v/v) DMSO (VC), 100 µM and 200 µM of CDDP (positive apoptotic control) or treated with 10 µM and 20 µM of selected

silver(I) phosphine complexes. The Zeiss AxioCam MRC camera with Axiovision 3.1 imaging software were used to capture micrographs at either 200 x and/or 400 x magnification.

3.2.2.2. Measuring GAPDH activity

The KDalert™ GAPDH Assay kit was used to determine the function of GAPDH in accordance with the manufacturer's guidelines (*colorimetric assay protocol*). Using the automated cell counter Countess™, an optimal concentration of 6 x 10^5 cells/ml was calculated. Each well of a tissue culture-treated 96-well plate was seeded with 100 µl (6 x 10^3) of cells. Cells were treated differently as detailed in point *3.2.1.2*. Before treatment, the cells were plated in three replicates and left to proliferate for an additional 24 h. Each sample received 100 µl of KDalert™ lysate buffer after the removal of the respective media. All cell lysates were homogenized by pipetting up and down between four and five times, after a 20 min incubation at 4°C. Twenty microliters cell extract, GAPDH enzyme dilution (positive GAPDH activity control), WWM (ddH_2O and master mix control) were transferred to a clear 96-well plate in triplicate. One hundred and eighty microlitres of the master mix was then added to each sample. Plates were kept at room temperature, in the dark for 30 min before examination. Absorbance was analyzed with a multimode plate reader VICTOR® Nivo™. An excitation wavelength of 615 nm was selected. For the purpose of standardizing background absorbance, 200 µl ddH_2O was included as a negative control.

3.2.2.3 CellTiter-Glo® luminescent cell viability assay

As a measure of cellular respiration related to mitochondrial activity, the CellTiter-Glo® Luminescent Cell Viability Assay was used to quantify the amount of ATP produced. Twenty-five microlitres of Substrate Solution™ were added to 25 µl of differentially treated cells (1:1 ratio) (point *3.2.1.2*). This was pipetted into the wells of a 96-well black plate with a round bottom as three replicates. Prior to whole luminescence analysis, cells were kept in the dark, at room temperature for 15 min. A VICTOR® Nivo™ multimode plate reader was used to analyze luminescence. An excitation wavelength of 700 nm short pass was selected. For the purpose of standardizing background luminescence, 100 µl cell-free culture media was included as a negative control.

3.2.2.4. Quantification of cellular populations' reactive oxygen species

The flow cytometric Muse® Oxidative Stress reagent was used to measure the amount of superoxide radicals in oxidatively stressed cells. Guidelines provided by the manufacturer were followed with limited changes. Following a dilution of 2 µl of Muse® Oxidative Stress Stock Solution with 198 µl of 1X Assay Buffer (1:100) (provided within the kit), the intermediate solution was prepared. This solution was then diluted by a factor of 1:80 with 1X Assay Buffer in order to obtain a working solution. Before labelling, differentially treated cells were washed with 500 µl pre-warmed 1X phosphate buffered saline (PBS; 37 °C) and gathered at 300 x*g* for 4 min. Sixty microlitres of 1X

Assay Buffer was used to resuspend the samples. One hundred and ninety microlitres of the working solution was added to the samples and vortexed. The samples were kept in the dark for 30 min at 37°C in a CO_2 incubator, after which 3000 events were recorded on the Muse® Cell Analyzer. Using Muse® Software V1.4.0.0 and the Guava® Muse® Oxidative Stress Kit User's Guide, cells were statistically evaluated. For compensation and gating, untreated control cells were gated by adjusting the ROS versus cell size index plot to a threshold that excluded any cellular debris. This gate was subsequently applied to all treated cells. Based on the analysis of this data, histograms were generated.

3.2.2.5. Measuring the change in mitochondrial membrane potential ($\Delta\Psi m$)

To measure the change in mitochondrial potential and cellular plasma permeabilization, the Muse® MitoPotential kit was used. Guidelines provided by the manufacturer were followed with limited changes. An optimal cell density of 3×10^5 cells/ml was used for analysis. Before labelling, a working solution was prepared by diluting (1:1000) Muse® MitoPotential dye with 1X Assay Buffer. Five hundred microlitres of a 1X PBS (37 °C) solution were used to wash the differentially treated cells. Cell pellets were collected at 300 x*g* for 4 min. Fifty microlitres of 1X Assay Buffer was used to resuspend the cell pellets. This was then added with vortexing to 47.5 µl of the working solution. Following an incubation of 20 min in a 37°C CO_2 incubator, each sample received 1.25 µl Muse® Mitopotential 7-AAD reagent. The samples were kept in the dark for 5 min. Thereafter, 5000 events were recorded on the Muse® Cell Analyzer. According to the Guava® Muse® MitoPotential Kit User's Guide, Muse® Software V1.4.0.0. statistically analyzes cell populations. Adjusting the MitoPotential versus cell size index plot to a threshold that negated any cellular debris was used to gate the untreated control cells. This gate was subsequently applied to the differentially treated cells, and the associated information were displayed as dot plots.

3.2.2.6. Determining potential mode of cell death

The Muse® Annexin V and Dead Cell kit was utilized to identify the possible mode of cell death. Guidelines provided by the manufacturer were followed with limited changes. An optimal cell density of 3×10^5 cells/ml was used for analysis. Differentially treated cells were washed with 500 µl 1X PBS (37 °C). The cells were then accumulated at 300 x*g* for 4 min. Fifty microlitres of 1X Assay Buffer was used to resuspend the cell pellets. Fifty microliters of Annexin V and Dead Cell Reagent were added to each sample. The samples were kept in the dark, at room temperature for 20 min. Thereafter, 5000 events were recorded on the Muse® Cell Analyzer. According to the Guava® Muse® Annexin V and Dead Cell Kit User's Guide, Muse® Software V1.4.0.0. statistically analyzes cell populations. For compensation and gating, untreated control cells were gated by adjusting the Annexin V versus cell size index to plot a threshold that negated any cellular debris. This gate was

subsequently applied to the differentially treated cells, and the associated information was displayed as dot plots.

3.2.2.7. Measuring cytochrome P450 (CYP1B1) activity

Using a Cytochrome P450-GLO™ Assay Kit, as per the manufacturer's guidelines, CYP1B1 activity was measured. As specified in points *3.2.1.1* and *3.2.1.2*, cells were seeded and treated as follows. After 24 h, the used media was discarded. Using 500 µl of 1X PBS (37°C), cells were rinsed twice. A 20 µM Luciferin-CEE stock was diluted by a factor of 1:50 in 100 µM fresh DMEM media without supplements (FCS-free). Differentially treated cells were washed with 500 µl 1X PBS (37 °C). The cells were then accumulated at 300 x*g* for 4 min. After which, samples were resuspended in 50 µl of the diluted substrate. They were then kept in a 37°C CO_2 incubator for 3 h. The samples were transferred in triplicate to a white 96-well plate, and 25 µl of Luciferin detection reagent was added to each well. The samples were kept at room temperature for 20 min. A VICTOR® Nivo™ multimode plate reader was used to analyze luminescence. An excitation wavelength of 700 nm short pass was selected. For the purpose of standardizing background luminescence, 100 µl cell-free culture media was included as a negative control.

3.2.3. Investigation into possible antimetastatic activity of silver(I) phosphine complexes

3.2.3.1. Determining the inhibition of A549 lateral motility by selected silver(I) phosphine complexes

To reveal if selected silver(I) phosphine complexes inhibit cell motility and proliferation, an *in vitro* wound healing scratch assay was used. As specified in points *3.2.1.1* and *3.2.1.2*, A549 malignant cells were seeded and treated as follows. Using a sterile 200 µl pipette tip, two wound tracks were scored in the confluent monolayer of each plate, slightly off-centre. The cells were rinsed twice with the DMEM media. This was to ensure no cell debris was present and floating in the media. Cells were differentially treated as follows: either not treated (UC) or treated with 1% (v/v) DMSO (VC) or treated with non-lethal concentrations of CDDP and complexes **1** - **4**, **6** and **7** in fresh FCS-free DMEM media. Non-lethal concentrations were calculated for CDDP: 3.75 µM and silver(I) phosphine complexes: 1.5 µM, through the analysis of dose-responsive studies (IC_{50} data) obtained in chapter two (**Figure 2.14**). Cell populations were examined 0 h, 24 h and 48 h after treatment using a Zeiss Primovert inverted light microscope. Micrographs were captured with the AxioCam ERc 5s camera and Zen 2.6 Lite Blue Edition imaging software at 4 x magnification. They were analyzed using ImageJ software with the wound healing size tool, an ImageJ/Fiji® plugin.

3.2.4. Statistical analysis

A representation of $n = 6$ was achieved using data consisting of three separate biological repeats and two independent technical repeats. To determine statistically significant variations, the Standard

Deviation, Standard Error of the Mean (SEM), and a two-tailed heteroscedastic Student's t-test were used, as suitable. The SEM for each differential treatment was represented as the errors bars on the bar graphs. The probability value (*P* value) of * $P < 0.05$, ** $P < 0.01$ and *** $P < 0.001$ were statistically significant in relation with DMSO-treated cells. Statistical analyzes was performed in Microsoft Office Excel 2013.

3.3. Results

3.3.1. Morphological changes

Alterations in morphology of the malignant cells treated with silver(I) phosphine complexes were analyzed using light microscopy. After 24 h, images were compared to the untreated and vehicle control treated cells. For all three cells lines, A549 (**Figure 3.1**), HEP-G2 (**Figure 3.2**) and HT-29 (**Figure 3.3**), the vehicle control-treated cells resembled the untreated control cells, with similar morphological traits unique to each cell line. There was no sign of cellular stress and the cells looked healthy. While cells treated with 100 µM CDDP, an inducer of apoptosis, showed some typical features characteristic of this cell death pathway, such as cellular rounding and apoptotic bodies (red arrows), with a few healthy cells still attached (**Figures 3.2** and **3.3**). Cells that had received 200 µM CDDP, 10 µM and 20 µM complexes appeared stressed and presented apoptotic features such as cellular rounding, apoptotic blebbing, and bodies (red arrows). With the 20 µM doses of complexes **1**, **2**, and **3**, fewer cells were seen in the A549 cells. The same observation was seen in the HEP-G2 cells when treated with complexes **2** and **4**, and when compared to the 10 µM treatments. HT-29 cells treated with 10 µM of complex **4** caused cellular rounding, while cells treated with 20 µM caused apoptotic blebbing with a reduction in cell volume (red arrows; **Figure 3.3**). This occurred as a consequence of cells detaching from the cell culture dish. These cells were suspended in culture media and appeared diminished when compared to the healthy, adherent, control-treated cells (UC and 1% DMSO).

3.3.2. Metabolic changes

Viability and metabolic activity were monitored in A549, HEP-G2 and HT-29 cells using three different viability assays. The function of GAPDH was measured using a KDalert™ GAPDH assay (**Figure 3.4**). This assay utilizes GAPDH, an enzyme that catalyzes the oxidation of G-3-P to BPG and the conversion of NAD^+ to NADH and is quantifiable at 615 nm. The rate of NADH production is directly proportional to a functioning amount of GAPDH protein present within the cell. In addition, the alamarBlue® cell proliferation assay data presented in chapter two is represented here once more in combination with the CellTiter-Glo® luminescent cell viability assay data (**Figure 3.5**). Both of these assays are mitochondrial based. The CellTiter-Glo® assay is based on a luciferase reaction. In the presence of ATP, luciferin is converted into oxyluciferin, which is luminescent.

Ultimately, the quantity of light produced by a cell is directly proportional to its ATP content. Presenting the cellular viability data alongside ATP levels gives an insight into the effect these complexes have on malignant cells.

It should be emphasized that the screening data was collected using 10 μM treatments, whereas the investigations discussed in this chapter used 20 μM treatments. This decision was based on the IC_{50} values obtained in chapter two, as many of these values were close to 10 μM (**Table 2.2**, chapter two). Furthermore, the assays described in this chapter specifically target the mechanisms of cell death. To effectively study these processes, a higher concentration (20 μM) of silver(I) phosphine treatments were used. This concentration was chosen given that it resulted in a significant decreases in cell viability (< 50%).

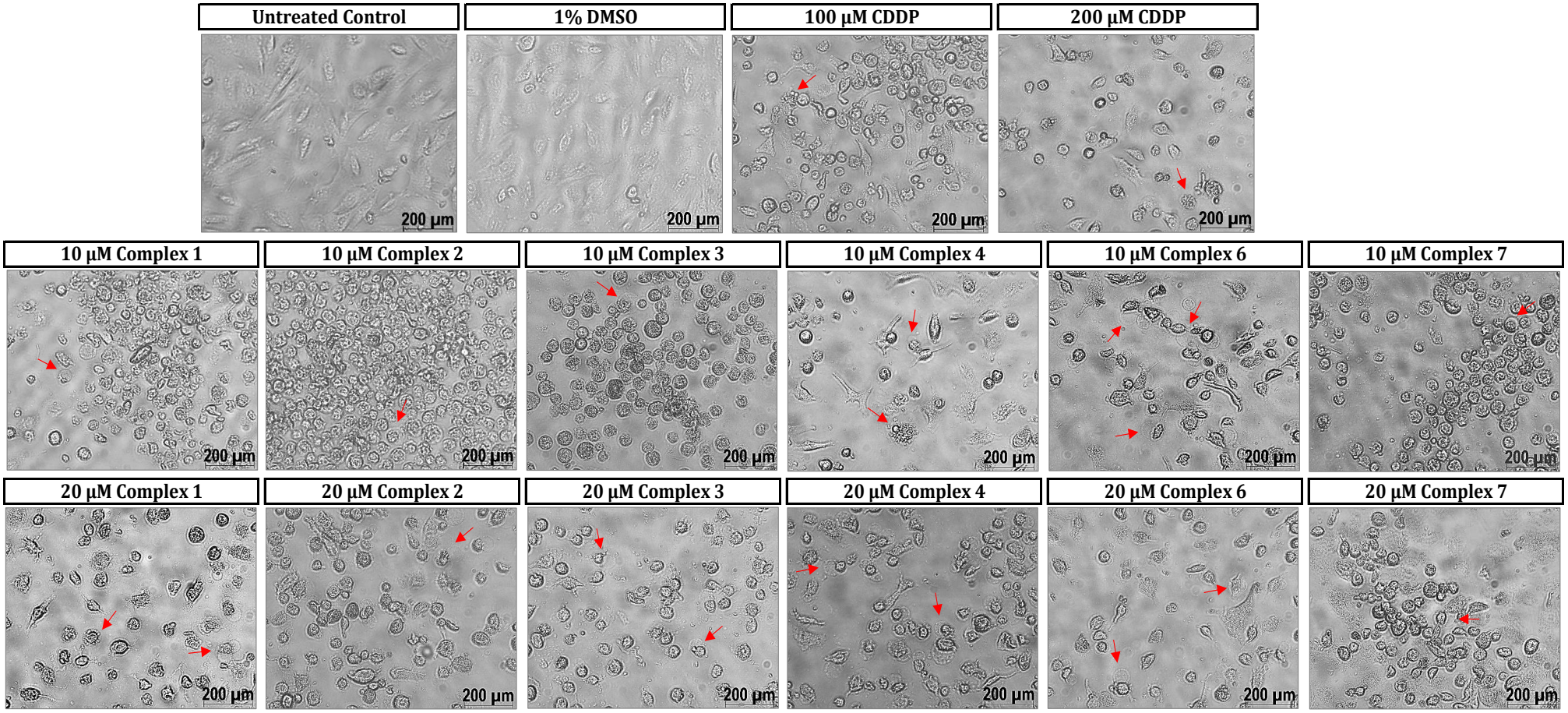


Figure 3.1. Morphological changes of malignant **A549** cells induced by differential treatments after 24 h. The following treatments were added to the cells: no treatment or treated with 1% DMSO, 100 µM and 200 µM CDDP; 10 µM and 20 µM silver(I) phosphine complexes **1 - 4**, **6** and **7**, respectively. Control-treated cells show typical, healthy A549 cells. Following 24 h incubation, CDDP-treated cells, and respective silver(I) phosphine complexes induced typical morphological changes to cells diagnostic of apoptosis such condensation, rounding, apoptotic blebbing and bodies (indicated by the red arrow). Light micrographs were captured with a Zeiss Axiovert 25 inverted light microscope and Axio Vision 3.1 software at 200 x magnification.

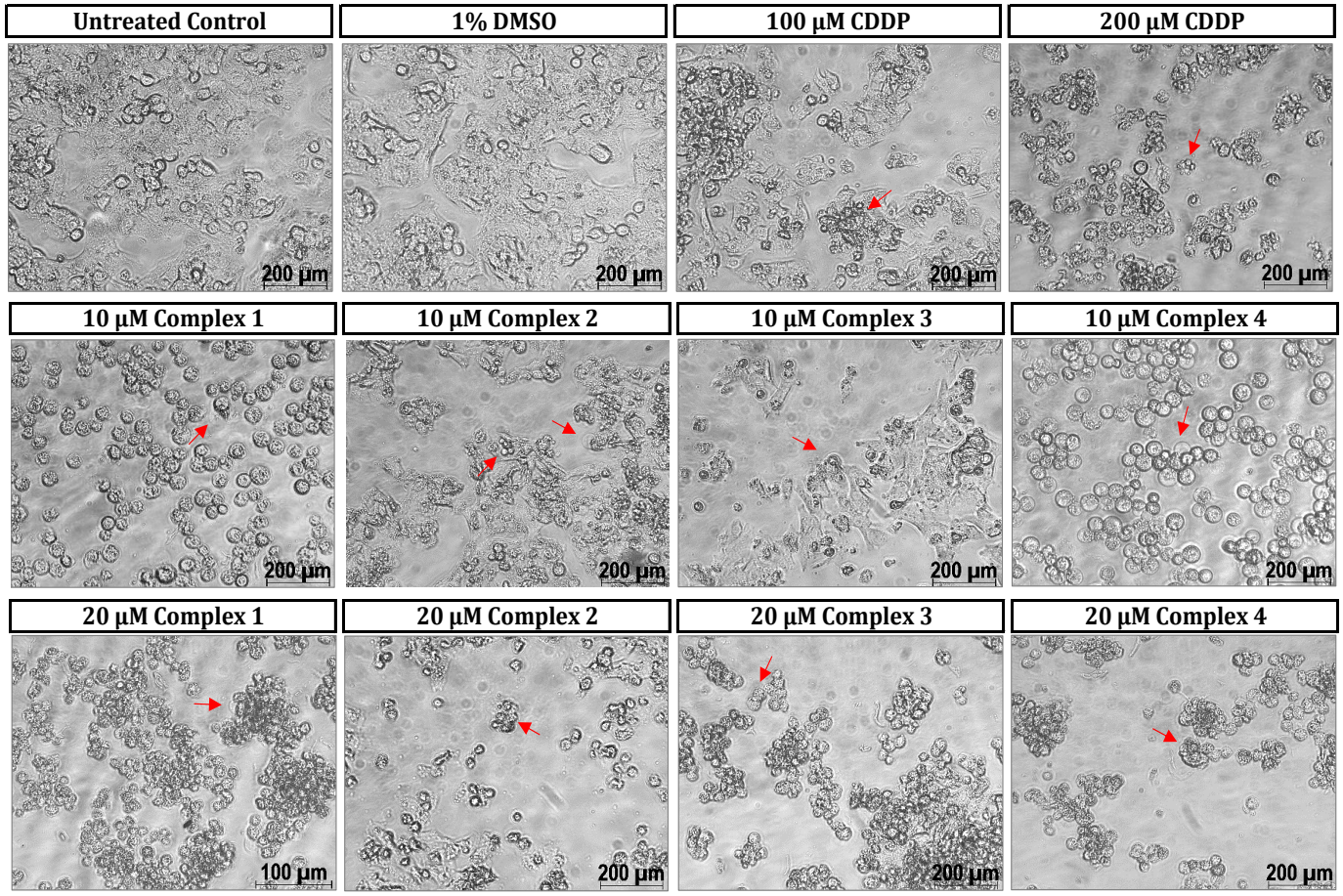


Figure 3.2. Morphological changes of malignant **HEP-G2** cells induced by differential treatments after 24 h. The following treatments were added to the cells: no treatment or treated with 1% DMSO, 100 µM and 200 µM CDDP; 10 µM and 20 µM silver(I) phosphine complexes **1 - 4,** respectively. Control-treated cells show typical, healthy HEP-G2 cells. Following 24 h incubation, CDDP-treated cells, and respective silver(I) phosphine complexes induced typical morphological changes to cells diagnostic of apoptosis such as condensation, rounding and apoptotic blebbing and bodies (indicated by the red arrow). Light micrographs were captured with a Zeiss Axiovert 25 inverted light microscope and Axio Vision 3.1 software at 200 x magnification.

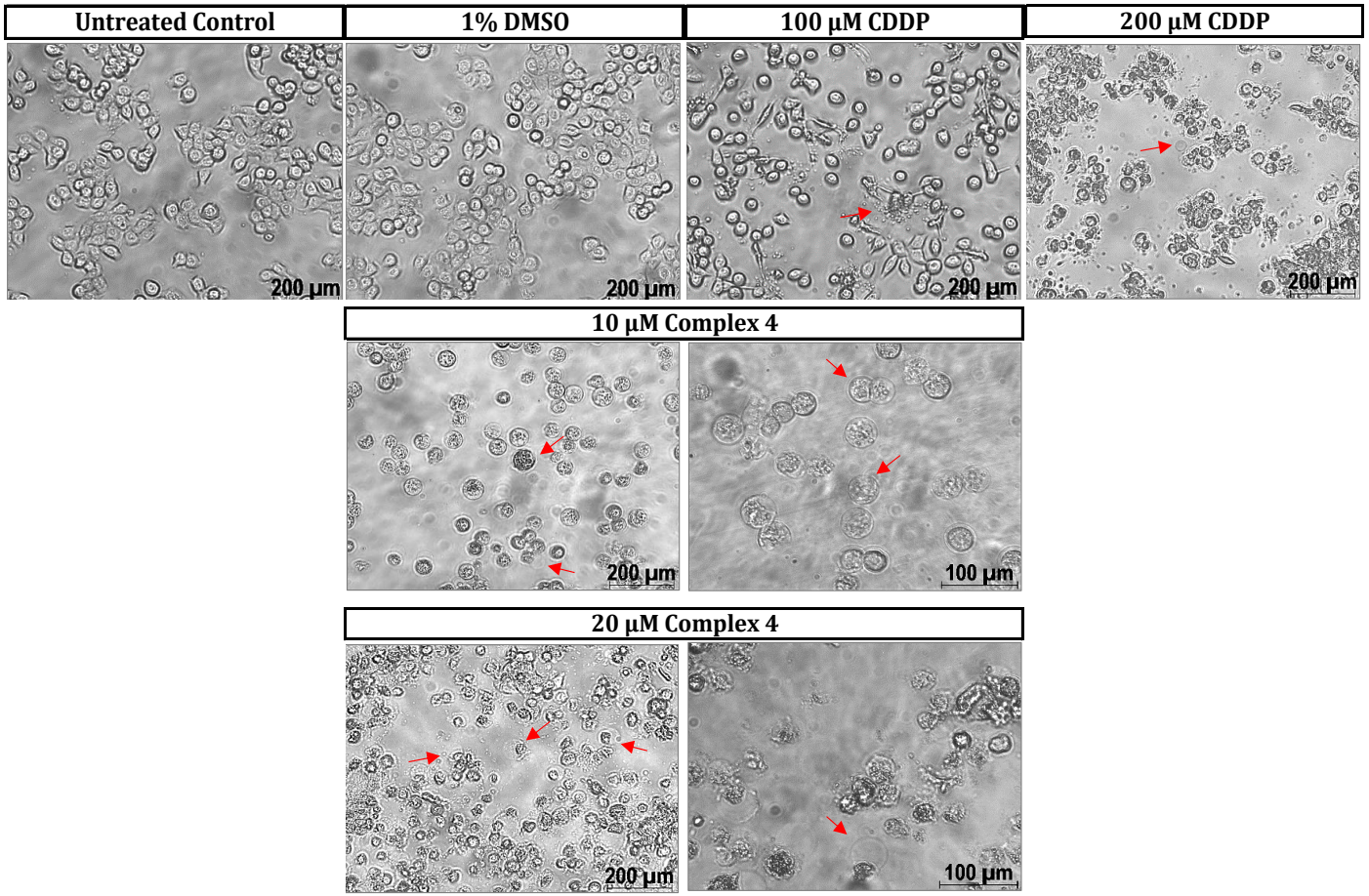


Figure 3.3. Morphological changes of malignant **HT-29** cells induced by differential treatments after 24 h. The following treatments were added to the cells: no treatment or treated with 1% DMSO, 100 µM and 200 µM CDDP; and 10 µM and 20 µM of silver(I) phosphine complex **4,** respectively. Control-treated cells show healthy HT-29 cells. After 24 h, CDDP-treated cells and complex **4** induced typical morphological changes to cells diagnostic of apoptosis such as condensation, rounding and apoptotic blebbing and bodies (indicated by the red arrow). Light micrographs were captured with a Zeiss Axiovert 25 inverted light microscope and Axio Vision 3.1 software at either 200 x and/or 400 x magnification where cellular rounding (10 µM) and apoptotic blebbing (20 µM) can be seen clearly.

In the A549 cells and HT-29 cells, an increase in GAPDH activity was observed. However, only significant increases were induced by complexes **2**, **3**, **6**, **7** ($P < 0.01$) and **4** ($P < 0.05$) in the A549 cells. Complex **7** resulted in the highest GAPDH activity of 3.15 units, closely followed by complexes **6** (2.97), **3** (2.96), **2** (2.91) and **4** (2.79) (**Figure 3.4-A**). Complex **4** induced a significant ($P < 0.05$) increase (relative activity of 2.49 units) in the HT-29 cells, comparable to the positive GAPDH activity control (relative activity of 2.61 units) (**Figure 3.4-C**). The opposite was shown in the complex treated HEP-G2 cells, as the complexes did not cause a significant increase in GAPDH function after 24 h of treatment (**Figure 3.4-B**). Complexes **3** and **4** showed a slight decrease (although insignificant) in GAPDH activity, with relative units of only 0.51 and 0.52, respectively. Interestingly, CDDP resulted in different GAPDH activities in each respective cell line. The most activity was observed in the A549 cells (2.12), followed by the HT-29 cells (1.45), and lastly the HEP-G2 cells (0.70).

After 24 h of treatment with selected complexes, all three cell lines exhibited significant decreases in ATP levels and cellular viability (**Figure 3.5**). Complexes **1** and **2**, both synthesized with AgSCN salt resulted in ATP levels that had significantly ($P < 0.001$) declined as low as 1.36% and 0.93% in A549 cells and 1.85% and 0.69% in HEP-G2 cells, respectively. Complex **2** appeared to be the most cytotoxic to the A549 cells with the lowest ATP level and cellular viability of 3.85% (**Figure 3.5-A**). Complex **3** appeared to be the most cytotoxic to the HEP-G2 cells, with the lowest ATP levels of 0.60% and cellular viability of 13.63%, with complex **2** closely following with only a 0.69% ATP levels and 14.89% viability (**Figure 3.5-B**). In HT-29 cells, complex **4** significantly ($P < 0.001$) decreased the amount of ATP to 20.99%, and viability to 35.11%; while CDDP significantly ($P < 0.01$) decreased ATP levels to 60.15%, cellular viability did not significantly decrease (81.06%). Compared to the A549 and HEP-G2 cells, complex **4** is significantly less cytotoxic to HT-29 cells (**Figure 3.5-C**), but more cytotoxic than CDDP.

Complexes were arranged from most to least cytotoxic for A549 and HEP-G2 cells and were the following, respectively. CDDP was included for comparison purposes and shows silver(I) phosphine complexes were more effective. For A549, although values lie in close proximity to each other, they are as follows: complex **2** (mentioned above), **1** (ATP 1.36%, viability 15.96%), **3** (ATP 5.84%, viability 50.77%), **7** (ATP 12.90%, viability 21.59%), **4** (ATP 14.52%, viability 28.45%), **6** (ATP 15.08%, viability 28.37%) and CDDP (ATP 60.35%, viability 58.21%). For HEP-G2, complex **3**, **2** (mentioned above), **1** (ATP 1.85%, viability 13.93%), **4** (ATP 3.26%, viability 14.67%), and CDDP (ATP 19.62%, viability 54.94%). The decrease in intracellular ATP levels indicates silver(I) phosphine complexes hinder the mitochondria and its associated ATP production mechanism.

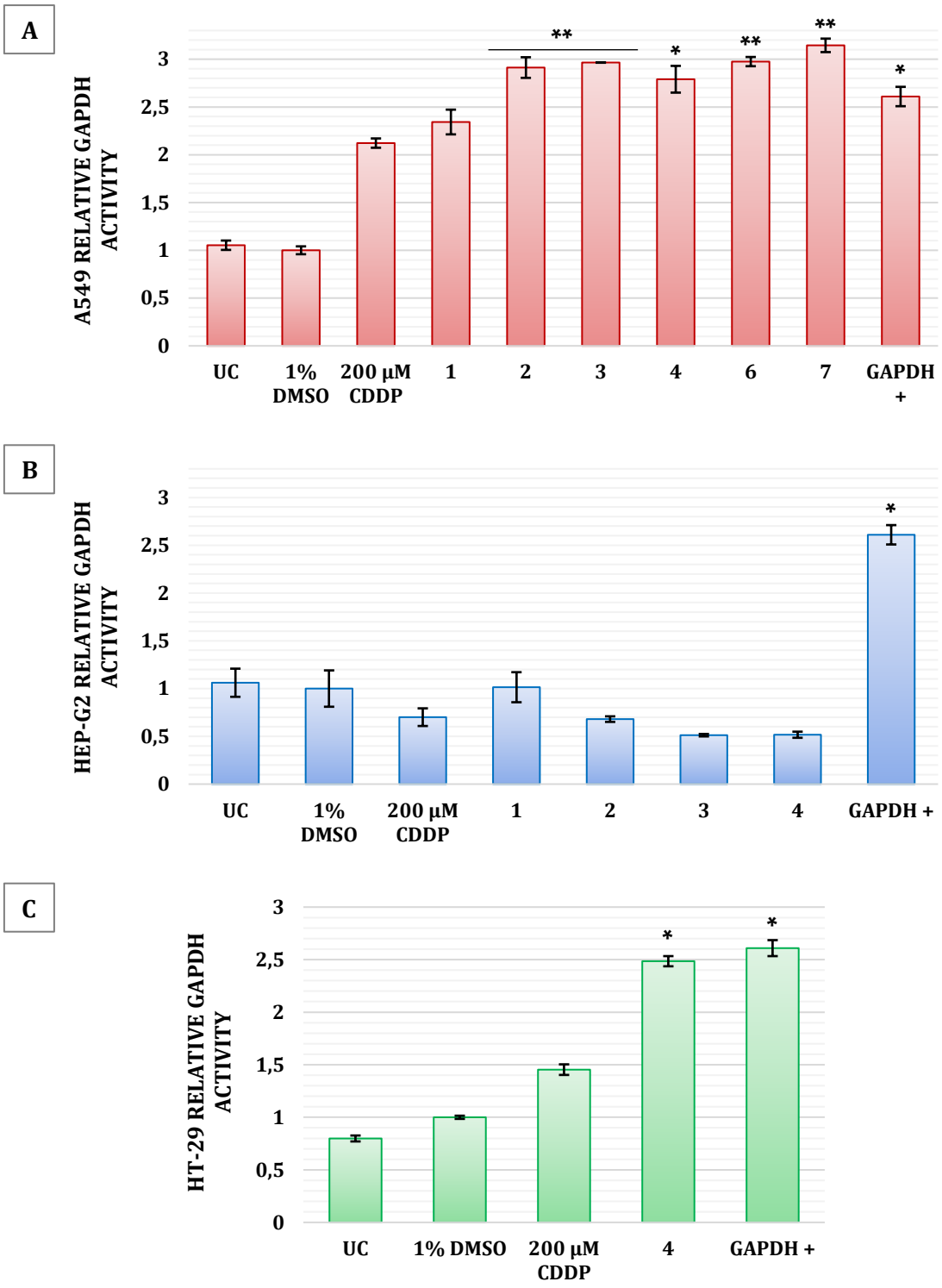


Figure 3.4. GAPDH activity in malignant **(A)** **A549**, **(B)** **HEP-G2** and **(C)** **HT-29** cells determined by a KDalert™ GAPDH assay. Cells were treated as follows: not treated (untreated control) or treated with 1% DMSO (vehicle control), 20 µM of complexes **1 - 4**, **6** and **7**, or 200 µM CDDP (positive apoptotic control) for 24 h. Percentages were expressed in relation to 1% DMSO (100%, 1 relative unit). A positive GAPDH activity control (GAPDH⁺) was included for comparison. The ± SEM (n = 6) were represented as error bars and using a two-tail Student's t-test, P values were calculated. Significant differences are denoted by asterisks (* $P < 0.05$; ** $P < 0.01$ and *** $P < 0.001$).

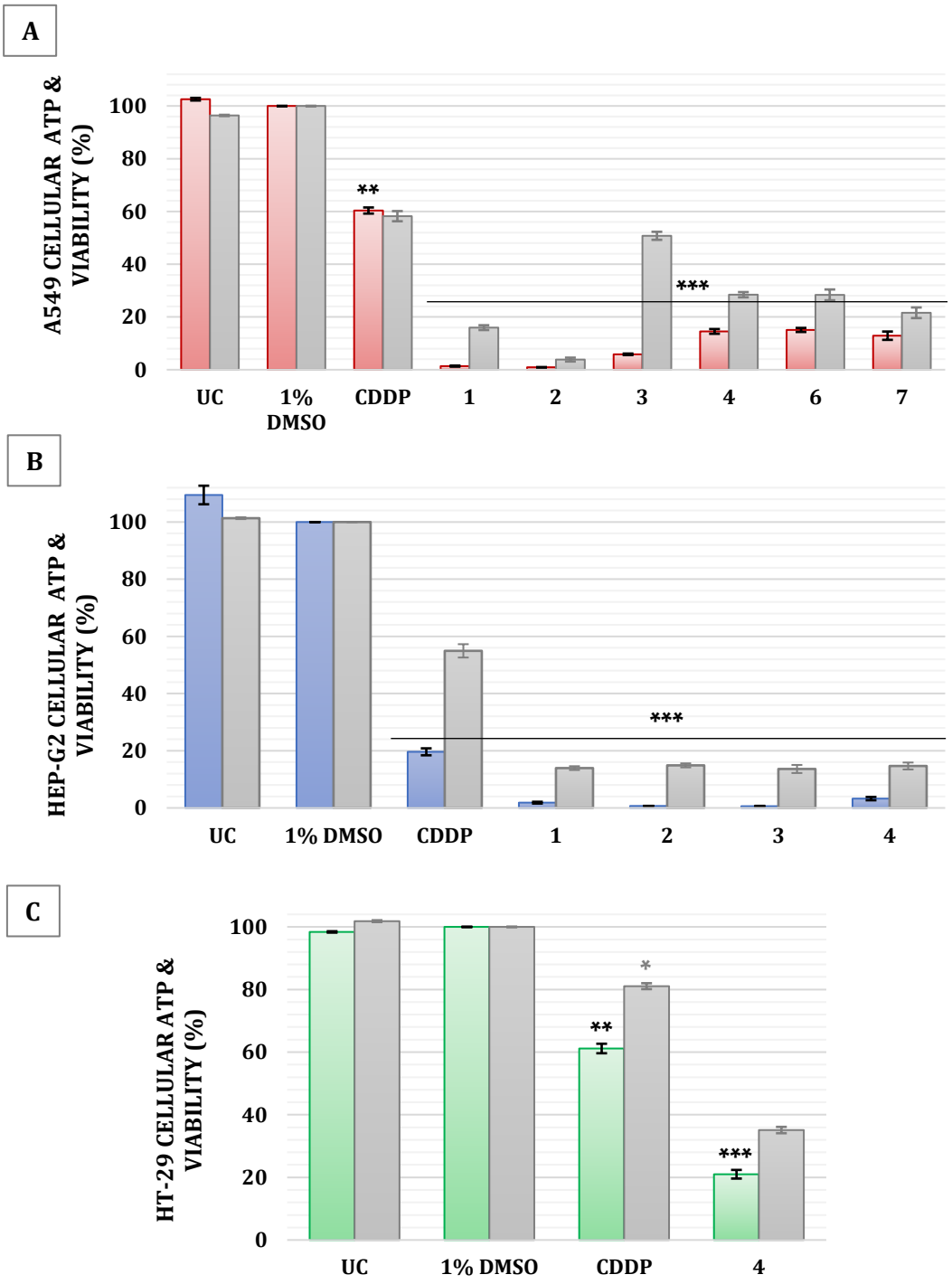
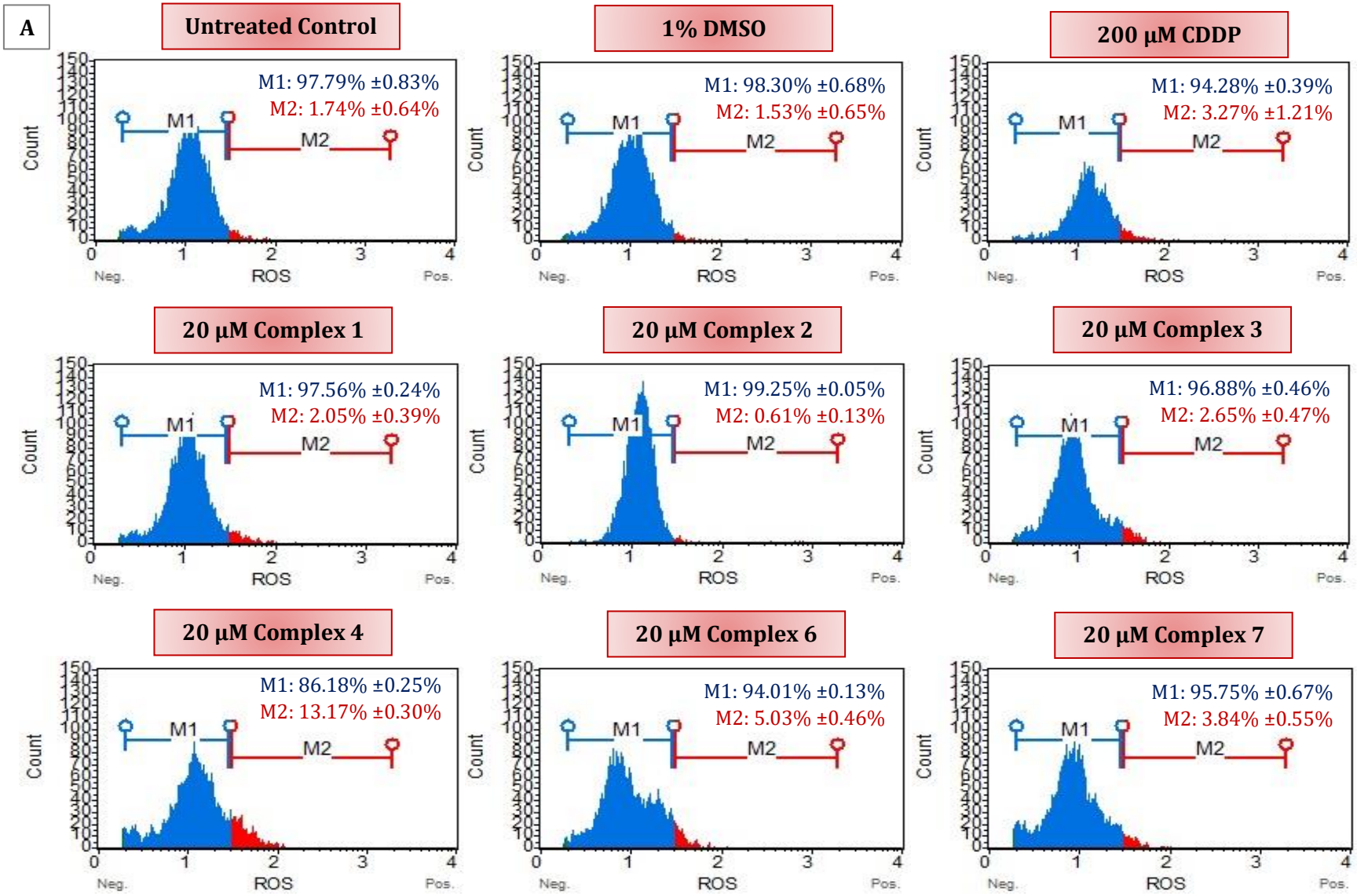


Figure 3.5. The percentage cellular ATP (*coloured bar graph*) and viability (*grey bar graph*) in malignant **(A)** **A549** **(B)** **HEP-G2** and **(C)** **HT-29** cells measured by the CellTiter-Glo® assay and alamarBlue® proliferation assay, respectively. Cells were treated as follows: either not treated (untreated control) or treated with 1% DMSO (vehicle control), 20 µM (ATP) or 10 µM (viability) of complexes **1 - 4**, **6** and **7**, or 200 µM (ATP) or 100 µM (viability) CDDP (positive apoptotic control) for 24 h. Percentages were expressed in relation to 1% DMSO (100%). The ± SEM (n = 6) were represented as error bars and using a two-tail Student's t-test, P values were calculated. Significant differences are denoted by asterisks (* P < 0.05; ** P < 0.01 and *** P < 0.001). If the significant differences were the same between assays they were represented in *black*, while *grey* asterisks indicate a different significance in cellular viability.

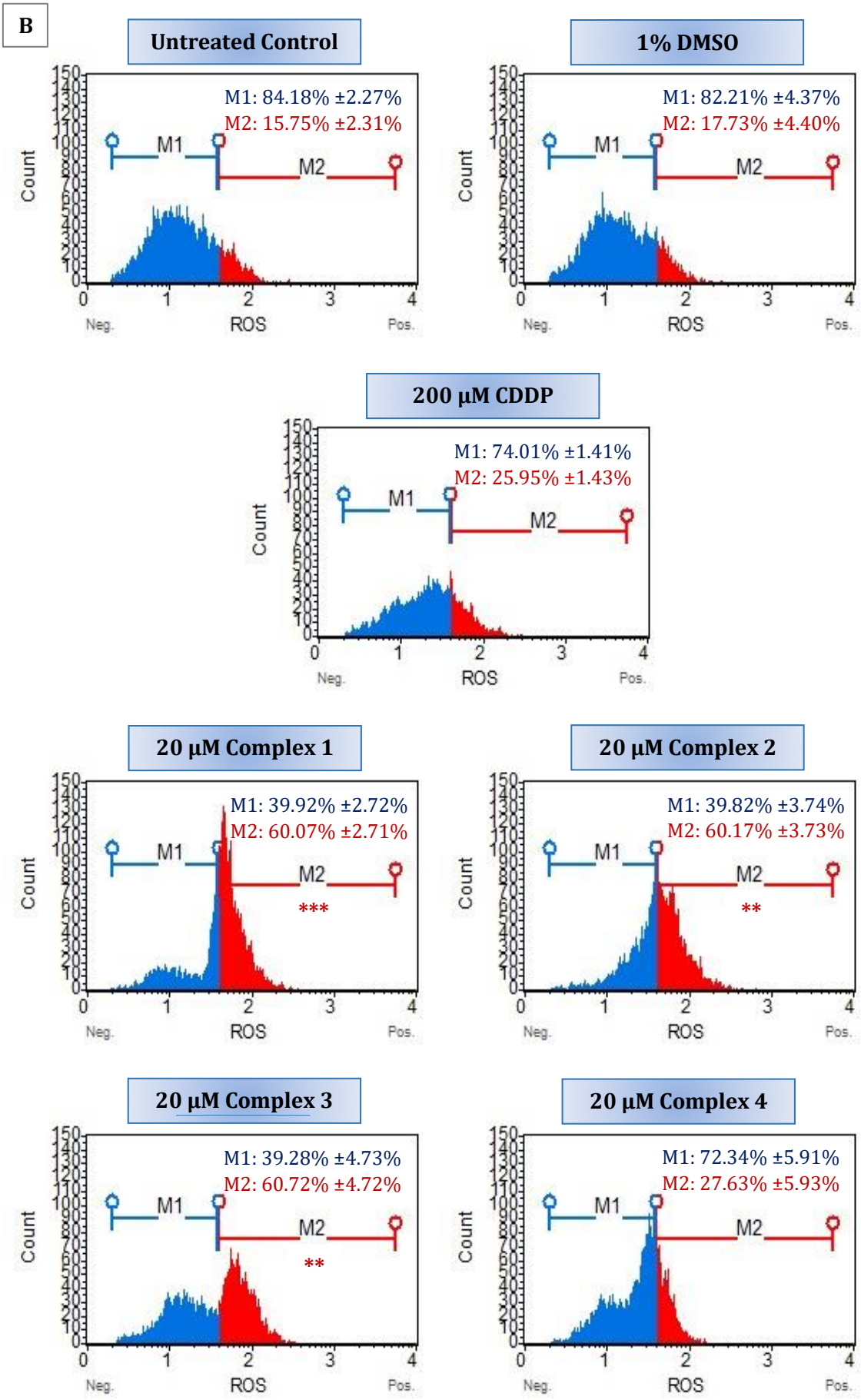
3.3.3. Production of reactive oxygen species

As by-products of metabolic processes within the cell, reactive oxygen species (ROS) are produced. Malignant cells have increased metabolic activity and mitochondrial malfunction. This results in elevated levels of ROS in cancer cells relative to normal, untransformed cells. When there is an excessive amount of ROS and antioxidant defense mechanisms fail to maintain redox homeostasis, oxidative stress occurs (Manda *et al.*, 2009; Ray *et al.*, 2013; Reczek and Chandel, 2017). To determine whether the selected complexes induced ROS in the A549, HEP-G2 and HT-29 cell lines, intracellular superoxide anions were quantified in cell populations undergoing oxidative stress using the Muse® Oxidative Stress kit. The kit makes use of a cell-permeable probe, dihydroethidium (DHE), which is oxidized to ethidium bromide by superoxide anions. This results in a red fluorescence that is proportional to the total amount of superoxide within the cell (Lou *et al.*, 2002). Two populations were differentiated as ROS negative ($^-$) (M1 marker) or ROS positive ($^+$) (M2 marker) (Al-Asmari *et al.*, 2017). The A549, HEP-G2 and HT-29 cells were analyzed for ROS production 24 h after treatment, and the data obtained were represented as histograms (**Figure 3.6**).

Complexes **1 - 4**, **6** and **7** did not significantly increase ROS activity in A549 cells when compared to DMSO (**Figure 3.6-A**). The number of ROS^+ cells remained below 6% for complexes **1**, **2**, **3**, **6** and **7**, with complex **4** resulting in a slightly, yet insignificant shift of 13.17% ROS^+ cells. The opposite observations were made for the HEP-G2 and HT-29 cells. Complexes **1** ($P < 0.001$), **2** and **3** ($P < 0.01$) significantly increased the number of ROS^+ HEP-G2 cells in comparison to DMSO and the untreated cells. However, complex **4**, did not significantly increase ROS activity in the HEP-G2 cell, although there was a slight shift in the population that resulted in 27.63% of ROS^+ cells. Complex **3** induced the highest number of ROS^+ cells, with 60.72% of the cell population undergoing oxidative stress, closely followed by complexes **2** (60.17%), and **1** (60.07%) (**Figure 3.6-B**). Interestingly, complex **4** increased the quantity of ROS activity in HT-29 cells significantly ($P < 0.001$), with half the population being ROS^+ (53.88%) (**Figure 3.6-C**). CDDP did not result in a significant amount of ROS^+ A549, HEP-G2 and HT-29 cells.


A
Untreated Control
M1: 97.79% ±0.83%
M2: 1.74% ±0.64%
1% DMSO
M1: 98.30% ±0.68%
M2: 1.53% ±0.65%
200 µM CDDP
M1: 94.28% ±0.39%
M2: 3.27% ±1.21%
20 µM Complex 1
M1: 97.56% ±0.24%
M2: 2.05% ±0.39%
20 µM Complex 2
M1: 99.25% ±0.05%
M2: 0.61% ±0.13%
20 µM Complex 3
M1: 96.88% ±0.46%
M2: 2.65% ±0.47%
20 µM Complex 4
M1: 86.18% ±0.25%
M2: 13.17% ±0.30%
20 µM Complex 6
M1: 94.01% ±0.13%
M2: 5.03% ±0.46%
20 µM Complex 7
M1: 95.75% ±0.67%
M2: 3.84% ±0.55%
Count
ROS
Neg.
Pos.

B


Untreated Control
M1: 84.18% ±2.27%
M2: 15.75% ±2.31%
1% DMSO
M1: 82.21% ±4.37%
M2: 17.73% ±4.40%
200 µM CDDP
M1: 74.01% ±1.41%
M2: 25.95% ±1.43%
20 µM Complex 1
M1: 39.92% ±2.72%
M2: 60.07% ±2.71%
***
20 µM Complex 2
M1: 39.82% ±3.74%
M2: 60.17% ±3.73%
**
20 µM Complex 3
M1: 39.28% ±4.73%
M2: 60.72% ±4.72%
**
20 µM Complex 4
M1: 72.34% ±5.91%
M2: 27.63% ±5.93%
Count
ROS
Neg.
Pos.
M1
M2

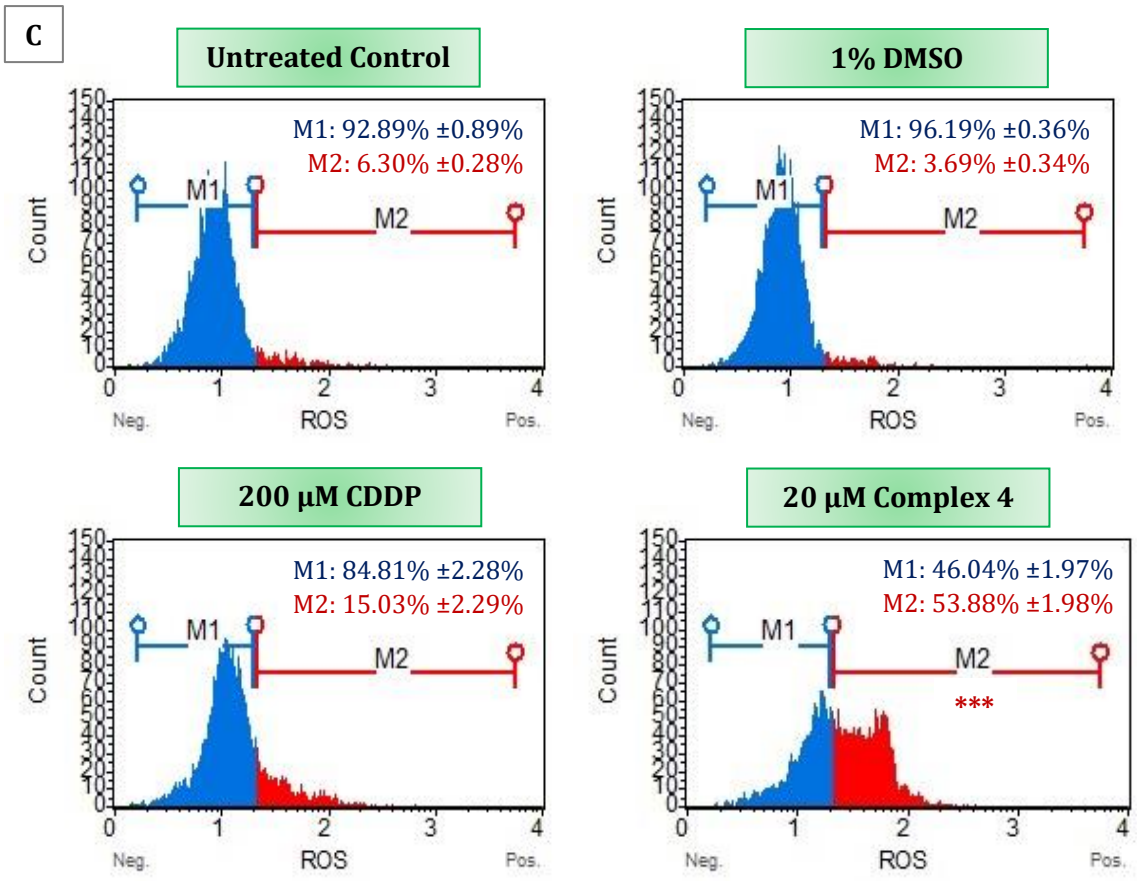


Figure 3.6. The detection of the total amount of ROS in malignant **(A) A549 (B) HEP-G2** and **(C) HT-29** cells was quantified using a Muse® Oxidative Stress kit. The following treatments were an untreated control or treated with 1% DMSO (vehicle control), 200 µM CDDP (positive apoptotic control) or 20 µM of selected complexes **1 - 4**, **6** and **7** (respective to the specific cell line) for 24 h. ROS negative (M1, blue) or ROS positive (M2, red) populations are shown by their respective percentages. Averaged percentage values and the ± SEM (n = 3) are represented within each histogram. Significant differences are denoted by asterisks among complex treatments and 1% DMSO for ROS-positive activity (* $P < 0.05$; ** $P < 0.01$ and *** $P < 0.001$).

3.3.4. Mechanism of action

To determine whether the mitochondria of malignant cells are affected by the silver(I) phosphine complexes, differentially treated A549, HEP-G2 and HT-29 cell populations using the Muse® MitoPotential assay and the Muse® Annexin V and Dead Cell assay, were quantitatively measured. These flow cytometric assays target important key points in a dying cell, the mitochondrial potential, cellular plasma permeabilization, and the mode of cell death.

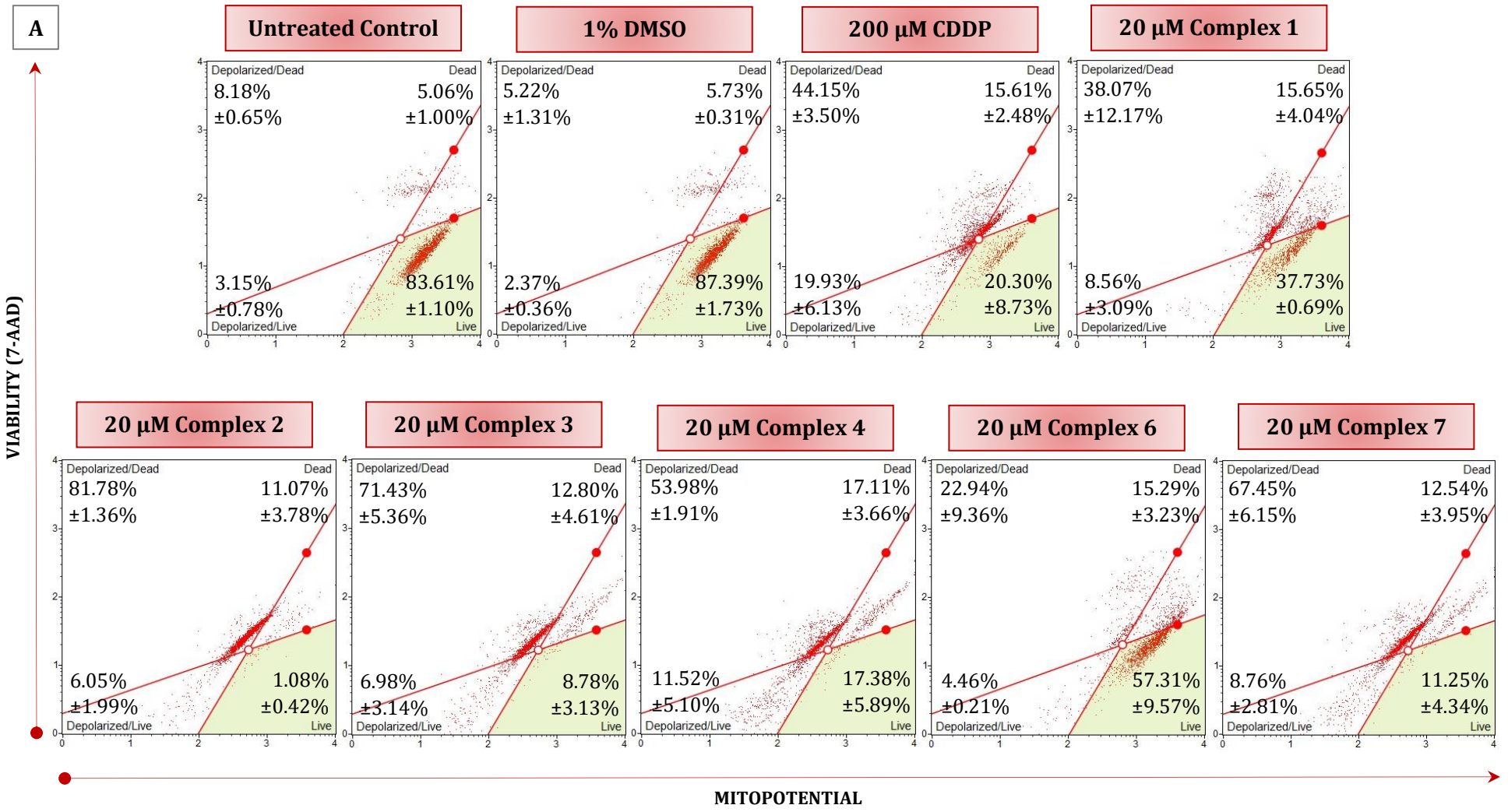
The Muse® MitoPotential makes use of two dyes simultaneously. A cationic, lipophilic mitopotential dye that detects changes in the ΔΨm. This dye will accumulate if the inner membrane is intact, resulting in high fluorescence (live cells), while an upward shift of the cell population indicates a depolarized live/dead mitochondria and the loss of trans-membrane potential. 7-aminoactinomycin D (7-AAD) is a fluorescent dye that integrates into double-stranded DNA when membrane integrity is compromised or when cell membranes are permeable. This is an indicator of late apoptosis or necrosis, as 7-AAD is excluded from live, healthy cells (Yu *et al.,* 2022).

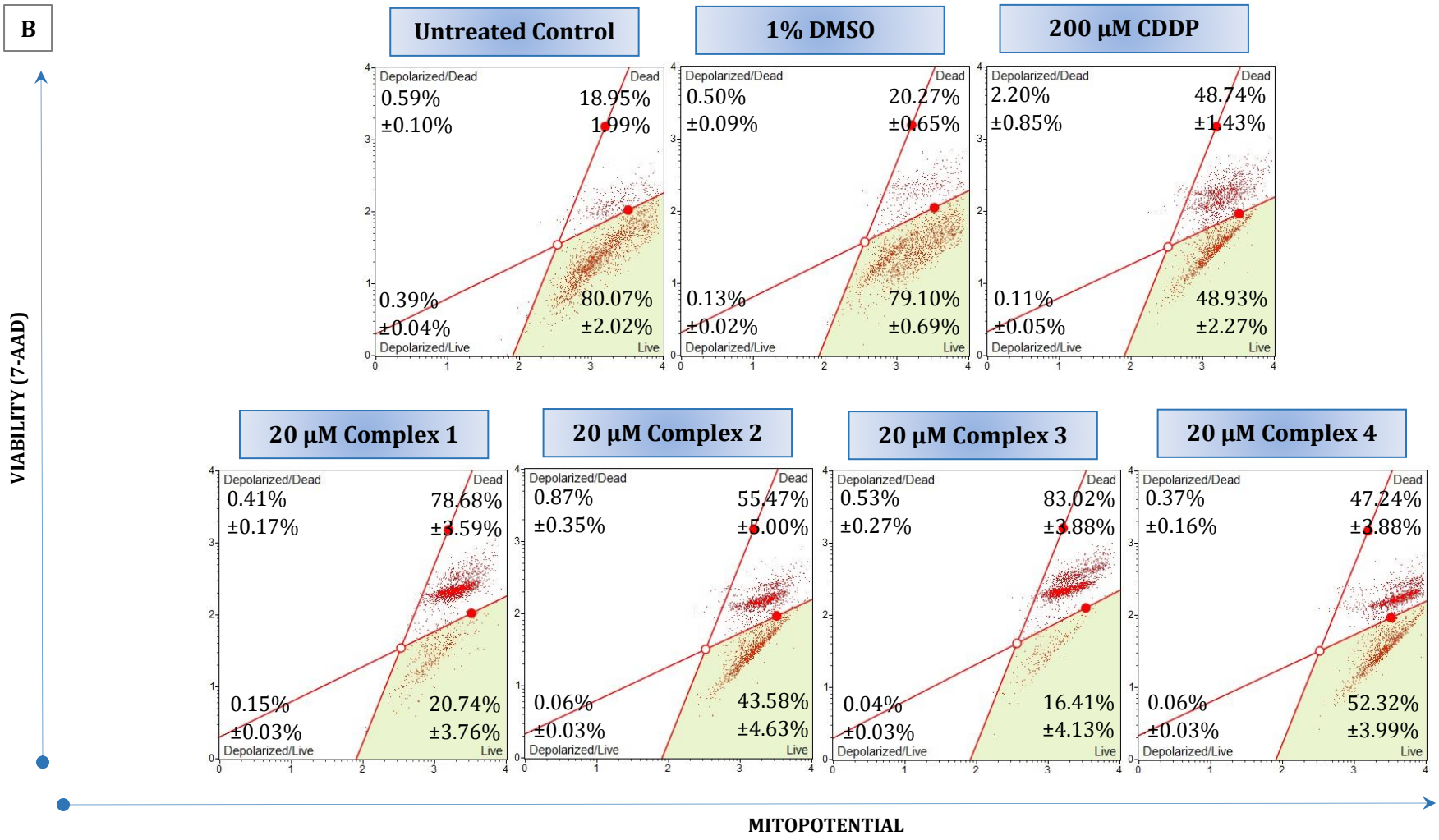
Significant increases in the number of total depolarized/dead A549 cells were observed with 20 µM of complexes **2** (87.78%; $P < 0.01$), **3** (71.43%), **4** (53.98%) and **7** (67.45%; $P < 0.05$) in contrast to DMSO and control cells without treatment. The structural integrity of these cells was damaged by a depolarized mitochondrial membrane. The cell population shifted into the upper quadrant (**Figure 3.7-A**), while for complex **6**, 57.31% of the population remained viable, followed by complex **1** (37.73% live cells). When compared to CDDP, a total of 44.15% of the A549 cells were depolarized/dead and only 20.30% of the population remained viable. A loss of ΔΨm was only observed in the A549 CDDP-treated cells. HEP-G2 and HT-29 CDDP-treated cells revealed populations of 48.74% live and 47.74% dead cells, and 62.79% live and 31.89% depolarized live cells, respectively for each cell line (**Figures 3.7-B** and **3.7-C**). Interestingly, significant increases in the number of dead HEP-G2 cells (damaged structural integrity) and not depolarized cells were observed after treatment with 20 µM of complexes **1** (78.68%), **3** (83.02%; $P < 0.001$) and **2** (55.47%; $P < 0.05$), in contrast to the control-treated cells. HT-29 cells treated with complex **4** caused significant shifts into the depolarized/live (36.99%, $P < 0.05$) and depolarized/dead (46.48%, $P < 0.05$) quadrants in contrast to the untreated (90.06% live) cells and DMSO (91.61% live) cells (**Figure 3.7-C**).

The Muse® Annexin V and Dead Cell assay's 7-AAD dye and Annexin V were used to determine the extent of apoptosis induction and confirm the mode of cell death herein. Ptd-L-Ser is translocated and exposed to the outer cell surface during the initial stages of apoptosis, whereby the Ca^{2+}-dependent phospholipid-binding protein, Annexin V binds to Ptd-L-Ser (Vermes *et al.,* 1995). The

7-AAD dye confirmed the integrity of the cell membrane, an indicator of late apoptosis or necrosis (Yu *et al.*, 2022).

Ptd-L-Ser externalization was present in A549 (**Figure 3.8-A**), HEP-G2 (**Figure 3.8-B**) and HT-29 cells (**Figure 3.8-C**) treated with 20 µM of selected complexes after 24 h. Comparative controls for apoptosis (200 µM CDDP) and necrosis (50 % H_2O_2) were included. Significant ($P < 0.001$) differences in the number of late apoptotic/dead cells were observed in A549 cells treated with complexes **1** (90.35%), **2** (90.23%), **3** (81.18%), **4** (60.37%), **6** (63.05%) and **7** (63.45%) when compared to a live population of 88.19% DMSO-treated cells. Similarly, late apoptotic/dead populations were seen once more in HEP-G2 and HT-29 cells treated with complexes **1** (44.27%; $P < 0.05$), **2** (42.15%; $P < 0.05$), **3** (62.69%; $P < 0.01$) and **4** (61.61%, $P < 0.001$ and 75.73%, $P < 0.001$; respective to each cell line). These populations were significant in contrast to the control-treated cells. Due to higher treatments of 20 µM and a longer time study of 24 h, there were no significant numbers of cells observed undergoing early apoptosis (< 3%). The largest proportion of A549 cells undergoing late apoptosis was caused by complexes **1** and **2**, these complexes were also the most cytotoxic (**Figure 3.5-A**). Whereas complexes **3** and **4** resulted in larger late apoptotic populations in the HEP-G2 cells, with complex **3** being the most cytotoxic (**Figure 3.5-B**). In each of the three cell lines treated with their selected complexes, the proportion of apoptotic cells was higher than in cells treated with CDDP. Insignificant populations of late apoptosis were observed in A549 (19.54%), HEP-G2 (36.23%), and HT-29 (13.6%) cells relative to the vehicle control cells. Most of the cell population remained viable, with a remaining live population of 77.88% HT-29 cells. Cells treated with 50% H_2O_2 resulted in expected necrotic populations of 61.33% (A549) and 83.50% (HEP-G2) respectively. Dissimilarly, HT-29 cells treated with 50% H_2O_2 were 94.79% late apoptotic cells and not necrotic. CDDP was also unsuccessful in eliciting an apoptotic response. This and the finding that only complex **4** was successful as an antiproliferative agent stress the difficulty and resistance of colon cancer treatment. Notably, all complexes tested on the respective cells lines (A549, HEP-G2 and HT-29), significantly increased late apoptotic/dead cell populations after 24 h.


A
Untreated Control
1% DMSO
200 µM CDDP
20 µM Complex 1
20 µM Complex 2
20 µM Complex 3
20 µM Complex 4
20 µM Complex 6
20 µM Complex 7
Depolarized/Dead
Dead
Depolarized/Live
Live
8.18% ±0.65%
5.06% ±1.00%
3.15% ±0.78%
83.61% ±1.10%
5.22% ±1.31%
5.73% ±0.31%
2.37% ±0.36%
87.39% ±1.73%
44.15% ±3.50%
15.61% ±2.48%
19.93% ±6.13%
20.30% ±8.73%
38.07% ±12.17%
15.65% ±4.04%
8.56% ±3.09%
37.73% ±0.69%
81.78% ±1.36%
11.07% ±3.78%
6.05% ±1.99%
1.08% ±0.42%
71.43% ±5.36%
12.80% ±4.61%
6.98% ±3.14%
8.78% ±3.13%
53.98% ±1.91%
17.11% ±3.66%
11.52% ±5.10%
17.38% ±5.89%
22.94% ±9.36%
15.29% ±3.23%
4.46% ±0.21%
57.31% ±9.57%
67.45% ±6.15%
12.54% ±3.95%
8.76% ±2.81%
11.25% ±4.34%
VIABILITY (7-AAD)
MITOPOTENTIAL


B
Untreated Control
1% DMSO
200 µM CDDP
20 µM Complex 1
20 µM Complex 2
20 µM Complex 3
20 µM Complex 4
Depolarized/Dead
Dead
Depolarized/Live
Live
0.59% ±0.10%
18.95% ±1.99%
0.39% ±0.04%
80.07% ±2.02%
0.50% ±0.09%
20.27% ±0.65%
0.13% ±0.02%
79.10% ±0.69%
2.20% ±0.85%
48.74% ±1.43%
0.11% ±0.05%
48.93% ±2.27%
0.41% ±0.17%
78.68% ±3.59%
0.15% ±0.03%
20.74% ±3.76%
0.87% ±0.35%
55.47% ±5.00%
0.06% ±0.03%
43.58% ±4.63%
0.53% ±0.27%
83.02% ±3.88%
0.04% ±0.03%
16.41% ±4.13%
0.37% ±0.16%
47.24% ±3.88%
0.06% ±0.03%
52.32% ±3.99%
VIABILITY (7-AAD)
MITOPOTENTIAL

C

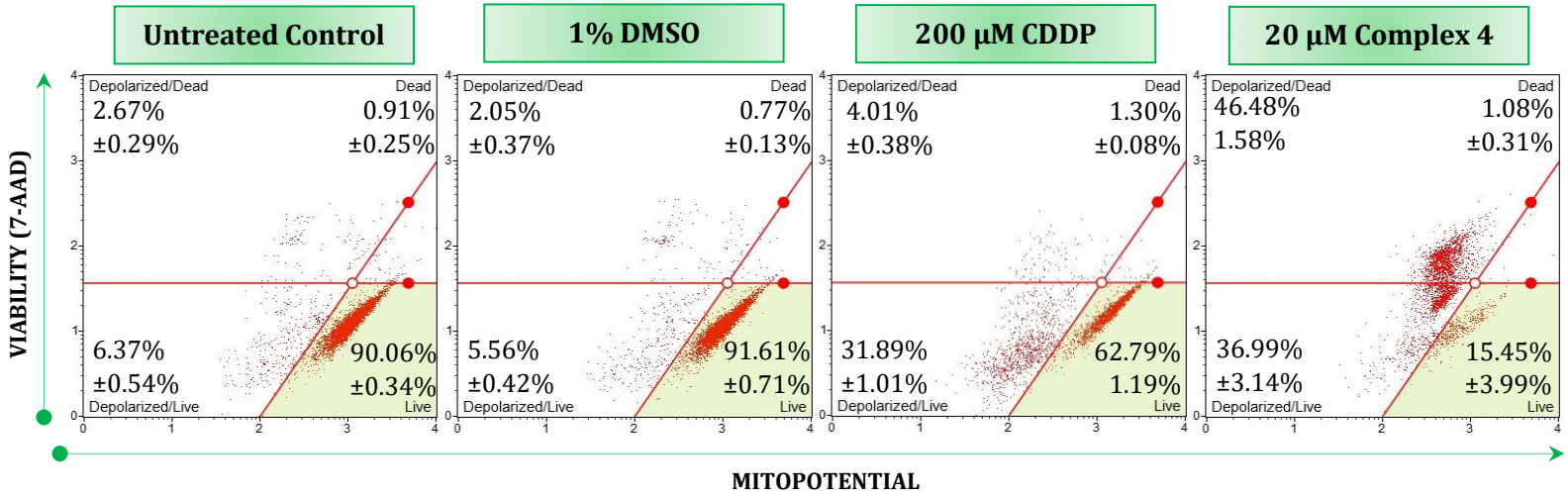
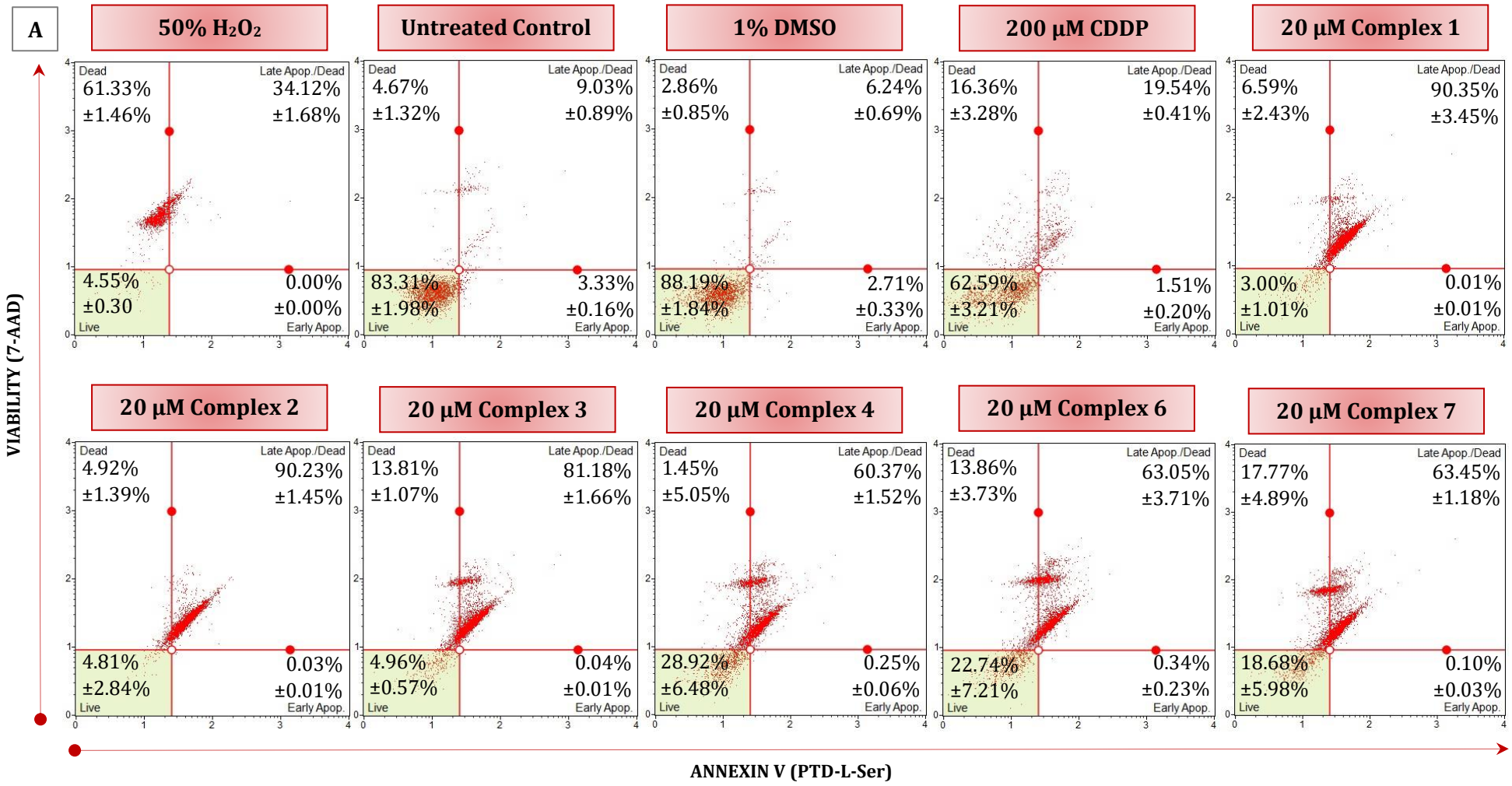
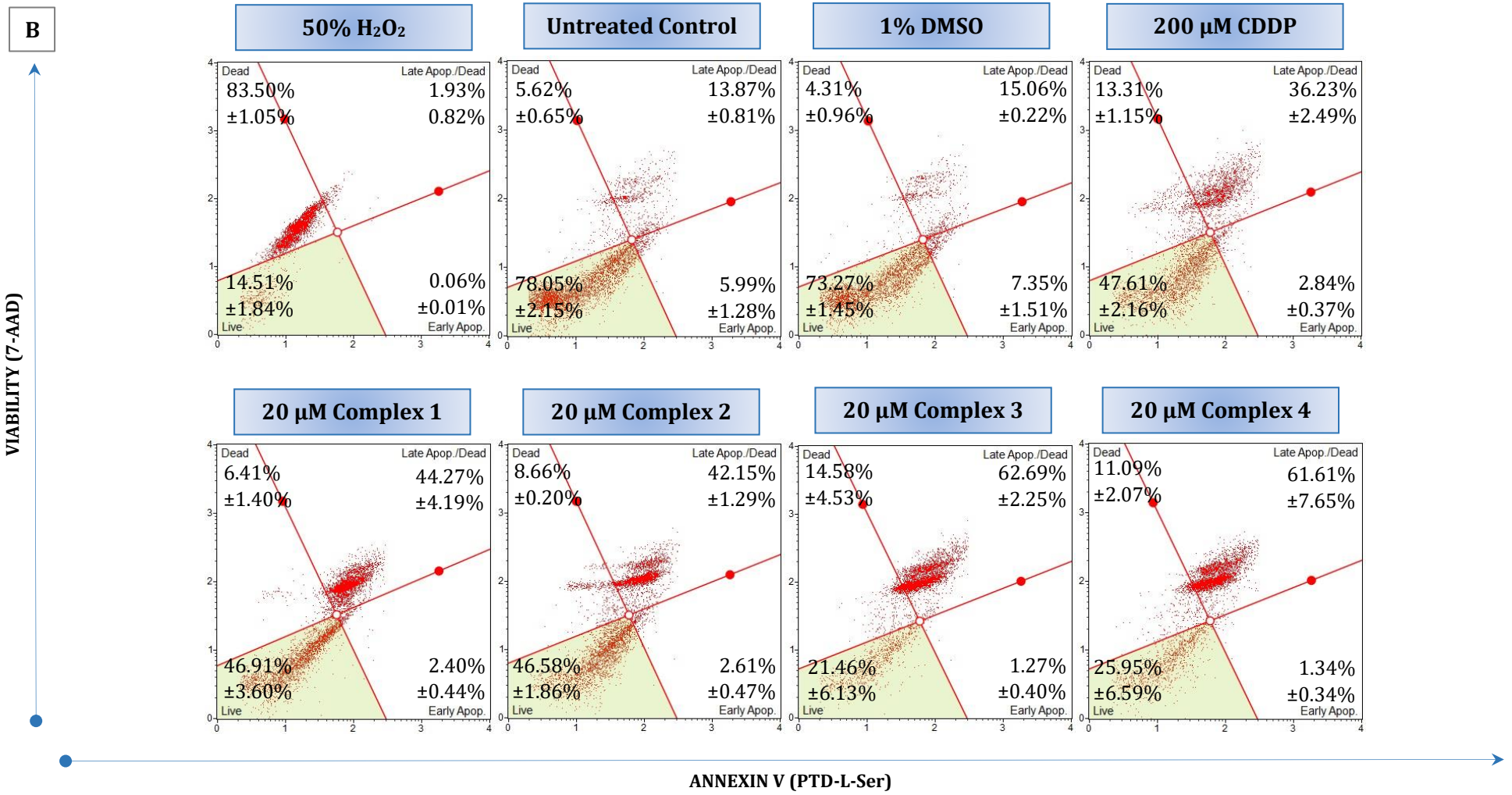


Figure 3.7. Mitochondrial potential and cellular plasma permeabilization were quantified in malignant **(A)** **A549**, **(B)** **HEP-G2** and **(C)** **HT-29** cells using a Muse® MitoPotential kit. The following treatments were an untreated control or treated with 1% DMSO (vehicle control), 200 µM CDDP (positive apoptotic control) or 20 µM of selected complexes **1** - **4**, **6** and **7** (respective to the specific cell line) for 24 h. Averaged percentages were calculated and are shown within the dot plots followed by the ± SEM (*n* = 6). Co-detection of MitoPotential dye and 7-AAD indicate an intact mitochondrion and cell death, respectively. Cells in the *live* quadrant (bottom right) are viable and have an intact mitochondrial membrane. These cells are negative for MitoPotential dye and 7-AAD. Cells in the *depolarized/live quadrant* (bottom left) are positive for MitoPotential dye only, indicating a depolarized mitochondrial membrane. The *depolarized/dead quadrant* (top right) represents cells that are positive for MitoPotential dye and 7-AAD, the structural integrity of these cells are damaged with a depolarized mitochondrial membrane. The *dead quadrant* (top right) represents dead cells with intact mitochondrial membranes that are 7-AAD positive.


A
50% H2O2
Untreated Control
1% DMSO
200 µM CDDP
20 µM Complex 1
20 µM Complex 2
20 µM Complex 3
20 µM Complex 4
20 µM Complex 6
20 µM Complex 7
Dead
Late Apop./Dead
61.33% ±1.46%
34.12% ±1.68%
4.55% ±0.30
Live
0.00% ±0.00%
Early Apop.
4.67% ±1.32%
9.03% ±0.89%
83.31% ±1.98%
3.33% ±0.16%
2.86% ±0.85%
6.24% ±0.69%
88.19% ±1.84%
2.71% ±0.33%
16.36% ±3.28%
19.54% ±0.41%
62.59% ±3.21%
1.51% ±0.20%
6.59% ±2.43%
90.35% ±3.45%
3.00% ±1.01%
0.01% ±0.01%
4.92% ±1.39%
90.23% ±1.45%
4.81% ±2.84%
0.03% ±0.01%
13.81% ±1.07%
81.18% ±1.66%
4.96% ±0.57%
0.04% ±0.01%
1.45% ±5.05%
60.37% ±1.52%
28.92% ±6.48%
0.25% ±0.06%
13.86% ±3.73%
63.05% ±3.71%
22.74% ±7.21%
0.34% ±0.23%
17.77% ±4.89%
63.45% ±1.18%
18.68% ±5.98%
0.10% ±0.03%
VIABILITY (7-AAD)
ANNEXIN V (PTD-L-Ser)


B
50% H2O2
Untreated Control
1% DMSO
200 µM CDDP
20 µM Complex 1
20 µM Complex 2
20 µM Complex 3
20 µM Complex 4
Dead
Late Apop./Dead
Live
Early Apop.
83.50% ±1.05%
1.93% 0.82%
14.51% ±1.84%
0.06% ±0.01%
5.62% ±0.65%
13.87% ±0.81%
78.05% ±2.15%
5.99% ±1.28%
4.31% ±0.96%
15.06% ±0.22%
73.27% ±1.45%
7.35% ±1.51%
13.31% ±1.15%
36.23% ±2.49%
47.61% ±2.16%
2.84% ±0.37%
6.41% ±1.40%
44.27% ±4.19%
46.91% ±3.60%
2.40% ±0.44%
8.66% ±0.20%
42.15% ±1.29%
46.58% ±1.86%
2.61% ±0.47%
14.58% ±4.53%
62.69% ±2.25%
21.46% ±6.13%
1.27% ±0.40%
11.09% ±2.07%
61.61% ±7.65%
25.95% ±6.59%
1.34% ±0.34%
VIABILITY (7-AAD)
ANNEXIN V (PTD-L-Ser)

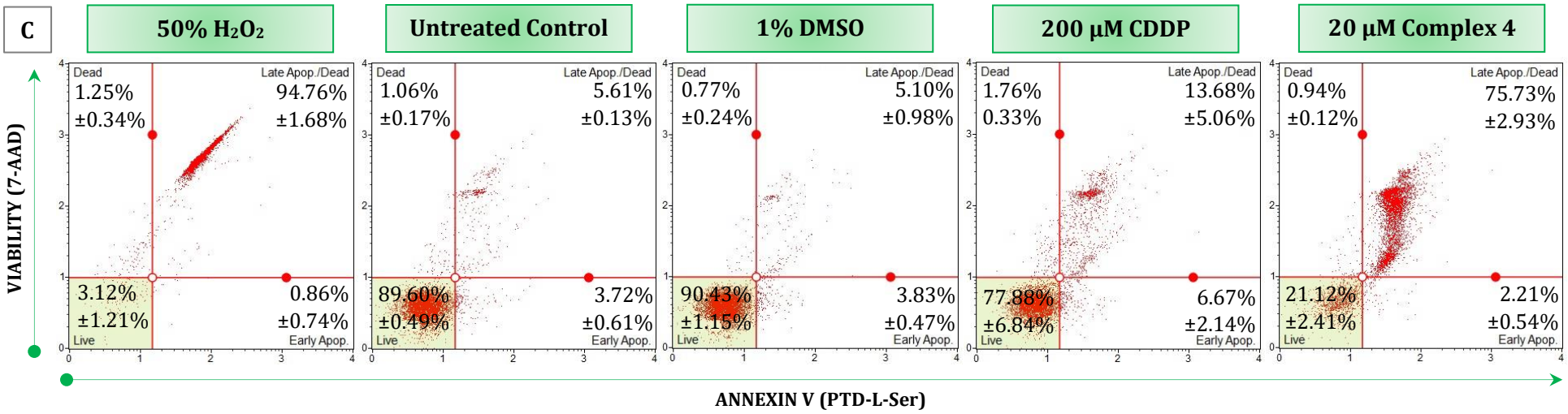


Figure 3.8. The mode of cell death was quantified in malignant **(A)** **A549**, **(B)** **HEP-G2** and **(C)** **HT-29** cells using a Muse® Annexin V & Dead Cell kit. The following treatments were an untreated control or treated with 1% DMSO (vehicle control), 200 µM CDDP (apoptotic control), 50% H_2O_2 (necrotic control) or 20 µM of selected complexes **1 - 4**, **6** and **7** (respective to the specific cell line) for 24 h. Averaged percentages were calculated and are shown within the dot plots followed by the ± SEM (*n* = 6). Annexin V (Ptd-L-Ser) and 7-AAD co-detection indicates apoptosis and/or necrosis, respectively. Cells in the *live* quadrant (bottom left) are viable, non-apoptotic and negative for Annexin V and 7-AAD. Cells in the *early apoptotic quadrant* (bottom right) are positive for Annexin V only, while the *late apoptotic/dead quadrant* (top right) represent Annexin V and 7-AAD positive cells. The *dead quadrant* (top left) represents mostly nuclear debris and are cells positive for 7-AAD only.

3.3.5. CYP450: a possible drug target

A possible target for chemotherapeutic treatment is cytochrome P450 (Bruno and Njar, 2007). Utilizing a Cytochrome P450-GLO^{TM} Assay Kit, the impact of selected complexes on the activity of the CYP1B1 isoform was determined. This assay makes use of luminogenic P450 substrates, which are converted by CYP450 to luciferin. The luminescence produced by the reaction between luciferin and luciferase is directly proportional to the enzyme activity of the CYP1B1 isoform (Cali *et al.*, 2006). The percentages of differential treatments were expressed in relation to the DMSO-treated cells (1 relative unit).

In the A549 cells (**Figure 3.9-A**), no notable change in CYP1B1 activity was seen in comparison to control-treated cells after 24 h. In the HEP-G2 cells, the untreated control (relative activity of 1.49 units) and CDDP-treated (1.77) cells induced significant ($P < 0.0001$ and $P < 0.01$, respectively) increases in CYP1B1 activity, while complexes **1** (0.82) and **4** (0.85) significantly ($P < 0.05$) lowered activity, and complexes **2** and **3** resulted in no significant change (**Figure 3.9-B**). Complex **4** caused a slight, yet significant ($P < 0.05$) decrease CYP1B1 activity in HT-29 cells (0.92), while CDDP resulted in no change in CYP1B1 activity (**Figure 3.9-C**) when compared to the DMSO-treated cells.

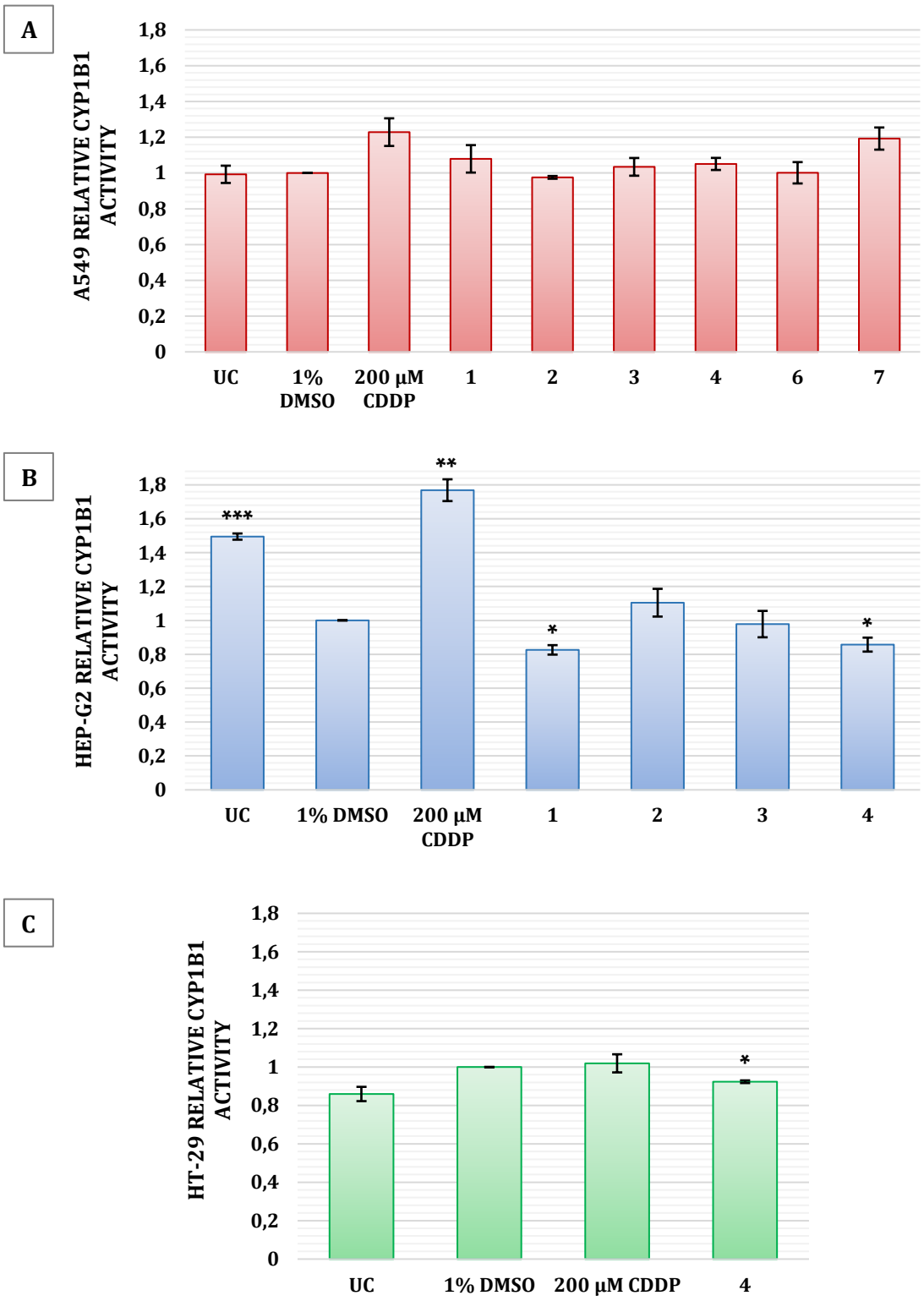


Figure 3.9. The CYP1B1 isoform activity in malignant **(A)** **A549**, **(B)** **HEP-G2** and **(C)** **HT-29** cells measured by a Cytochrome P450-Glo™ assay. The following treatments were an untreated control or treated with 1% DMSO, 20 µM of complexes **1** - **4**, **6** and **7** or 200 µM CDDP for 24 h. Percentages of the complex-treated cells were expressed in relation to the 1% DMSO treated-cells (100 % = 1 relative unit). Error bars represent the ± SEM (n = 6) and using a two-tail Student's t-test, P values were calculated. Significant differences are denoted by asterisks (* $P < 0.05$; ** $P < 0.01$ and *** $P < 0.001$).

3.3.6. Antimetastatic potential of silver(I) phosphine complexes on A549 cells

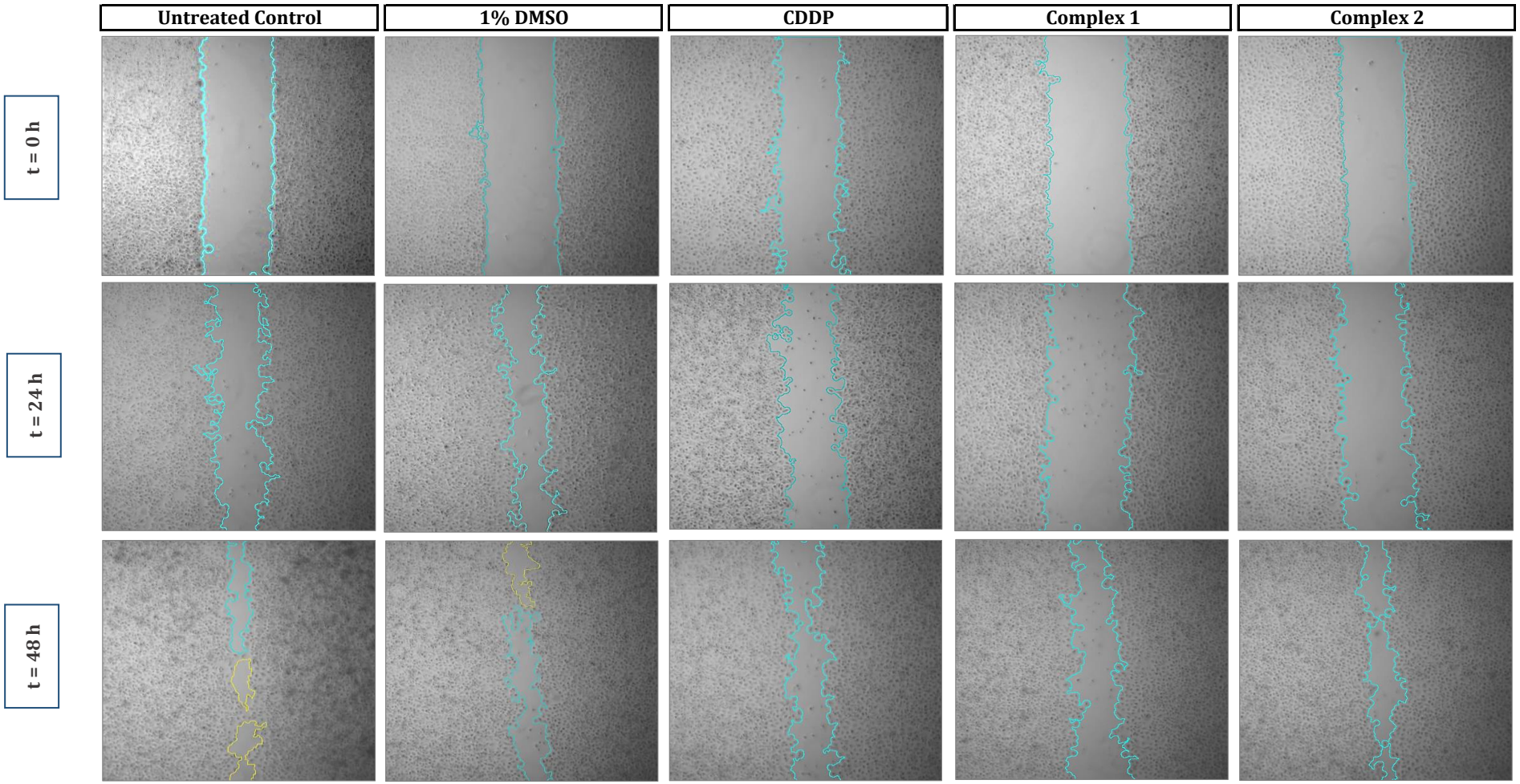
An investigation into the potential antimetastatic use of selected complexes on A549 cells was conducted. An *in vitro* wound healing scratch assay was used, whereby two wound tracks were scored in confluent monolayers of differentially treated A549 cells. Generating multiple wound tracks facilitates the accurate selection of the desired location when capturing time-lapse micrographs. Suarez-Arnedo *et al.* (2020) developed an optimized plugin for the open-source program ImageJ. This ImageJ/Fiji® plugin automatically recognizes the area and width of light micrographs after wound tracks were scored over consecutive time points (0 h, 24 h and 48 h after treatment). The area between the scratch wounds, the average wound width, the wound closure rate, and the rate of migration were quantified. The *in vitro* wound healing scratch assay analyzed with the ImageJ/Fiji® plugin indicates the metastatic/migratory potential of cells with higher accuracy than manual identification (Suarez-Arnedo *et al.*, 2020). Time lapsed micrographs of A549 cells were captured at 0 h, 24 h and 48 h after treatment. The control-treated cells were used for comparison purposes against cells treated with 3.75 µM CDDP and 1.5 µM of complexes **1 - 4**, **6** and **7**. Non-lethal concentrations were determined via the dose-responsive studies (**Figure 2.13**, chapter two), as higher concentrations would result in cell death after 24 h and the results would be deemed impractical (Behera and Saxena, 2021). As shown in **Figure 3.10**, untreated and vehicle control cells resulted in almost complete migration and closure of the wound after 48 h, indicated by different areas marked by blue and yellow borders. From the micrographs alone, it can be presumed that **1**, **3** and **4** inhibited cell migration most by visual inspection. However, these micrographs were analyzed further, and parameters were quantified. Quantified data is represented in **Figures 3.11**, **3.12** and **3.13.** The average wound area (µm^2) was calculated as below (**Figure 3.11-A**) whereas the ImageJ/Fiji® plugin quantified the average wound width (µm) (**Figure 3.11-B**) from the analyzed micrographs (Suarez-Arnedo *et al.*, 2020).

Average wound area (µm^2)

At = initial wound area at 0 h; AΔt = wound after *n* hours; *n* = after 48 h

$$\text{Average wound area} = \frac{At - A\Delta t}{At}$$

It can be seen that wound areas at 0 h ranged from 1079265,6000 µm^2 to 899265,2333 µm^2, this was determined by the scored wound, and values possibly differ due to the pressure used when making the score with a sterile 200 µl pipette tip. From **Figure 3.11-A**, untreated and vehicle control cells migrated more rapidly than cells treated with selected complexes, as their respective wound areas decreased the most after 48 h. Significant increases in the wound area after 24 h were observed by complexes **4**, **1**, **7**, **2**, CDDP ($P < 0.01$), **3** and **6** ($P < 0.05$). However, only complexes **1**, **4** and CDDP resulted in significant changes in wound area (i.e., the inhibition of cell migration) when compared to 1% DMSO vehicle control treated cells, after 48 h. Complex **1** resulted in a larger wound area still appearing after 48 h, while complex **7** resulted in the smallest wound area (µm^2).


Untreated Control
1% DMSO
CDDP
Complex 1
Complex 2
t = 0 h
t = 24 h
t = 48 h

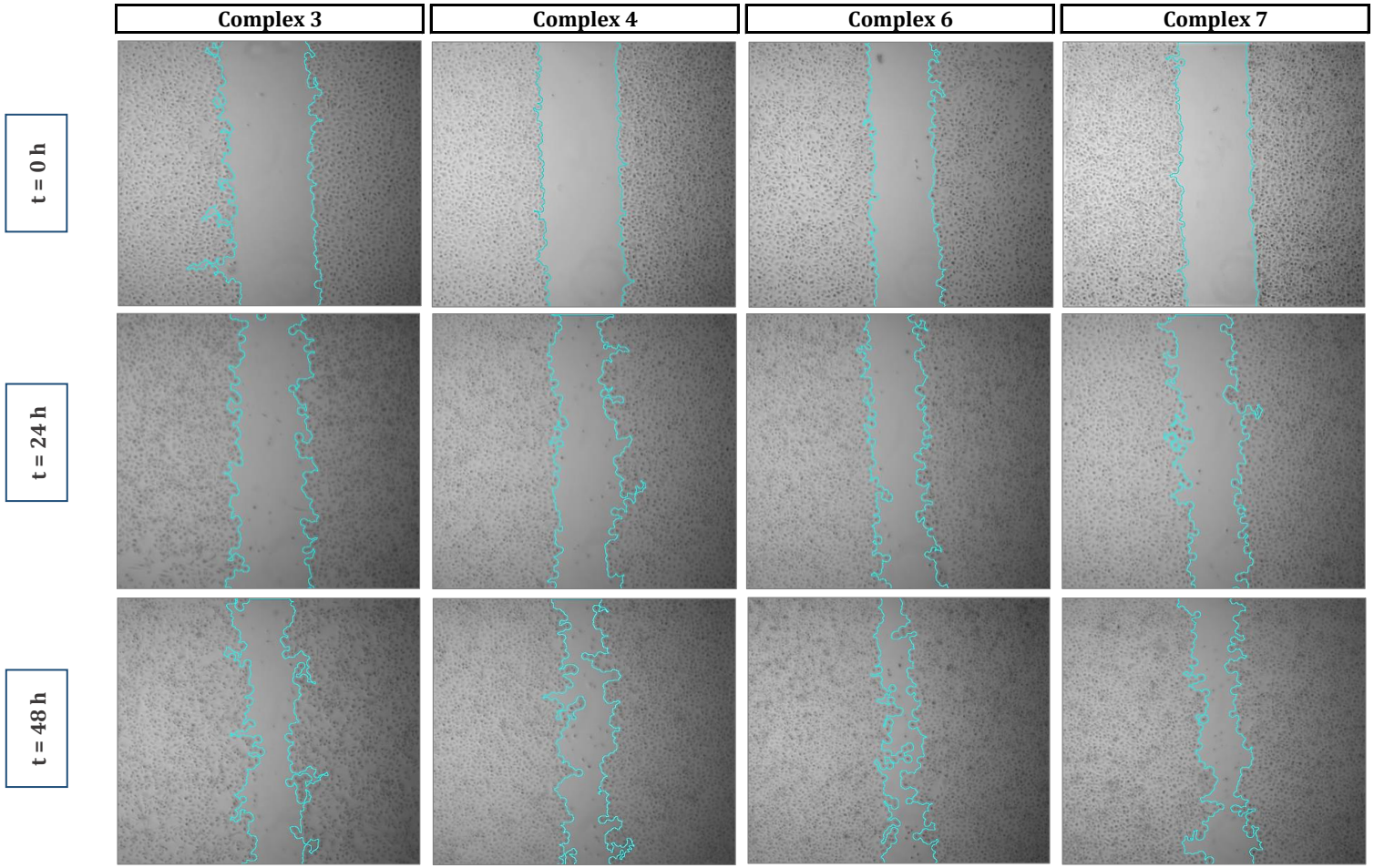


Figure 3.10. Time-lapse micrographs of malignant **A549** cells taken at **0 h**, **24 h** and **48 h** after wound tracks were scored and cells were differentially treated at **0 h**. The following treatments were an untreated control or treated with 1% DMSO, 3.75 μM CDDP or 1.5 μM of silver(I) phosphine complexes (**1 - 4, 6** and **7**). Micrographs were captured with a Zeiss Primovert inverted light microscope and Zen 2.6 Lite Blue Edition imaging software at 4 x magnification. The wound healing size tool, an ImageJ/Fiji® plugin was used to quantify parameters relating to the wound and the migration of the cells.

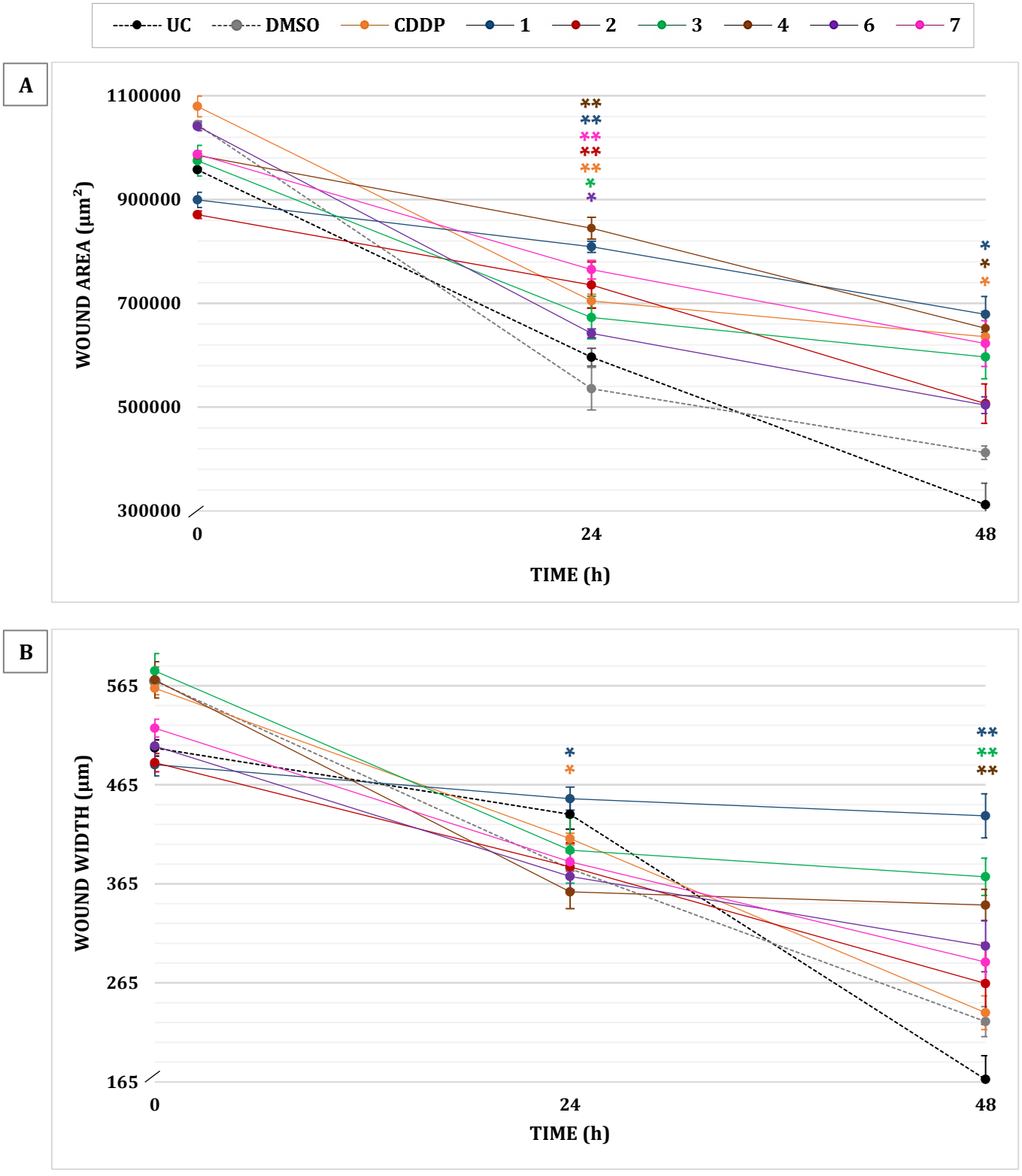


Figure 3.11. (A) Average wound area (µm²) and **(B)** average wound width (µm) of malignant **A549** at **0 h**, **24 h** and **48 h** after wound tracks were scored. Respective cells were differentially treated at **0 h**. Cells were not treated, or they were treated with 1% DMSO, 3.75 µM CDDP or 1.5 µM of silver(I) phosphine complexes (**1** - **4**, **6** and **7**). Total wound area and width were expressed in relation to 1% DMSO at the appropriate hour. Error bars represent the ± SEM (n = 6) and using a two-tail Student's t-test, P values were calculated. Significant differences are denoted by asterisks and are colour coded to the respective complex as represented in the legend (* $P < 0.05$; ** $P < 0.01$ and *** $P < 0.001$).

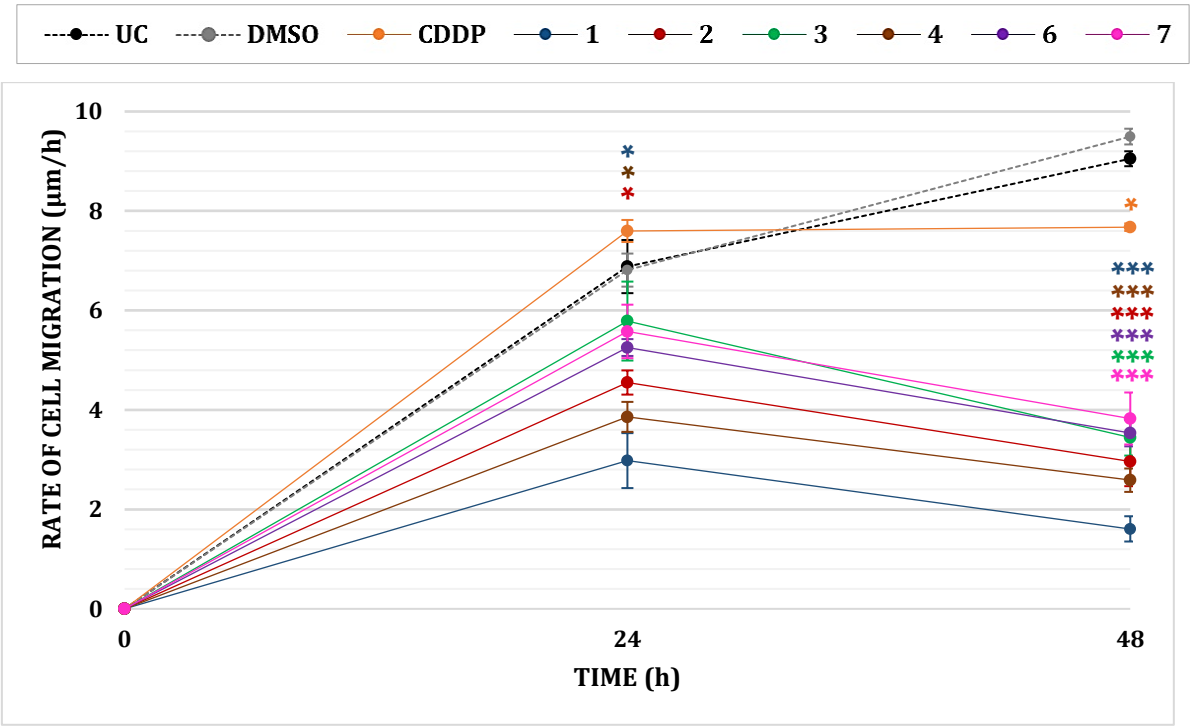


Figure 3.12. The rate of cell migration (µm/h) of malignant **A549** at **0 h**, **24 h** and **48 h** after wound tracks were scored and cells were differentially treated at **0 h**. Cell migration rates were expressed in relation to 1% DMSO at the appropriate hour. The± SEM (n = 6) is represented as error bars and using a two-tail Student's t-test, P values were calculated. Significant differences are denoted by asterisks and are colour coded to the respective complex as represented in the legend (* $P < 0.05$; ** $P < 0.01$ and *** $P < 0.001$).

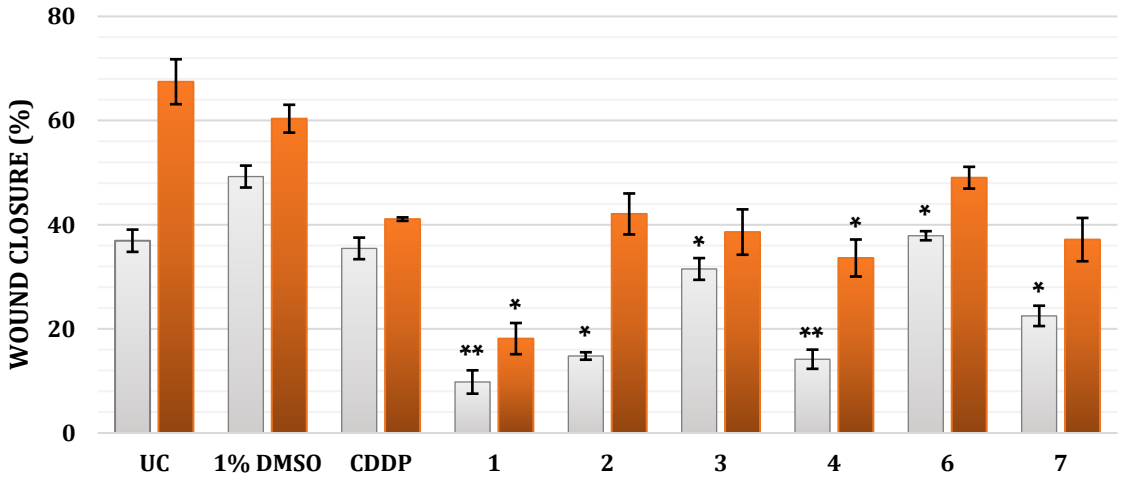


Figure 3.13. Percentage of wound closure of malignant **A549** at **24 h** and **48 h** after wound tracks were scored and cells were differentially treated at **0 h**. Percentages were expressed in relation to 1% DMSO at the appropriate hour. Grey gradient filled bars signify wound closure percentage **24 h** after treatment and the orange gradient filled bars signify wound closure percentage **48 h** after treatment. The ± SEM (n = 6) is represented as error bars and using a two-tail Student's t-test, P values were calculated. Significant differences are denoted by asterisks (* $P < 0.05$; ** $P < 0.01$ and *** $P < 0.001$).

From **Figure 3.11-B**, the average wound was analyzed, this width is the average distance measured between the edges of the wounds. Control-treated cells migrated more toward each other than cells treated with the selected complexes. The width of the treated cells was compared to the width of the 1% DMSO vehicle control-treated cells. Following the 24 h time point, only complex **1** and CDDP repressed cell migration and had a width slightly larger ($P < 0.05$) than the vehicle control wound width. However, after 48 h of treatment, complexes **1**, **3** and **4** repressed cell migration. These complexes had a wound width that was considerably ($P < 0.01$) larger in measured distance (µm). This was compared to control-treated A549 cells that migrated towards each other (seen in **Figure 3.10**).

From the above data, the rate of cell migration (R_M; µm/h) (**Figure 3.12**) and percentage of wound closure (**Figure 3.13**) were calculated as follows (Suarez-Arnedo *et al.* 2020):

Rate of cell migration (µm/h)

Wi = initial wound width at 0 h; Wf = final wound width after *n* hours; *n* = after 48 h; t = time span of assay in hours (48 h)

$$R_M = \frac{Wi - Wf}{t}$$

Percentage of wound closure

$$\text{Wound closure } \% = \left(\frac{At=0\ h - A\Delta t=48\ h}{At=0\ h}\right) x\ 100\ \%$$

After 24 h of treatment, it was observed that complexes **1** (2.98 µm/h), **4** (3.86 µm/h) and **2** (4.55 µm/h) significantly ($P < 0.05$) decreased the rate of cell migration (**Figure 3.12**). After 48 h, significant ($P < 0.01$) decreases in the rate of cell migration were observed for complexes **1** (1.61 µm/h), **4** (2.58 µm/h), **2** (2.96 µm/h), **6** (3.53 µm/h), **3** (3.44 µm/h), **7** (3.82 µm/h) and CDDP (7.67 µm/h; $P < 0.05$).

Overall, the silver(I) phosphine treated cells hindered the rate of cellular migration from 24 h to 48 h. Complex **6**, 24 h (5.25 µm/h) to 48 h (3.54 µm/h); complex **7**, 24 h (5.57 µm/h) to 48 h (3.82 µm/h) and complex **3**, 24 h (5.78 µm/h) to 48 h (3.44 µm/h). The untreated and vehicle control cells rates of migration were similar and increased from 24 h to 48 h; values were 6.88 µm/h to 9.05 µm/h and 6.81 µm/h to 9.49 µm/h, respectively. Cells treated with CDDP resulted in an increase after 24 h (7.59 µm/h), however, this plateaued, and after 48 h (7.67 µm/h) as little to no change was seen when compared to the 24 h findings.

By analyzing the difference in average wound area (μm^2) at 24 h and 48 h, the wound closure percentage was calculated from **Figure 3.13**. Complexes **1** and **4** were the most effective in impeding cell migration, as they significantly decreased wound closure after 24 h and 48 h of treatment, respectively. After 24 h, complex **1** resulted in a considerable ($P < 0.01$) decrease in wound closure of only 9.79% and complex **4** resulted in 14.16% ($P < 0.01$). After 48 h, complex **1** was slightly more effective than complex **4**. While complexes **1** and **4** continued to significantly ($P < 0.05$) decrease the percentage of wound closure, complex **1** resulted in only 20.11% decrease of the initial wound area (μm^2) while complex **4** resulted in a 33.60% decrease. Although complexes **2** (15.20%), **3** (31.49%), **6** (37.88%) and **7** (22.49%) all significantly ($P < 0.05$) decreased the closure of the wound after 24 h, there was no significant difference after 48 h in comparison to DMSO-treated cells (60.36%). The percentages obtained after 48 h for complexes **2**, **3**, **6** and **7** were comparable to CDDP (49.57%), nevertheless, they were still lower than the untreated control cells, with a decrease in 67.45% of the initial wound area at 0 h (cells migrated towards each other).

3.4. Discussion

The data (**Table 2.2**) from the cytotoxicity screening presented in chapter two identified the most effective silver(I) phosphine complexes for a specific cell line. These complexes have been shown to exhibit antiproliferative and cytotoxic properties, specifically targeting the hallmark of sustained proliferative signalling. However, identifying the mechanism of cell death is essential for the development of these complexes as anticancer agents. Lipophilicity is believed to improve the selectivity and mitochondrial targeting of anticancer drugs (Berners-Price *et al.*, 1986). According to Zinovkin and Zamyatnin (2019), lipophilic cations can permeate the mitochondrial membrane. Triphenylphosphine (TPP) is the most commonly used lipophilic cation, and many developing drugs are linked or developed using phosphine as it is a carrier into the mitochondria (Poyraz *et al.*, 2017). A stable Au(III) tetraphenyl-porphyrin chloride [Au(TPP)]Cl was shown to target the intrinsic mitochondrial pathway of apoptosis in HT-29 and HCT-116 colorectal cells (Dandash *et al.*, 2017). Numerous drugs have been synthesized based on lipophilic systems. Phosphine is lipophilic and can easily target the mitochondria of malignant cells. As a result of the lipophilic nature of silver(I) phosphine complexes within mitochondria, the effect on a number of mitochondrial mechanisms was studied in this investigation (Engelbrecht *et al.*, 2018; Meijboom *et al.*, 2009).

3.4.1. An investigation into the mitochondrial-mediated apoptotic pathway

For all three cell lines, A549 (**Figure 3.1**), HEP-G2 (**Figure 3.2**) and HT-29 (**Figure 3.3**), vehicle control treated cells resembled the healthy, untreated control cells, with similar morphological traits unique to each cell line. Morphological attributes associated with apoptosis can be distinguished by cell rounding, shrinkage, blebbing, condensation and the formation of apoptotic bodies (Redza-Dutordoir and Averill-Bates, 2016). These alterations to morphology were seen in all three malignant cell lines treated with 10 µM and 20 µM silver(I) phosphine complexes and 200 µM CDDP (**Figure 3.1 - 3.3**), which is consistent with previous findings when SNO cells were treated with silver(I) cyanide complexes after 24 h (Human-Engelbrecht *et al.*, 2017; Human *et al.*, 2015). Godwin *et al.* (2019), confirm that membrane blebbing, shrinkage of cells and loss of adhesion are classical morphological hallmarks of apoptosis (Kerr *et al.*, 1972). Ferreira *et al.* (2015) treated MCF-7 cells with 10 µM silver(I) thiocyanate complexes **1 - 4**, which resulted in cell rounding, shrinkage, and a reduction in cellular volume. Cells treated with 20 µM of selected complexes revealed a reduction in cellular volume when compared to the 10 µM treatments, possibly due to the detachment of weakened cells.

3.4.1.1. Insights into energy metabolism, reactive oxygen species and apoptosis

The mitochondria are vital organelles within the cell. Their primary function is the conversion of nutrients into ATP, they are the "powerhouse" organelles, and they export ATP throughout the cell. This functioning is facilitated by the outer mitochondrial membrane (OMM) and highly permeable inner mitochondrial membrane (IMM). The OMM participates in the transport and exchange of respiratory substrates and products between the mitochondria and cytosol, while the IMM is involved in regulating the electrochemical potential needed for the production of ATP as well as oxidative phosphorylation (Nikoletopoulou *et al.,* 2013; Redza-Dutordoir and Averill-Bates, 2016).

They remain an appealing target for cancer therapies because they are implicated in regulating cell death processes such as apoptosis. Corresponding ATP levels dictate the cell death mechanism, as decreased levels are known to induce apoptosis while highly depleted levels of ATP will induce necrosis (Nikoletopoulou *et al.*, 2013). Otto Warburg was the first to hypothesize that malignant cells can be eliminated by focusing on their mitochondria (Warburg, 1925; Warburg *et al.*, 1927). Malignant cells make use of the aerobic glycolytic pathway, whereby glucose uptake and lactate production are increased to produce additional ATP. This is to generate sufficient energy for increased proliferation and survival, and for the synthesis of proteins and macromolecules which are hallmarks of cancer (**Figure 1.1**, chapter one) (Li *et al.,* 2022; Hanahan and Weinberg, 2011). Mitochondrial ROS production is an early occurrence preceding the loss of membrane potential ($\Delta\Psi m$) which results in decreased ATP production. This causes an expulsion of apoptosis-inducing factors into the cytosol, such as cytochrome *c*, and the activation of caspases, inducing programmed cell death. Most drugs have been designed to compromise the mitochondria for these reasons (Caruso *et al.,* 2007; Bayir and Kagan, 2008).

(a) *Change in GAPDH activity, ATP levels and cellular viability*

GAPDH activity, ATP levels, and cellular viability were investigated in A549, HEP-G2 and HT-29 malignant cells treated with selected complexes after 24 h. Proliferating malignant cells must produce an appropriate amount of energy to enable rapid cell division and regular cellular functions (Amaral *et al.,* 2018). The dysfunction of the mitochondria is associated with reduced ATP levels however, the mitochondria mediate programmed cell death and a reduction, but sustained, biomolecular energy is needed to power these mechanisms. Significant reductions in ATP levels as well as cellular viability were observed in treated malignant cells (**Figure 3.5**). In previous studies, silver(I) thiocyanate 4-methoxyphenyl phosphine lowered ATP levels in oesophageal cancer (Englebrecht *et al.,* 2018b), and four 1:2 silver(I) thiocyanate complexes lowered ATP levels in MCF-7 cells (Ferreira *et al.,* 2015). A 90% decrease in ATP levels were observed in A549 and HEP-G2 cells treated with 20 µM of the respective complexes, comparable results were seen in Ferreira *et al.* (2015). Cellular proliferation decreased as the ATP synthase was affected and levels of ATP

decreased. The viability and ATP levels of CDDP-treated A549 and HT-29 cells were observed to be maintained at levels exceeding 50%. In contrast, HEP-G2 cells exhibited a viability above 20% even when exposed to a concentration that was 10 times less effective than the concentrations used for silver(I) phosphine complexes (**Figure 3.5**).

Ishitani *et al.* (1996) were the first to identify overexpression of the protein GAPDH prior to cerebellar granule cells undergoing apoptosis. Tarze *et al.* (2007) and Colell *et al.* (2009) explain that when a cell is exposed to oxidative stress, GAPDH is reversibly inactivated, and this allows the cell to maintain a balanced oxidation/reduction state. It is well-known that GAPDH is a protein sensitive to redox activity, whereby its cysteine (Cys^{152}) residue is covalently modified. This cysteine residue plays an essential role in signalling pathways that recognize oxidative stress (Colell *et al.*, 2009). This was observed in the A549 and HEP-G2 cells, respectively. In **Figure 3.4-A** it can be seen that complexes **2 - 4**, **6** and **7** significantly increased GAPDH activity, while none of the complexes resulted in an increased level of GAPDH activity in the HEP-G2 cells (**Figure 3.4-B**). This correlates to the oxidative stress data obtained. The silver(I) phosphine complexes resulted in minimal to no oxidative stress in the A549 cells (**Figure 3.6-A**), while there was a significant increase in ROS generation for complexes **1** (60.07%; $P < 0.0001$), **2** and **3** (60.17% and 60.72%; $P < 0.01$ respectively) in the HEP-G2 cells. The level of oxidative stress produced could have affected GAPDH activity present within the mitochondria of these two malignant cell lines. Studies conducted in *Caenorhabditis elegans* revealed the ability of GAPDH to maintain an optimal $NADH/NADP^+$ ratio when presented with oxidative stress by limiting the glycolytic pathway; however, this was not observed in treated A549 and HEP-G2 cells as inversely proportional relationships were observed between ROS and GAPDH activities (Colell *et al.*, 2009).

Findings differ in the HT-29 cells as complex **4** initiates a significant ($P < 0.0001$) amount of ROS activity (53.88%; **Figure 3.6-C**), while significantly ($P < 0.05$) increasing GAPDH activity. In recent findings, Xie *et al.* (2022) revealed that nitric oxide-induced *S*-nitrosated GAPDH translocates to the nucleus and initiates an apoptotic response. Here, an increase in GAPDH protein mediated apoptosis in C2C12 (mouse myoblast) cells, suffering from sarcopenia (age-related loss in muscle mass disorder). Previous studies suggest GAPDH levels had increased in the mitochondria prior to cell death (Chuang *et al.*, 2005; Colell *et al.*, 2009). Gioria *et al.* (2018) treated Caco-2 (colon) cells with silver nanoparticles (AgNPs). GAPDH was dysregulated through oxidation, which resulted in the insoluble aggregation of GAPDH, which further increased oxidative stress. The role GAPDH plays in the intrinsic apoptotic pathway still remains elusive, additional research is required to confirm any direct involvement GAPDH may have. The selected complexes increased GAPDH activity in only two malignant cell lines. Whether this directly affects the role GAPDH has in any apoptotic processes

within these cells remains under investigation. Therefore, it can be presumed silver(I) phosphine complexes slightly alter GAPDH expression within certain malignant cells.

(b) *Generation of reactive oxygen species*

Research has shown that elevated levels of ROS can induce apoptosis in both *in vitro* cell cultures and *in vivo* animal models. Over the years, investigations into potential anticancer agents that promote excessive levels of ROS have been of great interest. In malignant cells, cellular redox balance can be easily altered to lower or elevate the amount of ROS. When malignant cells are treated with an antioxidant, the decrease in the amount of ROS causes the cells to become senescent. However, when antioxidant levels are decreased, redox-regulation transduction mechanisms fail to maintain acceptable levels of ROS and oxidative stress occurs (Redza-Dutordoir and Averill-Bates, 2016).

An increase in the production of ROS and depolarization of the loss of membrane potential ($\Delta\Psi m$) have previously been linked to the signalling pathways that lead to apoptosis (Engelbrecht and Cronjé, 2018; Kriel and Coates, 2012; Landes and Martinou, 2011). Such oxidative stress significantly increases the vulnerability of mitochondria to membrane depolarization, initiated by the opening of non-specific MPTP (Ott *et al.*, 2007) in the inner mitochondrial membrane (IMM). Reczek and Chandel (2017), explain that since cancer cells generate higher amounts of ROS, by increasing ROS production, these cells are more susceptible to oxidative stress-induced cell death. Oxidative stress occurs when antioxidant defense mechanisms cannot "neutralize" the generation of ROS. Excessive oxidative stress compromises cellular viability as it damages proteins, lipids and nucleic acid bases within a cell (Manda *et al.*, 2009; Yilmaz *et al.*, 2018). Many anticancer treatment strategies exploit ROS to regulate proliferation and mediate apoptosis (Li *et al.*, 2010; Ray *et al.*, 2013).

Flow cytometry data revealed that complexes **3** and **4** produced the highest number of intracellular ROS in HEP-G2 cells (**Figure 3.6-B**, 60.07% ±2.71%) and HT-29 cells (**Figure 3.6-C**, 53.88% ±1.98%) respectively, after 24 h. Differences remained significant in comparison to the vehicle control cells, with 82.21% and 96.19% of the population's ROS^- (M1), for HEP-G2 and HT-29 cells, respectively. Studies conducted by Al-kawmani *et al.* (2020) revealed a similar increase in intracellular ROS^+ (M2) population in MCF-7 cells when treated with increasing concentrations of AgNPs after 24 h. It was found that a higher concentration of AgNPs eliminated antioxidants, ROS, and ultimately DNA damage. Further confirmation was observed in Engelbrecht and Cronjé (2018). They treated SNO cells with 10 µM of a silver(I) thiocyanate complex. This complex falls into the same phosphine silver monodentate family as complexes **2**, **3**, **4** and **7** used in this study (Meijboom *et al.*, 2009). Most of the cell population was ROS^+ (42.42%) when compared to the DMSO-treated

cells. This is comparable to the induced ROS^+ population in the HT-29 cells by 20 µM treatment of complex **4.** Whereas in the HEP-G2 cells, complexes **1** - **3** induced a ROS^+ population of approximately 60% and complex **4** only 27.63%. In contrast, despite exhibiting considerable toxicity (**Figure 2.6** and **Table 2.2**, chapter two), complexes **1** - **4**, **6** and **7** did not significantly increase ROS generation in A549 cells. Cyclophilin A, peptidyl-prolyl cis-trans isomerase (CypA), levels are known to be increased in human NSCLC. CypA is an intracellular interacting protein that serves a crucial function in the progression of cancer. Increasing evidence suggests it might be associated with metastasis (Gou *et al.,* 2018). Yang *et al.* (2007) found that correlations between CypA and tumour progression showed that CypA is sustainably upregulated in various cancer types, such as A549 cells. The higher endogenous levels of CypA have shown to prevent ROS production. A study by Li and Yang (2022), investigated the effect CypA has on oxidative stress. CypA was secreted in response to inflammatory stimulation to protect cardiomyocytes from apoptosis, caused by oxidative stress, by lowering the levels of ROS. Furthermore, they found that the overexpression of CypA in H1299 (NSCLC) and A549 cells, repressed ROS generation. Therefore, it can be deduced that the elevated endogenous levels of CypA in A549 cells potentially hindered the generation of ROS induced by silver(I) phosphine complexes 1 - **4**, **6** and **7**.

In a previous study by Lupidi *et al.* (2013), a synthesized gold(I) phosphine complex [Au(tBu_3P)(dppet)Cl] caused high cytotoxicity in HCT-116 colon cancer cells, by particularly inhibiting the enzyme thioredoxin reductase (TrxR). This enzyme is expressed in cancer cells and maintains a balanced redox state for growth, being primarily involved in the depletion of ROS. The inhibition thereof results in an accumulation of ROS levels within the cell, which inhibits ATP synthase. Additional research investigating the outcome of silver(I) phosphine complexes on the expression of TrxR in cells treated for varying amounts of time could shed light on the regulation of the *TrxR* gene and ROS activity. Additionally, Yilmaz *et al.* (2018) found that platinum(II) saccharin complexes containing tertiary phosphine ligands, promoted ROS production in MCF-7 and HCT-116 cells. In comparison with CDDP, their complexes damaged the respiratory chain and increased ROS activity. A549, HEP-G2 and HT-29 cells treated with CDDP resulted in no to minimal ROS^+ cells (3.27%, 25.95% and 15.03% respectively), a similar ROS^+ population of 17.35% in MCF-7 cells after 12 h was shown by Yilmaz *et al.* (2018).

(c) *Mitochondrial potential and cellular plasma permeabilization*

Mitochondrial dysfunction is a key role in the intrinsic mitochondrial-mediated cell death pathway. It involves changes to the membrane permeability, which alters the oxidation-reduction potential and results in the subsequent loss of the $\Delta\Psi m$ in the mitochondria (Caruso *et al.,* 2007).

As illustrated in **Figures 3.7-A** and **3.7-C**, A549 and HT-29 silver(I) phosphine treated cells show signs of mitochondrial depolarization, as reflected by the increase in the percentage of depolarized/dead cell populations. The loss of ΔΨm was significantly higher in A549 cells treated with complexes **2**, **3**, **4** ($P < 0.01$) and **7** ($P < 0.05$), and HT-29 cells treated with complex **4** when compared to CDDP. Comparable results were observed in Yilmaz *et al.* (2018) where platinum(II) saccharin complexes resulted in a loss of ΔΨm in MCF-7 and HCT-116 cells that were considerably higher than CDDP after 24 h (75.10% versus 59.95% depolarized/dead population). In addition, Kriel and Coates (2012) compared two complexes, a bridged gold(I) complex, bis(di(4-methoxyphenyl)phosphino)-1,2-diethylhydrazine di(gold(I) chloride; referred to as **3d**) and a silver(I) complex, bis(bis(di(4-methoxyphenyl)phosphino)dimethylhydrazine) silver nitrate (referred to as **4i**). These complexes were compared to a reference complex, $[Au(DPPE)_2]Cl$ established by Berners-Price *et al.* (1986). The loss of ΔΨm in treated peripheral blood mononuclear cells (PBMC) cells after 24 h decreased with an increase in **3d** concentration. This was comparable to $[Au(DPPE)_2]Cl$, while the concentration of **4i** was independent of the depolarization percentage of the membrane.

In contrast, the treatment of HEP-G2 cells with selected complexes led to a significant increase in the proportion of dead and not depolarized live or depolarized dead cells. This could be likely due to the 20 µM treatment used. A shift into the depolarized quadrants might have been observed at a lower concentration, similar to the low mean IC_{50} values (**Table 2.2**, chapter two) for HEP-G2 cells. Complex **2 - 4** were more effective on the HEP-G2 cells when compared to the other malignancies (6.50 µM, 3.02 µM and 5.75 µM respectively). Li *et al.* (2010) found the HEP-G2 cells to be highly susceptible to treatment of 3-(4-(benzo[d]thiazol-2-yl)-1-phenyl-1H-pyrazol-3-yl) phenyl acetate (DPB-5), when compared to MCF-7, gastric carcinoma (SGC 7901) and leukaemia (HL600). Following the lymph nodes, metastatic cancer is likely to spread to the liver. Combination therapies of surgery and chemotherapy are used to treat liver metastasis (Rashdian *et al.,* 2020). Sorafenib was the first approved targeted therapy and thereafter used a control in the development of linifanib, and brivanib alaninate, amongst other anticancer agents (Huang *et al.,* 2020). Cheng *et al.* 2020 highlight that patients with metastatic liver cancer respond differently to sorafenib and that new anticancer drugs are required. HEP-G2 cells treated with 5 µM sorafenib for 12 h suppressed ATP production, increased ROS levels and cytochrome *c* release. Similar results were shown in **Figures 3.5-B** and **3.6-B** respectively, whereby complexes **1 - 4**, decreased ATP levels and increased ROS levels (Ding *et al.,* 2018).

These results indicate that lipophilic silver(I) phosphine complexes affect mitochondria preferentially by causing the collapse of the mitochondrial membrane potential. The increase in ROS production correlates well with the mitochondrial dysfunction in the HT-29 cells. While silver(I)

phosphine complexes targeted the mitochondria without significantly increasing ROS production in the A549 cells. HEP-G2 cells significantly increased ROS production, perhaps a lower treatment concentration (~ 10 µM) or earlier time point (12 h) may have caused the loss of mitochondrial membrane potential and not significant populations of dead cells.

3.4.1.2. Identifying the mode of cell death in malignant cell lines

Ptd-L-Ser externalization

Ptd-L-Ser externalization was apparent in A549 (**Figure 3.8-A**), HEP-G2 (**Figure 3.8-B**) and HT-29 (**Figure 3.8-C**) cells treated with 20 µM of selected complexes. This was revealed by the number of cells positive for Annexin V. These cells treated with complexes **1** - **4**, **6** and **7** (correspondingly) exhibited a decrease in live cells and an increase in cells enduring late apoptosis.

Ptd-L-Ser externalization was shown in HT-29 cells treated with complex **4** (**Figure 3.8-C**). At the 20 µM treatment, complex **4** resulted in 75.73% of the population undergoing late apoptosis. Complex **4** resulted in a more prevalent apoptotic population than cells treated with 200 µM of CDDP (13.68%), while the vehicle control cells remained viable (90.43%). When compared to the positive necrotic H_2O_2 control, 94.76% of the population were late apoptotic at a higher H_2O_2 concentration (50%), whereas the concentration for complex **4** was much lower, but still resulted in an apoptotic population. Comparable results were shown by Altay *et al.* (2019), when MCF-7 cells were treated with silver(I) complexes [Ag_2(µmef)2(2-pymet)$_2$] and [Ag_2(µmef)2(2-pyet)$_2$]. As the concentration of the silver complexes increased from 12.5 µM to 50 µM, an increase in late apoptotic populations up to 63.90 % was observed. Ferreira *et al.* (2015) treated MCF-7 cells with different silver(I) thiocyanate-phosphine complexes. A decrease in cellular viability and an increase in apoptotic mechanisms were observed. Di- and polynuclear silver(I) sac complexes with four various tertiary phosphane ligands were studied by Yilmaz *et al.* (2017). These silver complexes showed greater anticancer activity and Ptd-L-Ser externalization when adjuvanted with phosphine and were toxic to MCF-7 and lung (A549) cells. They resulted in IC_{50} concentrations larger in value than that of CDDP yet exhibited a strong inhibitory effect and selectivity towards MCF-7 cells. Dissimilar IC_{50} findings were seen with regards to complex **4** (**Table 2.2**), but a similar sustained inhibitory effect towards A549, HEP-G2 and HT-29 cells was evident. In summary, all complexes were effective against A549, HEP-G2 and HT-29 cells, as there were significant decreases in cellular viability and increases in late apoptotic/dead cells after 24 h.

3.4.1.3. Targeting the drug metabolizing CYP450 enzyme

From chapter two, several silver(I) phosphine complexes were cytotoxic to various malignant cell lines and were more effective when compared to CDDP (**Table 2.2**). The development of anticancer drugs can be improved by identifying probable targets or biomarkers such as cytochrome P450.

Cytochrome P450s (CYP450) are versatile monooxygenase isoforms that catalyze a multitude of reactions within the body. The *CYP450* gene encodes for diverse isoforms, functionally classified into two groups. They are crucial to either (1) the metabolism of endogenous molecules (i.e., hormones) or (2) the processing of exogenous molecules (i.e., drugs or xenobiotics) (Bruno and Njar, 2007; Mishra *et al.*, 2010). In this study, the CYP1B1 isoform was of interest as it participates in the oxidative metabolism of xenobiotics and is highly expressed in many cancer types (Bruno and Njar, 2007; Presa *et al.*, 2021). Targeting CYP1B1 offers potential beneficial insights into cancer therapy.

The majority of CYP450s are highly expressed in the liver, in both healthy and malignant hepatic tissue. Notably, CYP1B1 activity was significantly lower in HEP-G2, and HT-29 cells treated with selected complexes (**Figure 3.9-B** and **3.9-C**) in contrast to the DMSO-treated cells. However, the untreated HEP-G2 control cells expressed higher levels of CYP1B1. D'Uva *et al.* (2018) show that CYP1B1 is frequently over-expressed in numerous malignancies. Previous findings in Saini *et al.* (2009), revealed that when endometrial carcinoma cells were depleted of CYP1B1, proliferation decreased, and TRAIL was expressed. This is suggestive of an extrinsic apoptotic response. Similarly, Presa *et al.* (2021) observed that the expression of CYP1B1 in various *in vivo* head and neck cancer (HNC) cell lines was significantly lower in comparison to control-treated cells and cells treated with duocarmycin, a natural product exhibiting cytotoxic and anticancer activity. Although complexes **1** and **4** significantly lowered CYP1B1 expression in HEP-G2 and HT-29 cells, depletion of the enzyme did not occur. Gerets *et al.* (2012) describe that HEP-G2 cells present limitations in their metabolic capacities and usually have lower levels of CYP450s when compared with primary hepatocytes. CYP1B1 was only slightly altered in this study, with A549 cells showing no change in CYP1B1 activity (**Figure 3.9-A**). Therefore, it can be presumed that silver(I) phosphine complexes do not therapeutically target CYP1B1.

In summary, apoptosis is a well-regulated and characterized process, distinguished by morphological features, an increase in ROS generation, the loss of $\Delta\Psi m$ and the externalization of Ptd-L-Ser. Based on the outcomes discussed in this and the previous chapter, silver(I) phosphine complexes are selective towards malignant cell models. Silver(I) phosphine complexes initiated anticancer activity at 10 µM and 20 µM treatments. Complexes deemed effective in the A549 cells were **1** - **4**, **6** and **7**; in the HEP-G2 cells, complexes were **1** - **4** and in the HT-29 cells was complex **4**. These silver(I) phosphine complexes target key changes indicative of the mitochondrial-mediated apoptotic pathway and are presumed to induce this programmed cell death cascade. Future studies targeting executioner caspases-3,-6 and/or -9, as well as Bid and Bax would further confirm this. In addition, previous studies by Engelbrecht *et al.* (2018) reported cleavage of caspase-9 and the downstream cleavage of caspase-3/7 in SNO cells treated with $[AgSCN\{P(4\text{-}MeOC_6H_4)_3\}_2]_2$, a silver(I) phosphine complex that falls within the same family of complexes studied herein.

3.4.2. Silver(I) phosphine complexes inhibit A549 cell migration

In order for cells to adapt to change and execute function, they have the ability to migrate. This process is important for gastrulation, the translocation of immune cells, and cellular homeostasis. However, cancer cells can regulate their movement and contribute to pathological processes such as inflammation and metastasis. The progression of metastasis occurs when cells from the original tumour at the primary site, disseminate via the circulatory and lymphatic systems to colonize distant organs within the body (Friedl and Weigelin, 2008; Pijuan *et al.*, 2019). Repressing or even regulating metastatic-associated factors such as cell migration may significantly slow down this progression (Cheng *et al.*, 2015).

The *in vitro* wound healing scratch assay is typically used to evaluate the closure of a manually produced scratch/wound on a monolayer of malignant cells. The purpose of this assay was to determine the impact of selected silver(I) phosphine complexes on the lateral motility of A549 cells. The data quantified herein gives insight on the inhibition or impediment of metastasis by selected silver(I) complexes in A549 malignant cells. The data obtained revealed that complexes **1** and **4** exhibited stronger antimetastatic activity by repressing cell migration than complexes **2**, **3**, **6** and **7**. The rate of cell migration and the percentage of wound closure represent comparable data indicative of lateral motility inhibition (**Figures 3.12** and **3.13**, respectively).

Cheng *et al.* (2015) treated A549 cells with calycosin, an effector chemical previously reported to regulate metastatic activity. After which the *in vitro* wound healing scratch assay was conducted, and micrographs were captured at 0 h and 24 h. It was found that the concentration of calycosin used was inversely proportional to the percentage of wound closure. The percentage of wound closure following treatment with 20 µM calycosin was 41.81% after 24 h; silver(I) phosphine complexes seemed to be slightly more effective at a much lower concentration of 1.5 µM, with all complexes resulting in wound closure percentages below 37.88 % after 24 h and 51.20% after 48 h of treatment (**Figure 3.13**). Cheng *et al.* (2015) obtained significantly lower percentages of wound closure when stimulating A549 cells with the protein, tissue plasminogen activator (TPA). However, when compared to the untreated control cells (13.31%), treated cells resulted in wound closure percentages that were significantly higher. In this study, A549 cells were not stimulated with any protein along with the silver(I) phosphine complex treatments, and yet results remained similar to TPA-induced cells. In addition, Yang *et al.* (2018) treated A375 cells with the flavonoid, kaempferol at an IC_{50} of 20 µM for a period of 20 h. This reduced the migratory potential of A375 cells, and the data obtained was based on captured micrographs. Notably, a shorter time period was captured, probably due to the higher IC_{50} treatment used.

An earlier study by Aceituno *et al.* (2016) demonstrated the inhibitory response of silver nanoparticles on A549 cell migration. In this study, the average reduction in the distance between the wound edges was measured. As shown in **Figure 3.10**, untreated A549 cells exhibited migration towards each other within 24 h, resulting in a decrease of approximately 90% in the original distance measured at 0 h. Conversely, cells treated with AgNPs significantly repressed the lateral mobility of the A549 cells. The association between cell migration and an increased level of epidermal growth factor receptors (EGFR) in cancer cells is widely recognized (Chougule *et al.,* 2023). Following a 24 h treatment period, the migration of A549 cells that were elevated with EGFR were inhibited by AgNPs. Moreover, Aceituno *et al.* (2016) investigated the amounts of EGFR mRNA and protein. After 48 h of treatment with AgNPs, the mRNA levels of EGFR and ETS like-1 protein (ELK1) were shown to be lower. Regarding silver(I) phosphine complexes and their effect on EGFR, future PCR and Western blot investigations on the mRNA and protein levels of EGFR should be considered to determine whether EGFR is a possible mechanism by which silver(I) phosphine complexes reduce cell migration in A549 cells.

Overall, cell migration was significantly inhibited, predominantly by complexes **1** and **4**. This demonstrates the antimetastatic potential that silver(I) phosphine complexes may possess. Additional studies would confirm whether the same inhibition will be seen across a broad range of malignancies known for their aggressive metastatic potential, such as triple negative breast cancer and hepatocellular carcinoma.

CHAPTER FOUR:
A MINI-COMPARATIVE STUDY INVESTIGATING KEY ANTICANCER ACTIVITIES OF THREE SILVER(I) PHOSPHINE COMPLEXES IN MCF-7 AND MDA-MB-231 BREAST CELL LINES

4.1. Prologue

In this chapter, a comparative study between hormone-dependent breast cells and TNBC was investigated. The choice to investigate breast cancer as the subject of this study was motivated by its status as the prevailing form of cancer among women worldwide. The rational of this study was to investigate the efficacy of silver(I) phosphine complexes as initiators of anticancer activity in the two types of breast cancer. For this purpose, silver(I) phosphine complexes **2**, **4** and **7** were chosen based on their selectivity and efficacy to decrease cell viability in the MDA-MB-231 TNBC cell line (**Table 2.2**, data presented in chapter two). Theodosius *et al.* (2019) explain that MCF-7 and MDA-MB-231 cells are phenotypically and genotypically distinct from one another despite originating from the same primary site (the duct within the breast) and are therefore homogeneous (**Figure 1.3**, chapter one). Including the hormone receptor differences and insensitivity of MDA-MB-231 cells to hormone therapy/antiestrogens, MDA-MB-231 cells display a mesenchymal phenotype, whereas MCF-7 cells display an epithelial phenotype. These cell lines were chosen due to their well-documented characteristics (explained in chapter one) (Amaral *et al.*, 2018; Arnold *et al.*, 2022; Barzaman *et al.*, 2020; Tan *et al.*, 2009).

Previous research (Barzaman *et al.*, 2020; Vedoya *et al.*, 2021; Welsh, 2013) has confirmed that the absence of ER, PR, and HER-2 in MDA-MB-231 cells has made them more resistant and insensitive to conventional therapeutic approaches than the MCF-7 cells. TNBC is aggressive, as it has the highest mortality rate among the intrinsic subtypes of breast cancer (Huang *et al.*, 2022; Theodosius *et al.*, 2019). Firdhouse and Lalitha (2015) biosynthesized AgNPs using an extract from the plant *Alternanthera sessilis* where they found significant cytotoxic activity in MCF-7 cells when compared to CDDP. In addition, Moses *et al.* (2016) developed gold nanoparticles that induced a cytotoxic effect in MDA-MB-231 cells while remaining non-toxic to healthy, non-malignant cells. Multiple treatment modalities are available for hormone-dependent breast cells, including tamoxifen, although chemotherapy and surgery continue to be the predominant therapeutic approaches for managing TNBC (Eid *et al.*, 2018; Muchtaridi *et al.*, 2017).

This mini-study compared whether selected silver(I) phosphine complexes target a comparable cell death mechanism in MCF-7 and MDA-MB-231 cells. The aim was to investigate whether complexes **2**, **4** and **7** induce the intrinsic mitochondrial-mediated apoptotic pathway in both breast cell lines by analyzing morphological changes, PS externalization, depolarized $\Delta\Psi m$, ROS production, the

integrity of DNA and mitochondria, as well as mitochondrial cytochrome *c* translocation into the cytosol.

4.2. Experimental methodology

All reagents and equipment were used according to the manufacturer's guidelines. **Appendix I** contains a comprehensive inventory of the manufacturer information for all materials and tools used in chapter four's experimental analyzes.

4.2.1. Cell culture

Prior to use, all reagents for culture, subculture, and plating were heated in a pre-set water bath of 37°C.

4.2.1.1. Plating of cells

As described in chapter two, points *2.2.2.3* and *2.2.2.4* respectively; the MCF-7 and MDA-MB-231 breast adenocarcinoma cells were collected and counted. An optimal concentration of 2 x 10^5 cells/ml in 3 ml of the DMEM media (6 x 10^5 cells) was calculated using a Countess™ automated cell counter and seeded in 35 mm tissue culture-treated dishes. Before treatment, cells were incubated to proliferate for 24 h.

4.2.1.2. Cell treatments

After 24 h of incubation, the used media was removed from the 35 mm culture dishes and 1 ml of fresh supplemented DMEM media was added. For all experimental assays (unless stated otherwise), cells were differentially treated as follows: not treated (UC) or treated with 1% (v/v) DMSO (VC), 200 µM of CDDP (positive apoptotic control), or treated with 20 µM of selected silver(I) phosphine complexes **2**, **4** and **7**. These complexes, in addition to CDDP were prepared as described in chapter two, point *2.2.1.15.* A necrotic positive control was included when applicable. One millilitre of 50% (v/v) $H_2O_2$was used to treat the cells. Cells were then incubated for an additional 24 h preceding antiproliferative and apoptogenic analyzes.

4.2.2. Antiproliferative and apoptogenic analyses

4.2.2.1. Cellular morphology

Using an Axiovert 25 inverted light microscope, variations in cellular morphology following differential treatment of MCF-7 and MDA-MB-231 breast cells were examined. Cells were differentially treated as follows: not treated (UC) or treated with 1% (v/v) DMSO (VC), 100 µM and 200 µM of CDDP (positive apoptotic control) or treated with 10 µM and 20 µM of selected silver(I)

phosphine complexes. Micrographs were captured using the AxioCam MRC camera with Axiovision 3.1 imaging software at 200 x magnification.

4.2.2.2. Quantification of cellular populations' reactive oxygen species

The same protocol and quantifiable values were used as explained in chapter three, point *3.2.2.4.*

4.2.2.3. Measuring the change in mitochondrial membrane potential ($\Delta\Psi m$)

The same protocol and quantifiable values were used as explained in chapter three, point *3.2.2.5.*

4.2.2.4. Determining potential mode of cell death

The same protocol and quantifiable values were used as explained in chapter three, point *3.2.2.6.*

4.2.2.5. Fluorescence microscopy analysis of mitochondrial integrity and the nuclear morphology

On glass coverslips measuring 20 mm by 20 mm, 6 x 10^5 cells were seeded at an optimal density of 2 x 10^5 cells/ml in 3 ml DMEM media. Coverslips were placed in 35 mm culture dished and cells were allowed to adhere for 24 h prior to treatment. The breast cells were treated as previously detailed in point *4.2.1.*2. and analyzed 24 h after. After removing the used media, 100 nM MitoTracker Orange CMTMRos probe® was introduced to pre-warmed DMEM culture media. Each culture dish received two millilitres of this solution, followed by incubation for 30 min at 37°C. The cells were washed three times with 2 ml pre-warmed PBS (37°C) for 5 minutes each, this eliminated any unbound probe. The cells were preserved for 20 min at 37°C in 2 ml of 4% (v/v) formaldehyde in PBS. After three washes of 5 min each, the cells were permeabilized for 15 min at 4°C with 0.1% (v/v) Triton X-100 in PBS. To avoid non-specific coupling, the cells received 2 ml of blocking buffer (1% (w/v) bovine serum albumin (BSA), 0.05% (v/v) Tween-20 in PBS, pH 7.4), cells were kept at room temperature for 30 min. After removing the blocking solution, 2 ml of Alexa-Fluor® 488-labeled anti-cytochrome *c* antibody in PBS (0.5 g/ml) was added to the cells and the plate was incubated for 1 h at room temperature. After washing the cells three times (5 min for each wash), 1 µg/ml of Hoechst-33258 pentahydrate (bis-benzimide) in pre-warmed PBS (37°C) was added to the cells and the plate was kept in the dark at room temperature on an orbital shaker, for 20 min. Any unbound dye was washed off the coverslip with 2 ml PBS three times (5 min for each wash). Using a drop of mounting media (PBS-buffered glycerol, 10% (v/v) PBS and 90% (v/v) glycerol), coverslips were affixed onto glass slides. The slides were stored in the dark at 4°C and edge-sealed with clear nail polish. Fixed cells were examined using an Axioplan 2 inverted fluorescent microscope. Micrographs were captured with the AxioCam HR camera and Axiovision 4.7 imaging software at 400 x magnification (control and 10 µM treated cells) and at 630 x magnification (20 µM treated cells). The fluorescence chemicals had the following excitation and emission wavelengths: MitoTracker Orange CMTMRos probe®, excitation 554 nm and emission 576 nm;

Alexa® 488, excitation 499 nm and emission 519 nm (bandpass of 546/12nm, Zeiss filter set number 15); and Hoechst-33258, excitation 343 nm and emission 483 nm (bandpass of 365/12nm, Zeiss filter set number 1).

4.2.3. Statistical analysis

Experimental data comprised of three independent biological repeats and two technical repeats to achieve a representation of $n = 6$. To determine statistically significant variations, the Standard Deviation, Standard Error of the Mean (SEM), and a two-tailed heteroscedastic Student's t-test were used, as suitable. The SEM for each differential treatment was represented as the errors bars on the bar graphs. The probability value (*P* value) of * $P < 0.05$, ** $P < 0.01$ and *** $P < 0.001$ were statistically significant in relation with DMSO-treated cells. Statistical analyzes were performed in Microsoft Office Excel 2013.

4.3. Results

4.3.1. Morphological changes

After 24 h, morphological alterations in the two breast cell lines treated with complexes **2**, **4**, and **7** were analyzed by light microscopy. Images were compared to control-treated cells. Vehicle control-treated MCF-7 and MDA-MB-231 cells appeared healthy and remained confluent with no signs of cellular stress, similar to the respective untreated control cells. In addition, the cells were treated with CDDP, a positive inducer of apoptosis. Cellular rounding and shrinkage were visible in the MCF-7 cells treated with 100 µM CDDP (red arrows) with few cells still attached. Similar morphological changes and fewer cells were seen when treated with 200 µM CDDP (**Figure 4.1**). MDA-MB-231 and MCF-7 cells that were treated with 100 µM CDDP and 10 µM complexes **2**, **4** and **7** appeared stressed and presented apoptotic features such as cellular rounding, apoptotic blebbing and bodies (red arrows). However, it appears that the healthy MDA-MB-231 cells were still attached (**Figure 4.2**), while the MCF-7 cells had completely detached (**Figure 4.1**). While fewer cells were observed with the 200 µM CDDP treatment. MCF-7 and MDA-MB-231 cells treated with 20 µM of complexes **2**, **4** and **7** resulted in an increase in cellular rounding, condensation (MCF-7) and apoptotic blebbing, and bodies (MDA-MB-231). Fewer cells were present when compared to the adherent confluent control cells (UC and 1% DMSO), considering that these cells had separated from the culture dish (**Figure 4.1** and **Figure 4.2**).

4.3.2. Production of reactive oxygen species

The MCF-7 and MDA-MB-231 cells were analyzed for ROS production 24 h after treatment, and the data obtained were represented as histograms (**Figure 4.3**). The principle of this assay has been previously explained in chapter three. In both breast cell lines, complex **2** did not significantly increase ROS activity when compared to DMSO. For the MCF-7 cells (**Figure 4.3-A**), complexes **4** and **7** resulted in a significant ($P < 0.05$) shift of 17.90% and 20.29% ROS^+ cells. Comparable findings were seen in MDA-MB-231 cells (**Figure 4.3-B**), where complexes **4** and **7** caused a significant ($P < 0.05$) shift of 10.96% and 12.48% ROS^+ cells, respectively. However, the shift in cell populations observed here was lower than MDA-MB-231 DMSO-treated cells (top left). CDDP caused a significant ($P < 0.01$) increase in ROS^+ MCF-7 cells (24.23%), while CDDP did not cause in a significant increase in ROS^+ MDA-MB-231 cells.

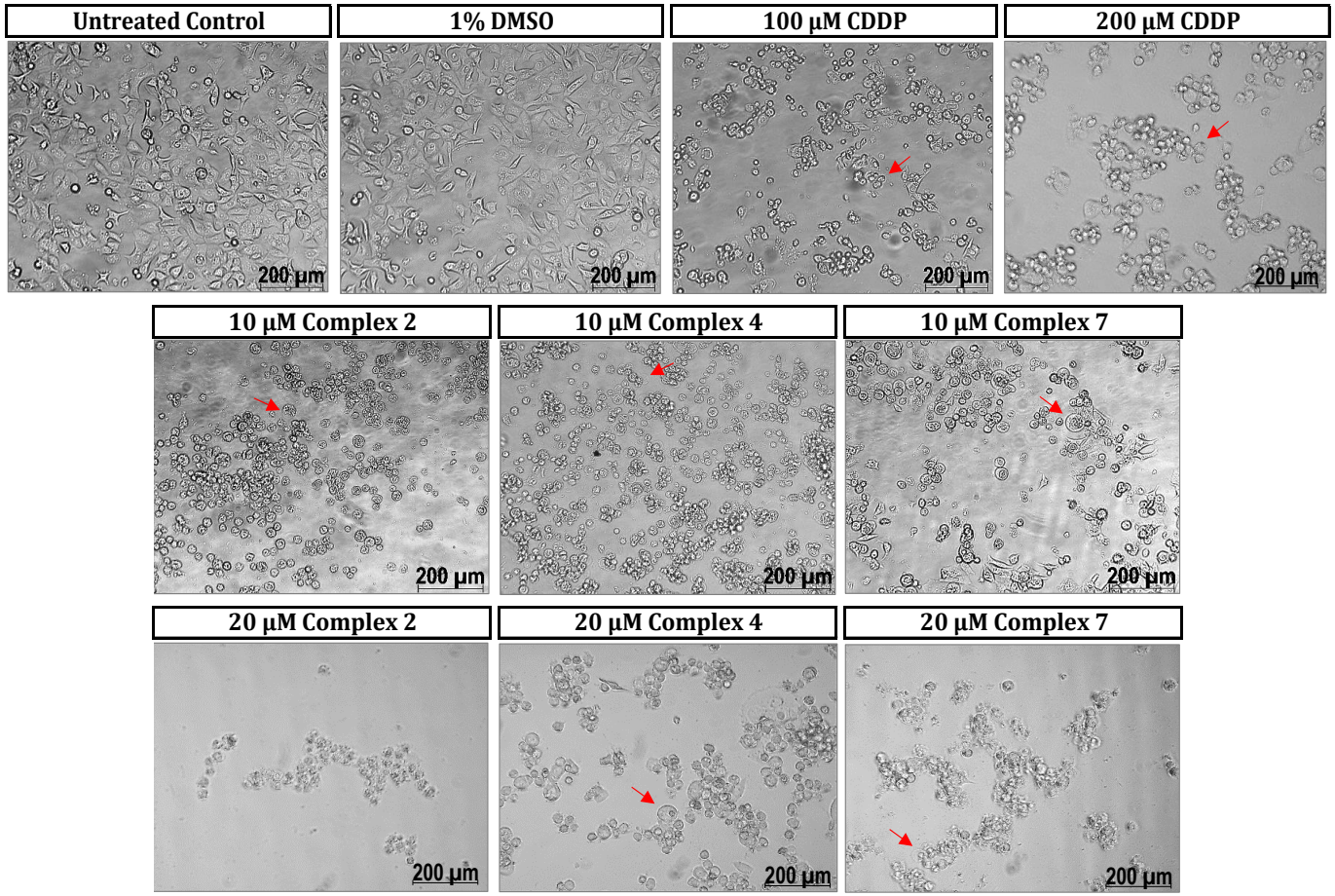


Figure 4.1. Morphological changes of malignant MCF-7 cells induced by differential treatments after 24 h. The following treatments were an untreated control or treated with 1% DMSO, 100 µM and 200 µM CDDP; and 10 µM and 20 µM silver(I) phosphine complexes **2**, **4** and **7** respectively. Control-treated cells show healthy MCF-7 cells. After 24 h, CDDP-treated cells, and respective silver(I) phosphine complexes induced typical morphological changes to cells diagnostic of apoptosis such as cell shrinkage, condensation, rounding and apoptotic blebbing and bodies (indicated by the red arrow). Images were captured either with a Zeiss Axiovert 25 inverted light microscope and Axio Vision 3.1 software, or the Zeiss Primovert inverted light microscope using Zen 2.6 Lite Blue Edition imaging software, at 200 x magnification.

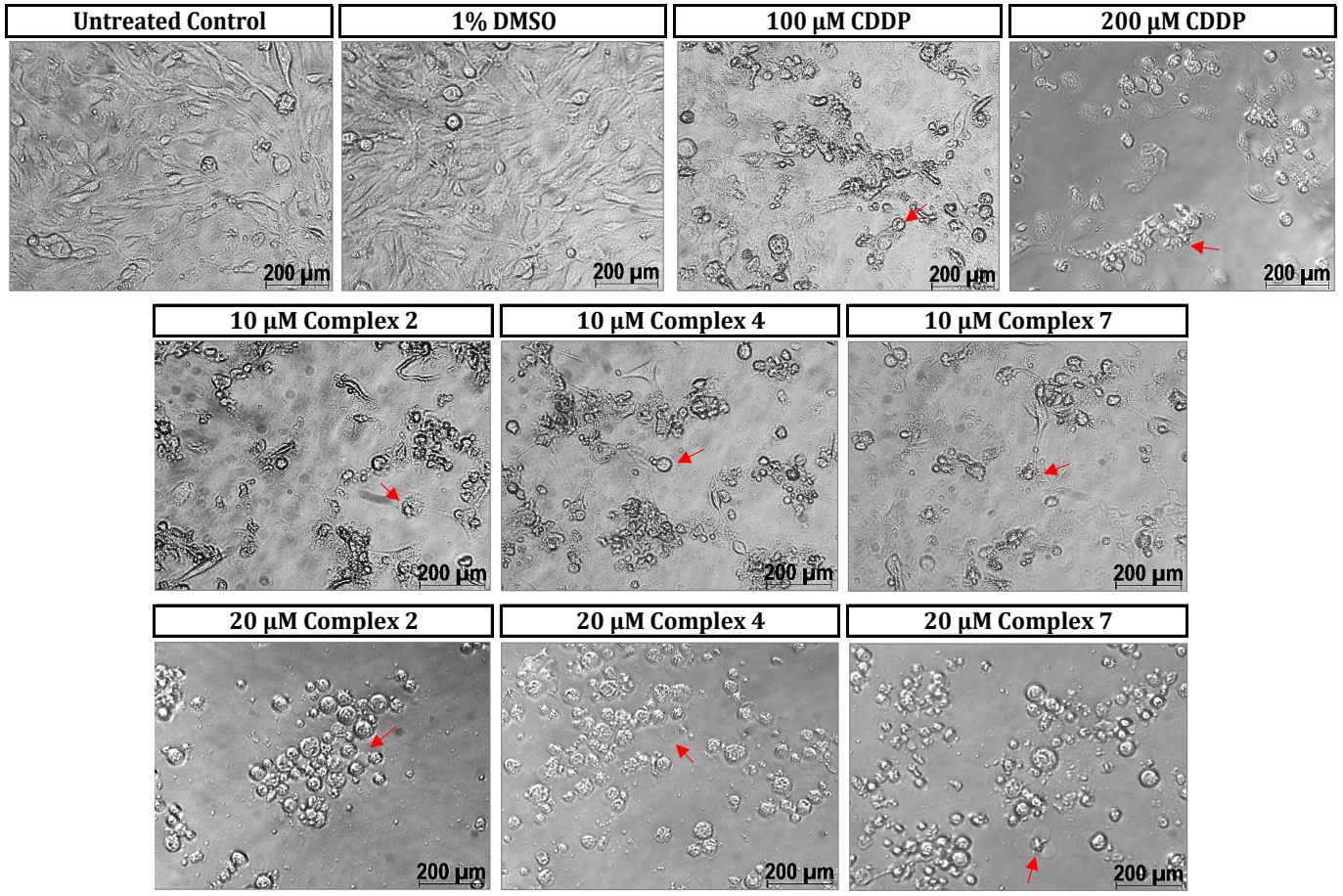
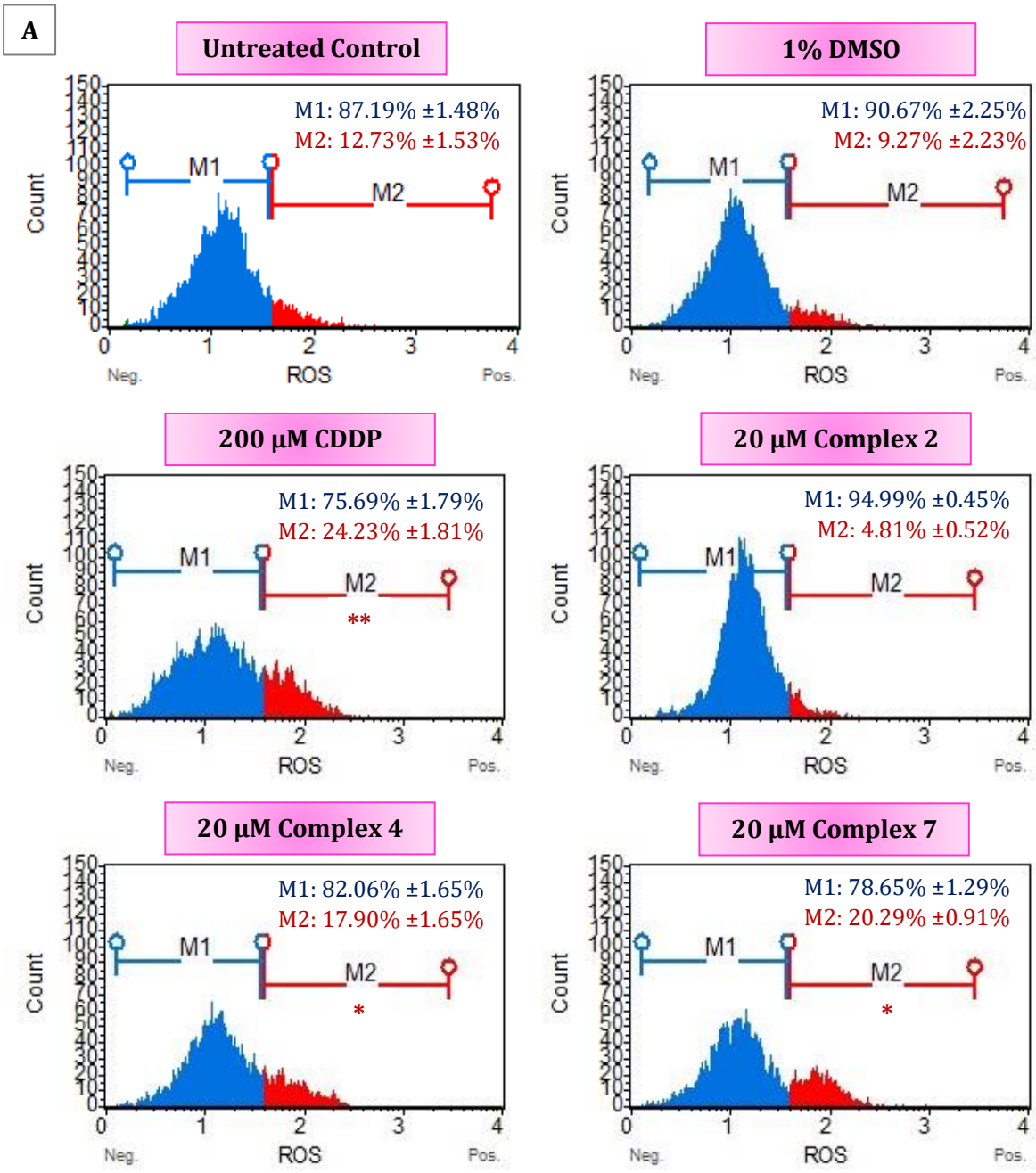


Figure 4.2. Morphological changes of malignant **MDA-MB-231** cells induced by differential treatments after 24 h. The following treatments were an untreated control or treated with 1% DMSO, 100 µM and 200 µM CDDP; and 10 µM and 20 µM silver(I) phosphine complexes **2**, **4** and **7**, respectively. Control-treated cells show healthy MDA-MB-231 cells. Following 24 h incubation, CDDP-treated cells, and respective silver(I) phosphine complexes induced typical morphological changes to cells diagnostic of apoptosis such as cell shrinkage, condensation, rounding and apoptotic blebbing and bodies (indicated by the red arrow). Images were captured with a Zeiss Axiovert 25 inverted light microscope and Axio Vision 3.1 software at 200 x magnification.

A


Untreated Control
M1: 87.19% ±1.48%
M2: 12.73% ±1.53%
1% DMSO
M1: 90.67% ±2.25%
M2: 9.27% ±2.23%
200 µM CDDP
M1: 75.69% ±1.79%
M2: 24.23% ±1.81%
**
20 µM Complex 2
M1: 94.99% ±0.45%
M2: 4.81% ±0.52%
20 µM Complex 4
M1: 82.06% ±1.65%
M2: 17.90% ±1.65%
*
20 µM Complex 7
M1: 78.65% ±1.29%
M2: 20.29% ±0.91%
*
Count
M1
M2
Neg.
ROS
Pos.

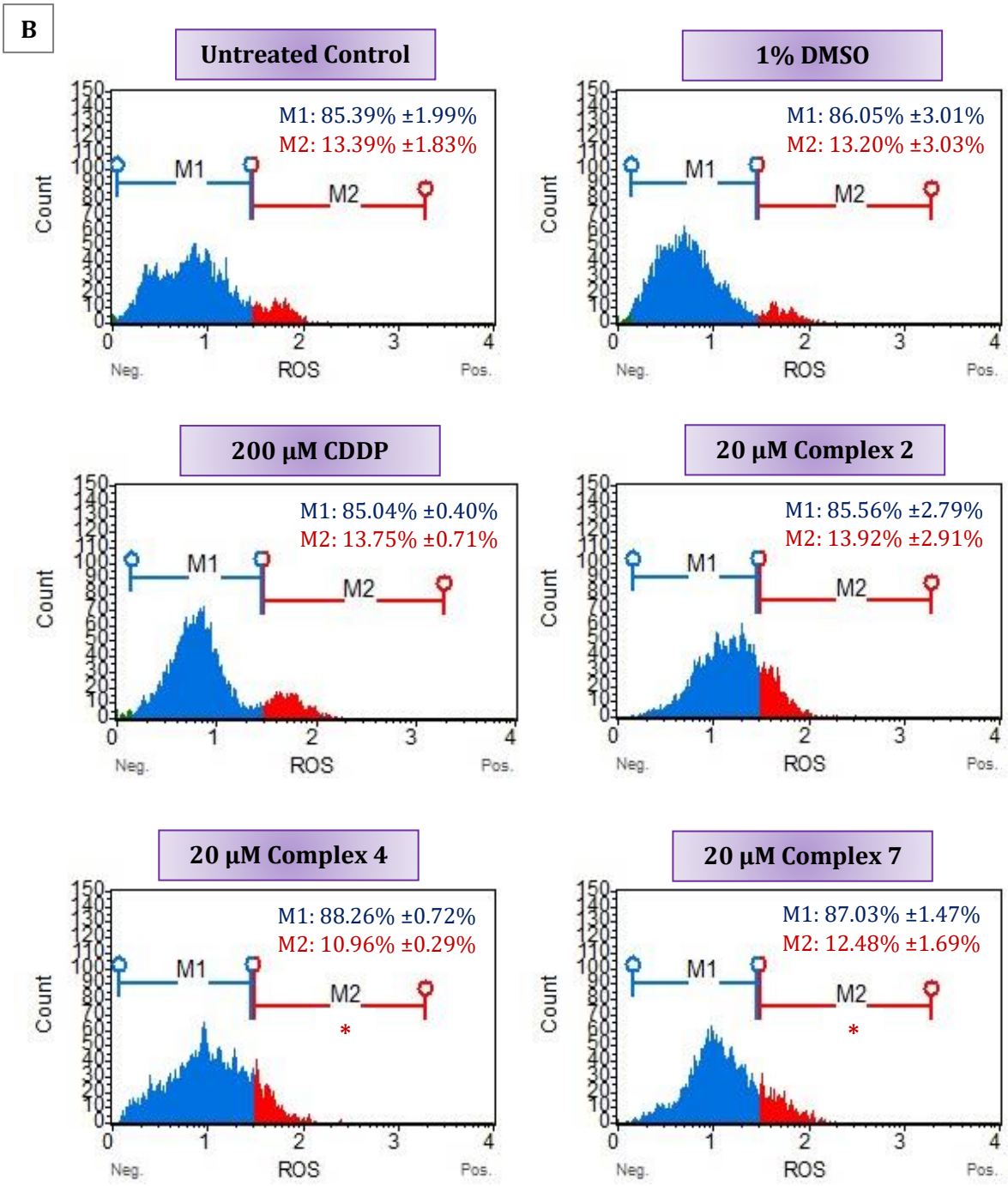


Figure 4.3. The detection of the total amount of ROS in malignant **(A)** MCF-7 and **(B)** MDA-MB-231 breast cells was quantified using a Muse® Oxidative Stress kit. The following treatments were an untreated control or treated with 1% DMSO (vehicle control), 200 µM CDDP (positive apoptotic control) or 20 µM of selected complexes **2**, **4** and **7** for 24 h. ROS negative (M1, blue) or ROS positive (M2, red) populations are shown by the percentages. Averaged percentage values and the ± SEM (n = 6) are represented within each histogram. Significant differences are denoted by asterisks between treatments and 1% DMSO for ROS-positive activity (* $P < 0.05$; ** $P < 0.01$ and *** $P < 0.001$).

4.3.3. Mechanism of action

To evaluate whether silver(I) phosphine complexes target the mitochondria of malignant breast cells, treated MCF-7 and MDA-MB-231 cell populations were quantified using the Muse® MitoPotential assay and the Muse® Annexin V and Dead Cell assay. These flow cytometric assays target important key points in a dying cell, the mitochondrial potential, cellular plasma permeabilization, and mode of cell death (Yu *et al.*, 2022). The concepts underlying these assays were previously described in chapter three.

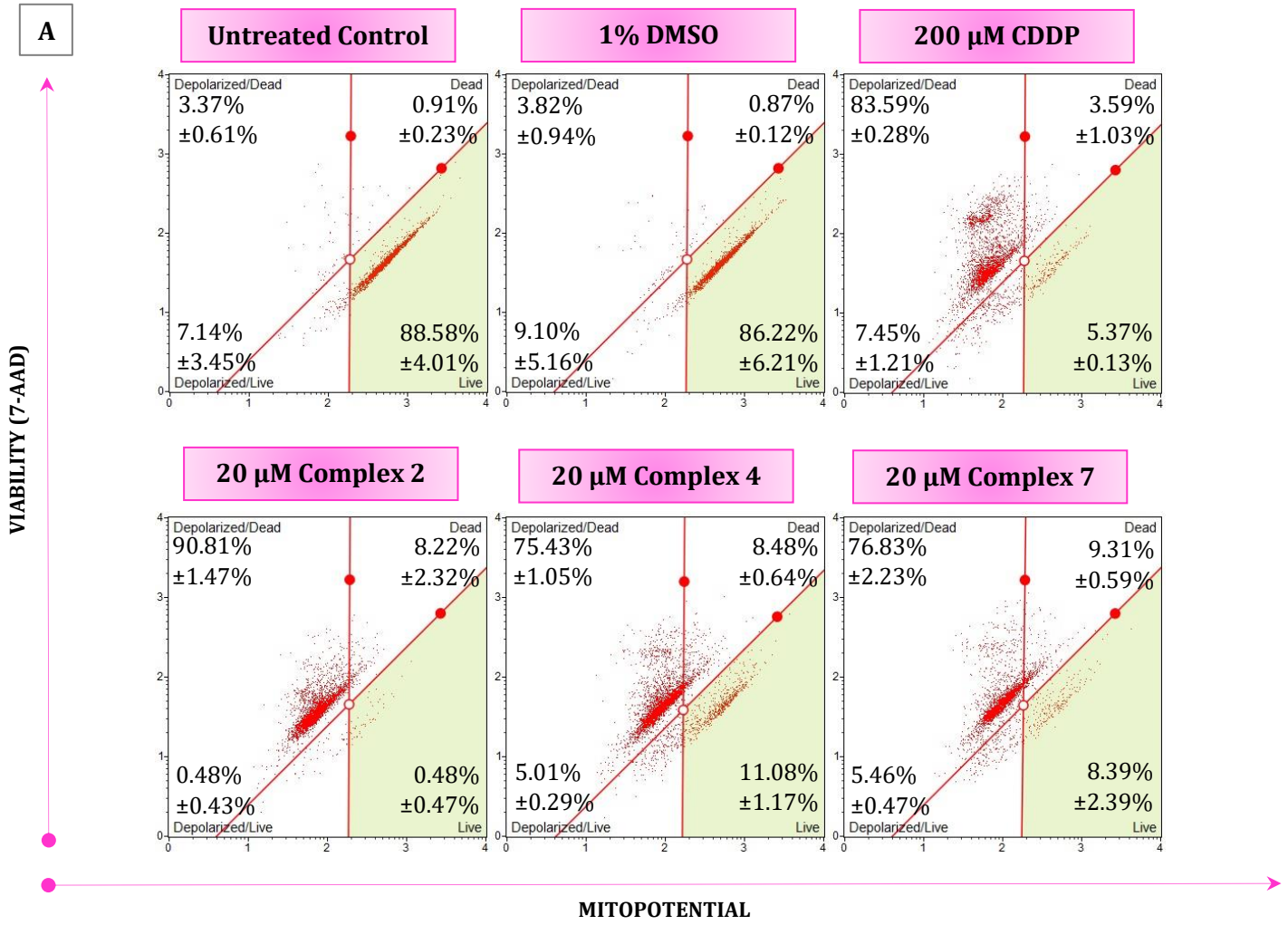
Observations indicate that the total number of depolarized/dead MCF-7 cells increased significantly ($P < 0.001$) (**Figure 4.4-A**) following treatment with 20 µM of complexes **2** (90.81%), **4** (75.43%), and **7** (76.83%) when compared to viable DMSO (86.22%) and the untreated control cells (88.58%). The structural integrity of these cells was damaged due to the depolarization of the mitochondrial membrane. The cell population shifted into the depolarized/necrotic quadrant (top left; **Figure 4.4-A**). When treated with CDDP, a high population of 83.59% the MCF-7 cells were depolarized/dead and only 5.37% of the population remained viable. Interestingly, a statistically significant ($P < 0.001$) rise in the number of dead MDA-MB-231 cells (**Figure 4.4-B**), and not depolarized cells was observed after 20 µM treatments of complexes **2** (89.15%), **4** (77.97%) and **7** (77.22%) when compared to the viable DMSO (73.95%) and the untreated control cells (75.90%). The CDDP-treated MDA-MB-231 cells also resulted in half of the population (57.42%) remaining viable while 25.46% shifted into the top right necrotic quadrant. This supports the chemoresistance factor of the TNBC cell lines (Orrantia-Borunda *et al.*, 2022). A loss of $\Delta\Psi m$ was observed in the MCF-7 treated cells, although depolarized live populations remained below 5.46%.

Muse® Annexin V and Dead Cell assay's 7-AAD dye and Annexin V were used to stain apoptotic and dead MCF-7 and MDA-MB-231 cells to establish the mode of cell death (**Figure 4.5**) induced by complexes **2**, **4** and **7**. Ptd-L-Ser externalization was present in MCF-7 (**Figure 4.5-A**) and MDA-MB-231 cells (**Figure 4.5-B**) treated with 20 µM of the selected silver(I) phosphine complexes **2**, **4** and **7** after 24 h. Comparative controls for apoptosis (200 µM CDDP) and necrosis (50% H_2O_2) were included. A significant ($P < 0.001$) difference in the amount of late apoptotic/dead cells was shown when complexes **2** (89.24%), **4** (67.91%), and **7** (65.07%) were used to treat MCF-7 cells, when compared to the live population of 83.80% DMSO-treated cells. Comparable and significant ($P < 0.001$) increases in the percentage of late apoptotic/dead cells were shown in MBA-MB-231 cells treated with complex **2** (76.96%), **4** (74.42%) and **7** (65.19%). Complex **2** resulted in the highest late apoptotic populations in both cell lines, followed by complex **4**. Complex **7** resulted in similar numbers of cells (±65% of the cell population) undergoing late apoptosis or death. These populations were significant when compared to the live populations of untreated (82.91%) and DMSO-treated cells (81.50%). Due to the higher treatment of 20 µM and the longer time study of 24 h, there were no significant number of early

apoptotic cells (< 2.04% for MCF-7 and < 3.24% for MDA-MB-231). In both cell lines, a lower number of late apoptotic or dead cells was observed when treated with CDDP. For the MCF-7 (**Figure 4.5-A**), half the population was late apoptotic with 58.14% in the top right, late apoptotic/necrotic quadrant. Whereas for the MDA-MB-231 (**Figure 4.5-B**), only 24.87% were present in this quadrant, while the majority of the population (65.46%) remained viable. MDA-MB-231 cells treated with 50% H_2O_2 resulted in an expected necrotic population of 86.24% while for the MCF-7 cells, 91.10% were late apoptotic and not in the necrotic quadrant.

To investigate and confirm if the silver(I) phosphine complexes effect the mitochondria (specifically the integrity) and stimulate the intrinsic apoptotic pathway, fluorescence micrographs were captured 24 h after treatment. Both breast cell lines were examined using the following fluorescence labels: Hoechst-33258 (blue), which stains the nuclei; MitoTracker® Orange CMTMRos (red), and Alexa-Flour® 488 mouse anti-cytochrome *c* specific antibody (green), which stain active mitochondria and cytochrome *c* respectively. Axio Vision 3.1 software and a Zeiss Axioplan 2 inverted fluorescence microscope were used to capture fluorescence micrographs at a 400 x magnification.

Figures 4.6-A and **4.6-B** show the MCF-7 and MDA-MB-231 control (1% DMSO and CDDP) cells alongside each other. All three fluorescence labels remained localized within intact nuclei and mitochondria after treatment with DMSO. Labelling remained localized when treated with 100 µM and 200 µM CDDP. Fluorescence labels remained within the organelles of MCF-7 cells treated with 10 µM of complexes **4** and **7** (**Figure 4.7**). Complex **4**-treated cells exhibit cytochrome *c* leakage from the mitochondria's intermembrane into the cytosol (indicated by white arrows). Complex **2** at 10 µM and 20 µM was highly cytotoxic, as cellular content and pyknotic (condensed) nuclear content leaked into the cytosol and no intact organelles were evident. At 10 µM, remaining nuclei were undergoing karyorrhexis (fragmentation). Similar observations were made in cells treated with 20 µM of complex **4**, where nuclei marginalization can be seen (white arrow) (**Figure 4.7**); however, cell volume had decreased dramatically. For the MDA-MB-231 (**Figure 4.8**), more cells are present and remained attached after treatment with 10 µM of complexes **2**, **4** and **7** when compared to 20 µM. Complex **2** resulted in damaged mitochondrial integrity, and the expulsion of the proapoptotic factor, cytochrome *c* (white arrow). Similar observations were shown in the MCF-7 cells, where complex **2** was the most cytotoxic. After 20 µM of treatment with complexes **4** and **7**, similar observations of dysfunctional mitochondria and cytochrome *c* release were observed. Complex **4** resulted in DNA condensation, while complex **7** resulted in pyknotic DNA (**Figure 4.8**).


A
Untreated Control
1% DMSO
200 µM CDDP
20 µM Complex 2
20 µM Complex 4
20 µM Complex 7
Depolarized/Dead
Dead
3.37% ±0.61%
0.91% ±0.23%
7.14% ±3.45%
88.58% ±4.01%
Depolarized/Live
Live
3.82% ±0.94%
0.87% ±0.12%
9.10% ±5.16%
86.22% ±6.21%
83.59% ±0.28%
3.59% ±1.03%
7.45% ±1.21%
5.37% ±0.13%
90.81% ±1.47%
8.22% ±2.32%
0.48% ±0.43%
0.48% ±0.47%
75.43% ±1.05%
8.48% ±0.64%
5.01% ±0.29%
11.08% ±1.17%
76.83% ±2.23%
9.31% ±0.59%
5.46% ±0.47%
8.39% ±2.39%
VIABILITY (7-AAD)
MITOPOTENTIAL

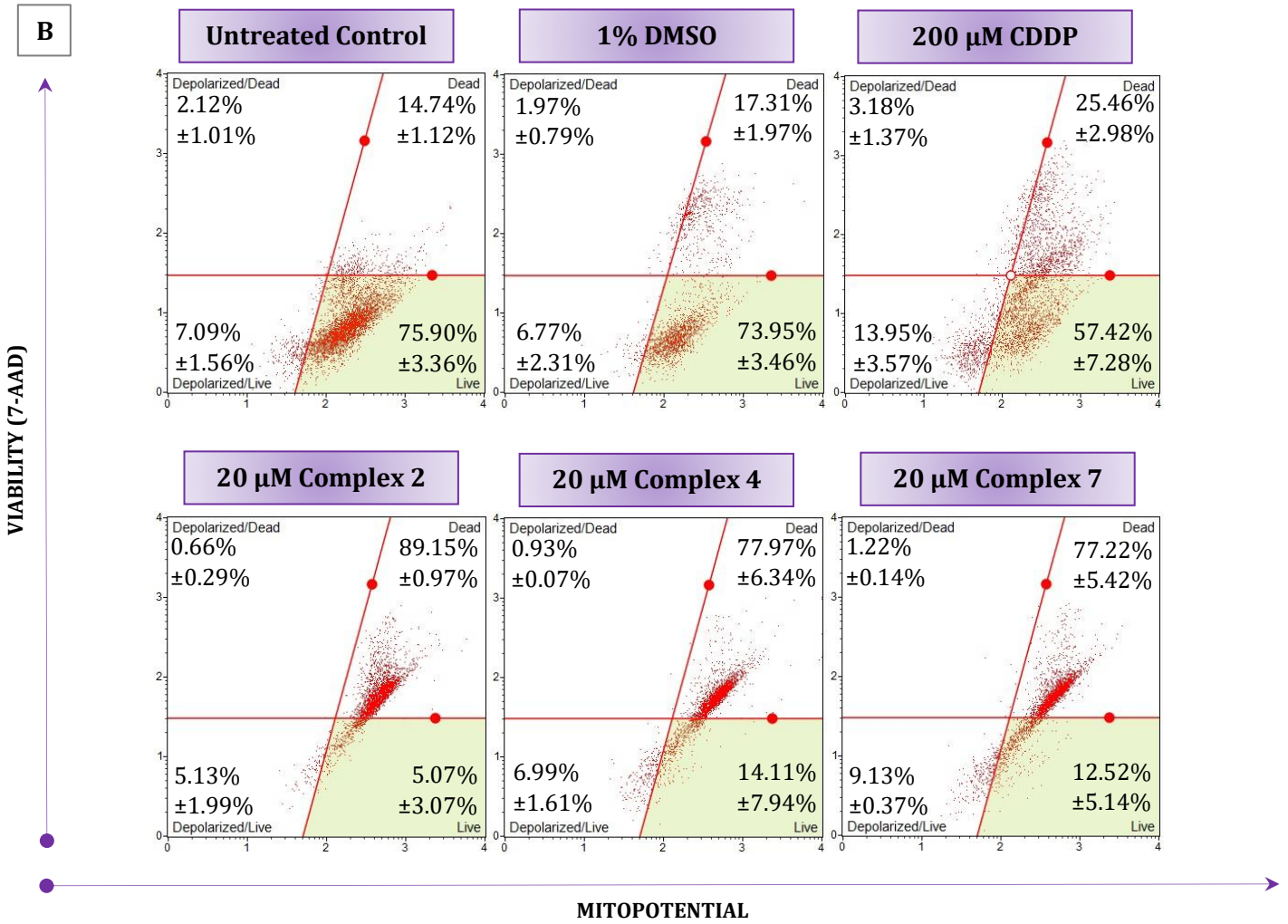
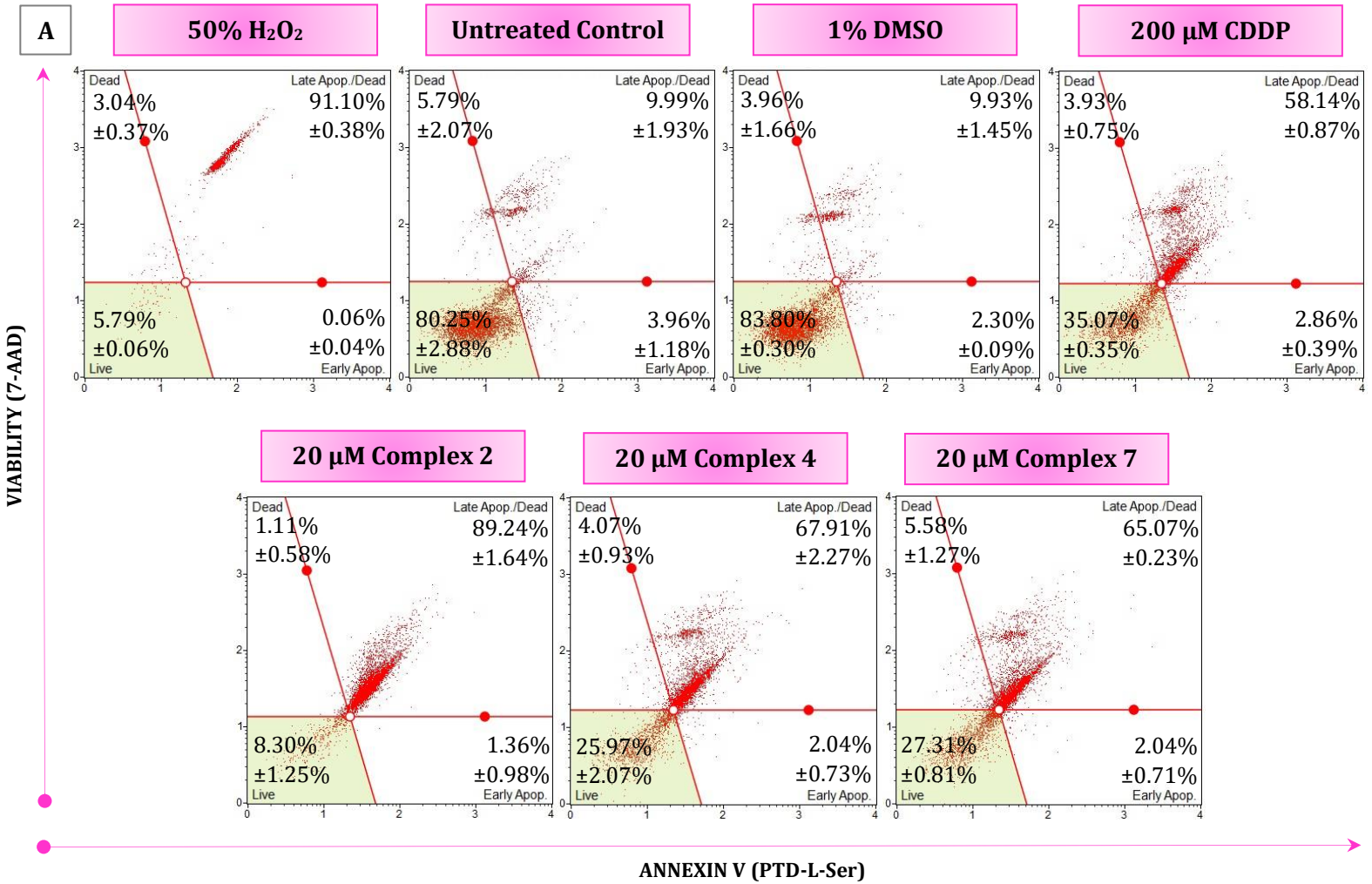


Figure 4.4. Mitochondrial potential and cellular plasma permeabilization were quantified in malignant **(A)** MCF-7 and **(B)** MDA-MB-231 breast cells using a Muse® MitoPotential kit. The following treatments were an untreated control or treated with 1% DMSO (vehicle control), 200 µM CDDP (positive apoptotic control) or 20 µM of selected complexes **2**, **4** and **7** for 24 h. Calculated average percentages are displayed in the dot diagrams, accompanied by the ±SEM (n = 6). Co-detection of MitoPotential dye and 7-AAD indicate intact mitochondria and cell death, respectively.


A
50% H2O2
Untreated Control
1% DMSO
200 µM CDDP
Dead
Late Apop./Dead
3.04% ±0.37%
91.10% ±0.38%
5.79% ±0.06%
Live
0.06% ±0.04%
Early Apop.
5.79% ±2.07%
9.99% ±1.93%
80.25% ±2.88%
3.96% ±1.18%
3.96% ±1.66%
9.93% ±1.45%
83.80% ±0.30%
2.30% ±0.09%
3.93% ±0.75%
58.14% ±0.87%
35.07% ±0.35%
2.86% ±0.39%
20 µM Complex 2
20 µM Complex 4
20 µM Complex 7
1.11% ±0.58%
89.24% ±1.64%
8.30% ±1.25%
1.36% ±0.98%
4.07% ±0.93%
67.91% ±2.27%
25.97% ±2.07%
2.04% ±0.73%
5.58% ±1.27%
65.07% ±0.23%
27.31% ±0.81%
2.04% ±0.71%
VIABILITY (7-AAD)
ANNEXIN V (PTD-L-Ser)

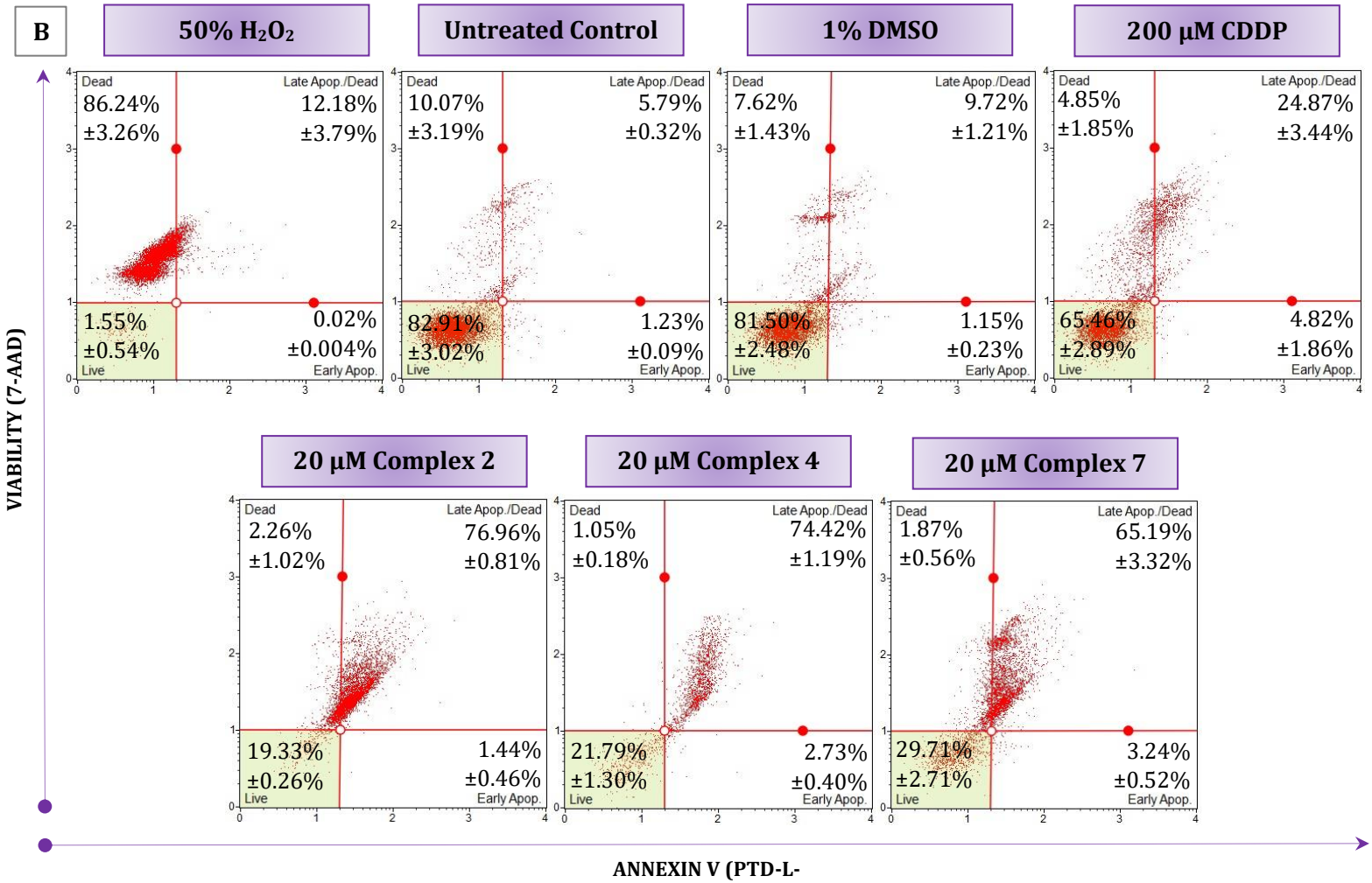


Figure 4.5. The mode of cell death was quantified in malignant **(A)** MCF-7 and **(B)** MDA-MB-231 breast cells using a Muse® Annexin V & Dead Cell kit. The following treatments were an untreated control or treated with 1% DMSO (vehicle control), 200 µM CDDP (positive apoptotic control), 50% H_2O_2 (positive necrotic control) or 20 µM of selected complexes **2**, **4** and **7** for 24 h. Calculated average percentages are displayed in the dot diagrams, accompanied by the ±SEM (n = 6). Annexin V (Ptd-L-Ser) and 7-AAD co-detection indicates apoptosis and/or necrosis, respectively.

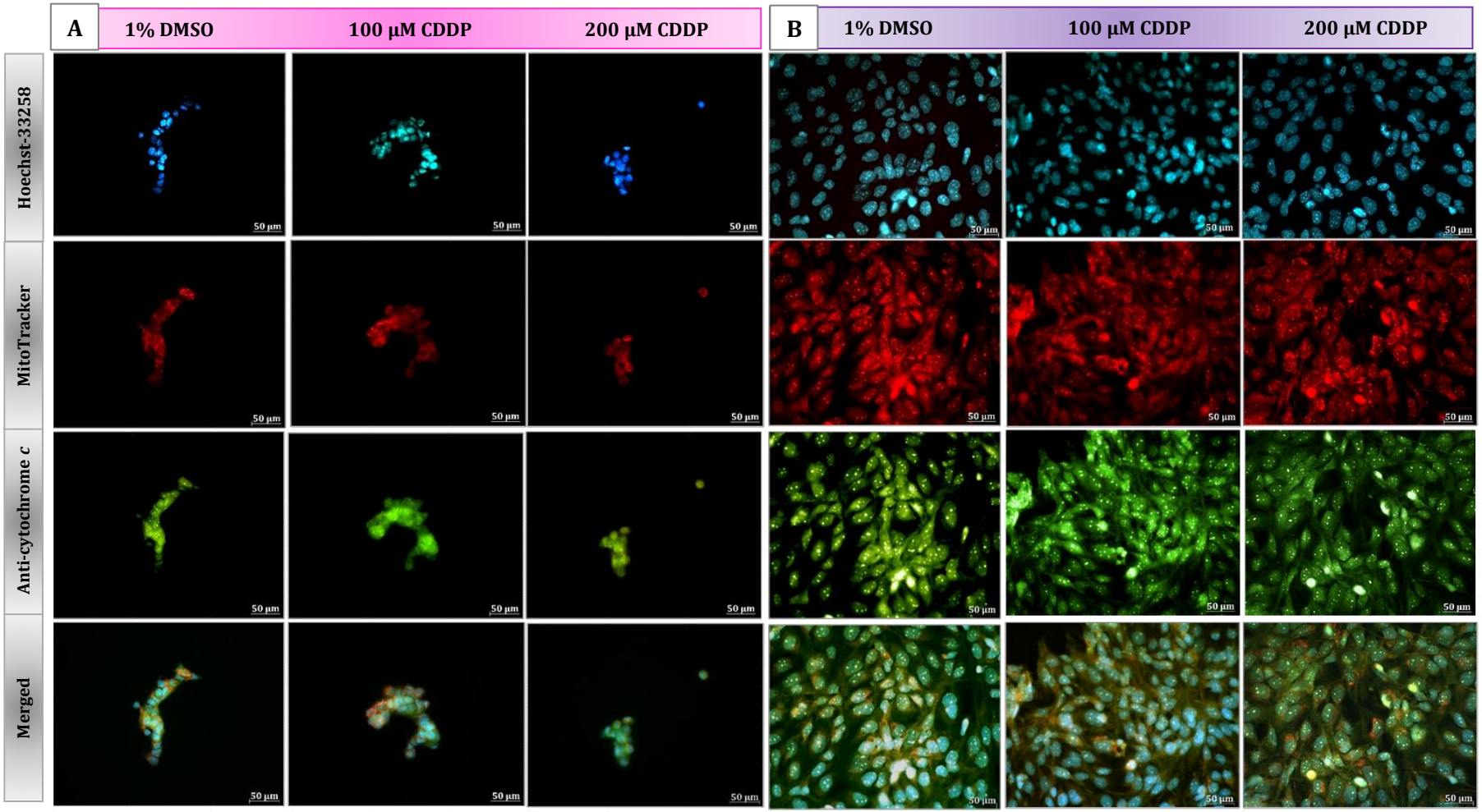


Figure 4.6. Fluorescence images of malignant **(A)** MCF-7 and **(B)** MDA-MB-231 cells induced by control treatments after 24 h. Cells were treated with 1% DMSO (vehicle control), 100 µM and 200 µM CDDP (positive apoptotic control) respectively. The cells were examined using Hoechst-33258 (blue) which stains the nuclei, MitoTracker® Orange CMTMRos (red) and Alexa-Flour® 488 mouse anti-cytochrome *c* specific antibody (green), which stains the mitochondria and cytochrome *c* respectively. Using a Zeiss Axioplan 2 inverted fluorescence microscope and Axio Vision 3.1 software, fluorescence micrographs were captured at 400 x magnification.

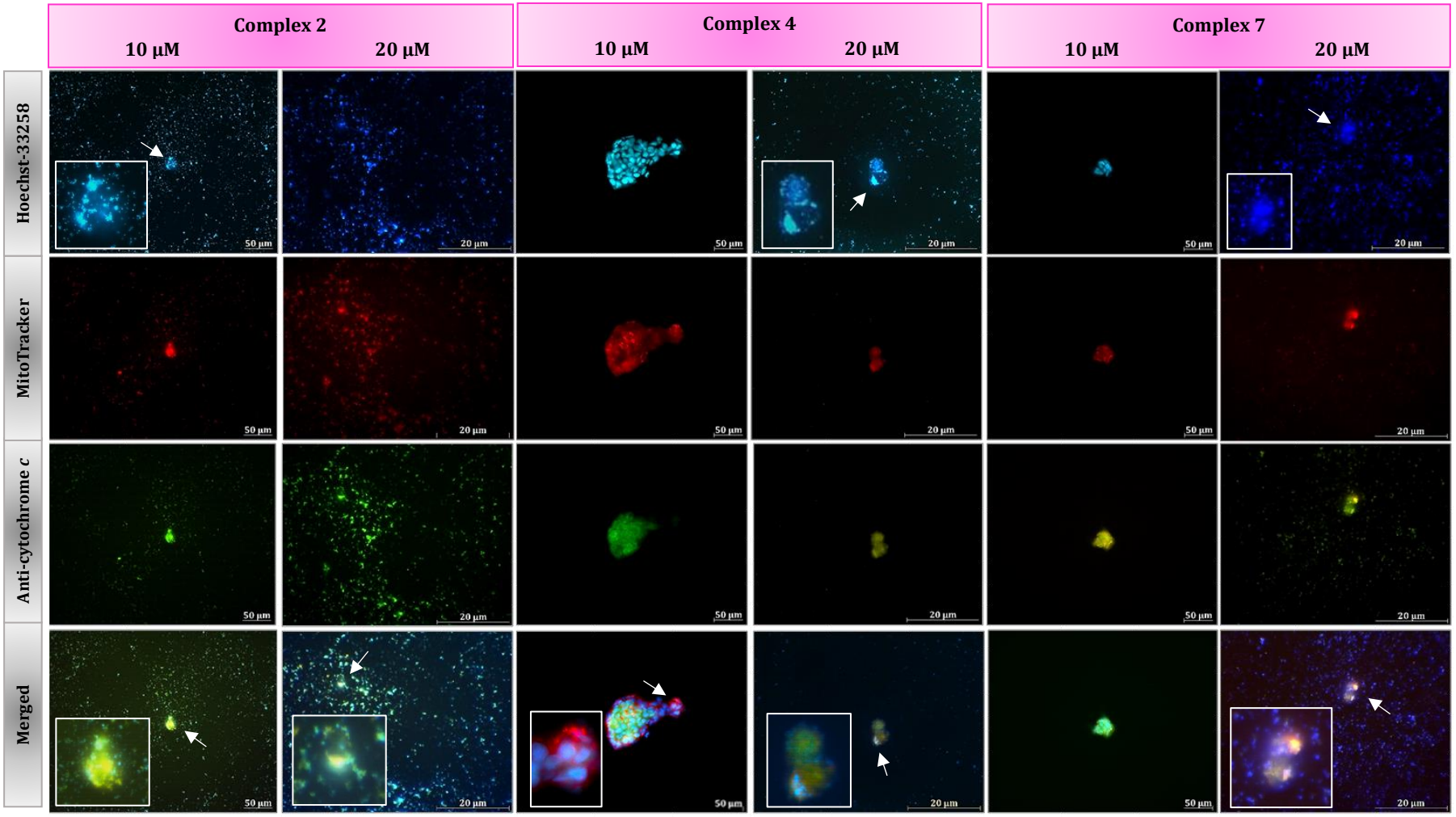


Figure 4.7. Fluorescence images of malignant MCF-7 cells induced by differential treatments after 24 h. Cells were treated with 10 µM and 20 µM silver(I) phosphine complexes **2**, **4** and **7** respectively. The cells were examined using Hoechst-33258 (blue), MitoTracker® Orange CMTMRos (red) and Alexa-Flour® 488 mouse anti-cytochrome *c* specific antibody (green). Using a Zeiss Axioplan 2 inverted fluorescence microscope and Axio Vision 3.1 software, fluorescence micrographs were captured. Cells treated with 10 µM were taken at 400 x magnification while cells treated with 20 µM were taken at 630 x magnification. White arrows indicate condensed DNA or nuclear debris, decreased mitochondria integrity and cytochrome *c* release. Digitally zoomed in images were included to highlight these changes.

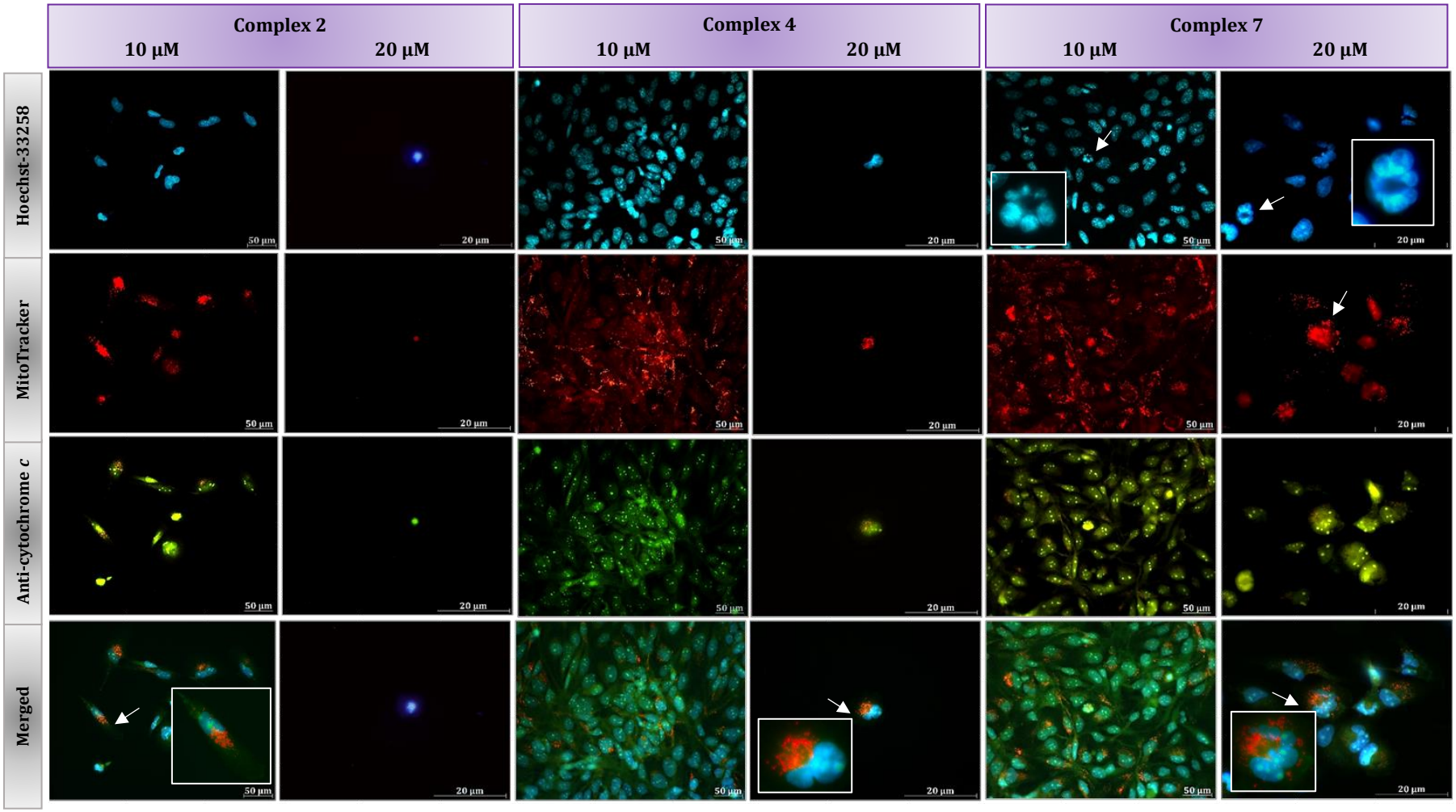


Figure 4.8. Fluorescence images of malignant **MDA-MB-231** cells induced by differential treatments after 24 h. Cells were treated with 10 µM and 20 µM silver(I) phosphine complexes **2**, **4** and **7** respectively. The cells were examined using Hoechst-33258 (blue), MitoTracker® Orange CMTMRos (red) and Alexa-Flour® 488 mouse anti-cytochrome *c* specific antibody (green). Using a Zeiss Axioplan 2 inverted fluorescence microscope and Axio Vision 3.1 software, fluorescence micrographs were captured. Cells treated with 10 µM and 20 µM were taken at 400 x or 630 x magnification. White arrows indicate condensed DNA, decreased mitochondria integrity and cytochrome *c* release. Digitally zoomed in images were included to highlight these changes in the cell.

4.4. Discussion

From chapter two, several silver(I) phosphine complexes decreased proliferation significantly after 48 h of treatment, in the MCF-7 cells; these were complexes **2**, **4**, **7**, **9**, **12** and **13** (**Figure 2.12**, chapter two). However, only three silver(I) phosphine complexes **2**, **4** and **7** were effective in decreasing cellular viability after 48 h in the MDA-MB-231 cell line (**Figure 2.11**, chapter two). To compare cell death activities between the MCF-7 and MDA-MB-231 cells, complexes **2**, **4** and **7** were selected for studies conducted herein. Cell assays targeting the mitochondria were used to determine whether these complexes induce an apoptotic cell pathway.

4.4.1. Mechanistic insights into the anticancer effects of silver(I) phosphine complexes in MCF-7 and MDA-MB-231 cells

Excessive ROS damage mitochondria by altering the potential of the mitochondrial membrane ($\Delta\Psi m$) during the early phases of apoptosis. The formation of PTP in the IMM allows for the release of various proapoptotic proteins, of particular interest is cytochrome *c* (detailed in point *1.4.1.* (b), in chapter one). These key processes were the focus of this comparative study (Aslam *et al.*, 2023; Hu *et al.*, 2022; Johnstone *et al.*, 2002; Kim *et al.*, 2017).

In addition, complexes **2**, **4** and **7** induced morphological changes characteristic of apoptosis. Comparable results of cell shrinkage, condensation, rounding, apoptotic blebbing, and bodies have been described before in malignant cells treated with other silver(I) phosphine complexes within the same family (Engelbrecht and Cronjé, 2018; Engelbrecht *et al.*, 2018; Human-Engelbrecht *et al.*, 2017; Human *et al.*, 2015; Ferreira *et al.*, 2015).

(a) *Generation of reactive oxygen species*

Flow cytometry data revealed that despite exhibiting significant toxicity (**Figures 2.11** and **2.12**, and **Table 2.3**, chapter two), after 24 h, the production of ROS in MCF-7 and MDA-MB-231 cells was not substantially increased by complex **2**. While complexes **4** and **7** produced slightly significant ($P < 0.05$) intracellular ROS levels in MCF-7 (**Figure 4.3-A**, **4**: 17.90% ±1.65% and **7**: 20.29% ±0.91%) and MDA-MB-231 cells (**Figure 4.3-B**, **4**: 10.96% ±0.29% and **7**: 12.48% ±1.69%), respectively. Acosta-Casique *et al.* (2023) investigated whether ROS production regulates the MAPK pathway in breast cancer. The activation of the RAS cascade is known to increase cell proliferation and migration (Anestopoulos *et al.*, 2022; Bertolotto, 2013). This pathway is altered in 40% of all cancer types. Acosta-Casique *et al.* (2023) treated MCF-7 and MDA-MB-231 cells with an antioxidant, N-acetyl-cysteine (NAC) resulting in abrogation of ROS production. They then treated the respective breast cells with 20 nM PD0325901 (MEK inhibitor) (Alessi *et al.*, 1995), which decreased ROS levels but induced morphological changes after only 60 min. They concluded that higher basal levels

of ROS within breast cells prevent excessive extracellular signal-regulated kinase (ERK) phosphorylation. Furthermore, a study by Ota *et al.* (2021) examined the anticancer properties of a silver thiosulfate complex (STS), $[Ag(S_2O_30_2]^{-3}$, on MCF-7 cells. In that study, it was observed that STS led to the accumulation of ROS and caused cell death. However, caspase-3 was not activated, and it was assumed STS did not initiate apoptosis, despite this, it remained cytotoxic in MCF-7 cells. This cytotoxicity was dependent on the concentration used. This suggests that the accumulation of ROS does not always necessarily induce apoptosis. Future studies investigating the effect silver(I) phosphine complexes have on ERK phosphorylation or in the MAPK signalling pathway could be of interest. In addition, ROS levels can be measured at different time points (for instance, at 3 h and/or 12 h). Since ROS production is an initial response to cellular stress, excessive levels may be produced at an earlier stage, prompting the subsequent loss of ΔΨm.

(b) *Mitochondrial potential and cellular plasma permeabilization*

As illustrated in **Figure 4.4-A**, the MCF-7 treated with silver(I) phosphines show signs of mitochondrial depolarization, as reflected by the increase in the percentage of depolarized dead cell populations. The loss of ΔΨm was significant in MCF-7 cells treated with complexes **2**, **4** and **7** ($P < 0.001$). Complex **2** produced the highest depolarized dead population of 90.81%, almost double the population percentage when compared to CDDP (58.14%). Altay *et al.* (2022) investigated the anticancer activity of $[Ag(\mu\text{-dice})]_n$ and $[AgH(nif)_2]$ complexes against MCF-7 cells. It is believed that the loss of ΔΨm was similar to the silver(I) phosphine complexes shown in this study and is an apoptotic mechanism. Previous studies by Kriel and Coates (2012) explain that the loss of ΔΨm is an inducer of apoptosis. Rackham *et al.* (2007) synthesized $[Au(d_2pypp)_2]Cl$, which resulted in a decrease of ΔΨm in treated MDA-MB-468 cells. Lipophilic-cationic properties of complexes target the mitochondria within malignant cells. Similar results were shown in MCF-7 silver(I) phosphine-treated cells (**Figure 4.4-A**). Whereas in **Figure 4.4-B**, MDA-MB-231 silver(I) phosphine-treated cells resulted in no significant number of depolarized live or depolarized dead cells, as the majority of the treated populations were dead cells (complex **2**: 89.15%; **4**: 77.97% and **7**: 77.22%). This could be due to the 20 µM treatment used. A shift into the depolarized quadrants might have been observed at a lower concentration, similar to the low mean IC_{50} values (**Table 2.3**, chapter two) for MDA-MB-231 cells. In addition, metallo-drugs are known to result in OMM dysfunction. Banti *et al.* (2019) treated MCF-7 cells with $[Ag_3(Gly)_2NO_3]_n$, and after 48 h of incubation, the mitochondrial membrane permeability collapsed (no loss of ΔΨm). It can be assumed that an apoptotic response may have occurred at an earlier time point in the MDA-MB-231 cells (**Figure 4.4-B**) and results are comparable here, as longer incubation times (24 h and 48 h) were investigated (Banti *et al.,* 2019).

3.4.1.2. Identifying the mode of cell death in malignant MCF-7 and MDA-MB-231 cell lines

(a) *Ptd-L-Ser externalization*

To evaluate the mode of cell death by silver(I) phosphine complexes, the Muse® Annexin V and Dead Cell assay was used. Ptd-L-Ser externalization was shown in MCF-7 (**Figure 4.5-A**) and MDA-MB-231 cells (**Figure 4.5-B**), treated with 20 µM of the complexes. Complex **2** resulted in the largest population of late apoptotic cells in both breast cell lines. These complexes had low IC_{50} concentrations of 4.58 µM and 6.21 µM for MCF-7 and MDA-MB-231 cells, respectively (**Table 2.3**, chapter two). In both silver(I) phosphine-treated cell lines, when compared to CDDP treatment, the proportion of apoptotic cells was higher. Comparable results were shown by Ferreira *et al.* (2015), where MCF-7 cells were treated with 10 µM of four silver thiocyanate complexes. Findings revealed Ptd-L-Ser externalization, in which the majority of cell populations were late apoptotic. Complex **2** is a variant within the same family as the silver thiocyanate complexes tested by Ferreira *et al.* (2015). In this study, 20 µM instead of 10 µM treatments was used, which is likely the reason a higher late apoptotic population was observed. In addition, Şahin-Bölükaşi *et al.* (2020) highlight the anticancer benefits of silver(I)N-heterocyclic carbene (Ag-NHC) complexes. They revealed their antiproliferative action towards MCF-7 and MDA-MB-231 cell lines and their non-toxicity to non-malignant cells. The same was shown with silver(I) phosphine complexes (data presented in chapter two). Habib *et al.* (2019) showed that two Ag-NHC complexes caused dose-dependent cytotoxicity and apoptosis in MDA-MB-231 cells after 6 h of incubation, with high apoptotic cells of 71.91% and 83.16%, respectively.

(b) *Cytochrome c release, mitochondrial integrity and DNA damage*

The experimental setup involved the use of Hoechst-33258, Alexi-Flour® 488 mouse anti-cytochrome *c* specific antibody, in conjunction with MitoTracker® Orange CMTMRos for the purpose of co-staining DNA, cytochrome *c* and metabolically active mitochondria, respectively. Cytochrome *c* is a mitochondrial respiratory chain electron transporter, and it is released into the cytoplasm upon permeabilization of the mitochondrial outer membrane/dysfunctional mitochondrial integrity. It then activates the intrinsic pathway of apoptosis (described in chapter one) (Cai *et al.*, 1998; Pessoa, 2022; Yang *et al.*, 2009). **Figures 4.7** and **4.8**, demonstrate the effects of treating MCF-7 cells with 10 µM and 20 µM of complex **2**. This resulted in cellular content and fragmented nuclear content spillage, while MDA-MB-231 treated cells resulted in pyknotic nuclei and cytochrome *c* release. Both breast cell lines treated with complexes **2**, **4** and **7** resulted in damaged DNA, either karyorrhexis or pyknotic, with dysfunctional mitochondria and cytochrome *c* release, suggestive of its translocation into the cytosol. Similar findings were observed by Engelbrecht *et al.* (2018), whereby fluorescence micrographs of treated SNO cells with 10 µM of complex $[AgSCN\{P(4\text{-}MeOC_6H_4)_3\}_2]_2$ revealed visible indications of nuclear fragmentation and condensation, the

expulsion of cytochrome *c* and mitochondrial disruption. The fact that $[AgSCN\{P(4\text{-}MeOC_6H_4)_3\}_2]_2$ belongs to the same family of silver mono-dentate phosphine complexes as **2**, **4**, and **7** used in this investigation, provides additional evidence that intrinsic apoptosis was initiated.

Overall, treatment of MDA-MB-231 cells with complexes **2**, **4** and **7** resulted in morphological changes, where cells had rounded with apoptotic blebbing. Although ROS levels remained insignificant, there was a collapse in mitochondrial membrane permeability (no evident loss of $\Delta\Psi m$). Findings showed a substantial increase in the quantity of late apoptotic cells, with the release of cytochrome *c* and damaged mitochondria and DNA. It can be assumed that an apoptotic response occurred at an earlier time point. Further investigations of the apoptotic pathway could confirm this. From the above data, it is evident that complexes **2**, **4** and **7** induce a probable apoptotic response in the MCF-7 cell line, with the presence of morphological changes such as cell rounding and apoptotic bodies, the loss of the $\Delta\Psi m$, translocation of Ptd-L-Ser and Annexin V binding, and the occurrence of cytochrome *c* release, damaged mitochondria and DNA. Complex **4** was investigated for its potential use as an additional therapeutic in treating MCF-7 cells, depending on whether it targets ER-α and ER-β. This was determined by using the *in silico* molecular docking methods described in chapter five.

CHAPTER FIVE:
IN SILICO MOLECULAR MODELLING OF COMPLEX 4 WITH ESTROGEN RECEPTORS ALPHA AND BETA

5.1. Prologue

Molecular docking is an *in silico* process used to predict ligand-receptor interactions. Molecular docking and computer modelling are important methods for studying the structure and function of molecular interactions. Ligand-protein/receptor docking aims to determine dominating binding model(s) of a ligand when it interacts with a protein or receptor, with a known three-dimensional structure. Software advancements to determine these structures and binding free energies (ΔG) have substantially benefited drug design throughout the years. These methods were further developed to give insight into the molecular mechanisms between various-sized molecules and have been widely used in drug discovery applications (Eid *et al.*, 2018; Fukunishni *et al.*, 2022; Karplus and McCammon, 2002; Li *et al.*, 2019; Pinzi and Rastelli, 2019).

Breast cancer, as previously mentioned, is the prominent cause of death in women (Arnold *et al.*, 2022). The estrogen receptor has two distinct forms: estrogen receptor alpha (ER-α) and estrogen receptor beta (ER-β). The abnormal expression of ER-α is prevalent in 75 - 80% of breast cancers (as well as cervical and ovarian cancers) and is responsible for their enhanced growth (Tan *et al.*, 2009; Sharma *et al.*, 2018). It is generally established that ER-α responds favourably to hormone therapy which improves prognosis. The ER can be functionally broken down into three distinct domains: the C-terminal ligand-binding domain, the N-terminal domain, and the DNA-binding domain. Targeting the C-terminal ligand-binding domain of ER-α is an attractive target for the treatment of hormone-dependent breast cancer (Maruthanila *et al.*, 2019).

Antiestrogens are agents that bind to estrogen and inhibit the transactivation site and, subsequently, estrogen-induced cell proliferation. A number of antiestrogen medications have been developed to block the estrogen signal. Among these are tamoxifen and bazdoxifene. Other inhibitors, such as letrozole, hinder the ovaries from producing hormones (Barzaman *et al.*, 2020). Maruthanila *et al.* (2019) explain that there is an increasing need for the development of antiestrogens that target the C-terminal ligand-binding domain. To determine whether complex **4** targets the ER-α and ER-β in MCF-7 cells, molecular docking simulations were studied. Complex **4** was chosen as it was the only complex to significantly decrease the viability across all malignancies (data presented in chapter two, **Table 2.2** and **Table 2.3**). In the A549, Hep-G2, HT-29, MCF-7 and MDA-MB-231 cells, complex **4** demonstrated substantial anticancer activity (data presented in chapters three and four). Overall, it can be presumed to be a potential hit-to-lead anticancer and antimetastatic complex. Data presented

herein will allow us to test other silver(I) phosphine complexes within the same family to determine their antiestrogen potential.

5.2. Methods

5.2.1. Molecular Dockings

The protocol, *Using AutoDock for Ligand-Receptor Docking* instructions was followed (Morris *et al.*, 2008) and run by Dr. Herna de Wit at the School of Chemistry, at the University of Witwatersrand, Johannesburg (South Africa).

5.2.1.1. Protein preparation

The crystallographic structures of estrogen receptor alpha in complex with receptor degrader 6 (PDB ID: 6WOK, resolution 2.31 Å, **Figure 4.1. A**) and sulfonamides as selective estrogen receptor beta agonists (PDB ID: 2YLY, resolution 3.20 Å **Figure 4.1. B**), were acquired from the Protein Data Bank (PDB). The proteins were prepared and docked using the MGLTools (https://ccsb.scripps.edu/mgltools/) package with AutoDockTools4 *version 4.2.6* (ADT4) (http://autodock.scripps.edu/). The proteins were arranged by eliminating water molecules and hydrogen atoms and inserting polar hydrogen atoms. Gasteiger(-Marsili) partial charges were calculated and added for each atom: 6WOK = -18.9706; 2YLY = 0.0143, and ADT4 atom types were assigned to each protein. Both proteins were saved as `.pdbqt` formatted files (`q` represents the partial atomic charge and `t` represents the torsion).

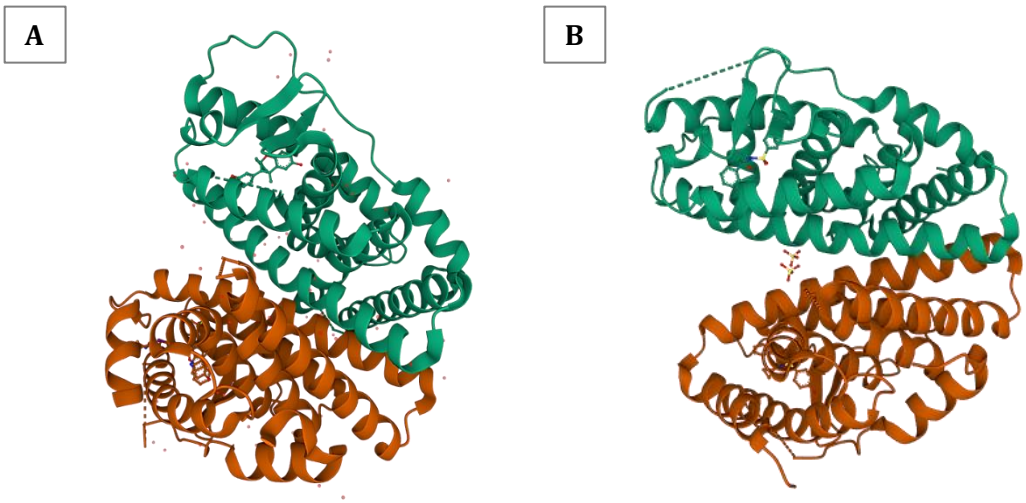


Figure 5.1. (A) 6WOK nuclear protein: crystal structure of **estrogen receptor alpha (ER-α)** in complex with receptor degrader 6 and **(B)** 2YLY receptor: sulfonamides as selective **estrogen receptor beta (ER-β)** agonists, obtained from the PDB and shown in ribbon style (https://www.rcsb.org/structure).

5.*2.1.2. Ligand (Complex **4**) preparation*

Ligand preparation was performed using the Discovery Studio Visualizer (DSV). The ligand was saved as a .pdb file. This file was imported into ADT4, where calculations for partial atomic charges for each atom were automatically completed, and the ligand was then saved as a .pdbqt file. ADT4 provides the interactive visualization of docked ligand-receptor conformations in three dimensions (Morris *et al.*, 2008). Forty-two non-polar hydrogens were combined, 51 aromatic carbons were identified, and 12 rotatable bonds were found. The TORSDOF is equal to 12.

Ligand (complex **4**) parameters:

Atom types: A, Ag, Br, NA, P

Centre of the molecule: 6.032; 3.610; 8.921

Active torsions = 12

Number of torsional degrees of freedom (TORSDOF) in the ligand = 12

Specify initial dihedrals: Yes

Random initial relative dihedrals

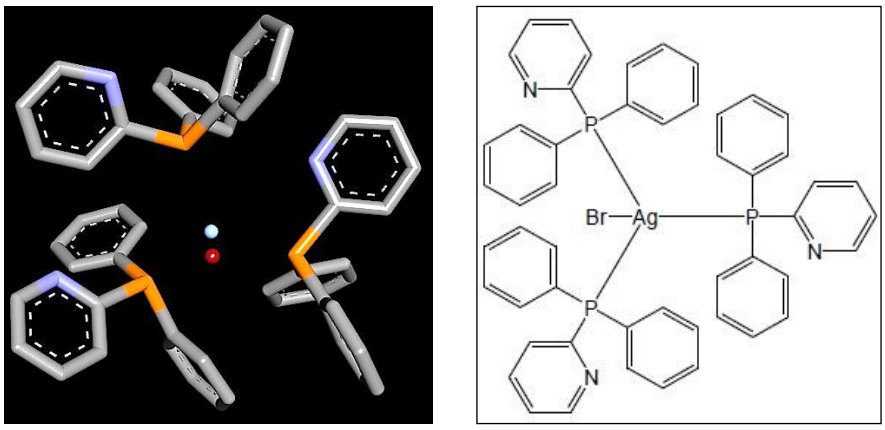


Figure 5.2. Molecular model and schematic structure of the ligand complex **4.** The three-dimensional preparation of complex **4**, [Silver(I) diphenyl-2-pyridylphosphine]Br in DSV. *Key:* Ag (light blue) Br (red) 1:3 diphenyl-2-pyridlphosphine ligand (**L2**) (N: dark blue; C: grey; phosphine: orange).

5.2.1.3. Grid parameter file preparation and dockings

The grid parameter formatted files (**.**gpf, **Appendix III**, **Data A1** and **A2**) were used in ADT4 to compute the types and locations of grid maps for docking. Grids were presented as a cubic box structure, and the number of points and coordinates are shown in **Table 5.1** for each protein, respectively. Thereafter docking parameter files (**.**dpf, **Appendix III**, **Data A3** and **A4**) were run in ADT4. These files provided information on which ligand to dock, the centre coordinates, the number

of torsions, the residue flexibility, the docking algorithm, and the total number of runs (Morris *et al.,* 2008; Forli *et al.,* 2016). The genetic algorithm (GA) was used to dock complex **4** with WOK6 and 2YLY, respectively. The parameters were summarized in **Table 5.2**. The two models with the lowest binding energies were selected as the best: ER-α: model **14** and ER-β: model **91**.

Table 5.1. The coordinates and number of points (npts) of the cubic box used for docking complex **4** to the 6WOK nuclear protein (ER-α) and 2YLY receptor (ER-β).

Receptor	Side	Coordinate	Number of points (Å)
6WOK (ER- α)	X	24.274	126
	Y	-5.788	126
	Z	16.409	126
2YLY (ER-β)	X	-44.414	126
	Y	-19.34	126
	Z	-25.466	126

Table 5.2. The GA parameters used for docking complex **4** to the 6WOK nuclear protein (ER-α) and 2YLY receptor (ER-β).

Parameter	Value
Number of GA runs	100
Torsional degrees of freedom	12
Number of individuals in population	150
Maximum number of energy evaluations	2500000
Maximum number of generations	27000
Number of top individuals to survive next generation	1
Rate of gene mutation	0.02
Rate of crossover	0.8

5.2.1.4. Visualisation and analysis of docking results

After docking, the best (minimum) scoring functions and root-mean-square deviations (RMSD, **Figure 5.3**) were calculated. Models **14** (ER-α) and **91** (ER-β) were visualized in two-dimensional view and three-dimensional structures in DSV, where hydrogen bonding, amino acid residues and surface annotations of complex **4**'s interaction with the proteins were evaluated (**Figure 5.4**).

5.3. Results

To determine whether complex **4** (**Figure 5.2**) could be utilized as a hormonal therapeutic modality, it was docked to ER-α (PBD ID: 6WOK nuclear protein) and ER-β (PDB ID: 2YLY receptor; **Figures 5.1-A** and **5.1-B**, respectively). One hundred docking runs were performed and the run (or model) with the lowest binding energies (kcal/mol) for each docking conformation was selected for further analysis in DSV.

TORSDOF (point *5.2.1.2*) is a keyword used to describe the number of rotational degrees of freedom in the ligand (i.e., complex **4**). Morris *et al.* (2008) explain that the total change in free energy can be calculated based on how much free energy is lost when binding. RMSD cluster analysis (**Figure 5.3**) determined the lowest binding energies of complex **4** docked with ER-α and ER-β. It was found that complex **4** revealed 41 distinct conformational clusters using an RMSD-tolerance of 2.0 Å, these energies ranged from -3.3 kcal/mol to -7.13 kcal/mol for ER-α (**Figure 5.3-A**) and -3.3 kcal/mol to -5.23 kcal/mol for ER-β (**Figure 5.3-B**). The average RMSD of the top-scoring ligand positions was compared. The final GA state for complex **4** docked with the 6WOK nuclear protein and the 2YLY receptor was model **14**, with an estimated final binding free energy of -7.40 kcal/mol (**Appendix III**, **Data A6**) and model **91**, with an estimated final binding free energy of -7.13 kcal/mol (**Appendix III**, **Data A7**). The data presented from here on is representative of these respective models with the best possible docking scores. The RMSD for complex **4** docked with ER-α was 16.922 Å and the estimated binding free energy was -7.40 kcal/mol, while the RMSD for complex **4** with ER-β was 60.480 Å and the estimated binding free energy was -7.13 kcal/mol.

Figures 5.4 and **5.5** show the three-dimensional models of ER-α and ER-β carrying docked complex **4**. The overview, front view, back view and side view (ER-β) of these interactions was shown here. The main amino acid residues in docked ER-α/ER-β systems confirm the stability of these interactions. From this data, complex **4** binds to ER-α and the 1:3 diphenyl-2-pyridlphosphine ligands with solvent-related forces such as hydrogen bonding. A side view was included for ER-β to examine the angles of the interactions involved. Two of the diphenyl-2-pyridlphosphine ligands as well as the Ag and Br atoms form hydrogen bonding with the receptor. Hydrogen bonding occurs when there are structural changes in the constant aqueous solvent (Fukunishni *et al.*, 2022).

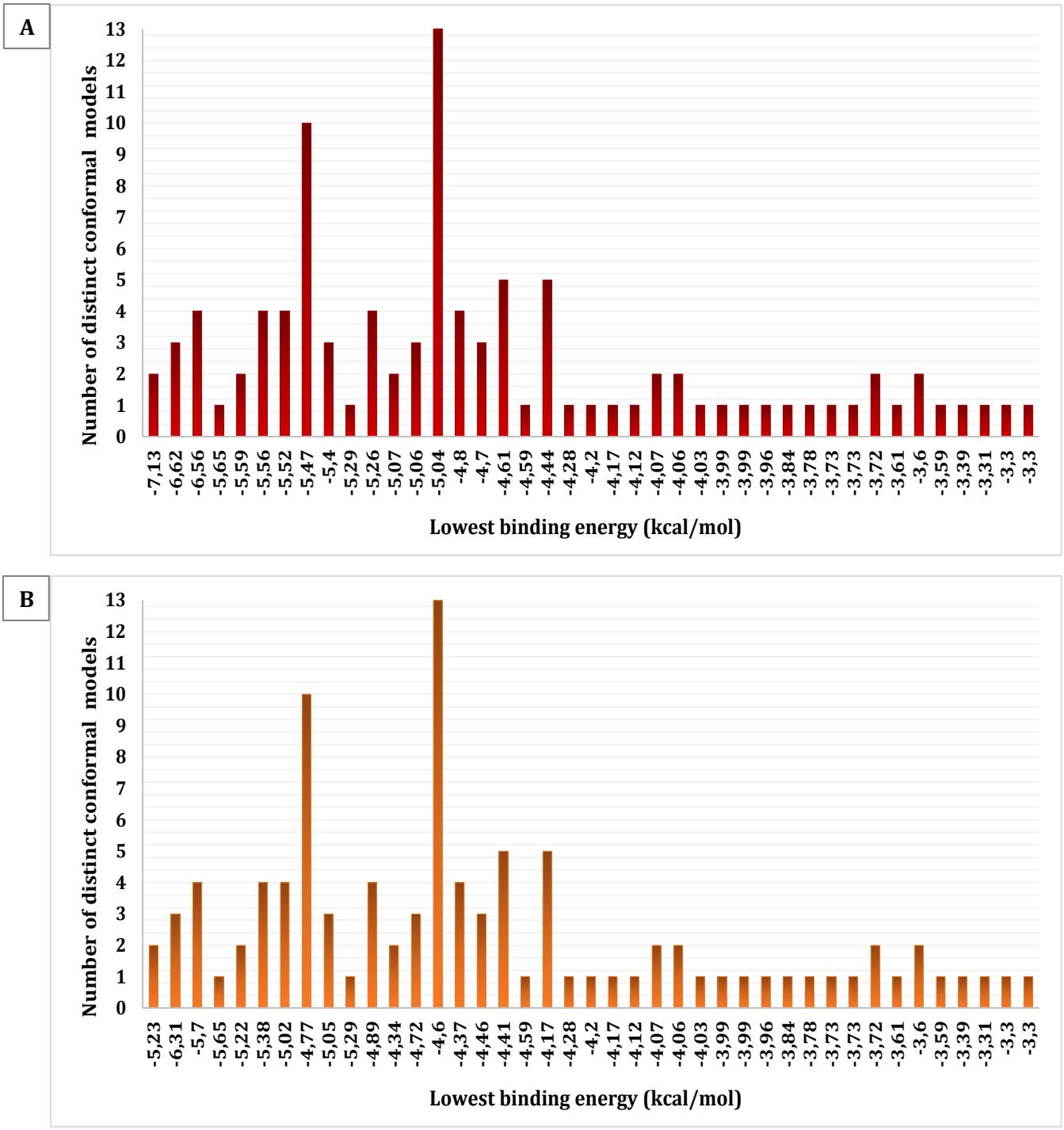


Figure 5.3. RMSD Cluster Analysis. Clustering histograms of complex **4** docked with **(A)** ER-α (PBD ID: 6WOK nuclear protein) and **(B)** ER-β (PDB ID: 2YLY receptor). The lowest binding energy (kcal/mol) with the number of models presenting this energy are shown. Out of 100 runs, 41 distinct conformational clusters were found using an RMSD-tolerance of 2.0 Å.

From the two-dimensional interaction views (**Figures 5.6-A** and **-B**), it was seen that complex **4** forms hydrogen bonds with ER-α through hydroxyl groups with residues Try D:526, Leu D:525, Thr D:347, Trp D:383, Asp D:351 and Pro D:535 and van der Waals forces with surrounding hydrophobic residues Leu D:539, Ser D:536, Met D:343 and Met D:528 with ER-α. With regard to ER-β, complex **4** forms hydrogen bonds through the hydroxyl groups of residues Met B:473, His A:467, Leu B:477, Tyr B:488, Arg B:329, Glu B:332 and Lys A: 471. It is known that binding efficiency increases with the number of current hydrogen bonds (Shivanik *et al.*, 2020).

The optimal physio-chemical scoring functions that interact with complex **4** within the binding sites are depicted in **Figure 5.7**, respectively. This is indicative of the potential energy shifts upon binding. A low negative or positive score indicates a feeble or non-existent binding interaction, while a negative score indicates a substantial binding interaction. The greater the negativity score (or smaller the binding energy), the greater the binding efficiency is (Li *et al.,* 2019; Matossian *et al.,* 2014; Shivanik *et al.,* 2020).

ADT4 was designed to associate Gibbs free binding energy (ΔG) as enthalpy, and this is expressed by ligand-protein van der Waals forces, hydrogen bonding, desolvation and the total intermolecular energy. From **Figure 5.7**, ER-α (represented as red bars) resulted in slightly lower energies of -11.11 kcal/mol and -10.98 kcal/mol, while ER-β (represented as orange bars) resulted in low energies of -10.71 kcal/mol and -10.71 kcal/mol respectively. The relationship between ΔG and entropy loss is represented in terms of unbound systems. When entropy is limited, the free energy is minimized, and the bound conformation is more stable. Due to docking occurring in a constant aqueous solvent, the ligand can have several conformations in surrounding water, but is fixed to a solitary configuration when docked to the receptor (Fukunishni *et al.,* 2022). For complex **4** with ER-α, unbound systems were -8.64 kcal/mol and with ER-β they were -9.14 kcal/mol. The most indicative energies of total interaction strength generated by ADT4 are the final binding energy, ligand proficiency, and the inhibition constant, Ki (Matossian *et al.,* 2014). From **Appendix III Data A5**, the inhibition constant for complex **4** docked to ER-α was 3.76 µM and from **Data A6**, the inhibtion constant for complex **4** docked to ER-β was 5.96 µM.

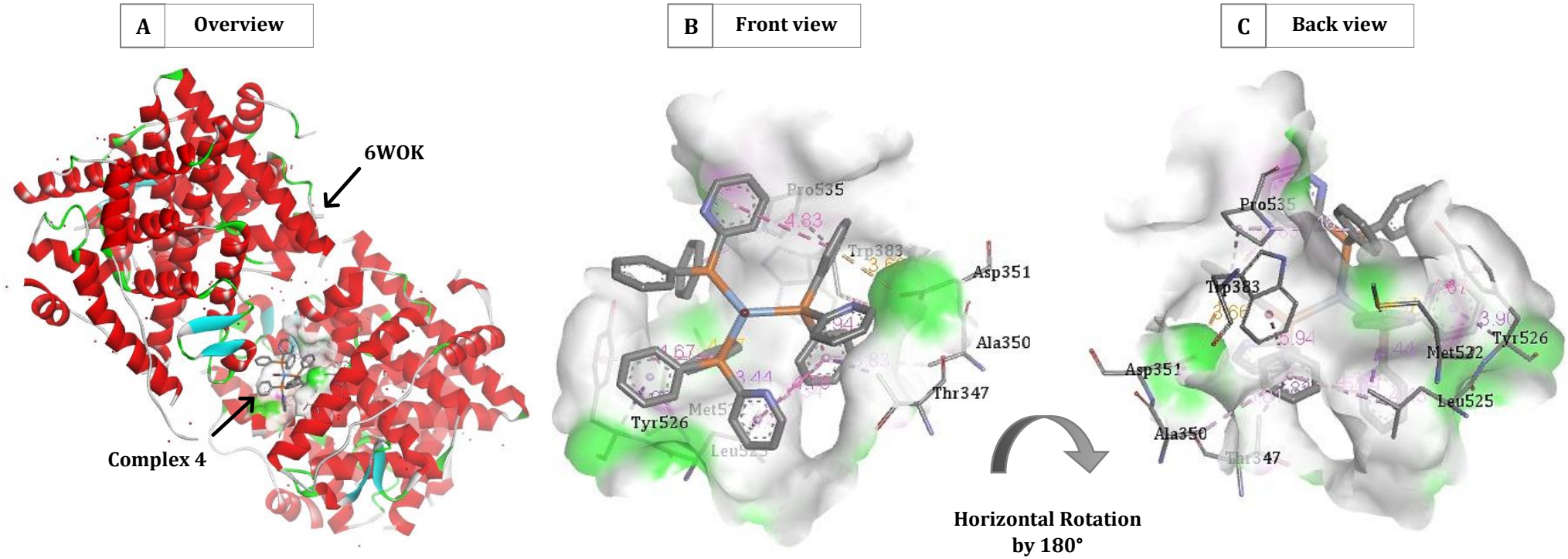


Figure 5.4. Three-dimensional model of ER-α (PBD ID: 6WOK) shown as a ribbon style carrying docked complex **4**. **(A)** Overview of docked complex **4** to ER-α, **(B)** front view and **(C)** back view of complex **4** with the interacting amino acid residues and hydrogen bonding (hydrogen acceptor bonds are represented by green and hydrogen donor bonds are represented by pink).

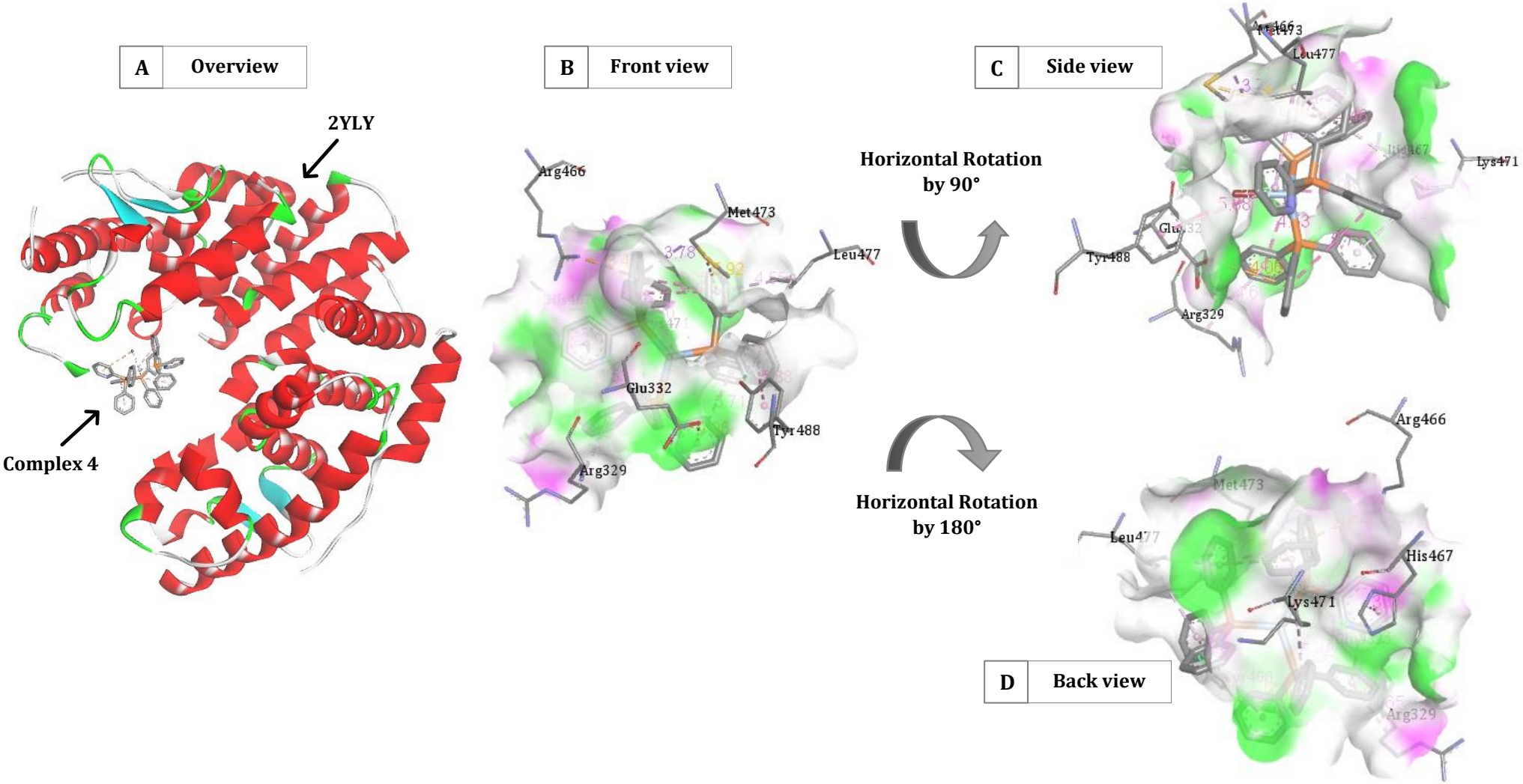


Figure 5.5. Three-dimensional model of ER-β (PBD ID: 2YLY) shown as a ribbon style carrying docked complex **4**. **(A)** Overview of docked complex **4** to ER-β, **(B)** front view, **(C)** side view and **(D)** back view of complex **4** with the interacting amino acid residues and hydrogen bonding (hydrogen acceptor bonds are represented by green and hydrogen donor bonds are represented by pink).

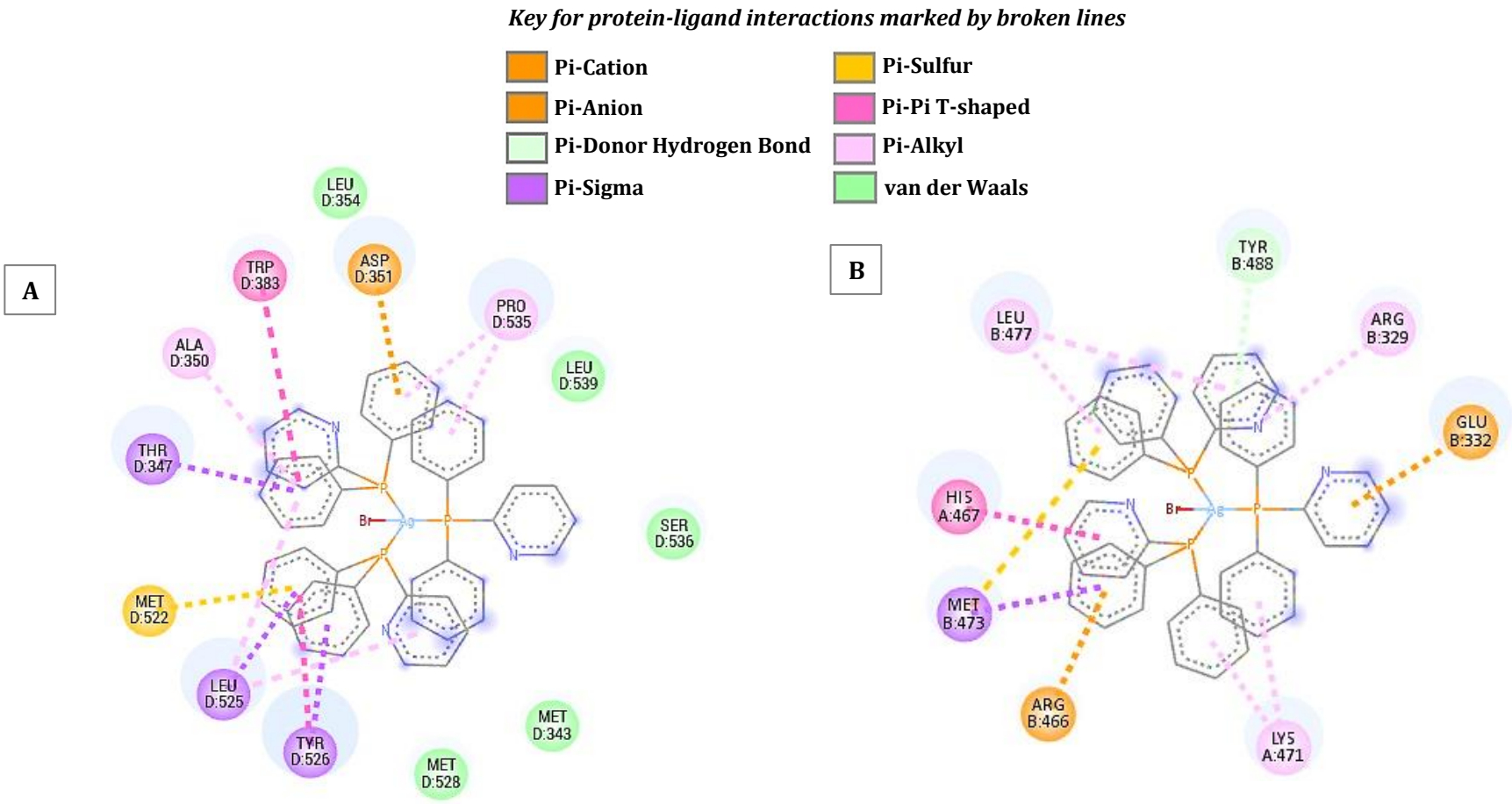


Figure 5.6. The two-dimensional view of the best docked pose of complex **4** with **(A)** ER-α (PBD ID: 6WOK) and **(B)** ER-β (PDB ID: 2YLY), showing the protein-ligand interactions involved between the ligand and amino acid residues. The main amino acid residues associated in the protein-ligand interactions with ER-α and ER-β are shown. Protein-ligand interactions are illustrated as broken lines in the representative colour indicated in the above key.

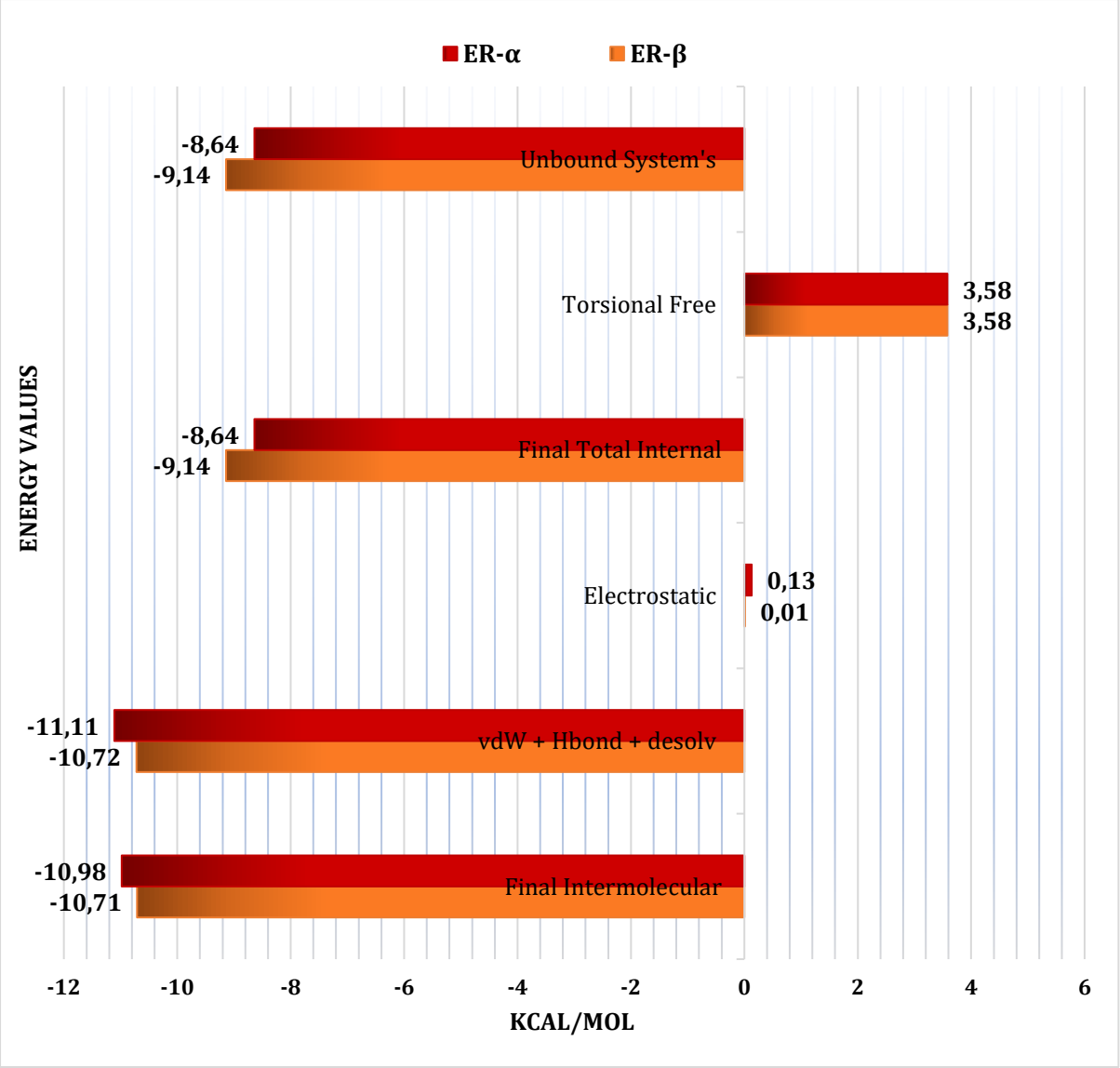


Figure 5.7. Physio-chemical scoring functions/energy values of bound conformational models (kcal/mol) between complex **4** and ER-α (PBD ID: 6WOK, red) and ER-β (PDB ID: 2YLY, orange). Conformations include energies from unbound systems, electrostatic, torsional free and final intermolecular and total internal energy as well as abbreviations: vdW, van der Waals energy; Hbond, Hydrogen-bonding; and desolv, desolvation.

5.4. Discussion

To improve the understanding of complex **4**'s binding approach, it was docked with the crystallographic structures of estrogen receptor alpha and estrogen receptor beta. Both structures were obtained from the PDB (**Figures 5.1-A** and **5.1-B**, respectively). Docking procedures consist of three steps: (1) the ligand (complex **4**) is allocated to the receptor's surface (ER-α and ER-β), resulting in numerous 'docking poses'; (2) these 'docking poses' are evaluated by their ΔG, and stable poses are selected; and (3) the selected poses are scored, where final dockings correspond to the ΔG values produced. Due to the presence of Ag and Br atoms in complex **4**, this study focused on physio-chemical scoring functions as components were integrated into the ligand. This approach can be used to discover alternative anticancer drugs that specifically target ERs (Eid *et al.*, 2018; Fukunishni *et al.*, 2022).

Ruvinsky (2007) showed that docked positions generated in ADT4 that were grouped into clusters, that contained ligand positions of a pre-set RMSD value, improved docking accuracy. RMSD are quantifiable coefficients that measure the average distance in angstroms (Å) between carbon atoms of the protein (receptor) or the atoms of the ligand (complex or drug) (Ballante and Marshall, 2016). RMSD measurements herein were a tolerance of 2.0 Å, this usually consists of 30 – 70 distinctive conformation clusters (Ruvinsky, 2007). After successful docking, conformations with the lowest binding energies (kcal/mol) were selected (**Figure 5.3**). Out of 100 runs, 41 distinctive conformational clusters were found. As shown, there were additional models present in the -5.04 kcal/mol and -4.6 kcal/mol clusters for each binding (**Figures 5.3-A** and **5.3-B**). For the purposes of this study, only the structures with the lowest energy were evaluated. Molecular modelling of complex **4** with ER-α and ER-β was stable. Future binding investigations can be conducted on the remaining models offered in these dockings.

Figure 5.4 and **Figure 5.5** indicate the three-dimensional models of ER-α and ER-β carrying docked complex **4**. Hydrogen bonding was present between the diphenyl-2-pyridlphosphine ligands, and ER-α as well as in two of the diphenyl-2-pyridlphosphine ligands and Ag and Br atoms and ER-β. Amino acid residues accessible for interaction are a defining feature of the receptor surface of proteins. Due to their functional importance in many proteins (especially enzymes), the accessible amino acid residues are typically well-known (Khazanov and Carlson, 2013). **Figures 5.6-A** and **-B** represent the main amino acid residues involved in the ER-α and ER-β interactions, with complex **4**. Fukunishni *et al.* (2022) explain that large aromatic amino acid residues are likely to bind. Findings herein reveal that the majority of residues share polar and hydrophobic interactions with ER-α and ER-β. In their study, Ferenczy and Kellermayer (2022) used molecular dynamics simulations to investigate the influence of polar and hydrophobic interactions on the stability of protein-ligand complexes. It was shown that the thermodynamic stability and mechanical properties of proteins are influenced by both polar and

hydrophobic interactions. The primary factor contributing to hydrophobicity is often linked to the presence of hydrogen bonding. Hydrogen bonds are considered to be the fourth most prevalent type of interaction between a protein and ligand. According to de Freitas and Schapira (2017), these bonds play a significant role in molecular recognition processes and contribute to overall stability. The importance of hydrophobic interactions in protein-ligated complexes increases proportionally with the size of the ligand, while polar interactions are dominant in complexes of fragment-sized ligands (Ferenczy and Kellermayer, 2022). Hence, a greater number of hydrophobic interactions (acceptor and donor bonds) were observed between complex **4** and both estrogen receptors (**Figure 5.4** and **Figure 5.5**). Two hydrophobic residues, Met D:343 and Met D:528 which form part of ER-α had low surface frequencies and were bound to complex **4** by van der Waals forces. Whereas only one Met B:473 residue, which formed part of ER-βwas bound to complex **4** through hydrogen bonding. Leu, which is a particularly hydrophobic residue of estrogen was bound to complex **4**; ER-α: Leu D:525 and ER-β: Leu B:477. Similar results were observed by Khazanov and Carlson (2013), whereby non-redundant binding sites were docked to protein ligands using the binding mother of all databases (MOAD). Their results revealed that binding of amino acid residues Try and Leu to ligands were more prevalent. Khazanov and Carlson (2013) explain that the majority of proteins retrieved from the PDB exist in aqueous environments and therefore hydrophilic amino acids will bind to the protein's surface. In addition, de Freitas and Schapira (2017) conducted an analysis on the frequency and impact of different forms of atomic interactions occurring between proteins and small-molecule ligands. It is well known that hydrophobic interactions are highly prevalent in proteins available in the PDB. This can be attributed to lead optimization methods used to enhance the occurrence of favourable hydrophobic interactions. The estrogen receptors were acquired from the PDB. **Figure 5.6** shows several interactions of complex **4** with ER-α and ER-β. Among these, cation-π interactions were observed between Met D:522, Asp D:351 and ER-α, as well as between Glu B:332, Arg B:466 and ER-β. These cation-π interactions are electrostatic and contribute to the protein-ligand stability.

Anastasiadou *et al.* (2020) used docking studies to determine the binding between silver(I) complexes and the human estrogen receptor alpha (hER-α) protein. DSV revealed that silver(I) complexes bound to the ligand binding domain of hER-α. The complex with the lowest binding energy revealed interactions with various amino acids; Trp383, Met522, Met528, Leu525, Leu536 and Leu539, similar to the amino acids shown herein. In addition, Eid *et al*. (2018) investigated the interaction of zerumbone (a chemical constituent found within ginger *Zingiber zerumbet*), with ER-α and ER-β. Zerumbone, as does complex **4**, exhibit anticancer activity and induce apoptosis in breast malignant cells (data presented in chapter four). Their molecular docking results revealed a better interaction profile of zerumbone with ER-β than with ER-α. The exhibited internal binding energies were -9.25 kcal/mol and -8.34 kcal/mol respectively (Eid *et al.,* 2018). These results were comparable to the internal binding energies revealed in this study, which were -9.14 kcal/mol for ER-β and -8.64 kcal/mol for ER-α (**Figure**

5.7). In addition, Scherbakvov *et al.* (2019) studied brassinosteroids (referred to as **BS4**), a plant-specific anticancer steroid hormone, and its effect on MCF-7 cells. The binding mode of **BS4** targeting ER-α was analyzed by molecular docking, and a stable conformation and binding score of -9.5 kcal/mol was obtained. The system's total internal energy contributes to the overall binding strength of the interaction.

Research into blocking estrogen activity is necessary to hinder the development of breast cancer (Sharma *et al.,* 2018). Overall, *in silico* computational predictions support a favourable and strong interaction between complex **4**. This supports antiestrogen activity in hormone-dependent breast cell lines. Complex **4** stabilized within the active sites of ER-α and ER-β, through the formation of hydrophobic interactions and modest binding energies of -7.40 kcal/mol and -7.13 kcal/mol, respectively. This is the first research to show that the silver(I) phosphine complex **4** can bind to ER-α and ER-β *in silico*. Prior results (chapter two**, Table 2.3** and findings in chapter four) suggest that complex **4** (IC_{50}: 7.18 ± 1.60 μM) exhibits anticancer activity, targeting intrinsic apoptosis in the MCF-7 cells. These preliminary findings encourage further research into the target site of ER-α and ER-β. Various molecular docking parameters such as binding constants and binding kinetics of complex **4** with ER-α and ER-β should be validated. However, these predictions offer a fundamental framework for the formulation and expansion of novel silver(I) phosphine complexes in combination therapy, particularly hormone and chemotherapy regimens.

CHAPTER SIX:
CONCLUSION

6.1. Summary of final conclusions

CDDP has limited therapeutic efficacy due to its adverse side effects and the failure to overcome the adaptability of cancer cells that repress its mechanism of action (Ranasinghe *et al.*, 2022). To overcome malignancies, it is necessary to develop novel metallo-drugs without a high toxicity profile to non-malignant cells.

Seven of the thirteen silver(I) phosphine complexes synthesized were successful. They significantly decreased cellular viability in various malignant cell lines and were selected for dose-responsive studies. These studies revealed a dose-dependent reduction in the viability of all malignant cell lines examined. Moreover, these complexes were selective because they were significantly less toxic to normal cells. CDDP resulted in IC_{50} concentrations exceeding 20 µM, whereas complex **7** had the lowest mean IC_{50} value for the A375, MDA-MB-231, and MCF-7 cells, with values of 5.82 µM, 4.85 µM, and 2.85 µM, respectively. In the A549 and SNO cells, complex **1** had the lowest mean IC_{50} value of 6.35 µM and 6.63 µM, respectively, followed by complex **2** in A549 cells and complex **7** in SNO cells. Complex **4** was the most effective, reducing cellular viability in all varieties of cancer studied.

It is proposed that selected silver(I) phosphine complexes exert significant anticancer effects on A549, HEP-G2, HT-29, MDA-MB-231, and MCF-7 cells. Changes such as morphological variances, the decrease in cell viability, increase in ROS production, depolarization of the mitochondrial membrane, and externalization of Ptd-L-Ser, are downstream events induced as a result of the apoptotic cascade. In the A549 cells, complexes **1** and **4** repress cell migration. The presence of damaged nuclei, metabolically inactive mitochondria, and cytochrome *c* translocation from the mitochondria's intermembrane to the cytosol in MCF-7 cells suggest an apoptotic cell death by complexes **2**, **4** and **7**. Overall, complex **4** may prove to be a key anticancer drug in treating a broad range of malignancies, as further confirmed through *in silico* molecular docking studies. Utilizing docking and molecular dynamics simulations, the molecular interaction between complex **4** and estrogen receptors was investigated. Both ER-α and ER-β receptors exhibited modest affinities, as demonstrated by the findings presented in chapter five. Similar binding interactions with the crystallographic structures of the respective receptors exhibited stable conformation with hydrophobic interactions. The RMSD and amino acid residue interactions in docked ER-α/ER-β systems authenticated this stability. These findings highlight the prospective applications of silver(I) phosphine complexes and their relevance in hormone therapy and/or combination therapy regimens.

6.2. Future studies

Further studies could provide insight into the following results:

- The selectivity index (SI) calculation is one method of assessing the silver(I) phosphine complexes selectivity. A high selectivity index indicates that the complex exhibits a more pronounced impact on malignant cell lines in comparison to non-malignant cell lines. This characteristic may indicate that silver(I) phosphine complexes specifically target cancer cells while limiting damage to non-cancerous cells. IC_{50} values for the two non-malignant cells lines should be determined in order to calculate the SI.
- Complexes **1** - **4**, **6** and **7** did not increase ROS production in A549 cells despite their high toxicity levels (**Figure 2.7** and **Table 2.2**, chapter two). The same was seen in MDA-MB-231 and MCF-7-treated cells with complexes **2**, **4** and **7** (**Figures 2.11** and **2.12**; and **Table 2.3**, chapter two), respectively. [a] CypA is produced in excess in response to inflammatory stimulation to reduce ROS and shield cells from oxidative stress-induced apoptosis. Targeting and analyzing the expression of CypA in A549 along with the MCF-7 and MDA-MB-231 cells may provide more insight into the results seen herein. [b] It may be possible that these complexes cause direct DNA damage in A549 and MDA-MB-231 cells, future agarose gel electrophoresis should be considered as to isolate the DNA in these complex-treated cells.
- Silver(I) phosphine complexes may inhibit *TrxR*, leading to the accumulation of ROS in HEP-G2 and HT-29 cells (**Figures 3.6-B** and **3.6-C**, chapter three). *TrxR* regulates ROS levels in cancerous cells to assure their continued growth. Future research will determine whether silver(I) phosphine complexes inhibit this enzyme by observing *TrxR* expression in the above mentioned cell lines at 3 h, 6 h, 9 h and 12 h treatment time points.
- Silver(I) phosphine complexes, notably **1** and **4**, inhibit cell migration in A549 cells. Additional research could determine whether the same inhibition holds true across a variety of malignancies.
- Regarding selected silver(I) phosphine complexes and their effect on EGFR, future PCR and Western blot investigations on the mRNA and protein levels of EGFR and ELK1 should be considered to determine whether EGFR is a possible mechanism by which silver(I) phosphine complexes reduce cell migration in A549 cells.
- Investigating the effect silver(I) phosphine complexes have on ERK activation within the RAS/MAPK pathway in the MCF-7 and MDA-MB-231 cell lines may provide additional insight into the insignificant amount of ROS observed in silver(I) phosphine-treated cells.
- Further research is suggested to fully understand whether the silver(I) phosphine complexes initiate an apoptotic pathway by targeting the key caspase enzymes, Bid and Bax as well as

PARP through Western blotting analyses (notably investigating the A549, HEP-G2 and MDA-MB-231 cell lines).

- Various molecular docking parameters such as binding constants and binding kinetics of complex **4** with ER-α and ER-β should be validated to confirm the *in silico* computational predictions presented in chapter 5.

In closing, silver(I) phosphine complexes have apoptotic-inducing properties and were effective in targeting the mitochondria in the various malignant cell lines tested. Complex **4** was effective across all malignancies, irrespective of the lack of homogeneity among these cell types. Given that complex **4** was successful in decreasing proliferation, hindering cell migration, and targeting the alpha and beta estrogen receptors, it should be considered a hit-to-lead anticancer agent. The results reported herein shed additional light on the use of silver(I) phosphine complexes to target cell death and metastatic mechanisms in malignant cell lines.

REFERENCE LIST

Abbott, M. and Ustoyev, Y. 2019. Cancer and the Immune System: The History and Background of Immunotherapy. *Seminars in Oncology Nursing.* 35: 1 - 5.

Aceituno, V.C., Ahn, S., Simu, S.Y., Wang, C., Mathiyalahan, R. and Yang, D.C. 2016. Silver nanoparticles from *Dendropanax morbifera* Léveille inhibit cell migration, induce apoptosis, and increase generation of reactive oxygen species in A549 lung cancer cells. *In Vitro Cellular & Developmental Biology - Animal.* 52: 1012 - 1019.

Acosta-Casique, A., Montes-Alvarado, J.B., Barragán, M., Larrauri-Rodríguez, K.A., Perez-Gonzalez, A., Delgado-Magallón, A., Millán-Perez-Peña, L., Rosas-Murrieta, N.H. and Maycotte, P. 2023. ERK activation modulates invasiveness and Reactive Oxygen Species (ROS) production in triple negative breast cancer cell lines. *Cellular Signalling.* 101: 1 - 8.

Akar, U., Chaves-Reyez, A., Barria, M., Tari, A., Sanguino, A., Kondo, Y., Kondo, S., Arun, B., Lopez-Berestein, G. and Ozpolat, B. 2008. Silencing of Bcl-2 expression by small interfering RNA induces autophagic cell death in MCF-7 breast cancer cells. *Autophagy*. 4(5): 669 - 679.

Alessi, D.R., Cuenda, A., Cohen, P., Dudley, D.T. and Saltiel, A.R. 1995. PD 098059 Is a Specific Inhibitor of the Activation of Mitogen-activated Protein Kinase Kinase *in Vitro* and *in Vivo*(*). *Journal of Biological Chemistry.* 270(46): 27489 - 27494.

Al-kawmani, A.A., Alania, K.M., Farah, M.A., Ali, M.A., Hailan, W.A.Q. and Al-Hemaid, M.A. 2020. Apoptosis-inducing potential of biosynthesized silver nanoparticles in breast cancer cells. *Journal of King Saud University*. 32: 2480 - 2488.

Allen, C., Her, S. and Jaffray, D.A. 2017. Radiotherapy for Cancer: Present and Future. *Advanced Drug Delivery Reviews.* 109: 1 – 2.

Allison, K.H. and Sledge, G.W. 2014. Heterogeneity and Cancer. *Oncology.* 28(9): 772.

Altay, A., Caglar, S., Caglar, B. and Sahin, Z.S. 2019. Novel silver(I) complexes bearing mefenamic acid And pyridine derivatives: Synthesis, chemical Characterization, and in vitro anticancer evaluation. *Inorganica Chimica Acta*. 493: 61 - 71.

Altay, A., Caglar, S and Caglar, B. 2022. Silver(I) complexes containing diclofenac and niflumic acid induce apoptosis in human-derived cancer cell lines. *The Journal of Metabolic Diseases.* 128 (1): 69 – 79.

Amaral, I., Silva, C., Correia-Branco, A. and Martel, F. 2018. Effect of metformin on estrogen and progesterone receptor-positive (MCF-7) and triple-negative (MDA-MB-231) breast cancer cells. *Biomedicine & Pharmacotherapy.* 102: 94 - 101.

American Association for the Advancement of Science (**AAAS**). 2020. EurekAlert! New family of promising, selective silver-based anti-cancer drugs discovered. Available from https://www.eurekalert.org/. (Accessed the 29th of September 2020).

Anastasiadou, D., Geromichalou, E., Tsavea, E., Psomas, G., Hatzidimitriou, A.G., Kolagiannis, S., Geromichalos, G., Trafalis, D., Dalezis, P. and Allanidis, P. 2020. Silver complexes with heterocyclic thioamide and tertiary arylphosphane ligands: Synthesis, crystal structures, in vitro and in silico antibacterial and cytotoxic activity, and interaction with DNA. *Journal of Inorganic Biochemistry.* 210 (111167): 1 - 17.

Anaya-Eugenio, G.D., Tan, C.Y., Rakotondraibe L.H. and de Blanco, E.C.C. 2020. Tumor suppressor p53 independent apoptosis in HT-29 cells by auransterol from *Penicillium aurantiacobrunneum. Journal of Biomedicine & Pharmacotherapy*. 127(110124): 1 - 9.

Anestopoulos, I., Kyriakou, S., Tragkola, V., Paraskevaidis, I., Tzika, E., Mitsiogianni, M., Deligiorgi, M.V., Petrakis, G., Trafalis, D.T., Botaitis, S., Giatromanolaki, S., Koukourakis, M.I., Franco, R., Pappa, J. and Panayiotidis M.I. 2022. Targeting the epigenome in malignant melanoma: Facts, challenges and therapeutic promises. *Pharmacology & Therapeutics.* 240: 1 -24.

Anwanwan, D., Singh, S.K., Singh, S., Saikam, V. and Singh, R. 2020. Challenges in liver cancer and possible treatment approaches. *BBA – Reviews in Cancer.* 1873: 1 - 7.

Arnold, M., Morgan, E., Rumgay, H., Mafra, A., Singh, D., Laversanne, M., Vignat, J., Gralow, J.R., Cardoso, F., Sieslang, S. and Soerjomataram, I. 2022. Current and future burden of breast cancer: Global statistics for 2020 and 2040. *The Breast.* 66: 15 - 23.

Arizti, P., Fang, L., Yin, Y., Solomon, E., Ouchi, T., Aaronson, S.A. and Lee, S.W. 2020. Tumor Suppressor p53 Is Required To Modulate BRCA1 Expression. *Molecular and Cellular Biology*. 20(20): 7450 - 7459.

Aslam, M., Augustine, S., Mathew, A.A., Kanthal, S.K. and Panonummal, R. 2023. Apoptosis promoting activity of selected plant steroid in MRMT-1 breast cancer cell line by modulating mitochondrial permeation pathway. *Steroids.* 190: 1 - 10.

Babar, Q., Saeed, A., Tabish, T.A., Pricl, S., Townley, H. and Thorat, N. 2022. Novel epigenetic therapeutic strategies and targets in cancer. *BBA - Molecular Basis of Disease.* 1868: 1 - 20.

Ballante, F. and Marshall, G.R. 2016. An Automated Strategy for Binding-Pose Selection and Docking Assessment in Structure-Based Drug Design. *Journal of Chemical Information and Modeling.* 56: 54 - 72.

Banti, C.N., Raptopoulou, C.P., Psycharis, V. and Hadjikakou, S.K. 2021. Novel silver glycinate conjugate with 3D polymeric intermolecular self-assembly architecture: an antiproliferative agent which induces apoptosis on human breast cancer cells. *Journal of Inorganic Biochemistry.* 216: 1 -13.

Barron, C.C., Wang, X. and Elimova, E. 2023. Neoadjuvant Strategies for Esophageal Cancer: Role of Immunotherapy and Positron emission tomography (PET)-Guided Strategies. *Thoracic Surgery Clinics.* 1 - 12.

Barzaman, K., Kaeami, J., Zarei, Z., Hosseinzadeh, A., Kazemi, M.H., Moradi-Kalbolandi, S., Safari, E. and Farahmand, L. 2020. Breast Cancer: Biology, biomarkers, and treatments. *International Immunopharmacology.* 84: 1 - 10.

Bayir, H. and Kagan, V.E. 2008. Bench-to-bedside review: Mitochondrial injury, oxidative stress and apoptosis–there is nothing more practical than a good theory. *Critical Care*. 12(1):206.

Berner-Price, S.J., Mirabelli, C.K., Johnson, R.K., Mattern, M.R., McCabe, F.L., Faucette, L.F., Sung, C-M., Mong, S-M., Sadler, P.J. and Crooke, S.T. 1986. *In Vivo* Antitumor Activity and *in Vitro* Cytotoxic Properties of Bis[1,2-bis(diphenylphosphino)ethane]gold(I) Chloride. *Cancer Research.* 46(1): 5408 – 5493.

Berry, M.D. and Boulton, A.A. 2000. Glyceraldehyde-3-Phosphate Dehydrogenase and Apoptosis. *Journal of Neuroscience Research.* 60: 150 - 154.

Boice, A. and Bouchier-Hayes, L. 2020. Targeting apoptotic caspases in cancer. *BBA – Molecular Cell Research.* 1867: 1 - 15.

Bold, R.J., Termuhlen, P.M. and McConkey, D.J. (1997). Apoptosis, cancer and cancer therapy. *Surgical Oncology.* 6(3): 133 - 142.

Borst, P., Rottenberg, S. and Jonkers, J. 2008. How do real tumors become resistant to cisplatin? *Cell Cycle*. 7(10): 1353 - 1359.

Bray, F., Ferlay, J., Soerjomataram, I., Siegel, R.L., Torre, L.A., and Jemal, A. 2018. Global cancer statistics 2018: Globocan estimates of incidence and mortality worldwide for 36 cancers in 185 countries. *CA: A Cancer Journal for Clinicians*. 68: 394 - 424.

Behera, S.P. and Saxena, R.K. 2021. Nanodiamonds inhibit scratch-wound repair in lung epithelial cell monolayers by blocking cell migration and inhibiting cell proliferation. *Toxicology Letters*. 314: 83 - 93.

Berners-Price ,S.J., Mirabelli, C.K., Johnson, R.K., Mattern, M.R., McCabe, F.L., Faucette, L.F., Sung, C.M., Mong, S.M., Sadler, P.J. and Crooke, S.T. 1986. *In vivo* antitumor activity and *in vitro* cytotoxic properties of bis [1, 2-bis (diphenylphosphino) ethane] gold (I) chloride. *Cancer research.* 46(11): 5486 - 5493.

Bertolotto, C. 2013. Melanoma: from Melanocyte to genetic Alterations and Clinical Options. *Scientifica*. 1 - 22.

Bresciani, G., Busto, N., Ceccherini, V., Bortoluzzi, M., Pampaloni, G., Garcia, B. and Marchetti, F. 2022. Screening the biological properties of transition metal carbamates reveals gold(I) and silver(I) complexes as potent cytotoxic and antimicrobial agents. *Journal of Inorganic Biochemistry.* 227: 1 - 10.

Bruno, R.D. and Njar, V.C.O. 2007. Targeting cytochrome P450 enzymes: A new approach in anti-cancer drug development. *Bioorganic & Medicinal Chemistry.* 15: 5047 - 5060.

Cai, J., Yang, J. and Jones, D.P. 1998. Mitochondrial control of apoptosis: the role of cytochrome *c. Biochimica et Biophysica Acta*. 1366: 139 - 149.

Cai, Z. and Liu, Q. 2021. Understanding the Global Cancer Statistics 2018: Implications for cancer control. Science China Life Sciences. 64: 1017 - 1020.

Cali, J.J., Ma, D., Sobol, M., Simpson, D.J., Frackman, S and Good, T.D. 2006. Luminogenic cytochrome P450 assays. *Expert Opinion on Drug Metabolism & Toxicology*. 2(4): 629 - 645.

Čanović, P., Simović, A.R., Radisavljević, S., Bratsos, I., Demitri, N., Mitrović, M., Zelen, I. and Bugarčić, Z.D. 2017. Impact of aromaticity on anticancer activity of polypyridyl ruthenium(II) complexes: synthesis, structure, DNA/protein binding, lipophilicity and anticancer activity. *Journal of Inorganic Chemistry.* 22: 1007 - 1028.

Caruso, F., Villa, R., Rossi, M., Pettinari, C., Padovano, F., Pennati, M., Daidone, M.G. and Zaffaroni, N. 2007. Mitochondria are primary targets in apoptosis induced by the mixed phosphine gold species chlorotriphenylphosphine-1, 3-bis(diphenylphosphino)propanegold(I) in melanoma cell lines. *Biochemical Pharmacology*. 73: 773 - 781.

Cevik-Yildiz, E., Şahin, N. and Sahin-Bölükbaşi, S. 2020. Synthesis, characterization, and investigation of antiproliferative activity of novel Ag(I)-N-Heterocyclic Carbene (NHN) compounds. *Journal of Molecular Structure.* 5(1199): 1 - 8.

Chen, X., Pappo, A. and Dyer, M.A., 2015. Pediatric solid tumor genomics and developmental pliancy. *Oncogene.* 34, 5207 - 5215.

Cheng, X., Gu, J., Yuan, J., Feng, L. and Jia, X. 2015. Suppression of A549 cell proliferation and metastasis by calycosin via inhibition of the PKC-α/ERK1/2 pathway: An *in vitro* investigation. *Molecular and Medicine Reports.* 12: 7992 - 8002.

Chougale, A., Chandrani, P., Noronha, V., Pange, P., Kale, S., Nikam, A., Nambir, K., Marchande, D., Durve, A., Gupta, V., Jagtap, V., Tiwrekar, P., Menon, N., Joshi, A., Kaushal, R., Pai, T., Patil, V.M., Dutt, A., Banavali, S.D. and Prabhash, K. 2023. Real world evidence of EGFR targeted therapy in non-small cell lung cancer– a brief report of decade long single centre experience. *JTO Clinical and Research Reports.* 1 – 10.

Chrysouli, M.P., Banti, C.N. Kourkoumelis, N., Panayiotou, N., Markopoulos, G.S., Tasiopoulos, A.J. and Hadjikakou, S.K. 2018. Chloro(triphenylphosphine)gold(I) a forefront reagent in gold chemistry as apoptotic agent for cancer cells. *Journal of Inorganic Biochemistry.* 179: 107 - 120.

Chuang, D-M., Hough, C. and Senatorov, V.V. 2005. Glyceraldehyde-3-phosphate dehydrogenase, apoptosis, and neurodegenerative diseases. *Annual Review of Pharmacology and Toxicology.* 45: 269 - 290.

Colell, A., Green, D.R. and Ricci J-E. 2009. Novel roles for GADPH in cell death and carcinogenesis. *Cell Death and Differentiation*. 16: 1573 - 1581.

Collins, L.G., Haines, C., Perkel, R. and Enck, R. 2007. Lung Cancer: Diagnosis and Management. *American Family Physician.* 75(1): 56 - 63.

Costa, M.A., Pellerito, L., Izzo, V., Fiore, T., Pellerito, C., Melis, M., Musmeci, M.T. and Barbieri, G. 2006. Diorganotin (IV) and triorganotin (IV) complexes of meso-tetra (4-sulfonatophenyl) porphine induce apoptosis in A375 human melanoma cells. *Cancer Letters.* 238: 284 - 294.

Cullen SP, Martin SJ. 2015. Fas and TRAIL 'death receptors' as initiators of inflammation: Implications for cancer. *Seminars in Cellular Developmental Biology.* 39: 26 - 34.

de Abreu Costa, L., Ottoni, M.H.F., dos Santos, M.G., Meireles, A.B., de Almeida, V.G., de Fátima Pereira, W., de Avelar-Freitas, B. and Brito-Melo, G.E.A. 2017. Dimethyl Sulfoxide (DMSO) Decreases Cell Proliferation and TNF-α, IFN-γ, and IL-2 Cytokines Production in Cultures of Peripheral Blood Lymphocytes. *Molecules.* 22(1789): 1 - 10.

De Freitas, R.F. and Schapira, M. 2017. A systematic analysis of atomic protein-ligand interactions in the PBD. *Medical Chemistry Communications.* 8: 1970 – 1981.

Dandash, F., Léger, D.Y., Fidanzi-Dugus, C., Nasri, S., Brégiar, F., Granet, R., Karam, W., Diab-Assaf, M., Sol, V. and Liagre, B. 2017. *In vitro* anticancer activity of new gold(III) porphyrin complexes in colon cancer cells. *Journal of Inorganic Biochemistry.* 177: 27 - 38.

D'Arcy, M.S. 2019. Cell death: a review of the major forms of apoptosis, necrosis and autophagy. *Cell Biology International.* 43: 582 - 592.

Dare, A.J., Anderson, B.O., Sullivan, R., Pramesh, C.S., Ander, I., Adewole, I.F., Badwe, R.A. and Gauvreau, C.L. 2015. *Cancer: Disease Control Priorities* (3rd ed) Vol 3. Chapter 13: Surgical Services for Cancer Care. Washington (DC): The International Bank for Reconstruction and Development / The World Bank (pg. 223 - 267).

Davids, L.M. and Kleemann, B. 2013. *Melanoma – From Early Detection to Treatment.* Chapter 22: The Menace of Melanoma: A Photodynamic Approach to Adjunctive Cancer Therapy (pg. 583 - 627).

Dela-Cruz, C.S., Tanoue, L.T. and Matthay, R.A. 2011. Lung Cancer: Epidemiology, Etiology, and Prevention. *Clinics in Chest Medicine.* 32(4): 1 - 61.

Deli, T., Orosz, M. and Jakob, A. 2020. Hormone Replacement Therapy in Cancer Survivors – Review of the Literature. *Pathology & Oncology Research.* 26: 63 – 78.

Devnarain, N., Tiloke, C., Nagiah, S. and Chuturgoon, A.A. 2017. Fusaric acid induces oxidative stress and apoptosis in human cancerous oesophageal SNO cell. *Toxicon*. 126: 4 - 11.

Diaz, M., Garcia, M., Vidal, C., Santiago, A., Gnutti, G., Gómez, D., Trapero-Bertran M., Fu, M., on behalf of the Lung Cancer Prevention LUCAPREV research group. 2021. Health and economic impact at a population level of both primary and secondary lung cancer interventions: A model-based cost-effective analysis. *Lung Cancer.* 159: 153 - 161.

Ding, X., Sun, W. and Chen, J. 2018. IL-2 augments the sorafenib-induced apoptosis in liver cancer by promoting mitochondrial fission and activating the JNK/TAZ pathway. *Cancer Cell International.* 18(176): 1 - 15.

Disis, M.L. 2014. Mechanism of action of immunotherapy. *Seminars in Oncology*. 41: S3 - S13.

D'Uva, G., Baci, D., Albini, A. and Noonan, D.M. 2018. Cancer chemoprevention revisited: Cytochrome P450 family 1B1 as a target in the tumor and the microenvironment. *Cancer Treatment Reviews.* 63: 1 - 18.

Dwyer, F.P., Gyarfas, E.C., Rogers, W.P. and Kock, J.H. 1952. Biological Activity of Complex Ions. *Nature.* 170: 190 - 191.

Eid, E.E.M., Azam, F., Hassan, M., Taban, I.M., and Halim, M.A. 2018. Zerumbone binding to estrogen receptors: an in-silico investigation. *Journal of Receptors and Signal Transduction.* 38(4): 342 - 351.

Elmore, S. 2007. Apoptosis: A Review of Programmed Cell Death. *Toxicologic Pathology.* 35(4): 495 – 516.

Engelbrecht, Z. and Cronjé, M.J. 2018. The ability of silver(I) thiocyanate 4-methoxyphenyl phosphine to induce apoptotic cell death in esophageal cancer cells is correlated to mitochondrial perturbations. *BioMetals.* 31: 189 - 202.

Engelbrecht, Z., Meijboom, R. and Cronjé. M.J. 2017. Apoptosis-inducing ability of silver(I) cyanide phosphines useful for anti-cancer studies. *Cytotechnology*. 69(4): 591 - 600.

Engelbrecht, Z., Potgieter, K., Mpela, Z., Malgas-Enus, R., Meijboom, R. and Cronjé, M.J. 2018. A comparison of the toxicity of mono, bis, tris and tetrakis phosphine silver complexes on SNO esophageal cancer cells. *Anti-Cancer Agents in Medicinal Chemistry*. 18: 1 - 10. (b)

Engelbrecht, Z., Roberts, K.E, Hussan, A., Amenuvor, G., Cronjé, M.J., Darkwa, B.C.E. and Sitole, L. 2020. Synthesis and anti-cancer activity of bis-amino-phosphine ligand and its ruthenium(II) complexes. *Bioorganic & Medicinal Chemistry Letters.* 30(127492): 1 - 6.

Eunji, J., Park, S.J., Choi, Y.S., Jeon, W. and Kim B.C. 2015. Kaempferol suppresses transforming growth factor-β1-induced epithelial-to-mesenchymal transition and migration of A549 lung cancer cells by inhibiting Akt1-mediated phosphorylation of Smad3 at threonine-179. *Neoplasia.* 17: 525 - 537.

Farazi, P.A. and DePinho, R.A. 2006. Hepatocellular carcinoma pathogenesis: from genes to environment. *Nature Reviews.* 6: 674 - 687.

Ferenczy, G.G. and Kellermayer, M. 2022. Contribution of hydrophobic interactions to protein mechanical stability. *Computational and Structural Biotechnology Journal.* 20: 1946 – 1956.

Feinberg, A. P., Ohlsson, R. and Henikoff, S. 2006. The epigenetic progenitor origin of human cancer. *Nature Reviews Genetics*. 7(1): 21 - 33.

Ferreira, E., Munyaneza, A., Omondi, B., Meijboom, R. and Cronjé, M.J. 2015. The effect of 1:2 Ag(I) thiocyanate complexes in MCF-7 breast cancer cells. *BioMetals.* 28: 765 - 781.

Festjens, N., Vanden Berghe, T. and Vandenabeele, P. 2006. Necrosis, a well-orchestrated form of cell demise: signalling cascades, important mediators and concomitant immune response. *Biochimica et Biophysica Acta*. 1757(9-10): 1371 - 1387.

Firdhouse, M.J. and Lalitha, P. 2015. Apoptotic efficacy of biogenic silver nanoparticles on human breast cancer MCF-7 cell lines. *Progress in Biomaterials.* 4: 113 - 121.

Forli, S., Huey, R., Pique, M.E., Sanner, M., Goodshell, D.S. and Olson, A.J. 2016. Computational protein-ligand docking and virtual drug screening with the AutoDock suite. *Nature protocols*. 11(5): 905 - 919.

Friedl, P. and Weigelin, B. 2008. Interstitial leukocyte migration and immune function. *Natural Immunology*. 9: 960 - 969.

Fujisawa, Y., Yoshino, K., Otsuka, A., Funakoshi, T., Uchi, H., Fujimura, T., Matsushita, S., Hata, H., Okuhira, H., Tanaka, R., Nagai, K., Ishida, Y., Nakamura, Y., Furudate, S., Yamamura, K., Imafuku, K. and Yamamoto, Y. 2018. Retrospective study of advanced melanoma patients treated with ipilimumab after nivolumab: Analysis of 60 Japanese patients. *Journal of Dermatological Science*. 89: 60 – 66.

Fukunishni, Y., Higo, J. and Kasahara, K. 2022. Computer simulation of molecular recognition in Biomolecular system: from *in silico* screening to generalized ensembles. *Biophysical Reviews.* 14: 1423 - 1447.

Gao, X., Lv, X., Zhang, R., Luo, Y., Wang, M., Chen, J., Zhang, Y., Sun, B., Sun, J., Liu, Y. and Liu, C. 2021. Design, synthesis and in vitro anticancer research of novel tetrandrine and fangchinoline derivatives. *Bioorganic Chemistry.* 109(104694): 1 - 13.

Gao, Z., Huang, S., Wang, S., Tang, D., Xu, W., Zeng, R. and Qiao, G. 2023. Efficacy and safety of immunochemotherapy, immunotherapy, chemotherapy, and targeted therapy as first-line treatment for advanced and metastatic esophageal cancer: a systematic review and network meta-analysis. *The Lancet Regional Health – Western Pacific.* 38(100841): 1 – 13.

Gasser, G. and Metzler-Nolte, N. 2012. The potential of organometallic complexes in medicinal chemistry. *Current Opinion in Chemical Biology.* 16(1-2): 84 - 91.

Gerets, H.H.J., Tilmant, K., Gerin, B., Chanteux, H., Depelchin, B.O., Dhalluin, S and Atienzar, F.A. 2012. Characterization of primary human hepatocytes, HepG2 cells and HepaRG cells at the mRNA level and CYP activity in response to inducers and their predictivity for the detection of human hepatotoxins. *Cell Biology and Toxicology.* 28; 69 - 87.

Gioria, S., Urbán, P., Hajduch, M., Barboro, P., Cabaleiro, N., Spina, R.L. and Chassaigne, H. 2018. Proteomics study of silver nanoparticles on Caco-2 cells. *Toxicity in Vitro*. 50: 347 - 372.

Godwin, W.C., Hoffmann, G.F., Gray, T.J. and Hughes, R.M. 2019. Imaging of morphological and Biochemical hallmarks of apoptosis with optimized optogenetic tools. *Journal of Biological Chemistry.* 294(45): 16918 - 16929.

Gou, Y., Jiang, M., Zhao, X., Gu, M., Wang, Z., Xu, S. and Yue, W. 2018. Cyclophilin A promotes non-small cell lung cancer metastasis via p38 MAPK. *Thoracic Cancer.* 9(1): 120 - 128.

Grijalva, M., Gómez, N., Salazar, L., Vallejo, M.J., María, E.C., Bermeo, A.J. and Castillo, L. 2019. Antioxidant and oxidative Stress Modulation Properties of *Azorella pedunculata* Methanolic Extract on A549 Cancer Cells. *International Journal of Pharmaceutical and Phytopharmacological Research.* 9(4): 10 - 22.

Habib, A., Nazari, M., Iqbal, M.A., Bhatti, H.N., Khadeer Ahmed, M.B.K. and Abdul Majid, A.M.S. 2019. Unsymmetrically substituted benzimidazolium based Silver(I)-N-heterocyclic carbene complexes: Synthesis, characterization and in vitro anticancer study against human breast cancer and colon cancer. *Journal of Saudi Chemical Society.* 23: 795 - 808.

Häcker, G. 2000. The morphology of apoptosis. *Cell and Tissue Research.* 301: 5 - 17.

Halpern, A.C., Marghoob, A.A. and Reiter, O. 2022. Melanoma Treatment: Historic Progress, New Options. More Hope. The Skin Cancer Foundation A 501(c)(3) non-profit organization. Available from: https://www.skincancer.org.

Hanahan, D.A. 2022. Hallmarks of Cancer: New Dimensions. *Cancer Discovery.* 31 – 46.

Hanahan, D.A. and Weinberg, R.A. 2000. The Hallmarks of Cancer. *Cell.* 100(1): 57 - 70.

Hanahan, D.A. and Weinberg, R.A. 2011. Hallmarks of Cancer: The Next Generation. *Cell.* 144(5): 646 - 674.

Hart, I.R. 2004. Biology of cancer. *Medicine Cancer Biology.* 32(3): 1 - 5.

He, M., Liao, Q., Liu, D., Dai, X., Shan, M., Yang, M., Zhang, Y., Zhai, L., Chen, L., Xiang, L., He, M., Li, S., Chen, A., Sun, L. and Lain, J. 2023. Dihydroergotamine mesylate enhances the anti-tumor effect of sorafenib in liver cancer cells. *Biochemical Pharmacology.* 211: 1 – 11.

Hu, X., Zhang, L., Wang, W., Zhang., Y and Wang, J. 2022. Mitochondria-targeted and multistage synergistic ROS-elevated drug delivery system based on surface decorated MnO2 with CeO2 for enhanced chemodynamic/chemotherapy. *Colloids and Surfaces A: Physicochemical and Engineering Aspects*. 656(2023): 1 - 13.

Huang, K., Yao, H., Yan, M., Zhang, H., Yuan, G., Wang, Q., Xue, J., Li, J. and Chen, J. 2022. A MCL-1-targeted photosensitizer to combat triple-negative breast cancer with enhanced photodynamic efficacy, sensitization to ROS-induced damage, and immune response. *Journal of Inorganic Biochemistry.* 237: 1 - 11.

Huang, A., Yang, X-R., Chung, W-Y., Dennison, A.R. and Zhou, J. 2020. Targeted therapy for hepatocellular carcinoma. *Nature: Signal Transduction and Targeted Therapy.* 5(146): 1 - 13.

Huang, F-L. and Yu, S-J. 2018. Esophageal cancer: Risk factors, genetic association, and treatment. *Asian Journal of Surgery.* 41: 210 - 215.

Human-Engelbrecht, Z., Meijboom, R. and Cronjé, M.J. 2017. Apoptosis-inducing ability of silver(I) cyanide-phosphines useful for anti-cancer studies. *Cytotechnology.* 69: 591 - 600.

Human, Z., Munyaneza, A., Omondi, B., Sanabria, N.M., Meijboom, R. and Cronjé, M.J. 2015. The induction of cell death by phosphine silver (I) thiocyanate complexes in SNO-esophageal cancer cells. *BioMetals.* 28(1): 219 - 228.

Ishitani, R., Sunaga, K., Hirano, A., Suanders, P., Katsube, N. and Chuang, D.J. 1996. Evidence that glyceraldehyde-3-phosphate dehydrogenase is involved in age-induced apoptosis in mature cerebellar neurons in culture. *Journal of Neurochemistry.* 66(3): 928 - 935.

Jajosky, A. and Elliot, D.R.F. 2022. Esophageal Cancer Genetics and Clinical Translation. *Thoracic Surgery Clinics.* 32: 425 - 435.

Jiang. W., Yan Chen M.X., Li, G., Hao, J., Pan, J., Hu, S., Guo, P., Li, W., Wang, R., and Zuo, Y. 2020. Aspirin enhances the sensitivity of colon cancer cells to cisplatin by abrogating the binding of NF-κB to the COX-2 promoter. *Aging.* 12(1): 611.

Johnstone, R.W., Ruefli, A.A. and Loew, S.W. 2002. Apoptosis: A Link between Cancer Genetics and Chemotherapy. *Cell*. 108: 153 - 164.

Kalinowska-Lis, U., Felczak, A., Chęińska, L., Szabłowsak-Gadomsak, I., Patyna, E., Małecki, M., Lisowska, K. and Ochochi, J. 2016. Antibacterial Activity and Cytotoxicity of Silver(I) Complexes of Pyridine and (Benz)Imidazole Derivatives. X-ray Crystal Structure of [Ag(2,6-di(CH2OH)py)2]NO_3. *Molecules.* 21(2): 87.

Karplus, M. and McCammon, J.A. 2002. Molecular dynamics simulations of biomolecules. *Nature Structural Biology*. 9(9): 646 - 652.

Katz, M.H., Francescatti, A.B., Hunt, K.K. and behalf of Cancer Surgery Standards Program of the American College of Surgeons. Technical Standards for Cancer Surgery: Commission on Cancer Standards 5.3-5.8. *Annals of Surgical Oncology* 29: 6549 - 6558.

Kaur, S., Pandit., K., Chandel, M. and Kaur, S. 2020. Antiproliferative and apoptogenic effects of *Cassia fistula* L. n-hexane fraction against human cervical cancer (HeLa) cells. *Environmental Science and Pollution Research.* 27: 32017 - 32033.

Kennedy, L.B. and Salama, A.K.S. 2020. A Review of Cancer Immunotherapy Toxicity. *CA: A Cancer Journal for Clinicians.* 70: 86 - 104.

Kerr, J.F., Wyllie, A.H. and Currie, A.R. 1972. Apoptosis: a basic biological phenomenon with wide-ranging implications in tissue kinetics. *British Journal of Cancer.* 26: 239-257.

Khazanov, N.A. and Carlson, H.A. 2013. Exploring the Composition of Protein-Ligand Binding Sites on a Large Scale. *PLoS Computational Biology*. 9(11): 1 - 14.

Kim, H.K., Noh, Y.H., Nilius, B., Ko, K.S., Rhee, B.D., Kim, N. and Han, J. 2017. Current and upcoming mitochondrial targets for cancer therapy. Seminars in Cancer Biology. *Seminars in Cancer Biology.* 47: 154 - 167.

Kim, J.H., Reeder, E., Parkin, S. and Awuah, S.G. 2019. Gold(I/III)-Phosphine Complexes as Potent Antiproliferative Agents. *Nature Research: Scientific Reports.* 9(12335): 1 – 18.

Kim, K.H. and Lee, M-S. 2014. Autophagy – a key player in cellular and body metabolism. *Nature Reviews: Endocrinology.* 10: 322 - 337.

Kumar R, Herbert PE, Warrens AN. An introduction to death receptors in apoptosis. 2005. *International Journal of Surgery.* 3: 268 - 277.

Kumar, P., Singh, A.K., Pandey, R. and Pandy, D.S. 2011. Bio-catalysts and catalysts based on ruthenium(II) polypyridyl complexes imparting diphenyl-(2-pyridyl)-phosphine as a co-ligand. *Journal of Organometallic Chemistry.* 696: 3454 - 3464.

Kriel, F.H., and Coates, J. 2012. Synthesis and Antitumour Activity of Gold(I) and Silver(I) Complexes of Hydrazine-Bridged Diphosphine Ligands. South African Journal of Chemistry. 65:2 71 - 279.

Kyros, L., Kourkoumelis, N., Kubicki, M., Male, L., Hursthouse, M.B., Verginadis, I.I., Gouma, E., Karkabounas, S., Charalabopoulos, K. and Hadjikakou, S.K. 2010. Structural Properties, Cytotoxicity, and Anti-Inflammatory Activity of Silver(I) Complexes with tris(p-tolyl)Phosphine and 5-Chloro-2-Mercaptobenzothiazole. *Bioinorganic Chemistry and Applications.* 2010: 1 - 12.

Labianca, R., Beretta, G.D., Kildani, B., Milesi, L., Merline, F., Mosconi, S., Pessi, M.A., Prochilo, T., Quadri, A., Gatta, G., de Braud, F. and Wils, J. 2010. Colon Cancer. *Critical reviews in Oncology/Hematology*. 74: 106 - 133.

Landes, T. and Martinou, J-C. 2011. Mitochondrial outer membrane permeabilization during apoptosis: The role of mitochondrial fission. *Biochimica et Biophysica Acta.* 1813: 540 - 545.

Larsson, P., Engqvist, H., Biermann, J., Rönnerman, E.W., Forssell-Aronsson, E., Kovács, A., Karlsson, P., Helou, K. and Parris, T.Z. 2020. Optimization of cell viability assays to improve replicability and reproducibility of cancer drug sensitivity screens. *Scientific Reports.* 10(5798): 1 - 12.

Lee, J.H. and Berger, J.M. 2019. Cell Cycle-Dependent Control and Roles of DNA Topoisomerase II. *Genes.* 10(859): 1- 18.

Lee, K.L., Carpenter, B.L., Wen, A.W., Ghiladi, R.A. and Steinmetz, N.F. 2016. High Aspect Ratio Nanotubes Formed by Tobacco Mosaic Virus for Delivery of Photodynamic Agents Targeting Melanoma. *ACS Biomaterials Science and Engineering.* 2: 838 - 844.

Lee, S.L., Kim, C.Y. and Nam, T-G. 2020. Ruthenium Complexes as Anticancer Agents: A Brief History and Perspectives. *Drug, Design, Development and Therapy*. 14: 5373 - 5392.

Li, J., Fu, A. and Zhang, L. 2019. An Overview of Scoring Functions Used for Protein–Ligand Interactions in Molecular Docking. *Interdisciplinary Sciences: Computational Life Sciences.* 11: 320 - 382.

Li, J., Qu, P., Zhou, X-Z., Ji., Y-X., Yuan, S., Liu, S-P. and Zhang, Q-G. 2022. Pimozide inhibits the growth of breast cancer cells by alleviating the Warburg effect through the P53 signaling pathway. *Biomedicine & Pharmacotherapy.* 150: 1 - 15.

Li, J., Xu, Z., Tan, M., Su, Q and Gong X. 2010. 3-(4-(Benzo[d]thiazol-2-yl)-1-phenyl-1H-pyrazol-3-yl) phenyl acetate induced Hep G2 cell apoptosis through a ROS-mediated pathway. *Chemico-Biological Interactions.* 183: 341 - 348.

Li, X., Yang, J., Peng, L., Sahin, A.A., Huo, L., Ward, K.C., Regan, R.O., Torres, M.A. and Meisel, J.L. 2017. Triple-negative breast cancer has worse overall survival and cause-specific survival than non-triple-negative breast cancer. *Journal of Breast Cancer Research and Treatment.* 161: 279 - 287.

Li, Y. and Yang, L. 2022. Cyclophilin a represses reactive oxygen species generation and death of hypoxic non-small-cell lung cancer cells by degrading thioredoxin-interacting protein. *Cell Cycle.* 21(8): 1996 - 2007.

Liang, L., Wu, X., Shi, C., Wen, H., Wu, S., Chen, J., Huang, C., Wang, Y. and Liu, Y. 2022. Synthesis and characterization of polypyridine ruthenium(II) complexes and anticancer efficacy studies *in vivo* and *in vitro*. *Journal of Inorganic Chemistry.* 236: 111963.

Llovet, J.M., Kelley, R.K., Villanueva, A., Singa, A.G., Pikarsky, E., Roayaie, S., Lencioni, R., Koike, K., Zucman-Rossi, J. and Finn, R.S. 2021. Hepatocellular carcinoma. *Nature Reviews: Disease Primers.* 7(6): 1 - 28(111963): 1 – 16.

Locke, W.J., Guanzon, D., Ma, C., Liew, Y.J., Duesing, K.R., Fung, K.Y.C. and Ross, J.P. 2019. DNA Methylation Cancer Biomarkers: Translation to the Clinic. *Frontiers in Genetics*, 10: 1 - 22.

Luo, C. and Shen, J. 2017. Research progress in advanced melanoma. *Cancer Letters*. 397: 120 – 126.

Luo, J., Li, N., Robinson, P. and Shi, R. 2002. Detection of reactive oxygen species by flow cytometry after spinal cord injury. *Journal of Neuroscience Methods.* 120: 105 - 112.

Lupidi, G., Avenali, L., Bramucci, M., Quassinti, L., Pettinari, R., Khalife, H.K., Gali-Muhtasib, H., Marchetti, F. and Pettinari, C. 2013. Synthesis, properties, and antitumor effects of a new mixed phosphine gold(I) compound in human colon cancer cells. *Journal of Inorganic Biochemistry*. 124: 78 - 87.

Malm, M., Saghaleyni, R., Lundqvist, M., Giudici, M., Chotteau, V., Field, R., Varley, P.G., Hatton, D., Grassi, L., Svensson, T., Nielsen, J. and Rockberg, J. 2020. Evolution from adherent to suspension: systems biology of HEK293 cell line development. *Scientific Reports.* 10: 1 - 15.

Manda, G., Nechifor, M. and Neagu, M. 2009. Reactive Oxygen Species, Cancer and Anti-Cancer Therapies. *Current Chemical Biology.* 3: 342 - 366.

Mann, F.G., Well, A.F., Purdie, D. 1937. The construction of complex metallic salts: Part IV. *Journal of the Chemical Society-Dalton Transactions*. 1830 - 1938.

Martín-Ecinas, E., Conejo-Rodríguez, V., Miguel, J.A., Martínez-Ilarduya, J.M., Rubiales, G., Knudsen, B.R., Palacios, F. and Alonso, C. 2020. Novel phosphine sulphide gold(I) complexes: topoisomerase I inhibitors and antiproliferative agents. *Dalton Transactions.* 49: 7852 - 7861.

Maruthanila, V.L., Elancheran, R., Roy, N.K., Bhattacharya, A., Kunnumakkara, A.B., Kabilan, S. and Kotoky, J. 2019. *In Silico* Modelling of Selected Natural Ligands and their Binding Features with Estrogen Receptor Alpha. *Current Computer-Aided Drug Design*. 15: 89 - 96.

Mashat, K.H., Babgi, B.A., Hussien, M.A., Arshad, M.N. and Abdellattif, M.H. 2019. Synthesis, structures, DNA-binding and anticancer activities of some copper(I)-phosphine complexes. *Polyhedron.* 158: 164 - 172.

Matossian, M., VanGelderen, C., Papagerakis, P., Zheng, L., Wolf, G.T. and Papagerakis, S. 2014. In silico modeling of the molecular interactions of antacid medication with the endothelium: novel therapeutic implications in head and neck carcinomas. *International Journal of Immunopathology Pharmacology*. 27(4): 573 - 583.

McBride, H.M., Neuspiel, M. and Wasiak, S. 2006. Mitochondria: More Than Just a Powerhouse. *Current Biology*. 16(14): 551 - 560.

McGuire, J., Utset-Ward, T.J., Reed, D.R. and Lynch, C.C. 2017. Re-calculating! Navigating through the osteosarcoma treatment roadblock. *Pharmacological Research.* 117: (54 - 64).

McKeage, M.J., Papathanasiou, P., Salem, G., Sjaarda, A., Swiegers, G.F., Waring, P. and Wild, S.B. 1998. Antitumour Activity of Gold(I), Silver(I) and Copper(I) Complexes Containing Chiral Tertiary Phosphines. *Metal-Based Drugs*. 5(4): 217 – 223.

McKeage, M.J., Berners-Price, S.J., Galettis, P., Bowen, R.J., Brouwer, W., Ding, L., Zhuang, L. and Baguley, B.C. 2000. Role of lipophilicity in determining cellular uptake and antitumour activity of gold phosphine complexes. *Cancer Chemotherapy and Pharmacology.* 46: 343 – 350.

Meijboom, R., Bowen, R.J., Berners-Price, S.J. 2009. Coordination complexes of silver(I) with tertiary phosphine and related ligands. *Coordination Chemistry Reviews*. 235: 325 - 342.

Miraflor, A.P., de Abreu, F.B., Peterson, J.D., Turner, S.A., Amos, C.I., Tsongalis, G.J. and Yan, S. 2017. Somatic mutation analysis in melanoma using targeted next generation sequencing. *Experimental and Molecular Pathology*. 103: 172 - 177.

Mishra, N.K., Agarwal, S. and Raghava, G.P. 2010. Prediction of cytochrome P450 isoform responsible for metabolizing a drug molecule. *BMC Pharmacology*. 10(8): 1 - 9.

Mitra, S., Lami, M.S., Ghosh, A., Das, R., Tallei, T.E., Fatimawali, Islam, F., Dhame, K., Begum, M.Y., Aldahish, A., Chidambaram, K. and Emran, T.B. 2022. Hormonal Therapy for Gynaecological Cancers: How Far Has Science Progressed toward Clinical Applications? *Cancers.* 14(759): 1 - 26.

Moffitt, K.L., Martin, S.L. and Walker, B. 2010. From sentencing to execution - the process of apoptosis. *Journal of Pharmacy and Pharmacology*. 62: 547 - 562.

Morris, G.M., Huey, R. and Olsen, A.J. 2008. Using AutoDock for Ligand-Receptor Docking. *Current Protocols in Bioinformatics.* 24: 8.14.1 - 8.14.40.

Moses, S.L., Edwards, V.M. and Brantley, E. 2016. Cytotoxicity in MCF-7 and MDA-MB-231 Breast Cancer Cells, without Harming MCF-10A Healthy Cells. *Journal of Nanomedicine & Nanotechnology.* 7(2): 1 - 11.

Mroz, P., Yaroslavsky, A., Kharkwal, G.B. and Hamblin, M.R. 2011. Cell Death Pathways in Photodynamic Therapy of Cancer. *Cancers*. 3(2): 2516 - 2539.

Muchtaridi, M., Shahida, H,N., Subarnas, A., Yusuf, M., Bryant, S.D. and Langer, T. 2017. Molecular Docking and 3D-Pharmacophore Modeling to Study the Interactions of Chalcone Derivatives with Estrogen Receptor Alpha. *Pharmaceuticals.* 10(81): 1 - 12.

Nikoletopoulou, V., Markaki, M., Palikaras, K. and Tavernarakis, N. 2013. Crosstalk between apoptosis, necrosis and autophagy. *Biochimica et Biophysica Acta*. 1833: 3448 - 3459.

Nyga, A., Ganguli, S., Matthews, H.K. and Baum, B. 2022. The role of RAS oncogenes in controlling epithelial mechanics. *Trends in Cell Biology.* 33(1): 60 - 69.

Ota, A., Tajima, M., Mori, K., Sugiyama, E., Sato, V.H and Sato, H. 2021. The selective cytotoxicity of silver thiosulfate, a silver complex, on MCF-7 breast cancer cells through ROS-induced cell death. *Pharmacological Reports.* 73: 847 - 857.

Ott, I. 2009. On the medicinal chemistry of gold complexes as anticancer drugs. *Coordination Chemistry Reviews.* 253(11): 1670 - 1681.

Ott, M., Gogvadze, V., Orrenius, S. and Zhivotovsky, B. 2007. Mitochondria, oxidative stress and cell death. *Apoptosis.* 12: 913 - 922.

Onorati, A., Dyczynski, M., Ojha, R. and Amaravadi, R.K. 2018. Targeting autophagy in cancer. *Cancer*. 124(16): 3307 - 3318.

Orrantia-Borunda, E., Anchondo-Nuñez, P., Acuña-Aguilar, L.E., Gómez-Valles, F.O. and Ramírez Valderspino, C.A. 2022. *Breast Cancer*. Chapter 3: Subtypes of Breast Cancer. (pg. 32 - 42).

Ozdemir, U.O., Ozbek, N., Genc, Z. K., Ilbiz, F. and Gündüzalp. 2017. New bioactive silver(I) complexes: Synthesis, characterization, anticancer, antibacterial and anticarbonic anhydrase II activities. *Journal of Molecular Structure.* 1138: 55 - 63.

Pathaw, L., Khamrang, T., Selvakumaran, B., Murali, M., Prakash, P.A., Jaabir, M.S.M. and Velusamy, M. 2020. Synthesis, structure, characterization and biological evaluation of 3-substituted 1-pyridin-2-ylimidazo[1,5-a]pyridine-based copper(I)–phosphine complexes for anticancer drug screening. *Applied Organometallic Chemistry.* 35: 1 - 19.

Peña-Blanco, A. and Garcia-Sàez, A.J. 2018. Bax, Bak and beyond—mitochondrial performance in apoptosis. *Federation of European Biochemical Societies.* 285: 416 - 431.

Peng, D-F., Hu, T-L., Soutto, M., Belkhiri, A. and El-Rifai, W. 2014. Loss of glutathione peroxidase 7 promotes TNF-α-induced NF-κB activation in Barrett's carcinogenesis. *Carcinogenesis.* 35(7): 1620 - 1628.

Pessoa, J. 2022. Cytochrome *c* in cancer therapy and prognosis. *Bioscience Reports*. 42: 1 - 17.

Pijuan, J., Barceló, C., Moreno, D., Maiques, O., Sisó, P., Marti, R.M., Marcià, A. and Panosa, A. 2019. *In vitro* Cell Migration, Invasion, and Adhesion Assays: From Cell Imaging to Data Analysis. *Journal Frontiers in Cell and Developmental Biology.* 107(7): 1 - 16.

Pinzi, L. and Rastelli, G. 2019. Molecular Docking: Shifting Paradigms in Drug Discovery. *International Journal of Molecular Sciences.* 20(4331): 2 - 23.

Potgieter, K., Cronjé, M.J. and Meijboom, R. 2015. Synthesis and characterization of silver(I) benzyldiphenylphosphine complexes: Towards the biological evaluation on SNO cells. *Inorganica Chimica Acta*. 437: 195 - 200.

Potgieter, K., Cronjé, M.J. and Meijboom, R. 2016. Synthesis of silver(I) *p*-substituted diphenyl phosphine complexes with the evaluation of the toxicity on SNO cancer cell line. *Inorganica Chimica Acta*. 453: 443 - 451.

Potgieter, K., Engelbrecht, Z., Naganagowda, G., Cronjé, M.J. and Meijboom, R. 2017. Anticancer activity of silver (I) cyclohexyldiphenylphosphine complexes toward SNO cancer cells. *Journal of Coordination Chemistry.* 70(15): 2644 - 2658.

Poyraz, M, Banti, C.N., Kourkoumelis, N. and Hadjikakou, S. 2011. Synthesis, structural characterization and biological studies of novel mixed ligand Ag(I) complexes with triphenylphosphine and aspirin or salicylic acid. *Inorganica Chimica Acta.* 375: 114 - 121.

Poyraz, M., Berber, H., Banti, C.N., Kourkoumelis, N., manos, M.J. and Hadjikakou, S.K. 2017. Synthesis characterization and biological activity of mixed ligand silver(I) complex of 2-benzimidazolylurea and triphenylphosphine. *Polyhedron.* 128: 95 - 103.

Rackham, O., Nichols, S.J., Leedman, P.J., Berners-Price, S.J. and Filipovska, A. 2007. A gold (I) phosphine complex selectively induces apoptosis in breast cancer cells: implications for anticancer therapeutics targeted to mitochondria. *Biochemical Pharmacology*. 74(7): 992 - 1002.

Ralph, S.J., Rodríguez-Enríquez, S., Neuzil, J., Saavedra, E. and Moreno-Sánchez, R. 2010. The causes of cancer revisited: "Mitochondrial malignancy" and ROS-induced oncogenic transformation - Why mitochondria are targets for cancer therapy. *Molecular Aspects of Medicine.* 31: 145 - 170.

Raju, S.K., Karunakaran, A., Kumar, S., Sekar, M.M. and Karthikeyan, M. 2022. Silver Complexes as Anticancer Agents: A Perspective Review. *German Journal of Pharmaceuticals and Biomaterials*. 1(1): 6 - 28.

Ranasinghe, R., Mathai, M.L. and Zulli, A. 2022. Cisplatin for cancer therapy and overcoming chemoresistance. *Heliyon*. 8(e10608): 1 - 17.

Rashidian, N., Alseidi, A. and Kirks, R.C. 2020. Cancer Metastatic to the Liver. *Surgical Clinics of North America.* 100(3): 551 - 563.

Raviadaran, R., Han Ng, M., Chandran, D., Ooi, K.K. and Manickam, S. 2021. Stable W/O/W multiple nanoemulsion encapsulating natural tocotrienols and caffeic acid with cisplatin synergistically treated cancer cell lines (A549 and HEP G2) and reduced toxicity on normal cell line (HEK 293). *Materials Science & Engineering C.* 121: 1 - 13.

Ray, P.D., Huang, B-W. and Tsuji, Y. 2013. Reactive oxygen species (ROS) homeostasis and redox regulation in cellular signalling. *Cellular Signalling.* 24(5): 981 - 990.

Reczek, C.R. and Chandel., N.S. 2017. The Two Faces of Reactive Oxygen Species in Cancer. *Annual Review of Cancer Biology.* 1: 79 - 98.

Redza-Dutordoir, M. and Averill-Bates, D.A. 2016. Activation of apoptosis signalling pathways by reactive oxygen species. *Biochimica et Biophysica Acta.* 1863: 2977 - 2992.

Ricci, M.S. and Zong, W. 2006. Chemotherapeutic Approaches for Targeting Cell Death Pathways. *Oncologist*. 11(4): 342 - 357.

Riley, R.S., June, C.H., Langer, R. and Mitchell, M.J. 2019. Delivery technologies for cancer immunotherapy. *Nature Reviews Drug Discovery.* 18(3): 175 - 196.

Rippey, J.J. and Rippey, E. 1984. Epidemiology of malignant melanoma of the skin in South Africa. *South African Medical Journal.* 65: 595 - 598.

Romeo, M.A., Montani, M.S.G., Benedetti, R., Arena, A., Maretto, M., Bassetti, E., Caiazzo, R., D'Orazi, G. and Cirone, M. 2021. Anticancer effect of AZD2461 PARP inhibitor against colon cancer cells carrying wt or dysfunctional p53. *Experimental Cell Research.* 408(2): 1 - 9.

Roy, P. and Sakia, B. 2016. Cancer and cure: A critical analysis. *Indian Journal of Cancer.* 53: 441 - 442.

Ruvinsky, A.M. 2007. Role of Binding Entropy in the Refinement of Protein–Ligand Docking Predictions: Analysis Based on the Use of 11 Scoring Functions. *Journal of Computational Chemistry.* 28(8): 1364 - 1372.

Saelens, X.S., Festjens. N., Walle, L.V., van Gurp, M., van Loo, G. and Vandenabeele, P. 2004. Toxic proteins released from mitochondria in cell death. *Oncogene*. 23: 2861 - 2874.

Şahin-Bölükaşi, S., Cantürk-Kiliçkaya, P and Kiliçkaya, O. 2020. Silver(I)-N-heterocyclic carbene complexes challenge cancer; evaluation of their anticancer properties and *in silico* studies. *Drug Development Research.* 82: 907 - 926.

Sakaguchi, R.L. and Powers, J.M. 2012. *Craig's Restorative Dental Materials*. (13th ed.). USA: Elsevier. Chapter 6 - Biocompatibility and Tissue Reaction to Biomaterials. (pg 109 - 111).

Saini, S., Hirata, H., Majid, S. and Dahiya, R. (2009). Functional significance of cytochrome P450 1B1 in endometrial carcinogenesis. *Cancer Research.* 69(17): 7038 - 7045.

Santini, C., Pellei, M. Papini, G., Morresi, B., Galassi, R., Ricci, S., Tisato, F., Porchia, M., Rigobello, M.P., Gandin, V. and Marzano, C. 2011. In vitro antitumour activity of water soluble Cu(I), Ag(I) and Au(I) complexes supported by hydrophilic alkyl phosphine ligands. *Journal of Inorganic Biochemistry.* 105(2): 232 - 240.

Scherbakov, A.M., Zhabinskii, V.N., Khripach, V.A., Shcherbinin, D.S., Mekhtiev, A.R., Shchegolev, Y.Y., Savochka, A.P. and Andreeva, O.E. 2019. Biological Evaluation of a New Brassinosteroid: Antiproliferative Effects and Targeting Estrogen Receptor α Pathways. *Chemistry & Biodiversity*. 16(9): 1 -10.

Schuppe-Koistinen, I., Moldéus, P., Bergman, T. and Cotgreave, I.A. 1994. S-thiolation of human endothelial cell glyceraldehyde-3-phosphate dehydrogenase after hydrogen peroxide treatment. *European Journal of Biochemistry*. 221(3):1033 - 1037.

Sharma, D., Kumar, S. and Narasimhan, B. 2018. Estrogen alpha receptor antagonists for the treatment of breast cancer: a review. *Chemistry Central Journal.* 12(107): 1 - 32.

Shi, Y., Ye, P and Long, X. 2017. Differential Expression Profiles of the Transcriptome in Breast Cancer Cell Lines Revealed by Next Generation Sequencing. *Cellular Physiology and Biochemistry.* 44(2): 804 - 816.

Shivanik, C., Deepak, K.S., Ragunathan, V., Tiwari, P., Sumitha, A. and Brindi, D.P. 2020. Molecular docking, validation, dynamics simulations, and pharmacokinetic prediction of natural compounds against the SARS-CoV-2 main-protease. *Journal of Biomolecular Structure and Dynamics.* 1 - 25.

Siegel, R.L., Miller, K.D., Fuchs, H.E. and Jemal, A. 2021. Cancer Statistics, 2022. *CA: A Cancer Journal for Clinicians*. 71: 7 - 33.

Siegel, R.L., Miller, K.D., Fuchs, H.E. and Jemal, A. 2022. Cancer Statistics, 2023. *CA: A Cancer Journal for Clinicians*. 73: 17 - 48.

Singh, M.P., Chauhan, A.K. and Kang, S.C. 2018. Morin hydrate ameliorates cisplatin-induced ER stress, inflammation and autophagy in HEK-293 cells and mice kidney via PARP-1 regulation. *International Immunopharmacology.* 56: 156 - 167.

Soengas, M.S., Capodieci, P., Polsky, D., Mora, J., Esteller, M., Opitz-Araya, X., McCombie, R., Herman, J.G., Gerald, W.L., Lazebnik, Y.A., Cordón-Cardó, C. and Lowe, S.W. 2001. Inactivation of the apoptosis effector *Apaf-1* in malignant melanoma. *Nature.* 409: 207 - 211.

Sofyan, N.R.F.M., Nordin, F.J., Mohd Abd Razak, M.R., Áin Abdul Halim, S.N., Mohd Khir, N.A.F., Muhammad, A., Rajab, N.F. and Sarip, R. 2018. New Silver Complexes with Mixed Thiazolidine and Phosphine Ligands as Highly Potent Antimalarial and Anticancer Agents. *Journal of Chemistry.* 1 - 10.

Stoian, M., State, N., Stoica, V. and Radulian, G. 2014. Apoptosis in Colorectal Cancer. *Journal of Medicine and Life.* 7(2): 160 - 164.

Suarez-Arnedo, A., Figueroa, F.T., Clavijo, C., Arbeláez, P., Cruz, J.V., Muñoz-Camargo, C. 2020. An image J plugin for the high throughput image analysis of in vitro scratch wound healing assays. PLoS ONE. 15(7): 1 - 14.

Sung, H., Ferlay, J., Siegal, R.L., Laversanne, M., Soerjomataram, I., Jemal, A. and Bray, F. 2021. Global Cancer Statistics 2020: GLOBOCAN Estimates of Incidence and Mortality Worldwide for 36 Cancers in 185 Countries. *CA: A Cancer Journal for Clinicians.* 71: 209 - 249.

Synytsya, A., Kral, V., Synytsya, A., Volka, K. and Sessler, J.L. 2003. *In vitro* interaction of macrocyclic photosensitizers with intact mitochondria: a spectroscopic study. *Biochimica et Biophysica Acta*. 1620: 85 - 96.

Tan, H., Zhong, Y and Pan, Z. 2009. Autocrine regulation of cell proliferation by estrogen receptor-alpha in estrogen receptor-alpha-positive breast cancer cell lines. 2009. *BioMed Central.* 9(31): 1 - 12.

Tarze, A., Deniaud, A., Le Bras, M., Maillier, E., Molle, D., Larochette, N., Zamzami, N., Jan, G., Kroemer, G and Brenner, C. 2007. GAPDH, a novel regulator of the pro-apoptotic mitochondrial membrane permeabilization. *Oncogene.* 26: 266 - 2620.

Tatton, W.G., Chalmers-Redman, R.M.E., Elstner, M., Leesch, W., Jagodzinski, F.B., Stupak, D.P., Sugrue. M.M. and Tatton, N.A. 2000. *Springer Medicine: Advances in Research on Neurodegeneration*. Glyceraldehyde-3-phosphate dehydrogenase in neurodegeneration and apoptosis signaling. Springer, Vienna. Vol 8, (pg. 77 -100).

Theodossiou, T.A., Ali, M., Grigalavicius, M., Grallert, B., Dillard, P., Schink, K.O., Olsen, C.E., Wälchi, S., Inderberg, E,M., Kubin, A., Peng, Q. and Berg, K. 2019. Simultaneous defeat of MCF-7 and MDA-MB-231 resistances by a hypericin PDT-tamoxifen hybrid therapy. *Breast Cancer.* 13: 1 - 10.

Tower, J. 2015. Programmed cell death in aging. *Ageing Research Reviews*. 23: 90 - 100.

Tristan, C., Shahani, N., Sedlak, TW., Sawa, A. 2011. The diverse functions of GAPDH: views from different subcellular compartments. *Cellular Signaling*. 23(2): 317 - 323.

Tsvetkov, P., Coy, S., Petrova, B., Dreishpoon, M., Verma, A., Abdusamad, M., Rossen, J., Joesch-Cohen, L., Humeidi, R., Spangler, R.D., Eaton, J.K., Frenkel. E., Kocak, M., Corsello, S.M., Lutsenko, S., Kanarek, N., Santagata, S and Golub, T.R. 2022. Copper induces cell death by targeting lipoylated TCA cycle proteins. *Science.* 375: 1254 - 1261.

Vedoya, G.M., López Nigro, M.M. and Martín, G.A. 2021. The secretome of non-tumorigenic mammary cells MCF-10A elicits DNA damage in MCF-7 and MDA-MB-231 breast cancer cells. *Toxicology in Vitro*. 70: 1 - 13.

Vermes, I., Hannen, C., Steffens-Nakken, H and Reutelingsperger, C. 1995. A novel assay for apoptosis: Flow cytometric detection of phosphatidylserine early apoptotic cells using fluorescein labelled expression on Annexin V. *Journal of Immunological Methods.* 184: 39 - 51.

von Arx, C., De Placido, P., Caltavituro, A., Di Rienzo, R., Bounaiuto, R., De Laurentiis, M., Arpino, G., Puglisi, F., Giuliano, M. and Del Mastro, L. 2023. The evolving therapeutic landscape of trastuzumab-drug conjugates: Future perspectives beyond HER2-positive breast cancer. *Cancer Treatment Reviews.* 113: 1 - 13.

Walczak H. 2013. Death receptor–ligand systems in cancer, cell death, and inflammation. *Cold Spring Harbor Perspectives in Boil.* 5: 1 - 18.

Wang, H. 2020. MicroRNAs and Apoptosis in Colorectal Cancer. *International Journal of Molecular Sciences.* 21: 1 - 15.

Wang, Y. and Chen, E. 2021. Interventional bronchoscopic treatment of lung cancer. *Laparoscopic, Endoscopic and Robotic Surgery.* 5: 52 - 56.

Warburg, O. 1925. The metabolism of carcinoma cells. *The Journal of Cancer Research*. 9(1): 148 - 163.

Warburg, O., Wind, F. and Negelein, E. 1927. The metabolism of tumors in the body. *The Journal of General Physiology*. 8(6): 519 - 530.

Wege, H., Schulze, K., von Felden, J., Calderaro, J., Reig, M., for the rare liver tumors working group of the European Reference Network on Hepatological Diseases (ERN RARE-LIVER). 2021. Rare variants of primary liver cancer: Fibrolamellar, combined, and sarcomatoid hepatocellular carcinomas. *European Journal of Medical Genetics.* 64(104131): 1 - 6.

Welsh, J. 2013. *Animal Models for the Study of Human Disease*. Chapter 40: Animal Models for Studying Prevention and Treatment of Breast Cancer. Elsevier, Academic Press. (pg. 997 - 1018).

World Health Organization (WHO). Updated 3rd March 2021. Cancer. Available from https://www.who.int/news-room/fact-sheets/detail/cancer. (Accessed the 9th of April 2021).

Xie, T., Qiao, X., Sun, C., Chu, B., Meng, J. and Chen, C. 2022. GAPDH S-nitrosation contributes to age-related sarcopenia through mediating apoptosis. *Nitric Oxide*. 120: 1 - 8.

Xu, C., Hou, Z., Zhan, P., Zhao, W., Chang, C., Zou, Z., Hu, H., Zhang, Y., Yao, X., Yu, L. and Yan, J. 2013. EZH2 regulates cancer cell migration through repressing TIMP-3 in non-small cell lung cancer. *Medical Oncology.* 30(713): 1 - 8.

Yang, H., Chen, J., Yang, J., Qiao, S., Zhao, S. and Yu, L. 2007. Cyclophilin A is upregulated in small cell lung cancer and activates ERK1/2signal. *Biochemical and Biophysical Research Communications.* 361: 763 – 767.

Yang, J., Xiao, P., Sun, J. and Guo, L. 2018. Anticancer effects of kaempferol in A375 human malignant melanoma cells are mediated via induction of apoptosis, cell cycle arrest, inhibition of cell migration and downregulation of m-TOR/PI3K/AKT pathway. *Journal of the Balkan Union of Oncology.* 23(1): 218 - 223.

Yang, S.Y., Sales, K.M., Fuller, B., Seifalian, A.M. and Winslet, M.C. 2009. Apoptosis and colorectal cancer: implications for therapy. *Cell Press. Trends in Molecular Medicine.* 15(5): 225 - 223.

Yilmaz, V.T., Icsel, C., Batur, J., Aydinlik, M.C. and Buyukgungor, O. 2017. Synthesis, structures and biomolecular interactions of new silver(I) 5,5 -diethylbarbiturate complexes of monophosphines targeting Gram-positive bacteria and breast cancer cells. *Dalton Transactions.* 46: 8110 - 8124.

Yilmaz, V.T., Icsel, C., Turgut, O.R., Aygun, M., Erkisa, M., Turkdemir, M.H. and Ulukaya, E. 2018. Synthesis, structures and anticancer potentials of platinum(II) saccharinate complexes of tertiary phosphines with phenyl and cyclohexyl groups targeting mitochondria and DNA. *European Journal of Medicinal Chemistry.* 155: 609 - 622.

Yu, C-L., Lee, H-L., Yang, S-F., Wang, S-W, Lin, C-P., Hsieh, Y-H. and Chiou, H-L. 2022. Protodioscin Induces Mitochondrial Apoptosis of Human Hepatocellular Carcinoma Cells Through Eliciting ER Stress-Mediated IP3R Targeting Mfn1/Bak Expression. *Journal of Hepatocellular Carcinoma*. 9: 327 – 341.

Yu, Z., Jiang, N., Su, W. and Zhou, Y. 2021. Necroptosis: A Novel Pathway in Neuroinflammation. *Frontiers on Pharmacology.* 12: 1 - 13.

Yuan, Q.X. and Liu, B. 2014. Self-assembled nanoparticles based on PEGylated conjugated polyelectrolyte and drug molecules for image-guided drug delivery and photodynamic therapy. *Applied Materials and Interfaces*. 6: 14903 - 14910.

Zaki, M., Arjmand, F. and Tabassum, S. 2016. Current and future potential of metallo drugs: Revisiting DNA- binding of metal containing molecules and their diverse mechanism of action. *Inorganica Chimica Acta.* 444: 1 - 22.

Zinovkin, R.A. and Zamyatnin Jr., A.A. 2019. Mitochondria-Targeted Drug. *Current Molecular Pharmacology*. 12: 202 - 214.

Zong, W. and Thompson, C.B. 2006. Necrotic death as a cell fate. *Genes & Development*. 20: 1 - 15.

APPENDIX I

The complete list of manufacturer information for all cell lines, equipment, reagents, materials and software utilized for experimental analyzes in chapters two to five.

Cell lines

Human malignant cell cultures

A375 non-pigmented melanoma *(Gifted by the University of Cape Town)*

A549 lung adenocarcinoma *(Cellonex™, RSA)*

HEP-G2 hepatocellular carcinoma *(Cellonex™, RSA)*

HT-29 colorectal adenocarcinoma *(Cellonex™, RSA)*

MCF-7 breast adenocarcinoma *(Cellonex™, RSA)*

MDA-MB-231 breast adenocarcinoma *(Gifted by the University of KwaZulu-Natal)*

SNO esophageal squamous cell carcinoma *(Gifted by the University of Witwatersrand)*

Human non-malignant cell cultures

HEK293 embryonic kidney cells *(Gifted by the University of KwaZulu-Natal)*

MRHF foreskin fibroblast cells *(Cellonex™, RSA)*

Equipment

AccuBlock™ Digital Dry Bath *(Labnet International, Inc., USA)*

AS 82/220.R2 Plus Analytical Balance *(RADWAG® Balances and Scales, UK)*

Axio Cam ERc 5s Camera *(Carl Zeiss, Germany)*

Axio Cam MRC Camera *(Carl Zeiss, Germany)*

Axioplan 2 Imaging Inverted Fluorescence Microscope *(Carl Zeiss, Germany)*

Axiovert 25 Inverted Light Microscope *(Carl Zeiss, Germany)*

Benchtop pH/mV Meter 210 *(Bante Instruments, China)*

Bruker Ultrashield Avance III 400 MHz NMR Spectrometer *(Bruker, USA)*

Countess™ Automated Cell Counter *(ThermoFisher Scientific, RSA)*

Digital Heating Magnetic Stirrer *(Lasec, RSA)*

EC 160 CO_2 Incubator *(Nüve, Turkey)*

Eppendorf® 5415R Bench Top Centrifuge *(Merck, RSA)*

Guava® Muse® Cell Analyzer *(Luminex Corporation, USA)*

Magnetic Stirrer *(FMH Instruments, RSA)*

MN 120 Microbiological Safety Cabinet *(Nüve, Turkey)*

NF 400R Benchtop Centrifuge *(Nüve, Turkey)*

Primovert Inverted Light Microscope *(Carl Zeiss, Germany)*

Shimadzu Analytical Balance AUW220D *(Shimadzu Cooperation, Japan)*

Stuart Scientific SMP10 Melting Point Instrument *(Sigma-Aldrich, USA)*

Thermo Flash 2000 series CHNS/O, Organic Elemental Analyzer (*Sigma-Aldrich, USA*)

Vacuum/Pressure pump Model No. DOA-P736-BN *(Pall Life Sciences Cooperation, USA)*

VICTOR® Nivo™ Multimode Plate Reader *(PerkinElmer, USA)*

Waterbath, Digital control, 20L *(Labcon Laboratory Equipment (PTY) Ltd, RSA)*

Reagents

4-(dimethylamino)-phenyldiphenyl-phosphine *(Sigma-Aldrich, USA)*

alamarBlue® proliferation assay *(Bio-Rad, UK)*

Alexa Fluor® 488 mouse Anti-Cytochrome *c* antibody [37BA11] *(Abcam Incorporated, USA)*

Benzyldiphenylphosphine *(Sigma-Aldrich, USA)*

Bovine Serum Albumin (Fraction V) *(Roche Diagnostics GMbH, Germany)*

CelltiterGlo™ Luminescent Cell Viability Assay *(Promega, USA)*

Cisplatin *(Molekula, UK)*

Cytochrome P450-Glo™ Assay Kit, specific for CYP1B1 isoform *(Promega, USA)*

Dicyclohexyl-phenylphosphine *(Sigma-Aldrich, USA)*

Dimethyl Sulphoxide (DMSO) *(Sigma-Aldrich, USA)*

Diphenyl-2-pyridylphosphine *(Sigma-Aldrich, USA)*

Dulbecco's Modified Eagle's Medium – High glucose *(Sigma-Aldrich, Germany)*

EDTA (Disodium Ethylenediaminetetraacetate dehydrate) *(Sigma-Aldrich, USA)*

Ethanol *(Sigma-Aldrich, Germany)*

Fetal Calf Serum *(Biowest, France; Gibco® Live Technologies, USA)*

Formaldehyde *(Sigma-Aldrich, USA)*

Hank's Balanced Salt Solution (10X) *(Gibco® Live Technologies, UK)*

Hepes Buffer 1M *(BioWhittaker®, Lonza, USA)*

Hoechst-33258 pentahydrate (bis-benzimide) *(Molecular Probes™ by Invitrogen Detection Technologies, USA)*

Hydrochloric acid (HCl) *(Saarchem (PTY) Ltd., RSA)*

Hydrogen peroxide 50% (200vols) (H_2O_2) *(Associated chemical enterprise, RSA)*

KDalert™ GADPH Assay Kit *(Ambion®, USA)*

McCoy's 5A Medium with stable Glutamine and 2.2 g/L $NaHCO_3$ *(PAN™ Biotech, Germany)*

Methanol *(Rochelle Chemicals, RSA)*

Mitotracker® Orange CMTMRos *(Molecular Probes™ by Live Technologies, USA)*

Muse® Annexin V and Dead Cell Kit *(Part Number: MCH100105, Luminex Corporation, USA)*

Muse® Instrument Cleaning Fluid (ICF) *(Part Number: 4200-0140, Luminex Corporation, USA)*

Muse® MitoPotential Kit *(Part Number: MCH100110, Luminex Corporation, USA)*

Muse® Oxidative Stress Kit *(Part Number: MCH100111, Luminex Corporation, USA)*

Muse® System Check Kit *(Part Number: MCH100101, Luminex Corporation, USA)*

Penicillin/Streptomycin, Amphotericin B (100X) *(BioWhittaker®, Lonza, USA)*

pH calibration solutions, pH 4 red coloured and pH 7 green coloured *(VWR Chemicals, BDH PROLABO®, France)*

Phosphate buffered saline tablets (50 tablets) *(Sigma-Aldrich, Germany)*

Pierce™ RIPA buffer *(Thermo Scientific, USA)*

Precision Plus Protein™ Standards, Dual Colour (170-10 kDa range) *(Bio-Rad, USA)*

Propidium Iodide (PI) DNA dye assay *(Molecular Probes™ by Live Technologies, USA)*

SIGMAFAST™ protease inhibitor cocktail tablet, EDTA free *(Sigma-Aldrich, USA)*

Sodium bicarbonate *(Melford Biolaboratories Ltd., UK)*

Sodium chloride *(Associated Chemical Enterprises (PTY) Ltd., RSA)*

Sodium hydroxide pellets *(Saarchem Holpro Analytic (PTY) Ltd., RSA)*

Recombinant PE Anti-Estrogen Receptor alpha antibody [E115] (ab209288) *(Abcam Incorporated, USA)*

Triton X-100 *(BDH Merck Laboratories, Germany)*

Trypan blue dye *(Sigma-Aldrich, USA)*

Trypsin 10X with Versene *(BioWhittaker®, Lonza, USA)*

Tween® 20, for electrophoresis *(Sigma-Aldrich, Germany)*

Materials

Cell culture clear plate, 96 well, tissue culture treated *(NEST Biotechnology Co., Ltd., China)*

Cell culture dish, tissue culture treated (35mm) *(NEST Biotechnology Co., Ltd., China)*

Cell culture flask canted neck, tissue culture treated, and vent capped (75 cm^3) *(NEST Biotechnology Co., Ltd., China)*

Corning® CellBIND® surface clear plate, 96 well, flat bottom with lid *(Corning Incorporated, USA)*

Corning® CellBIND® white plate, 96 well, flat bottom with lid *(Corning Incorporated, USA)*

Corning® Costar® cell culture clear plate, 24 well, flat bottom with lid *(Sigma-Aldrich, Germany)*

Corning® Costar® cell culture black plate, 96 well, flat bottom with lid *(Sigma-Aldrich, Germany)*

Counting slides, dual chamber for cell counter *(Bio-Rad, USA)*

Cryogenic vials 2.0 ml *(NEST Biotechnology Co., Ltd., China)*

Deckgläser cover glasses 20 x 20 mm *(Superior Marienfeld, Germany)*

FALCON® polypropylene conical tube (50 ml) *(Corning Incorporated, USA)*

Graduated microcentrifuge tubes (Eppendorf) with flat top, natural (2 ml) *(Quality Scientific*

Plastics, Thermo Scientific, USA)

HistoBond® microscope slides *(Paul Marienfeld GmbH & Co, Germany)*

Steritop®/Receiver Flask, vacuum-driven filtration systems *(EMD Millipore Corporation, USA)*

Software

AutoDockTools (*The Scripps Research Institute, USA)*

Auto Dock Version 4.2.6 Software (*The Scripps Research Institute, USA)*

Axio Version 3.1 Software *(Carl Zeiss, Germany)*

BioRender *(USA) (Access: https://www.biorender.com/)*

BIOVIA Discovery Studio Visualizer *(Dassault Systémes, France)*

ImageJ *(National Institutes of Health, USA)*

MGLTools Version 1.5.4 *(Molecular Graphics Laboratory, The Scripps Research Institute, USA)*

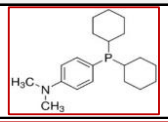
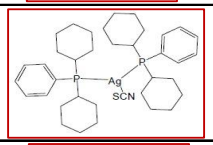
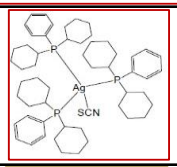
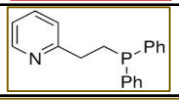
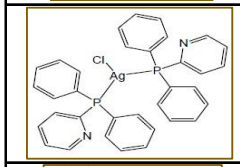
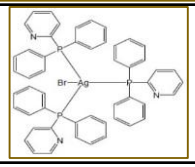
Microsoft® Excel and Word 2010

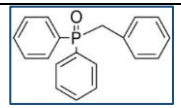
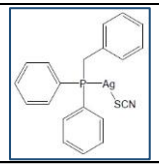
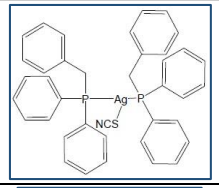
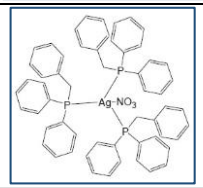
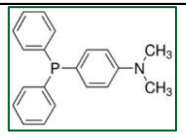
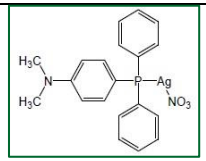
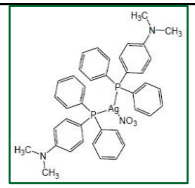
Muse® Software Version 1.4.0.0 *(Luminex Corporation, USA)*

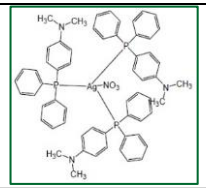
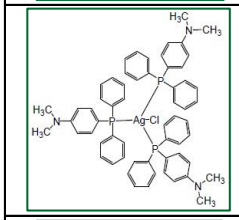
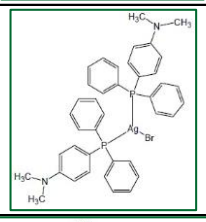
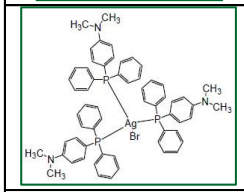
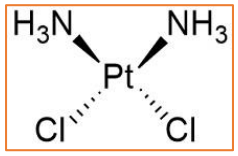
Python 2.5 *(Python Software Foundation, USA)*

APPENDIX II

Table A1. Single-dose screening (percentage cellular viability) of nine human cell lines were performed, using the alamarBlue® proliferation assay. Cells were treated with 100 µM CDDP (positive apoptotic control), 10 µM of silver(I) phosphine complexes (**1 - 13**) and 10 µM of respective ligands (**L1 - L4**) for 24 h. The ±SEM is indicated in brackets and the polynomial function of six independent repeats were used. Viabilities shaded in grey are the successful silver(I) phosphine complexes and were evaluated further.

Complex structure	Ligand/Complex	HEK-293	MRHF	A375	A549	HEP-G2	HT-29	MCF-7	MDA-MB-231	SNO
	L1	98.80 (± 3.60)	104.28 (±1.64)	102.33 (± 1.79)	96.87 (± 1.81)	106.42 (± 3.87)	100.01 (± 2.10)	101.02 (± 2.87)	98.74 (± 1.32)	103.69 (± 2.12)
	1	89.49 (± 4.93)	87.99 (±3.23)	6.38 (±4.53)	15.96 (± 1.81)	7.63 (± 1.23)	83.78 (± 8.26)	27.89 (± 1.80)	87.93 (± 1.53)	12.71 (± 4.90)
	2	92.03 (± 3.79)	95.79 (±1.53)	10.88 (± 0.98)	3.85 (± 1.45)	5.45 (± 0.16)	56.81 (± 2.78)	14.70 (± 1.80)	32.21 (± 3.45)	9.90 (± 3.53)
	L2	102.78 (± 2.97)	101.29 (± 1.99)	103.41 (± 1.36)	100.14 (± 2.24)	89.17 (± 0.55)	86.05 (± 3.19)	86.76 (± 3.17)	88.42 (± 0.94)	103.85 (± 1.63)
	3	94.76 (± 5.08)	97.98 (± 2.02)	43.46 (± 2.93)	50.77 (± 3.05)	13.63 (± 2.82)	50.34 (± 0.74)	42.42 (± 3.36)	68.52 (± 5.52)	20.23 (± 5.25)
	4	85.89 (± 4.82)	93.94 (± 2.60)	36.26 (± 2.36)	28.45 (± 1.96)	14.67 (± 2.42)	35.11 (± 2.02)	42.21 (± 1.43)	38.88 (± 3.18)	24.05 (± 3.67)

	**L3**	100.04 (± 3.11)	103.67 (± 2.17)	107.60 (± 2.23)	101.94 (± 0.81)	86.78 (± 0.67)	101.98 (± 0.70)	98.37 (± 7.29)	96.74 (± 1.82)	104.87 (± 2.60)
	**5**	80.00 (± 5.08)	108.83 (± 5.30)	83.66 (± 3.72)	69.56 (± 2.68)	88.78 (± 2.88)	66.19 (± 0.93)	82.43 (± 3.31)	85.07 (± 2.49)	74.90 (± 4.59)
	**6**	85.71 (± 5.72)	110.75 (± 6.25)	68.03 (± 2.93)	28.37 (± 4.10)	79.75 (± 0.73)	74.63 (± 4.90)	79.83 (± 7.56)	97.58 (± 1.14)	105.09 (± 0.88)
	**7**	94.13 (± 5.99)	108.73 (± 6.63)	48.59 (± 2.81)	21.59 (± 3.48)	87.46 (± 1.73)	71.98 (± 2.70)	6.82 (± 1.19)	52.13 (± 3.97)	48.08 (± 3.39)
	**L4**	90.08 (± 2.10)	106.27 (± 1.84)	99.74 (± 2.62)	100.81 (± 2.82)	95.04 (± 2.54)	100.85 (± 3.99)	103.50 (± 7.24)	104.10 (± 1.88)	112.44 (± 0.26)
	**8**	94.71 (± 6.30)	113.56 (± 1.84)	97.74 (± 2.62)	76.03 (± 1.63)	95.36 (± 0.66)	84.61 (± 8.03)	94.18 (± 2.24)	91.35 (± 3.54)	82.68 (± 3.76)
	**9**	93.95 (± 2.93)	111.72 (± 4.85)	111.60 (± 3.54)	87.88 (± 1.41)	89.26 (± 1.12)	77.02 (± 3.03)	59.14 (± 2.39)	67.17 (± 1.49)	61.31 (± 1.70)

	**10**	**91.99 (± 5.68)**	**72.73 (± 2.32)**	**104.33 (± 4,26)**	**89.14 (± 1.28)**	**91.20 (± 0.44)**	**98.49 (± 0.73)**	**55.62 (± 2.78)**	**72.10 (± 1.49)**	**51.74 (± 2.62)**
	**11**	**91.11 (± 1.15)**	**60.86 (± 2.33)**	**81.78 (± 3.10)**	**84.85 (± 1.05)**	**95.76 (± 0.27)**	**94.92 (± 2.79)**	**56.80 (± 5.77)**	**79.60 (± 2.08)**	**64.42 (± 2.05)**
	**12**	**96.98 (± 1.55)**	**74.25 (± 2.37)**	**87.13 (± 5.63)**	**84.04 (± 1.80)**	**95.79 (± 0.95)**	**110.21 (± 0.83)**	**45.84 (± 2.72)**	**72.76 (± 1.40)**	**84.28 (± 4.86)**
	**13**	**97.96 (± 3.75)**	**82.07 (± 1.72)**	**69.78 (± 3.11)**	**79.87 (± 0.92)**	**97.12 (± 1.33)**	**93.40 (± 4.99)**	**60.73 (± 7.39)**	**60.08 (± 1.37)**	**74.74 (± .23)**
	**CDDP**	**73.06 (± 3.60)**	**105.40 (± 3.16)**	**39.85 (± 3.91)**	**58.21 (± 3.85)**	**65.20 (± 1.25)**	**59.75 (± 0.92)**	**68.05 (± 2.98)**	**64.36 (± 0.73)**	**43.98 (± 1.89)**

APPENDIX III

Data A1. The ADT4 grid parameter file (`.gpf`) for 6WOK nuclear protein: crystal structure of estrogen receptor alpha in complex with receptor degrader 6, obtained from the PDB.

```
npts 126 126 126                  # num.grid points in xyz
parameter_file AD4_parameters.dat # force field default parameter file
gridfld 6wok_prep.maps.fld        # grid_data_file
spacing 0.375                     # spacing(A)
receptor_types A C HD N NA OA SA  # receptor atom types
ligand_types A P Br Ag NA         # ligand atom types
receptor 6wok_prep.pdbqt          # macromolecule
gridcenter 24.274 -5.788 16.409   # xyz-coordinates or auto centre
smooth 0.5                        # store minimum energy w/in rad(A)
map 6wok_prep.A.map               # atom-specific affinity map
map 6wok_prep.P.map               # atom-specific affinity map
map 6wok_prep.Br.map              # atom-specific affinity map
map 6wok_prep.Ag.map              # atom-specific affinity map
map 6wok_prep.NA.map              # atom-specific affinity map
elecmap 6wok_prep.e.map           # electrostatic potential map
dsolvmap 6wok_prep.d.map          # desolvation potential map
dielectric -0.1465            # <0, AD4 distance dep.diel;>0,constant
```

Data A2. The ADT4 grid parameter file (`.gpf`) for 2YLY receptor: sulfonamides as selective estrogen receptor beta agonists, obtained from the PDB.

```
npts 126 126 126                  # num.grid points in xyz
parameter_file AD4_parameters.dat # force field default parameter file
gridfld 2yly_prep.maps.fld        # grid_data_file
spacing 0.375                     # spacing(A)
receptor_types A C HD N OA SA     # receptor atom types
ligand_types A P Br Ag NA         # ligand atom types
receptor 2yly_prep.pdbqt          # macromolecule
gridcenter -44.414 -19.34 -25.466 # xyz-coordinates or auto centre
smooth 0.5                        # store minimum energy w/in rad(A)
map 2yly_prep.A.map               # atom-specific affinity map
map 2yly_prep.P.map               # atom-specific affinity map
map 2yly_prep.Br.map              # atom-specific affinity map
map 2yly_prep.Ag.map              # atom-specific affinity map
map 2yly_prep.NA.map              # atom-specific affinity map
elecmap 2yly_prep.e.map           # electrostatic potential map
dsolvmap 2yly_prep.d.map          # desolvation potential map
dielectric -0.1465           # <0, AD4 distance-dep.diel;>0,constant
```

Data A3. The ADT4 docking parameter file (`.dpf`) for 6WOK nuclear protein: crystal structure of estrogen receptor alpha in complex with receptor degrader 6 docked with complex **4**.

```
autodock_parameter_version 4.2 # used by autodock to validate parameter
set
parameter_file AD4.1_bound.dat # parameter library filename
intelec                        # calculate internal electrostatics
seed pid time                  # seeds for random generator
ligand_types A P Br Ag NA      # atoms types in ligand
fld 6wok_prep.maps.fld         # grid_data_file
map 6wok_prep.A.map            # atom-specific affinity map
map 6wok_prep.P.map            # atom-specific affinity map
map 6wok_prep.Br.map           # atom-specific affinity map
map 6wok_prep.Ag.map           # atom-specific affinity map
map 6wok_prep.NA.map           # atom-specific affinity map
elecmap 6wok_prep.e.map        # electrostatics map
desolvmap 6wok_prep.d.map      # desolvation map
move CIF_correct_model1.pdbqt  # small molecule
about 6.032 3.610 8.921     # small molecule center
tran0 random                # initial coordinates/A or random
quaternion0 random          # initial orientation
dihe0 random                # initial dihedrals (relative) or random
torsdof 12                  # torsional degrees of freedom
rmstol 2.0                  # cluster_tolerance/A
extnrg 1000.0               # external grid energy
e0max 0.0 10000             # max initial energy; max number of retries
ga_pop_size 150             # number of individuals in population
ga_num_evals 2500000        # maximum number of energy evaluations
ga_num_generations 27000    # maximum number of generations
ga_elitism 1    # number of top individuals to survive to next generation
ga_mutation_rate 0.02       # rate of gene mutation
ga_crossover_rate 0.8       # rate of crossover
ga_window_size 10           #
ga_cauchy_alpha 0.0         # Alpha parameter of Cauchy distribution
ga_cauchy_beta 1.0          # Beta parameter Cauchy distribution
set_ga                      # set the above parameters for GA or LGA
sw_max_its 300              # iterations of Solis & Wets local search
sw_max_succ 4               # consecutive successes before changing rho
sw_max_fail 4               # consecutive failures before changing rho
sw_rho 1.0                  # size of local search space to sample
sw_lb_rho 0.01              # lower bound on rho
ls_search_freq 0.06         # probability of performing local search on
individual
set_psw1              # set the above pseudo-Solis & Wets parameters
unbound_model bound         # state of unbound ligand
ga_run 100                  # do this many hybrid GA-LS runs
analysis                    # perform a ranked cluster analysis
```

Data A4. The ADT4 docking parameter file (`.dpf`) for 2YLY receptor: sulfonamides as selective estrogen receptor beta agonists docked with complex **4**.

```
autodock_parameter_version 4.2 # used by autodock to validate parameter
set
parameter_file AD4.1_bound.dat # parameter library filename
intelec                        # calculate internal electrostatics
seed pid time                  # seeds for random generator
ligand_types A P Br Ag NA      # atoms types in ligand
fld 2yly_prep.maps.fld         # grid_data_file
map 2yly_prep.A.map            # atom-specific affinity map
map 2yly_prep.P.map            # atom-specific affinity map
map 2yly_prep.Br.map           # atom-specific affinity map
map 2yly_prep.Ag.map           # atom-specific affinity map
map 2yly_prep.NA.map           # atom-specific affinity map
elecmap 2yly prep.e.map        # electrostatics map
desolvmap 2yly_prep.d.map      # desolvation map
move CIF_correct_model1.pdbqt  # small molecule
about 6.032 3.610 8.921     # small molecule center
tran0 random                # initial coordinates/A or random
quaternion0 random          # initial orientation
dihe0 random                # initial dihedrals (relative) or random
torsdof 12                  # torsional degrees of freedom
rmstol 2.0                  # cluster_tolerance/A
extnrg 1000.0               # external grid energy
e0max 0.0 10000             # max initial energy; max number of retries
ga_pop_size 150             # number of individuals in population
ga_num_evals 2500000        # maximum number of energy evaluations
ga_num_generations 27000    # maximum number of generations
ga_elitism 1    # number of top individuals to survive to next generation
ga_mutation_rate 0.02       # rate of gene mutation
ga_crossover_rate 0.8       # rate of crossover
ga_window_size 10           #
ga_cauchy_alpha 0.0         # Alpha parameter of Cauchy distribution
ga_cauchy_beta 1.0          # Beta parameter Cauchy distribution
set_ga                      # set the above parameters for GA or LGA
sw_max_its 300              # iterations of Solis & Wets local search
sw_max_succ 4               # consecutive successes before changing rho
sw_max_fail 4               # consecutive failures before changing rho
sw_rho 1.0                  # size of local search space to sample
sw_lb_rho 0.01              # lower bound on rho
ls_search_freq 0.06         # probability of performing local search on
individual
set_psw1               # set the above pseudo-Solis & Wets parameters
unbound_model bound         # state of unbound ligand
ga_run 100                  # do this many hybrid GA-LS runs
analysis                    # perform a ranked cluster analysis
```

Data A5. The final GA docked state for complex **4** docked with the 6WOK nuclear protein: crystal structure of estrogen receptor alpha in complex with receptor degrader 6. The best model is represented below.

```
MODEL       14
USER    Run = 14
USER    Cluster Rank = 1
USER    Number of conformations in this cluster = 4
USER
USER    RMSD from reference structure       = 16.922 A
USER
USER    Estimated Free Energy of Binding    =   -7.40 kcal/mol
[=(1)+(2)+(3)-(4)]
USER    Estimated Inhibition Constant, Ki   =    3.76 uM (micromolar)
[Temperature = 298.15 K]
USER
USER    (1) Final Intermolecular Energy     =  -10.98 kcal/mol
USER        vdW + Hbond + desolv Energy     =  -11.11 kcal/mol
USER        Electrostatic Energy            =   +0.13 kcal/mol
USER    (2) Final Total Internal Energy     =   -8.64 kcal/mol
USER    (3) Torsional Free Energy           =   +3.58 kcal/mol
USER    (4) Unbound System's Energy  [=(2)] =   -8.64 kcal/mol
USER
USER
USER
USER    DPF = C:/Users/Wits-
User/Desktop/Kim_docking/docking_6wok_lam.dpf
USER    NEWDPF move     CIF_correct_model1.pdbqt
USER    NEWDPF about    6.032000 3.610000 8.921000
USER    NEWDPF tran0    20.527120 3.527802 25.109203
USER    NEWDPF axisangle0     -0.032722 0.304393 0.951984 162.982573
USER    NEWDPF quaternion0    -0.032362 0.301043 0.941506 0.147960
USER    NEWDPF dihe0    -113.55 84.51 44.29 40.77 160.81 -83.16 -45.09
-155.47 -178.02 117.16 -47.76 102.10
USER
USER                                x       y       z    vdW   Elec
q     RMS
ATOM      1 AG1          0      20.284   4.157  24.658 -0.02 -0.00
+0.000    16.922
ATOM      2 BR1          0      19.247   6.089  23.070 -0.03 -0.00
+0.000    16.922
ATOM      3  P1          0      21.132   2.460  22.992 -0.08 -0.00
+0.004    16.922
ATOM      4  C42         0      21.553   0.832  23.778 -0.15 -0.00    -
0.021    16.922
ATOM      5  C50         0      20.689   0.244  24.609 -0.20 -0.00
+0.013    16.922
ATOM      6  C51         0      21.060  -0.894  25.149 -0.21 -0.00
+0.001    16.922
ATOM      7  C23         0      22.263  -1.537  24.909 -0.29 -0.00
+0.000    16.922
ATOM      8  C22         0      23.122  -0.924  24.062 -0.20 +0.00
+0.001    16.922
ATOM      9  C26         0      22.800   0.255  23.479 -0.18 +0.01
+0.013    16.922
ATOM     10  C32         0      19.908   1.945  21.719 -0.02 +0.01    -
0.021    16.922
ATOM     11  C49         0      18.949   2.856  21.392 -0.01 -0.00
+0.013    16.922
```

```
ATOM     12  C27         0      17.985   2.590  20.430 -0.01 -0.00
+0.001    16.922
ATOM     13  C43         0      17.959   1.391  19.802 -0.01 -0.00
+0.000    16.922
ATOM     14  C29         0      18.915   0.470  20.091 -0.03 -0.00
+0.001    16.922
ATOM     15  C48         0      19.907   0.733  21.061 -0.04 -0.00
+0.013    16.922
ATOM     16  C17         0      22.648   2.830  22.057 -0.10 +0.00
+0.064    16.922
ATOM     17  C52         0      23.711   3.380  22.757 -0.18 +0.01
+0.032    16.922
ATOM     18  C31         0      24.885   3.742  22.081 -0.23 +0.00
+0.001    16.922
ATOM     19  C33         0      25.012   3.547  20.760 -0.23 +0.00
+0.003    16.922
ATOM     20  C41         0      23.967   2.948  20.045 -0.11 -0.01
+0.160    16.922
ATOM     21  N2          0      22.774   2.580  20.681 -0.04 +0.02    -
0.277    16.922
ATOM     22  P3          0      21.891   5.481  26.109 -0.14 -0.00
+0.004    16.922
ATOM     23  C13         0      23.700   5.409  25.793 -0.16 +0.01    -
0.021    16.922
ATOM     24  C47         0      24.558   4.560  26.459 -0.28 -0.00
+0.013    16.922
ATOM     25  C46         0      25.930   4.548  26.185 -0.34 -0.00
+0.001    16.922
ATOM     26  C25         0      26.412   5.396  25.230 -0.32 -0.00
+0.000    16.922
ATOM     27  C16         0      25.580   6.232  24.540 -0.19 -0.00
+0.001    16.922
ATOM     28  C12         0      24.207   6.215  24.794 -0.13 -0.01
+0.013    16.922
ATOM     29  C24         0      21.539   7.273  25.969 -0.08 -0.04
+0.069    16.922
ATOM     30  C30         0      20.304   7.776  25.652 -0.05 -0.01
+0.033    16.922
ATOM     31  C37         0      20.122   9.149  25.628 -0.07 -0.00
+0.004    16.922
ATOM     32  C38         0      21.186   9.976  25.873 -0.10 -0.01
+0.019    16.922
ATOM     33  C34         0      22.400   9.429  26.113 -0.03 -0.14
+0.117    16.922
ATOM     34  N3          0      22.609   8.092  26.181 -0.10 +0.33    -
0.260    16.922
ATOM     35  C39         0      21.780   5.174  27.913 -0.17 +0.01    -
0.021    16.922
ATOM     36  C36         0      20.564   4.697  28.330 -0.17 -0.01
+0.013    16.922
ATOM     37  C45         0      20.410   4.443  29.631 -0.24 -0.00
+0.001    16.922
ATOM     38  C44         0      21.322   4.662  30.586 -0.31 -0.00
+0.000    16.922
ATOM     39  C40         0      22.543   5.182  30.158 -0.36 -0.00
+0.001    16.922
ATOM     40  C21         0      22.787   5.452  28.806 -0.28 -0.01
+0.013    16.922
ATOM     41  P2          0      18.317   3.163  25.929 -0.21 -0.00
+0.004    16.922
```

```
ATOM     42  C18         0      18.916   1.734  26.920 -0.28 +0.01    -
0.021    16.922
ATOM     43  C15         0      18.207   0.565  26.973 -0.39 -0.01
+0.013    16.922
ATOM     44  C14         0      18.751  -0.551  27.583 -0.51 -0.00
+0.001    16.922
ATOM     45  C19         0      19.991  -0.509  28.108 -0.47 -0.00
+0.000    16.922
ATOM     46  C20         0      20.738   0.688  28.070 -0.32 -0.00
+0.001    16.922
ATOM     47  C28         0      20.166   1.809  27.437 -0.24 -0.00
+0.013    16.922
ATOM     48  C6          0      16.923   2.443  24.988 -0.23 +0.01    -
0.021    16.922
ATOM     49  C11         0      15.628   2.775  25.346 -0.31 -0.01
+0.013    16.922
ATOM     50  C10         0      14.533   2.260  24.683 -0.34 -0.00
+0.001    16.922
ATOM     51  C9          0      14.719   1.385  23.677 -0.28 -0.00
+0.000    16.922
ATOM     52  C8          0      15.960   0.972  23.368 -0.18 -0.00
+0.001    16.922
ATOM     53  C7          0      17.068   1.510  24.013 -0.21 -0.01
+0.013    16.922
ATOM     54  C1          0      17.558   4.247  27.165 -0.19 -0.03
+0.069    16.922
ATOM     55  C2          0      16.662   3.714  28.069 -0.22 -0.02
+0.033    16.922
ATOM     56  C3          0      16.042   4.515  29.013 -0.37 -0.00
+0.004    16.922
ATOM     57  C4          0      16.298   5.842  29.077 -0.27 -0.01
+0.019    16.922
ATOM     58  C5          0      17.150   6.350  28.171 -0.17 -0.06
+0.117    16.922
ATOM     59  N1          0      17.808   5.585  27.198 -0.06 +0.12    -
0.260    16.922
TER
ENDMDL
```

Data A6. The final GA docked state for complex **4** docked with the 2YLY receptor: sulfonamides as selective estrogen receptor beta agonists. The best model is represented below.

```
MODEL       91
USER    Run = 91
USER    Cluster Rank = 1
USER    Number of conformations in this cluster = 2
USER
USER    RMSD from reference structure       = 60.480 A
USER
USER    Estimated Free Energy of Binding    =   -7.13 kcal/mol
[=(1)+(2)+(3)-(4)]
USER    Estimated Inhibition Constant, Ki   =    5.96 uM (micromolar)
[Temperature = 298.15 K]
USER
USER    (1) Final Intermolecular Energy     =  -10.71 kcal/mol
USER        vdW + Hbond + desolv Energy     =  -10.72 kcal/mol
USER        Electrostatic Energy            =   +0.01 kcal/mol
USER    (2) Final Total Internal Energy     =   -9.14 kcal/mol
USER    (3) Torsional Free Energy           =   +3.58 kcal/mol
USER    (4) Unbound System's Energy  [=(2)] =   -9.14 kcal/mol
USER
USER
USER
USER    DPF = C:/Users/Wits-User/Desktop/Kim_docking/2yly_docking.dpf
USER    NEWDPF move     CIF_correct_model1.pdbqt
USER    NEWDPF about    6.032000 3.610000 8.921000
USER    NEWDPF tran0    -48.689897 -6.300314 -25.961999
USER    NEWDPF axisangle0     0.522880 0.800734 -0.292271 -166.910401
USER    NEWDPF quaternion0    0.519472 0.795515 -0.290366 -0.113980
USER    NEWDPF dihe0    157.29 18.85 -23.70 110.61 -62.15 68.84 -33.04
5.06 -105.61 -20.59 -152.45 -166.22
USER
USER                                x       y       z    vdW   Elec
q     RMS
ATOM      1 AG1          0     -49.430  -6.524 -25.714 -0.03 -0.00
+0.000    60.480
ATOM      2 BR1          0     -51.976  -6.987 -24.919 -0.63 -0.00
+0.000    60.480
ATOM      3  P1          0     -48.472  -5.209 -23.782 -0.09 -0.00
+0.004    60.480
ATOM      4  C42         0     -48.641  -6.093 -22.159 -0.12 +0.01    -
0.021    60.480
ATOM      5  C50         0     -49.764  -6.757 -21.871 -0.28 -0.00
+0.013    60.480
ATOM      6  C51         0     -49.828  -7.340 -20.695 -0.34 -0.00
+0.001    60.480
ATOM      7  C23         0     -48.819  -7.335 -19.747 -0.38 +0.00
+0.000    60.480
ATOM      8  C22         0     -47.690  -6.657 -20.061 -0.23 +0.00
+0.001    60.480
ATOM      9  C26         0     -47.567  -6.030 -21.255 -0.11 -0.00
+0.013    60.480
ATOM     10  C32         0     -46.655  -4.931 -23.860 -0.05 +0.00    -
0.021    60.480
ATOM     11  C49         0     -45.901  -5.958 -24.344 -0.15 -0.00
+0.013    60.480
ATOM     12  C27         0     -44.524  -5.857 -24.469 -0.21 +0.00
+0.001    60.480
```

```
ATOM     13  C43         0     -43.883  -4.728 -24.085 -0.21 -0.00
+0.000    60.480
ATOM     14  C29         0     -44.609  -3.679 -23.618 -0.12 -0.00
+0.001    60.480
ATOM     15  C48         0     -46.013  -3.767 -23.495 -0.04 -0.00
+0.013    60.480
ATOM     16  C17         0     -49.177  -3.577 -23.397 -0.05 -0.03
+0.064    60.480
ATOM     17  C52         0     -49.812  -2.897 -24.424 -0.06 -0.02
+0.032    60.480
ATOM     18  C31         0     -50.323  -1.610 -24.205 -0.06 -0.00
+0.001    60.480
ATOM     19  C33         0     -50.229  -1.023 -23.003 -0.05 -0.00
+0.003    60.480
ATOM     20  C41         0     -49.633  -1.713 -21.940 -0.04 -0.08
+0.160    60.480
ATOM     21  N2          0     -49.102  -2.998 -22.119 -0.03 +0.14    -
0.277    60.480
ATOM     22  P3          0     -48.610  -8.868 -26.235 -0.18 -0.00
+0.004    60.480
ATOM     23  C13         0     -47.300  -9.134 -27.496 -0.13 +0.00    -
0.021    60.480
ATOM     24  C47         0     -47.062  -8.268 -28.543 -0.13 -0.00
+0.013    60.480
ATOM     25  C46         0     -46.054  -8.519 -29.480 -0.22 -0.00
+0.001    60.480
ATOM     26  C25         0     -45.296  -9.646 -29.338 -0.31 -0.00
+0.000    60.480
ATOM     27  C16         0     -45.498 -10.508 -28.298 -0.33 -0.00
+0.001    60.480
ATOM     28  C12         0     -46.482 -10.235 -27.346 -0.22 -0.00
+0.013    60.480
ATOM     29  C24         0     -47.873  -9.626 -24.739 -0.19 +0.00
+0.069    60.480
ATOM     30  C30         0     -47.643 -10.971 -24.612 -0.29 +0.01
+0.033    60.480
ATOM     31  C37         0     -47.027 -11.444 -23.465 -0.34 +0.00
+0.004    60.480
ATOM     32  C38         0     -46.703 -10.569 -22.462 -0.21 -0.00
+0.019    60.480
ATOM     33  C34         0     -47.014  -9.260 -22.609 -0.23 -0.01
+0.117    60.480
ATOM     34  N3          0     -47.583  -8.755 -23.730 -0.11 +0.00    -
0.260    60.480
ATOM     35  C39         0     -49.898 -10.077 -26.723 -0.23 -0.00    -
0.021    60.480
ATOM     36  C36         0     -49.633 -10.740 -27.894 -0.28 -0.00
+0.013    60.480
ATOM     37  C45         0     -50.523 -11.644 -28.311 -0.36 -0.00
+0.001    60.480
ATOM     38  C44         0     -51.689 -11.929 -27.717 -0.40 +0.00
+0.000    60.480
ATOM     39  C40         0     -51.967 -11.223 -26.546 -0.44 +0.00
+0.001    60.480
ATOM     40  C21         0     -51.070 -10.277 -26.035 -0.34 +0.00
+0.013    60.480
ATOM     41  P2          0     -49.596  -5.006 -27.750 -0.10 -0.00
+0.004    60.480
ATOM     42  C18         0     -49.598  -6.049 -29.265 -0.12 +0.01    -
0.021    60.480
```

```
ATOM     43  C15         0     -48.679  -5.851 -30.259 -0.13 -0.01
+0.013    60.480
ATOM     44  C14         0     -48.588  -6.746 -31.310 -0.18 -0.00
+0.001    60.480
ATOM     45  C19         0     -49.382  -7.834 -31.354 -0.29 -0.00
+0.000    60.480
ATOM     46  C20         0     -50.341  -8.055 -30.342 -0.24 -0.00
+0.001    60.480
ATOM     47  C28         0     -50.410  -7.134 -29.279 -0.21 -0.00
+0.013    60.480
ATOM     48  C6          0     -48.247  -3.816 -28.083 -0.03 +0.01    -
0.021    60.480
ATOM     49  C11         0     -46.969  -4.107 -27.636 -0.07 -0.00
+0.013    60.480
ATOM     50  C10         0     -45.910  -3.249 -27.847 -0.09 +0.00
+0.001    60.480
ATOM     51  C9          0     -46.122  -2.077 -28.476 -0.06 -0.00
+0.000    60.480
ATOM     52  C8          0     -47.367  -1.726 -28.839 -0.02 -0.00
+0.001    60.480
ATOM     53  C7          0     -48.433  -2.600 -28.655 -0.02 -0.00
+0.013    60.480
ATOM     54  C1          0     -51.128  -4.053 -27.889 -0.11 -0.02
+0.069    60.480
ATOM     55  C2          0     -52.160  -4.545 -28.662 -0.20 -0.01
+0.033    60.480
ATOM     56  C3          0     -53.338  -3.833 -28.814 -0.23 -0.00
+0.004    60.480
ATOM     57  C4          0     -53.513  -2.637 -28.206 -0.20 -0.01
+0.019    60.480
ATOM     58  C5          0     -52.488  -2.159 -27.481 -0.12 -0.05
+0.117    60.480
ATOM     59  N1          0     -51.277  -2.838 -27.292 -0.05 +0.10    -
0.260    60.480
TER
ENDMDL
```